ABSTRACT

Targeting Cancer through Inhibition of Cathepsin B by Non-peptidic Small Molecule Thiosemicarbazones and Disruption of Pre-existing Vasculature by Colchicine-like Benzosuberene Analogues

Amanda K. Sevcik, Ph.D.

Mentor: Mary Lynn Trawick, Ph.D.

Cancer is a leading cause of death in men and women under in the United States and is characterized by uncontrolled cellular proliferation and migration (metastasis) which can impinge on surrounding organs, modify ordinary biological functions, and lead to death. This study focuses on two strategies for cancer therapy: targeting cathepsin B, an enzyme linked to tumor metastasis and progression, and the disruption of pre-existing tumor vasculature as a means to starve tumors of oxygen and nutrients.

Cathepsin B is a cysteine protease involved in intra- and extracellular degradation of proteins. Increased expression of cathepsin B has been documented in a number of different cancers and is associated with a poor disease prognosis, and increased tumor vascularization, degradation of the extracellular matrix, invasion, and metastasis. Inhibition of cathepsin B has the potential to arrest cancer cell invasion and metastasis. In a collaborative project between the Trawick and Pinney laboratories at Baylor University, a focused synthetic library of non-peptidic, small molecule thiosemicarbazone derivatives was screened for their ability to inhibit cathepsin B activity as monitored by a fluorogenic

enzyme assay. Five compounds were found to be effective inhibitors of cathepsin B in the low micromolar range, and the best four were characterized for their mode of inhibition. Kinetic analysis revealed that two of the active thiosemicarbazone compounds were time dependent, competitive, tight binding, slowly reversible inhibitors of cathepsin B. The other compounds analyzed were rapidly reversible, competitive inhibitors with K_I values in the low micromolar range.

Vascular disrupting agents (VDAs) are a promising class of anticancer drugs that selectively disrupt tumor vasculature. Tubulin-binding VDAs disrupt microtubule dynamics of endothelial cells lining tumor vasculature. A lead benzosuberene analogue exhibited extreme cytotoxicity against a panel of human cancer cell lines. The lead compound and several of its analogues were investigated for their ability to inhibit tubulin polymerization, bind to the colchicine binding site of tubulin as determined by a competitive radiometric binding assay and arrest human breast cancer cells in the G2/M phase of the cell cycle as indicated by flow cytometry. The results support the mechanism of action of the lead benzosuberene analogues as VDAs.

Targeting Cancer through Inhibition of Cathepsin B by Non-peptidic Small Molecule Thiosemicarbazones and Disruption of Pre-existing Vasculature by Colchicine-like Benzosuberene Analogues

by

Amanda K. Sevcik, B.S.

A Dissertation

Department of Chemistry and Biochemistry

Patrick J. Farmer, Ph.D., Chairperson

Submitted to the Graduate Faculty of
Baylor University in Partial Fulfillment of
the Requirements for the Degree
of

Doctor of Philosophy

Approved by the Dissertation Committee

Mary Lynn Trawick, Ph.D., Chairperson

Patrick J. Farmer, Ph.D.

Kevin G. Pinney, Ph.D.

Bryan F. Shaw, Ph.D.

Erica D. Bruce, Ph.D.

Accepted by the Graduate School
December 2013

J. Larry Lyon, Ph.D., Dean

Page bearing signatures is kept on file in the Graduate School

TABLE OF CONTENTS

TABLE OF FIGURES

LIST OF TABLES

LIST OF ABBREVIATIONS

AIAs	Angiogenesis inhibiting agents
AIIT	Annexin II heterotetramer
AMC	7-Amido-4-methylcoumarin
ATCC	American Type Culture Collection
BAC	Bacterial Artificial Chromosome
BSA	Bovine serum albumin
CA-074	*N*-(3-Propylcarbamoyloxirane-2-Carbonyl)-Isoleucyl-Proline
CA-4	Combretastatin A-4
CCD	Charged coupled device
CPM	Counts per minute
CTSB	Cathepsin B
DAMA	*N*-deacetyl-*N*-(2-mercaptoacetyl)
DEA	Diethylaminoethyl
DMS	Dimethyl sulfoxide
DNA	Deoxyribonucleic acid
DOFA	[2-[2-(2,4-dioxo-1,3-thiazolidin-3-yl)ethylamino]2-oxoethyl] 2-furan-2-carbonylamino)acetate
DTT	Dithiothreitol
[E]	Enzyme concentration
ECM	Extracellular matrix
EDT	Ethylene diamine tetraacetic acid
EGF	Endothelial growth factor
EGT	Ethylene glyocol tetraacetic acid
EMT	Epithelial-mesenchymal transition
FDA	Federal drug administration
FISH	Fluorescent in situ hybridization
FITC	Fluorescein isothiocyanate
GAG	glycosaminoglycans
GDP	Guanosine 5′-diphosphate
GF/A	Glass fiber filter – absorption
GF/C	Glass fiber filter - combination
GF/F	Glass fiber filter – fine
GST	Glutathione S-transferase
GTP	Guanosine 5′-triphosphate
HIF1α	Hypoxia inducible factor
HUVEC	Human umbilical vein endothelial cells
[I]	Inhibitor concentration
IC_{50}	Half maximal inhibitory concentration
K_i	Dissociation constant for inhibitor binding
K_i^{app}	Apparent inhibition constant
K_M	Michealis-Menten constant
LDS	Lithium dodecyl sulfate

MAPs	Microtubule associated proteins
MDA-MB-231	M.D. Anderson medical branch cell line 231 (human breast carcinoma)
MES	2-(N-Morpholino) ethanesulfonic acid hydrate
MMP	Matrix metalloprotease
MPR	Mannose-6-phosphate receptors
mTOR	Mechanistic target of rapamycin
MW	Molecular weight
MYPT1	Myosin phosphate
NCI	National Cancer Institute
NF2	Neurofibromatosis type 2
NIH	National Institutes of Health
^{o}C	Degrees Celsius
OD	Optical Density
PDB	Protein databank
PEG	Polyethylene glycol
PES	Polyethersulfone
PI	Propidium iodide
PKA	cAMP-dependent protein kinase
PVDF	Polyvinylidene fluoride
RB	Retinoblastoma
RBD	Rho-binding domain
RC-DC	Reducing agent compatible/detergent compatible
RNAse A	Ribonuclease A
RFU	Relative fluorescence units
SAR	Structure activity relationship
SDS-PAGE	Sodium dodecylsulfate polyacrylamide gel electrophoresis
Src	Sarcoma
TBST	Tris buffered saline Tween 20
TEM	Tetraspanin-enriched microdomains
Tris	Tris(hydroxymethyl) aminomethane
TSC	Thiosemicarbazone
uPA	Urokinase plasminogen activator
UV-vis	Ultraviolet-visible
v_0	Reaction velocity (without inhibitor present)
VDA	Vascular Disrupting Agent
VEGF	Vascular endothelial growth factors
v_i	Reaction velocity with inhibitor present
V_{max}	Limiting velocity as substrate concentrations get large
Z-R-R-AMC	Benzoxycarbonyl arginyl-arginyl-7-amino-4-methylcoumarin hydrochloride

ACKNOWLEDGEMENTS

I would like to thank the Lord for placing people in my life to support me and lift me up when I am weak, reminding me that I do not have to do things alone. Thank you God for walking with me, holding my hand and guiding me in all my endeavors. Thank you to my husband, Richard, for embarking on this journey of grad school with me, I am so happy we have done this together; there is no one else I would rather have endured this time with. You never doubt my ability which means so much to me. I would like to thank my kids for being a constant reminder that there is more to life than just work. Thank you for all the hugs and kisses when I needed them most. Thank you to Morgan Cooper, my amazing friend, who has offered her support and time to help me finish my dissertation. You are awesome, thank you. Thank you to my parents for their support and love and unceasing prayers. Wendy, your battles with cancer through my graduate work have been painful and scary but have shown me how much I love you and how important research in the cancer field is. I can only hope that we lose less of our family members to this disease in the future. Thank you Dr. Mary Lynn Trawick for the amazing amount of time you have invested in me. I am grateful for all the effort you have spent helping me get to this point and for your continued understanding. Thank you to my research group Dr. Strecker, Morgan Cooper, Sam Odutola and Dr. Chavarria for all your helpful discussions and friendships.

Thank you to Dr. Pinney and his research group for their collaboration and entrusting me with their compounds for testing. I would like to thank Oxigene for their financial support of the projects I have worked on throughout graduate school. Thank you

to the Department of Chemistry and Biochemistry for allowing me to complete my required courses and research while at Baylor. To my committee, thank you for your time and extreme patience with me, I appreciated it. Thank you to Dr. Michelle Nemec and the Molecular Biosciences Center at Baylor University for the use of their facility and instrumentation. Thank you Dr. Karban, Dr. Moehnke and Anthony Pena for building support. Thank you to Ms. Kallus, Ms. Cook and Ms. Hynek for their assistance with the graduate school, department and supplies.

CHAPTER ONE

Introduction to Cancer

Characteristics of Cancer

The mammalian system is controlled by a wide variety of enzymes and catalytic processes to maintain a healthy cell growth environment. The highly regulated balance between various processes allows for the normal function of the human body. Cell growth under normal conditions in the mammalian model involves the constant growth, maintenance, and controlled death of the individual units. Although these functions increase in embryonic development and in processes such as wound healing, they remain under tight control. The delicate balance can be disrupted via mutation or loss of control of the once intricately regulated key biochemical processes, the combinations of such having the potential of leading to disease, although not in every case. Cancer can be described as a disturbance of these processes and is characterized by uncontrolled cellular proliferation in addition to migration (metastasis) which can impinge on surrounding organs, preventing or modifying ordinary biological functions. These newly formed rogue cells aggregate to create a tumor mass which upon successive dissipation of their cellular components stimulate metastasis, a process in which expands the tumor's reach to distant locations in the body external to the initiation site[1]. Herein the loss of biological balance between cell proliferation and cell death, resulting in the unmediated cell production, is observed.[2] Over-expression or up/down-regulated cell components are major factors in the development of cancer. The increase in susceptibility to cell malfunctions can also be caused by intrinsic factors including damaged genetic material,

family history/inherited mutations, radiant damage, hormones and genetics or other extrinsic/environmental factors, and chronic infection.[3];[4] DNA damage can occur via many mechanisms including exogenous factors or metabolites for example, and include covalent changes in DNA structure and noncovalent changes in abnormal structures such as mismatching of base-pairs.[5] These damages are a normal part of the cell cycle and are amended by responses such as DNA repair, DNA damage checkpoints, apoptosis and transcriptional responses.[5] The processes in place to ameliorate the damages can themselves be damaged or ineffective which could lead to mutated or malignant cell proliferation.[6]

Cancer is a leading cause of reported death in men and women in the United States and the second most common cause of death in 2012 with statistics indicating 1 in every 4 deaths being related to the disease.[7] Recent studies have shown an increase of new cases of cancer and cancer related deaths to approximately 1.5 million in the year 2009 with a projection of 45% increase of the number of diagnosed cases in the next 20 years.[8] In 2012, the National Cancer Institute has estimated the diagnosis of over 1.6 million new cases of cancer, further supporting its significance in research for prevention, detection and treatment. There are many different types of cancer which can be divided into over thirty sub-types according to the National Cancer Institute, categories based on the origination of the cancerous cells, many of which late diagnosis of the disease can in turn lead to reduction of patient life. The five major categories of cancer based on histological characteristics are carcinoma, sarcoma, leukemia, lymphoma, and myeloma. Carcinoma accounts for 80-90% of all cancer cases and is epithelial in origin, initiating in internal and external body lining as the epithelial tissue coats and lines organs, internal

channels such as the colon and the epidermis. This type of cancer also affects glandular secretion such as mucous or breast milk and is easily spread through the soft tissue in the body.[9] Sarcomas are malignant tumors that originate in the connective tissues (such as muscle, fibrous connective tissue or cartilage) and can occur as a mass on the bone for example. Osteosarcoma (or bone cancer) falls into this category in addition to smooth muscle and mixed connective tissue cancers all of which often resemble the tissues from which they originate.[10] Sarcomas, although often very rapidly growing, are less commonly the cause of malignancy in the connective tissue of epithelial organs where carcinomas are more prevalent.[11,12] Leukemia is a cancer that originates from normal hematopoietic cells, blood cells, and attacks the bone marrow where the blood cells are produced, causing increased susceptibility to infection and malfunctions in the clotting of blood. The tumor cells developed in the bone marrow pass into the blood stream along with normal cells and are therefore free to move around the body wherever the blood is transported.[12] In addition to other factors, leukemia can be caused by ionizing radiation or retroviruses which in turn causes DNA base damage or insertional mutagenesis.[13,14] Lymphoma is the cancer of the immune/lymphatic system which is a network that involves the body's response to infection and other diseases. Lymphatic tissue is widely dispersed in the body and therefore lymphoma can originate in many parts of the body and is commonly detected in a lymph node or gland.[9] In all types of lymphoma, lymph tissues cells begin to grow abnormally with the potential to spread to organs affected by the lymphatic system. Indolent lymphomas begin their growth pattern slowly, increasing to more aggressive forms in subsequent years whereas the aggressive forms diffuse and quickly progress.[15] Myeloma is the last of the five major categories of cancer and

originates in the plasma cells of the bone marrow. This plasma cell malignancy is associated with bone disease, hypercalcemia, renal dysfunction, and peripheral neuropathy and has grown to become uniformly fatal due to drug resistance.[16,17]

In effort to characterize and organize the disease for further understanding, there are six hallmarks of cancer proposed, all alterations in normal cell physiology. These biological capabilities of developing tumors include continuous cell division, sustained growth signals, bypassing or evasion of growth suppressors, avoidance and/or resistance to cell death (apoptosis), tumor blood vessel growth which in turn induces angiogenesis, and the activation of metastasis and invasion (seen in Figure 1.1).[18,19]

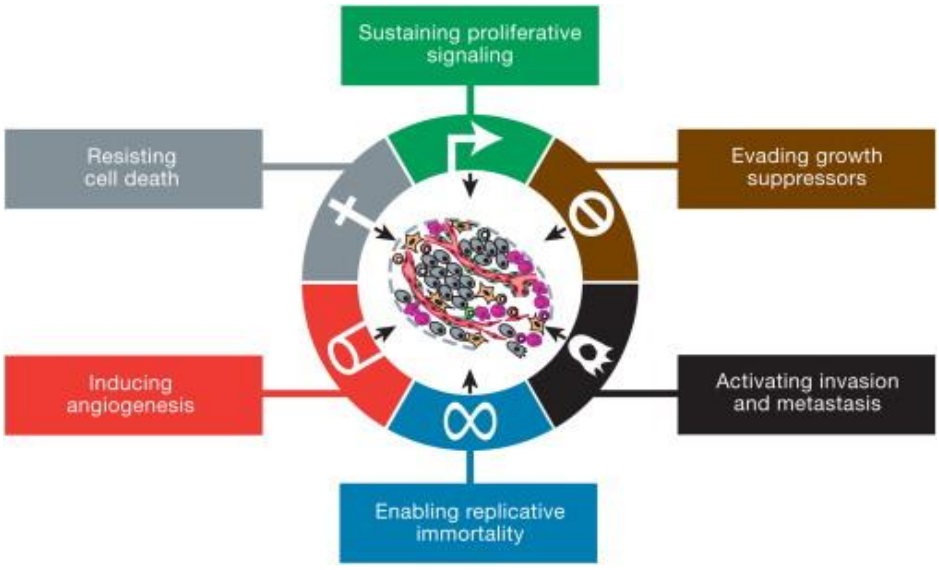

Figure 1.1 – Six hallmarks of cancer (reprinted with permission)[18]

Continuous Cell Division/Proliferation

Cell division in normal cells, as mentioned previously, is controlled by various checkpoints in the cell cycle as is seen in Figure 1.2 in addition to the production and release of growth promoting signals, allowing for cell entry into the cell cycle. Through

this regulation the body maintains a healthy cell number and size allowing for efficient use of nutrients and space without extensive cell death. The cell cycle consists of four ordered set of events or stages resulting in division of one cell into two daughter cells: G1, S, G2, and the M phase with the G0 phase for quiescent or resting cells.

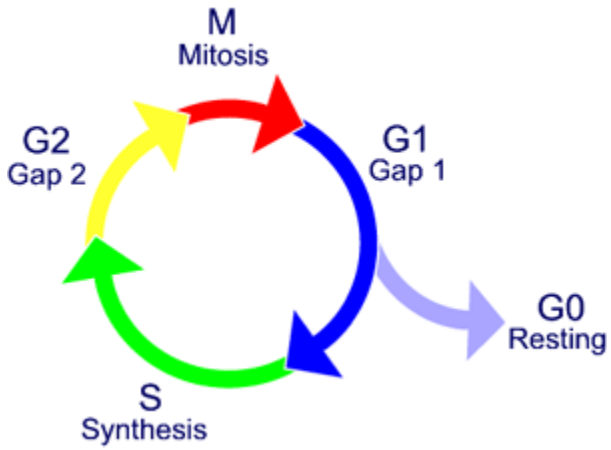

Figure 1.2 – Cell cycle (reprinted with permission by Goldwein, The Abramson Cancer Center of the University of Pennsylvania)

Interphase in the cell division is composed of G1, S and G2 phases. G1 is referred to as the gap or growth phase and is the longest part of the cycle. This phase is regarded as a pause where cells increase in size, carrying out normal metabolism and chromosome replication processes are prepared for the cells. Organelles are also duplicated in this phase. A checkpoint is located in this phase which is active in normal healthy cells and detects flaws in any critical events.[1] DNA replication occurs during the S phase, a period referred to as the synthesis phase. Here, the cell also synthesizes additional histones which are needed for doubling the chromosomal nucleosomes.[20] The G2 phase is another growth phase where the cell grows and prepares for mitosis. A second cell cycle checkpoint is located here. M phase, known as mitosis, occurs after the G2 phase and

here, the actual division from one cell into the two daughter cells occurs through the various mitotic steps: prophase, prometaphase, metaphase, anaphase, telophase and cytokinesis. G0 phase is the post-mitotic quiescent phase where the cells "rest" or remain temporarily or permanently. The arrested cells which have stopped dividing make up the majority of cells in the body.[20] The checkpoints/regulation points in the cycle of cancerous cells have sustained mutations or events which cause these checkpoints to function improperly, leading to unchecked errors in critical events and therefore the potential for uncontrolled cell division.[1] Telomere length at the end of chromosomes in addition to telomerase activity in normal cells allow for the senescence and crisis phases which induce eventual death, regulating cell division number. Cancer cells have either circumvented regulation by reduction or evasion of telomerase activity or have extended telomere length (or possible mechanism of maintenance of length), therefore creating immortality, commonly known as continuous or endless cell division.[18,21]

Sustained Growth/Proliferative Signals

Many cancer cells have the ability to sustain proliferative signaling whether via production of the growth factors themselves or by coercing healthy cells to produce and supply the abnormal cells with the necessary growth factors.[18] The cancerous cells can also deregulate receptor signaling of growth factors by increasing the amount of receptor proteins located on their surfaces, in turn allowing for an increase in sensitivity to any low abundant or concentration restricted growth factor ligands. Receptor tyrosine kinases, for example, are regulators in cell cycle and cell proliferation and mutations and activation of their signaling pathways in these RTKs in certain human tumors have been linked to cancerous activity.[22] Defects in negative feedback mechanisms, such as the Ras

oncoprotein, are also a cause of sustained proliferation where enhancement disrupts the homeostatic regulation of signal, leading to unmediated cellular events such as cellular growth.[18,23,24]

Evasion of Growth Suppressors

In addition to sustaining the growth/proliferative signals, cancers cells also must evade growth suppressors, natural and healthy gene related signals, to maintain their robust nature. One example is the suppression of the retinoblastoma gene in a broad range of cancers.[25] The RB gene is responsible for integrating various extra- and intra-cellular signals which permit or deny progression of cells into cycles of growth and division. Cells with mutations in the RB gene lose their critical regulation function associated with retinoblastoma, allowing for abnormal and potentially carcinogenic cells to proceed with growth and more critically, with division and proliferation.[18;11] Contact inhibition suppression is another example of evasion of growth suppressors. This commonly observed phenomenon in cell culture of cancer cells involves the neurofibromatosis type 2 (NF2) tumor suppressor gene which in combination with other proteins such as E-cadherin and the EGF receptor, mediates contact dependent inhibition of proliferation, as seen in Figure 3.[26,27] NF2 encodes for the protein Merlin which is a moesin-ezrin-radixin-like protein of the ERM (ezrin, radixin, moesin) family which are involved in the cross-linking between actin filaments and cell membrane proteins.[28] As is seen in Figure 1.3, tumor cells produce growth factors such as EGF or are supplied them via the tumor microenvironment. These factors assist in stimulating phosphorylation of Merlin via PKA (cAMP-dependent protein kinase) or PAK (p21-activated kinase) from

its closed, active form to its open, inactive form, permitting extensive tumor growth via the loss of contact inhibition signaling.

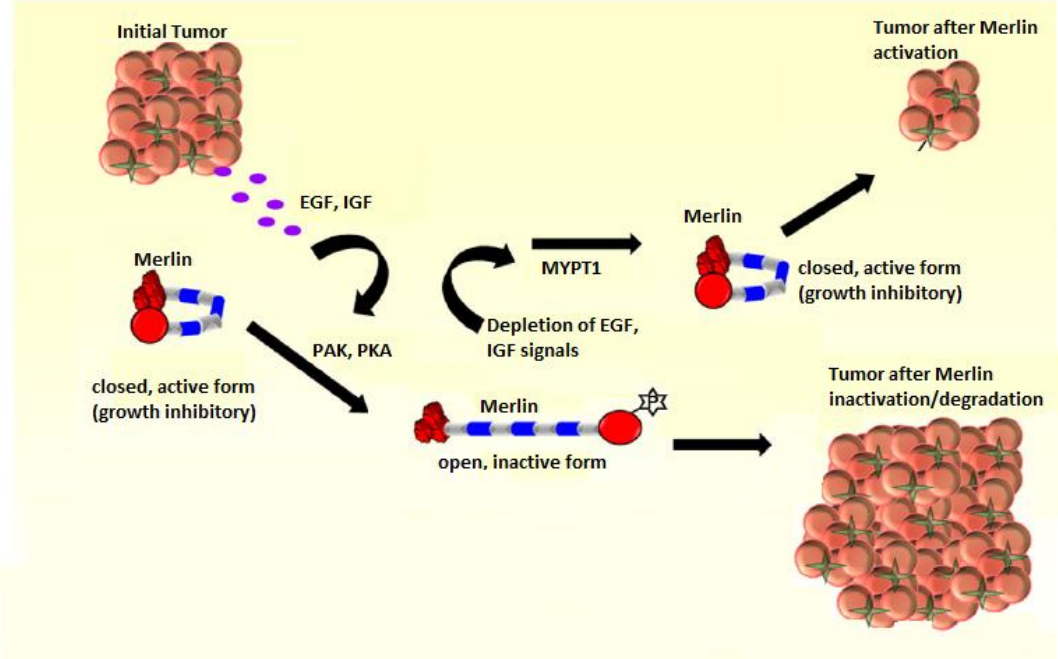

Figure 1.3 – Growth inhibition via cell-cell contact through NF2 (Merlin) activation (reprinted with permission)[27]

In contrast, the dephosphorylation of Merlin via MYPT1 (myosin phosphatase) activates the protein in response to high cell density, therefore inducing cell growth inhibition.[27] Healthy cells grown in culture will begin to slow in their growth when proximity to other cells increases. NF2 mutation or compromised expression leads to the loss of this function, allowing many cancer cell lines to flourish within a close cell-cell environment, one example of the cancerous cells' ability to evade or bypass growth suppressors.

Resistance to Cell Death/Apoptosis

Cell death occurs via at least three different mechanisms: apoptosis, necrosis and autophagy.[29] These processes in general serve as natural barriers to cancer development but can also be utilized to the tumor environment's advantage. Apoptosis is the naturally occurring biological event of programmed cell death to eradicate spent or redundant cells within a surviving population, maintaining physiologically appropriate cell numbers. Here, the process is an orderly set of events where the cell decreases in size, rounds up due to loss of cell-cell adhesion often forming blebs on the surface of the cell, condenses its chromatin and is engulfed by phagocytic or neighboring cells.[20,30] Apoptosis is caused by various controlled signaling events and can be triggered by physiological stress as is seen in Figure 1.4. In contrast, necrosis is premature cell death that is detrimentally caused by external factors such as infections or trauma. It involves a cluster or grouping of cell death in a specific area where the cytoplasm swells, chromatin becomes clumped and the nuclear and plasma membrane rupture.[11] The bursting cell can often cause surrounding tissue damage and in turn stimulate an inflammatory response.[30] Tumor cells have developed strategies to evade or decrease apoptotic cell death in multiple ways, one such avenue is the loss of function of the TP53 suppressor. TP53 is a sensor triggered by damaged DNA, specifically large amounts of DNA breaks or chromosomal abnormalities, to induce apoptosis via the regulation of two proteins, Noxa and Puma BH3. Carcinogenic cells bypass this abnormality sensor by increasing expression of anti-apoptotic regulators or by down-regulating the pro-apoptotic factors.[18] Autophagy is a process characterized by cell-physiological responses operating at low levels in which autodigestion of cells' organelles occurs in response to nutrient deprivation for cell

survival. Cells which have apoptotic defects have the ability to tolerate long term metabolic stress, in which case survival is often autophagy-dependent, see Figure 1.5.[32] Autophagy can be used by tumor cells in both survival as mentioned previously and also in the inhibition of autophagy processes, thereby evading cell death. Stress caused by metabolic, oncogenic or pharmaceutical sources is eluded and tumor growth continues.[33]

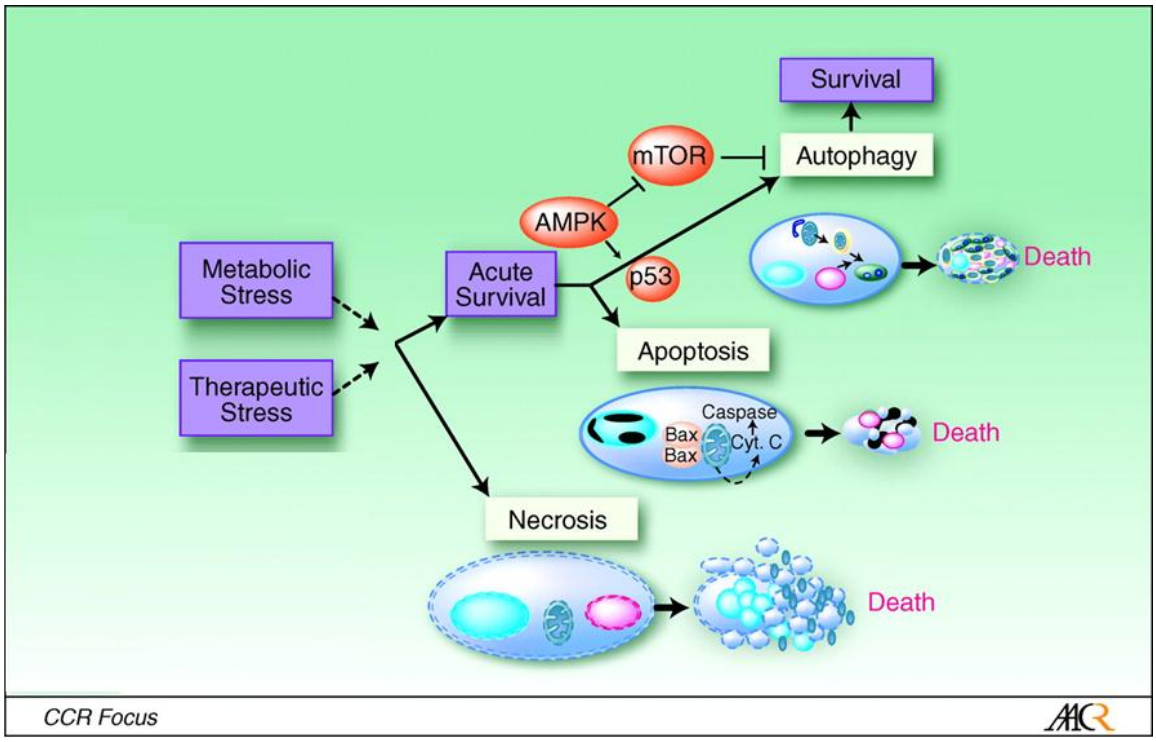

Figure 1.4 – Relationship between necrosis, autophagy and apoptosis (reprinted with permission)[31]

The mTOR kinase (mechanistic target of rapamycin) pathway is stimulated in cancer cells to block apoptotic activity and autophagy as a survival mechanism.[18] This pathway is one of many that can by modified or mutated in tumor cells to maintain resistance to death.

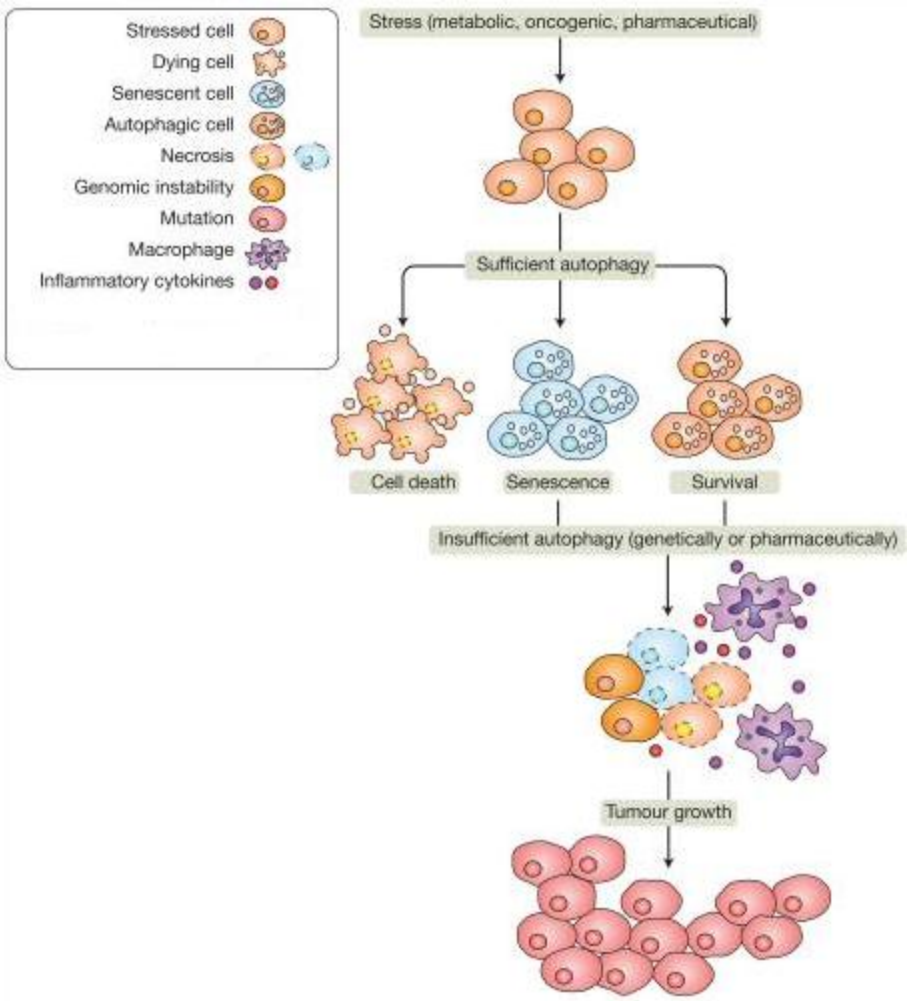

Figure 1.5 – Autophagy roles in tumor growth (reprinted with permission from Cambridge Press)[33]

Development of Tumor Vasculature/Angiogenesis

Healthy cells develop vasculature out of necessity as cell function and survival require the cells to maintain a relatively close proximity to capillary blood vessels, within 100 -200 μm in many cases.[19,34] Normal blood vessels are characterized by a well organized mature pattern, removing toxic and spent materials such as CO_2 and providing nutrients for the tissue source. These processes are regulated but after initial formation, normal vasculature becomes in the most part quiescent until necessity activates an

angiogenic switch whereby processes such as wound healing or reproductive cycling stimulate it.[18] Tumors are characterized by convoluted and excessive blood vessel branching, distorted or enlarged vessels, leakiness, erratic blood flow in addition to abnormal levels of endothelial cell proliferation as mentioned in the previous hallmarks of cancer.[35] In these cells, as the tumor grows in size, new blood vessel growth is stimulated via a process termed angiogenesis, allowing the cancerous tumor to remove necessary metabolic waste as the rapidly dividing cells produce it.[20] In normal wound healing, for example, angiogenesis is still chaotic but slower than in tumor growth and eventually becomes remodeled and growth begins to be slow. Normal microtubules, which are structural components in the vasculature, are responsive to growth factor stimulation and remain dynamic although they are more stabilize than tumor cells due to protein interactions. Tumor vasculature is overstimulated as there are multiple growth factors encompassing the neovasculature that have an effect before remodeling of structural features can occur. This unchecked "active angiogenic switch" causes the continuous formation of new vessels which support the continuing tumor growth.[36] The persistent new blood vessel growth prevents the tumor cells from becoming necrotic or apoptotic, thereby allowing for tumor volume increase unhindered by metabolic waste, cell death, and limited nutrient delivery.[37] The angiogenic switch is regulated by factors that can be thought of as a balance to maintain the correct and healthy on/off position as is diagramed in Figure 1.6. When the balance is tilted toward the pro-angiogenic factors (activators) such as vascular endothelial growth factors (VEGF), the switch is activated and an increase in tumor (or normal) angiogenesis and thus tumor growth can be observed.[38] Inhibitors produced by a balance in favor of the anti-angiogenic switch are

angiostatin which is produced by the primary tumor to mediate suppression of new blood vessel formation and thrombospondin-1 which is a large extracellular matrix glycoprotein also inhibiting neovascularization.[30]

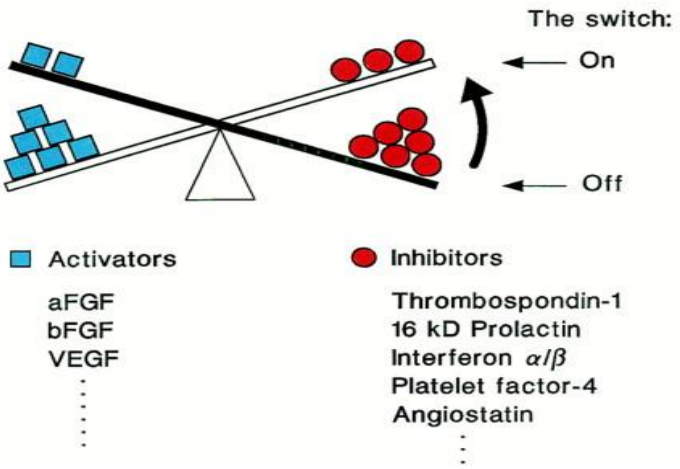

Figure 1.6 – The balance of the angiogenic switch (reprinted with permission)[36]

Angiogenesis can be promoted in cancer cells by (VEGF) to stimulate endothelial cells on surrounding blood vessels to proliferate. This pro-angiogenic factor is upregulated upon hypoxic conditions in addition to upstream regulation and oncogene signaling such as Ras.[36] Hypoxia is the lack of oxygen associated with rapidly growing tissue often seen in cancerous tumors. The pathway involving hypoxic conditions and VEGF is seen in Figure 1.7. Here, hypoxia inducible factor 1 (HIF1α) binding to the VEGF gene increases transcription rate, in turn increasing biologically active secreted VEGF, leading to downstream effects including angiogenesis. From Figure 1.7, it can be seen that angiogenesis is by no means a simple process and involves a number of additional factors (not all are represented in the pathway from Figure 1.7) such as various

forms of TGF-β, basic fibroblast growth factors and interleukin-8 in addition to several distinct types of cells which compose the capillary and larger vessel construction.[34]

Vasculature and Treatment

Vascular disrupting agents (VDAs) act by selectively disrupting the existing blood flow of tumor blood vessels essentially starving it of nutrients and oxygen and poisoning them with cell-produced metabolic waste, in contrast to angiogenesis inhibiting agents (AIAs) which target the growth of neovasculature.[40] The chaotic and immature nature of tumor vasculature is exploited by vascular disrupting agents as they facilitate vascular collapse.

Activation of Tumor Invasion and Metastasis

In order for cells to migrate to distant locations, a source of transport must be facilitated. Vasculature, as previously mentioned, is one route of travel as is the lymphatic system. Metastasis is defined as a "multistep process during which malignant cells spread from the primary tumor to discontiguous organs". These destructive cells relocate to various parts of the body in effort to re-colonize and distribute their cancerous properties to these tissues. Primary tumors in comparison to secondary tumors cause fewer debilitating side effects and deaths than do metastatic tumors as metastasis is the main causes of death within cancer patients.[30,41] There are 10 proposed steps in the complex metastatic process but 2 major phases include the physical dissociation of the cancer cells from their primary tumor to distant or surrounding tissue and the modification of these cells to the new environment, allowing for successful growth.[18]

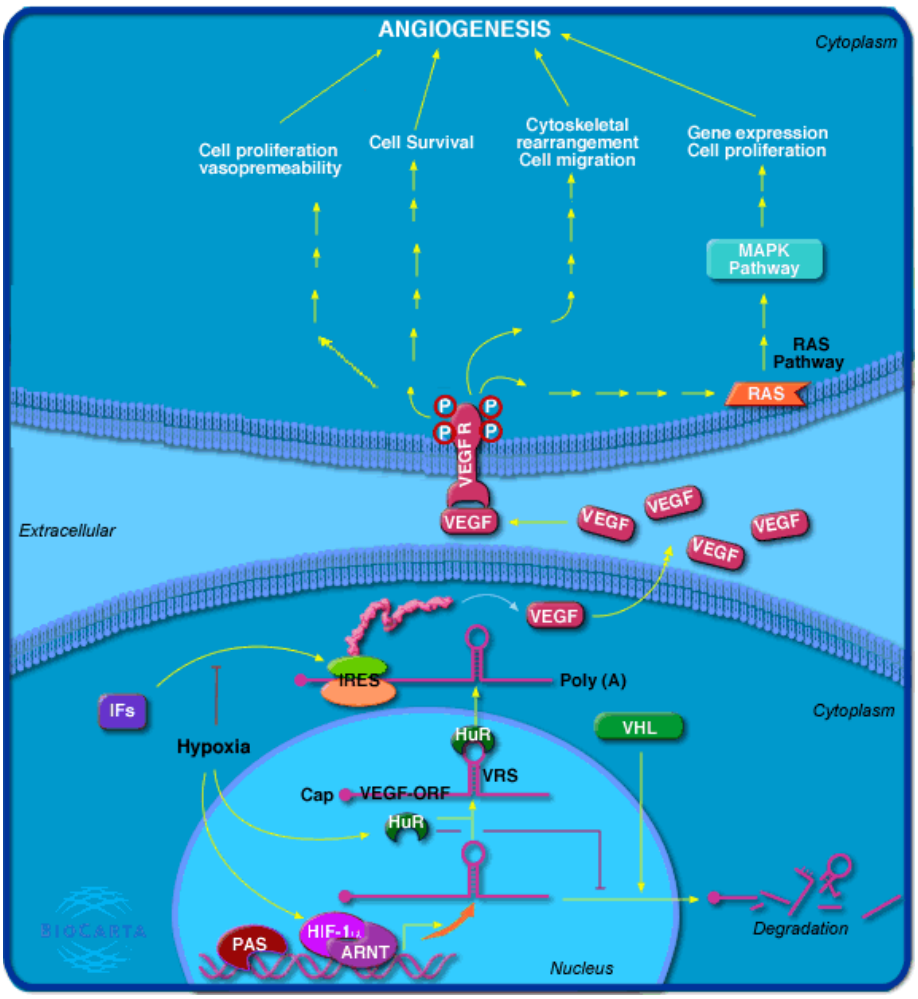

Figure 1.7 – VEGF/hypoxia effects on angiogenesis (reprinted with permission, Biocarta)[39]

Prerequisites for establishment of metastasis include loss of cellular adhesion, increase in invasiveness leading to invasion of cancer cells through the basement membrane into blood vessels (intravasation), survival within the blood vessels and extravasation from the blood stream.[42]Invasion is the process of transversing barriers, such as the extracellular matrix, in order for cells to migrate. Invasion and metastasis can be regulated by the epithelial-mesenchymal transition (EMT) in which neoplastic epithelial cells acquire a more mobile mesenchymal phenotype through over-expression of a set of transcription factors such as Snail or Slug, also inducing the loss of adherens

junctions, crucial for epithelial adhesion, and expression of matrix degrading enzymes, seen in Figure 1.8.[43,18] Here, normal epithelial cells lining the walls of the vasculature change their physical appearance to become more adenoma-like, a transition assisted by the loss of E-cadherin function. The EMT pathway is thought to orchestrate the necessary conditions required for the invasion-metastasis cascade, supplementing the major facilitating mechanisms of uncontrolled epithelial proliferation and angiogenesis.[44]

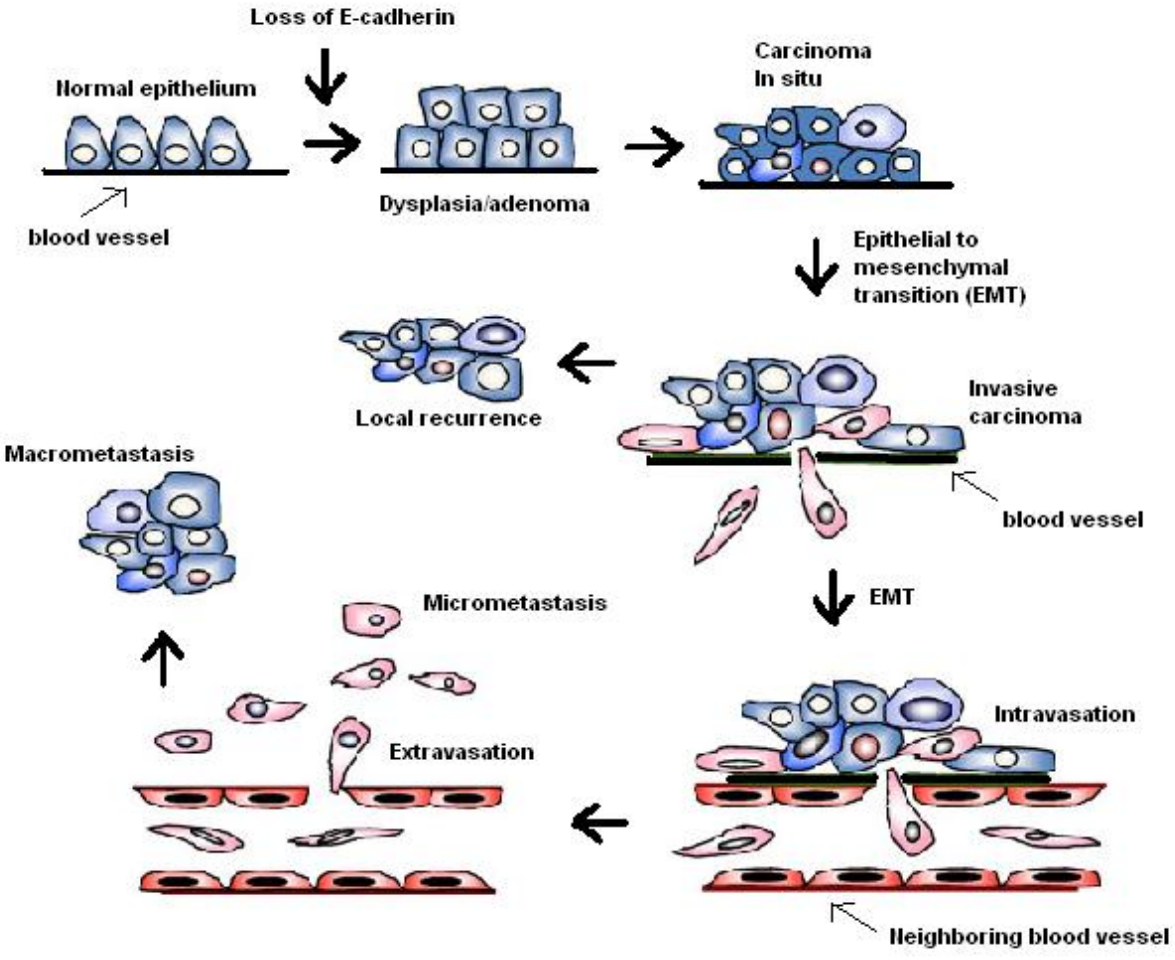

Figure 1.8-Epithelial to mesenchymal transition (reprinted with modification by permission)[44]

In addition, the transcription factors of invasive and metastatic cells have the ability to suppress E-cadherin gene expression which is one of the main molecular events responsible for control of motility and cellular adhesion, see Figure 1.8.[45] E-cadherin is tethered to cytoskeleton components such as actin via catenins providing tensile strength of cell-cell junctions, resisting epithelium to mesenchymal transition. Loss of E-cadherin allows for β-catenin to become freely associated in the cytosol, upon which it translocates to the nucleus and associates with various transcription factors that assist with the EMT scheme.[34] Once cells have transitioned to their dysplasia (abnormal) form, they continue their transformation into carcinoma-like cells where they gain the ability to become malignant and invasive in nature allowing for passage into the lymphatic or blood vascular systems via intravasation. Once inside the blood vessels, the circulating tumor cells can extravasate (leave the current vasculature) to secondary sites leading to micrometastasis and macrometastasis, where cells have the potential to lie dormant and undetected for years or to grow into new tumorous masses.[44] As seen in the other cancer hallmarks, there are many signals that trigger cancer metastasis and invasive ability; others include matrix metalloproteinases, small Ras-like GTPases and the Wnt protein.

Metastasis and Treatment

Cancer metastasis, as previously stated, is a major problem as it is the primary source of death among cancer patients and is not well treated. In various stages of tumor growth and metastasis, surgical removal of tumors is not effective and until further optical-imaging guided surgical techniques can be established, alternate methods of treatment are required. Targets for chemotherapy include destruction and collapse of the tumors themselves, targeting and inhibiting the specific enzymes that appear to be linked

to tumor metastasis and progression, and prevention of continued growth of pre-existing tumors. Many of the dysregulated enzymes implicated in cancer target decomposition of structural features in the cell promoting metastasis and often invasion.[46] Tumor vasculature provides an opportunity for selective intervention exploiting the differences from normal vasculature. Although many studies probing potential chemotherapeutic molecules have been performed to date, the search for a more efficient and highly selective drug therapy regime is on-going. Targeted therapy maintains the goal of increased efficacy with the reduction of deleterious side effects to healthy cells and the patients themselves.

Statement of Purpose

Specific Aim 1 –Ccathepsin B

There is an urgent need for therapeutic agents targeting the invasive potential of tumor cells. Cathepsin B targeted inhibition is the goal of project 1. The process of cancer invasion and metastasis is known to be mediated by a number of different proteases which catalyze the degradation of the basement membrane, a structure that confines the solid tumor.[47] Cathepsin B is a strong proteolytic enzyme that is secreted from the cell and is involved in the remodeling of the extracellular matrix and apoptosis in normal cells.[2] In many diseases including cancer, cathepsin B expression is increased and there is a change in enzyme localization which leads to the accessibility of the enzyme to ECM.[48] Degradation of the ECM can lead to intravasation and extravasation and in turn to colonization of tumor cells to new locations being a crucial step in invasion and metastasis.[49] Inhibitors capable of reducing the activity of cathepsin B have been found

effective in reducing the invasive potential of tumor cells but due to their peptidic nature, have low bioavailability and are not considered to be effective therapeutic candidates.[50] In a collaborative effort between the Trawick and Pinney laboratories (Baylor University) a focused library of small molecule non-peptidic thiosemicarbazone compounds (synthesized by the Pinney laboratory) provided a number of effective inhibitors of the enzymes cruzain (a cathepsin L like enzyme), cathepsin L and cathepsin K.[51-55] Therefore this library was screened against the related cysteine protease cathepsin B. Advanced kinetics studies were carried out on the most potent inhibitors to elucidate their mechanism of action.

Specific Aim 2– Vascular Disrupting Agents

The second project involves the targeting of existing vasculature, exploiting the structural components of tumor blood vessels and their disassembly. Tumor vasculature is disorganized, tortuous and hypoxic in many cases and is vital for tumor growth as it requires nutrients and oxygen. Vascular disrupting agents cause blood flow shutdown of the vasculature which is selective to the tumor environment based on these characteristics, subsequently causing tumor necrosis.[56,57] Vascular targeting has been shown to eliminate large tumors in animal studies but often leaves the tumor periphery known as the viable rim intact. Thus VDAs are now being investigated in combination therapy with standard chemotherapeutic agents in clinical trials.[57-59]

Inspired by the established tubulin binding VDAs, combretastatin A-4 (CA4) and colchicine, a series of benzosuberene analogues were designed and synthesized by the Pinney Laboratory in a collaborative project with the Trawick laboratory.[40,60] Several of these new analoges were found to be extremely cytotoxic against a panel of human

cancer cell lines. In this study the mechanism of action of the lead benzosuberene compound and several of its analogues were investigated for properties characteristic of VDAs: the ability to inhibit tubulin polymerization, binding to the colchicine binding site of tubulin as determined by a competitive radiometric binding assay and the ability to arrest human breast cancer cells in the G2/M phase of the cell cycle as indicated by flow cytometry.

CHAPTER TWO

Introduction to Cathepsin B

Cysteine Proteases-Introduction to Cathepsins

The process of cancer invasion and metastasis is mediated by a number of different proteolytic enzymes such as cysteine, serine, aspartic, and matrix metalloproteases which catalyze the degradation of the basement membrane, a structure that confines the solid tumor.[47] The papain family of cysteine proteases is the largest among the cysteine proteases and includes the cysteine cathepsins which in addition to playing a housekeeping role as mammalian lysosomal protein degrading enzymes, several are involved in the remodeling of the extracellular matrix. Structural features typically associated with enzymes within the papain family are two domains, an α-helical dominated left domain and a β-barrel motif right domain separated by a V-shaped cleft. The papain members also share a catalytic cysteine, histidine and asparagine which interact with the right and left domains, leaving the active site cleft in a conformation for substrates to bind in an extended orientation.[61,62] The active site cysteine is located on the left domain at the N-terminus of the central helix and forms a thiolate-imidazolium ion pair with the reactive site histidine, located within the β-barrel on the right domain, and is essential for the enzymes' proteolytic activity.[63] The sulfhydryl group of the active site cysteine mediates protein hydrolysis via nucleophilic attack on the substrate peptide, often with broad specificity cleaving preferentially after basic or hydrophobic residues.[64,63] The cathepsins are part of the CA clan and the papain family (cathepsin B, K, L, S, H, O, W, X/Z, etc.) and are predominantly endopeptidases that are localized

intracellularly in the endolysosomal vesicles where they function as key enzymes in processes such as cell membrane degradation and cell turnover, having enormous disruptive potential with lysosomal concentrations up to 1 mM.[61,2] Endopeptidase versus exopeptidase cleavage is seen in Figures 2.1 and 2.2.

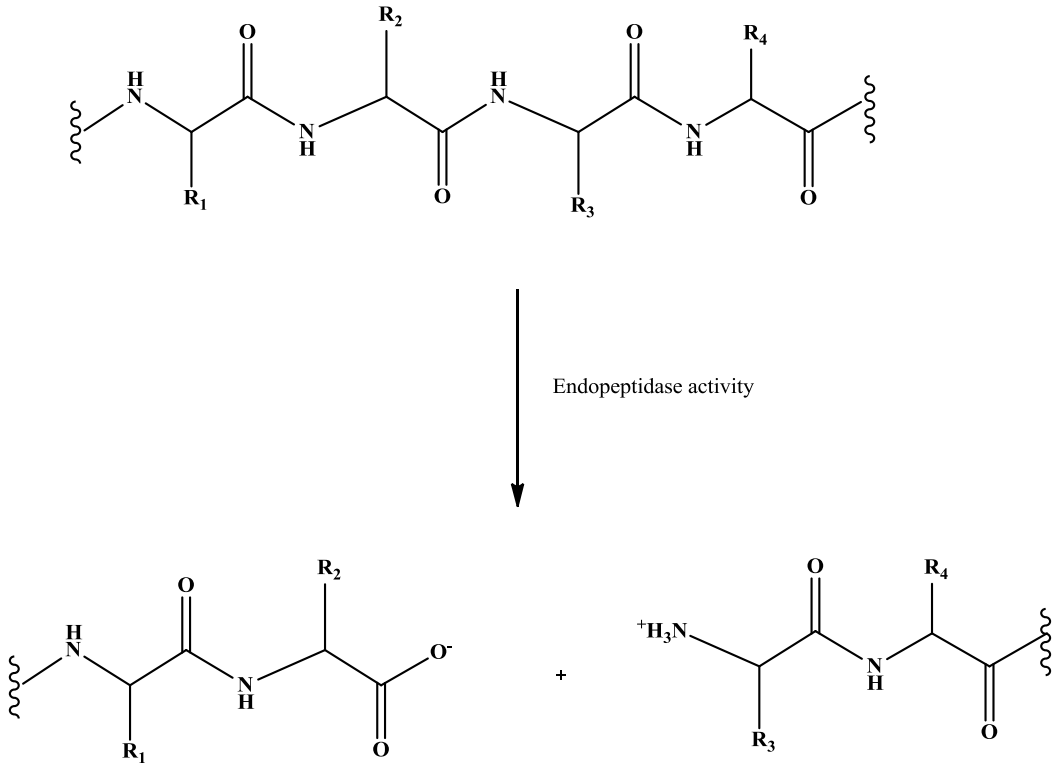

Figure 2.1 – Endopeptidase cleavage of peptide chain

Most cathepsins have endopeptidase activity, such as cathepsins S and L, or have the ability to act as both and endopeptidase and an exopeptidase, which is the case in cathepsins B and C.[46] Specifically cathepsin B is both an endopeptidase and a carboxydipeptidase (Figure 2.2). This class of enzymes is generally confined to the acidic environment of cellular compartments where they are optimally active but can be found outside these vesicles to assist with specific nuclear functions and mediate cell death processes.[65]

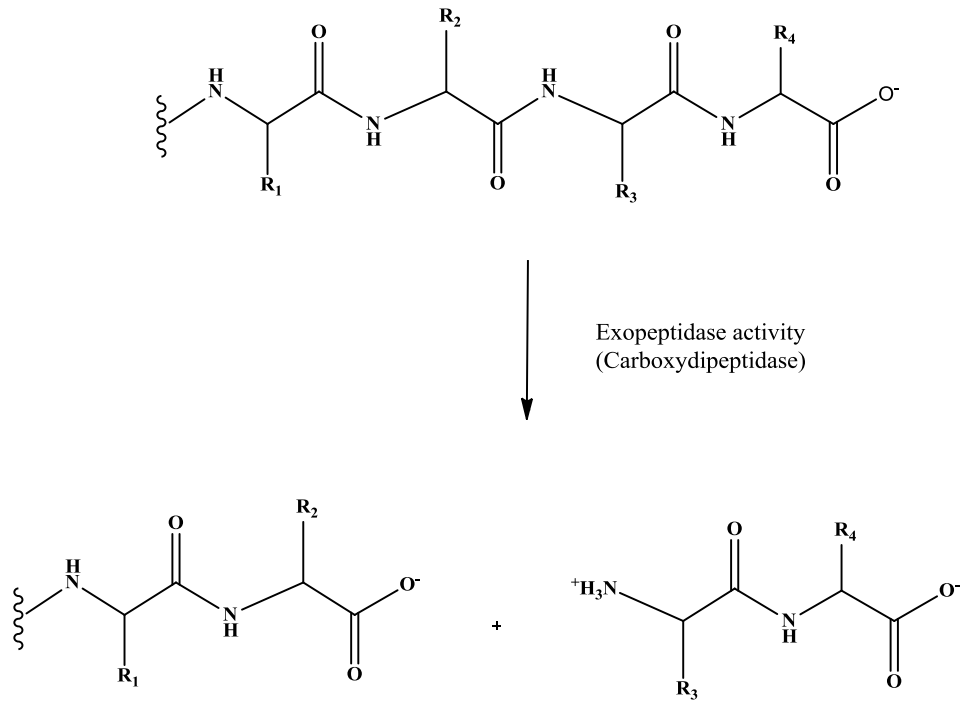

Figure 2.2 – Exopeptidase (carboxydipeptidase) cleavage of peptide chain

In addition to ECM degradation, they are also involved in the MHC class II antigen pathway (major histocompatibility complex) where they assist in antigen processing.[66] Lysosomal cysteine proteases are synthesized as inactive precursors, activated following cleavage and dissociation of the N-terminal portion. These proregions stabilize the protein against pH induced denaturation and are thought to be important for proper folding of the newly synthesized polypeptide chain.[62] Recent studies have shown cysteine cathepsins to be involved in the growth of metastatic tumors, formation of premalignant lesions, and angiogenesis.[67] In healthy cells, the activated forms of cathepsins are highly regulated by endogenous inhibitors known as the cystatins which can be grouped into stefins and kininogens.[68-69] These general cathepsin inhibitors aid in the maintenance of the enzymes' normal metabolic functions of protein turnover and

apoptosis, inhibiting the endopeptidase forms of cathepsins in the pM range and the exopeptidase forms in the nM range. [61]

Cathepsin B – Functions

Cathepsin B, EC 3.4.22.1 (enzyme classificiation number), is one of the most well characterized mammalian enzymes of the cysteine peptidases and was first identified in the 1970s with the amino acid sequence elucidated in the 80s followed by the crystal structure in the 90s.[61] This enzyme plays a causal role in the remodeling of the ECM, acting directly or indirectly upon the structure. In addition, cathepsin B is able to hydrolyze the ECM components collagen IV, fibronectin and laminin thereby allowing for the tumor cells to permeate surrounding tissues and vasculature.[68,70,71,63] Due to its ubiquitous nature, it is involved in various biological processes such as protein turnover in the lysosomes, bone remodeling, site-specific cleavage of human prorenin processing, and self-protection of cytotoxic T lymphocytes during degranulation.[72,48] In addition to these physiological processes, overexpression of cathepsin B is also implicated in disease related remodeling of tissue with connection to inflammation, Alzheimer's disease, and tumor metastasis in various types of cancers including lung, breast, colorectal, melanoma, glioma, and prostate.[48] In general, cathepsin B expression, activity, and secretion is increased in tumors in addition to a change in localization.[73] In healthy tissue, cathepsin B is localized in the perinuculear vesicles but adopting a more peripheral distribution and associating with the plasma membrane in carcinogenic cells.[48] Tissue remodeling is important in malignant tumor progression as it provides the correct environment for tumor growth, angiogenesis, invasion and metastasis.[74,75, 68, 69] Cathepsin B expression in tumors correlates with angiogenesis, remodeling the ECM to allow for

neovascularization, specifically in primary colon cancer where the overexpression of the enzyme leads to more amplified angiogenic effects.[76,77] Elevated serum levels of cathepsin B are associated with advanced tumor stages and progression of the disease, where the survival rate has been inversely correlated to the cathepsin B activity ratio.[78] In many cases, the increase in cathepsin B correlates with an increase in vascular density, tumor burden and poor survival of cancer patients.[65] A deficiency of this enzyme has shown slower cancer progression and reduced invasion in mouse models, with the ablation of cathepsin B (in combination with cathepsins L, S and H) resulting in impaired vascularization in angiogenesis driven cancers such as pancreatic.[65] In a 2007-2008 treatment study, combination of generic cysteine cathepsin inhibition with two chemotherapeutic administrations lead to increased pronounced tumor regression, a decrease in invasiveness and an increase in survival in a mouse model but due to poor bioavailablility and short circulation half lives, the studies were unsuccessful.[79,80] These studies also failed to affect distant metastasis efficiently. Further studies targeted cathepsin D, L and B *in vitro* in metastatic melanomas and primary lesions (in addition to *in vivo* mouse models with aggressive metastatic melanomas) with inhibitors specific for each protease seen in Figure 2.3; Pepstatin A, Cathepsin Inhibitor II and CA-074/CA-074Me, respectively.[81] This study showed that targeting cathepsin B significantly impaired the invasive and metastatic potential of cell, unlike that of the cathepsins D and L.[81] Subsequent animal trials utilizing the cathepsin B specific inhibitor CA-074 had an anti-metastatic effect at distant locations and were able to sustain the effect in the presence of aggressive tumors, proposing that specific targeting of the cathepsins leads to more effective therapeutic potential.[82] It was also postulated that due to the many roles of

cathepsin B within the metastatic cascade, specific targeted therapy of this enzyme in combination with general chemotherapy treatments has therapeutic and clinical potential.[82] Potential strategies suggested include the use of immunotherapeutic methods, specifically the *in vivo* studies targeting cathepsin B with antibodies against this cysteine protease.[81]

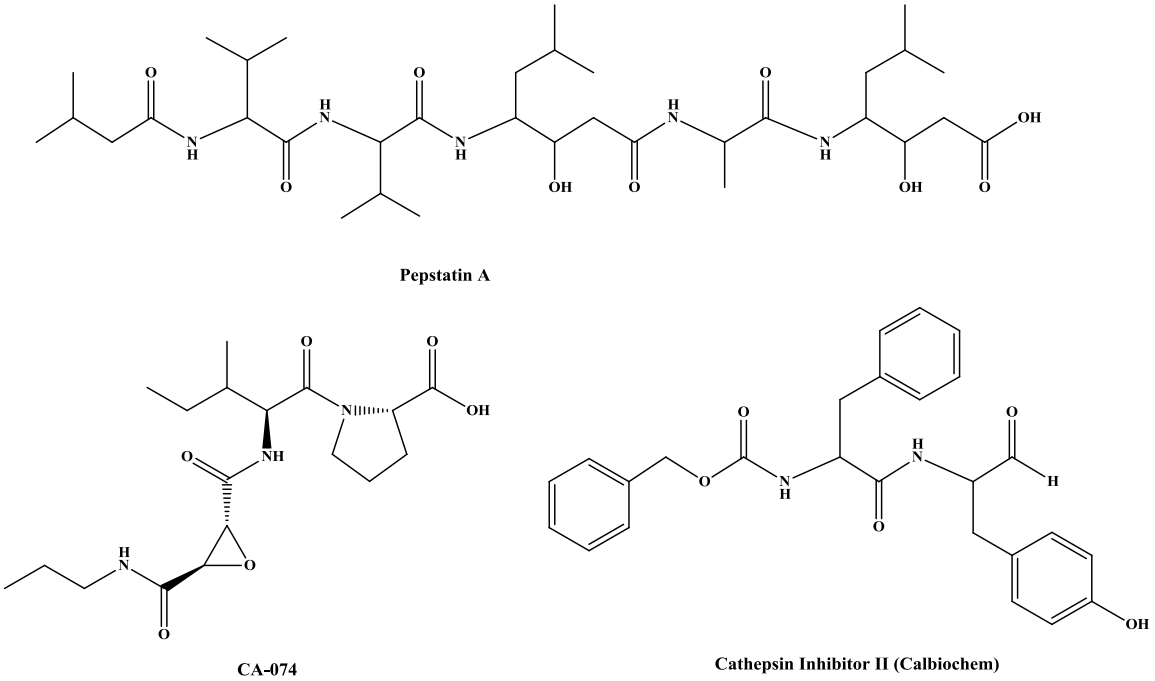

Figure 2.3 – Specific cathepsin inhibitors used in metastatic melanoma study[81]

Cathepsin B – Localization/Processing in Normal Cells
:

The complete amino acid sequence for cathepsin B prior to any processing is seen in Figure 2.4 where the signal peptide is in green (residues 1-8), the propeptide region in red (residues 9-79), the light chain in fuchsia (residues 80-128), and the heavy chain in blue (residues 129-333). Similar to many lysosomal enzymes, cathepsin B is synthesized as a virtually inactive precursor known as a preproenzyme. Although the proform

possesses almost no activity, this nascent state retains a very low level of catalytic activity.[84] Processing of cathepsin B in cells is seen in Figure 2.5.

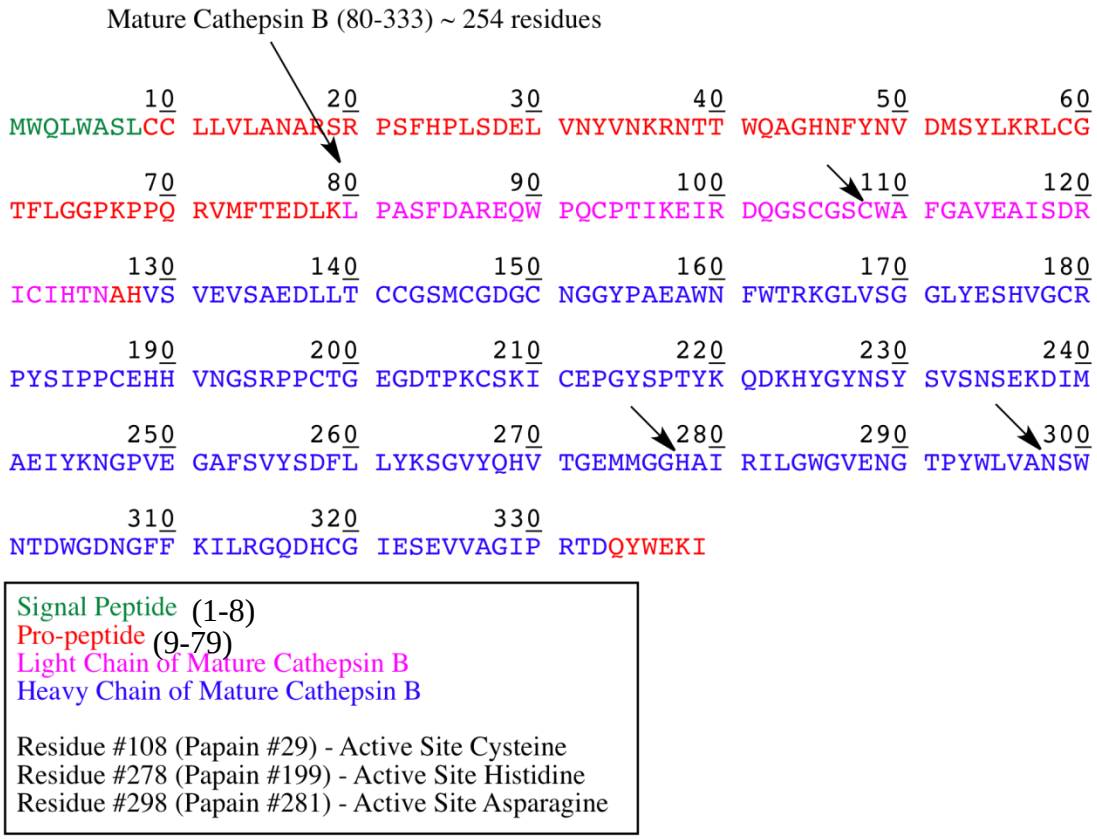

Figure 2.4 – Uniprot.org (PO7858) cathepsin B amino acid sequence[83]

It then folds down in the center as a helix and runs along the active site cleft in an opposite configuration to the substrate. This renders the enzyme inactive as it shields the active site from solvent and prevents substrate hydrolysis.[69,61,89] Activation can occur via three routes: autocatalyticly, glycosaminoglycan (GAG) interaction, and other protease interactions. In the first activation route, the "inactive" procathepsin is transported via late endosomes to the lysosomes where the acidic environment assists cleavage of the proform in a bimolecular process.[86] The propeptide experiences less affinity for the enzyme's mature region therefore autocatalytically cleaves from the active site,

producing mature cathepsin B.[84] The lysosomal location of this enzyme in normal cells is demonstrated by its sedimentation in subcellular fractions containing other lysosomal enzymes. Within the lysosome, the enzyme is processed to a single chain active form (31kDa) after dissociation from the MPRs.[90] Further processing produces a active double chain form composed of a 25/26kDa heavy chain and a 5kDa light chain.[90]

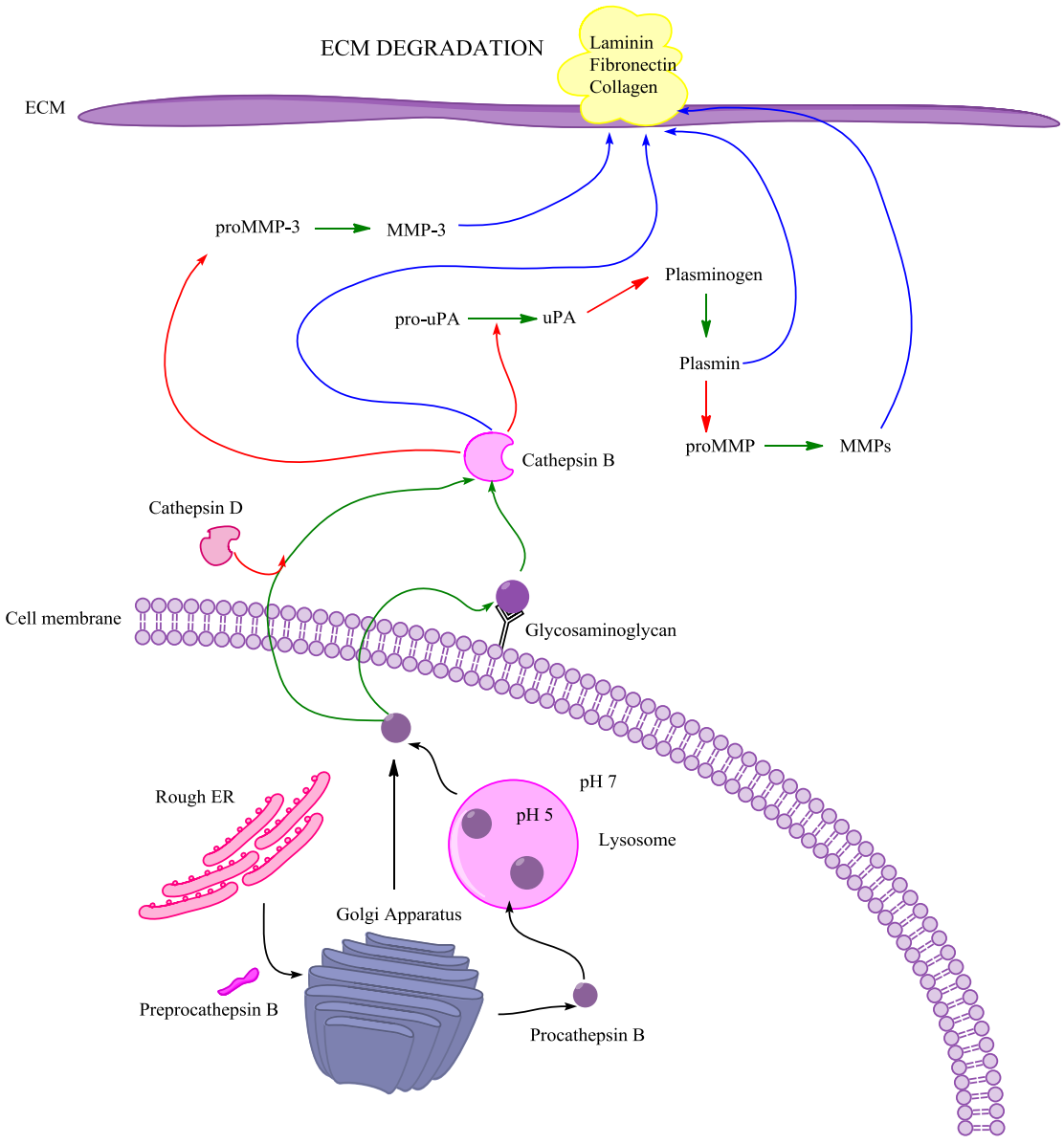

Figure 2.5 – Cathepsin B processing and role in extracelllar matrix degradation[85;86]

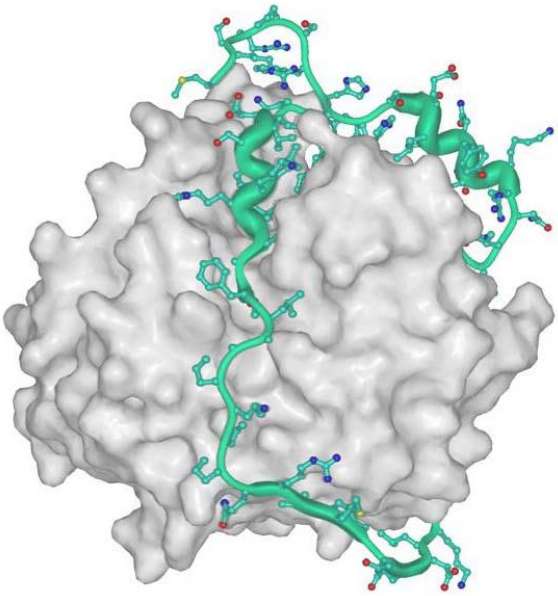

Figure 2.6 - Mature cathepsin B (grey) with propeptide portion (turquoise) anchored at the top right to the surface. (open access DOAJ)[69]

Under certain conditions, cathepsin B can be secreted extracellularly as a proenzyme that requires activation.[47] Activation can also occur through interaction with GAGs on the cell surface, (processing Figure) such as heparin, heparin sulfate and chondroitin sulfates A, B and C.[91] GAGs are heteropolysaccharides that consist of negatively charged repeating disaccharide units widely distributed in tissue; the charges due to carboxyl groups and sulfate substitutions.[92] Upon binding to the zymogen, GAGs cause conformational changes in procathepsin B via ionic interaction, converting the proform to a better substrate and therefore accelerating the cleavage of the propeptide.[86] Cleavage is achieved and the propeptide dissociates, leaving the GAGs dissociated and free to bind another molecule of cathepsin B.[86] The GAG and procathepsin B mode of interaction is unique from other protein/GAG mechanisms. Studies determined that although sulfation of the GAGs is important for greater efficiency of the acceleration effect of procathepsin B, the interaction is not dependent on the level of sulfation.[86] The

minimal oligosaccharide is also unusual in that procathepsin B interaction occurrs with tetrasaccharides whereas most proteins interacted with GAGs of greater than eight subunits.[86] An additional pathway for activation is via other proteases such as cathepsin D and G, discussed below.[61]

Cathepsin B – Localization/Processing in Tumor/Cancer Cells

Figure 2.7 is the proteolytic cascade of the degradation of the extracellular matrix (ECM) where fine solid lines represent activation steps, dark solid lines represent direct degradation, and dashed lines represent activators.[93]

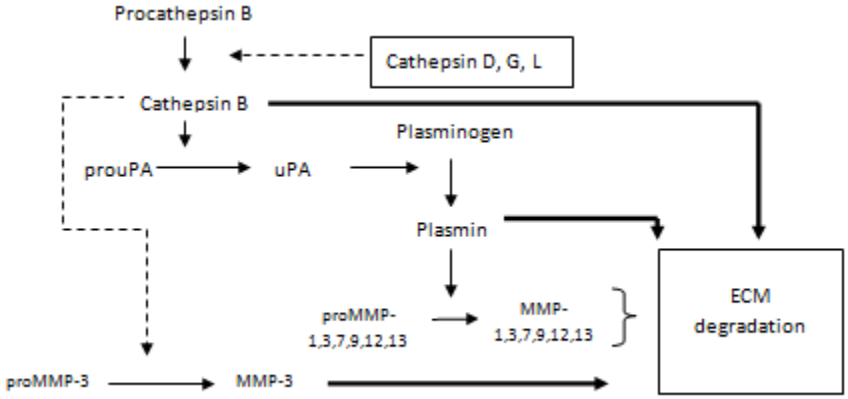

Figure 2.7 - The cathepsins and their role in extracellular matrix degradation (recreated)[93]

Procathepsin B is activated by cathepsins D, G or L to the active cathepsin B form. From this point, the active cathepsin can directly degrade the ECM or indirectly via a process of step-wise activation of components such as the initial activation of prouPA (urokinase plasminogen activator) to uPA which in turn activates plasminogen to plasmin. Plasmin acts directly on the ECM or via activation of proMMP (matrix metalloproteases) to MMPs which then degrades the extracellular matrix. Secretion of

cathepsin B from tumor cells occurs via two pathways: secretion of procathepsin by constitutive pathways and secretion of active forms via an inducible pathway.[94] Figure 2.8 illustrates the localization of cathepsin B on a tumor cell membrane. As previously mentioned, cathepsin B is localized in perinuclear vesicles such as lysosomes in normal cells. In tumor cells, the enzyme is localized in both perinuclear vesicles within the cytoplasm and at the periphery of the cell.[90] It is postulated that the localization might be mediated through association of individual cathepsins with binding partners in membrane microdomains such as lipid rafts, of which the caveolae are a subset that contain the structural protein caveolin which is involved in cell surface proteolysis.[95]

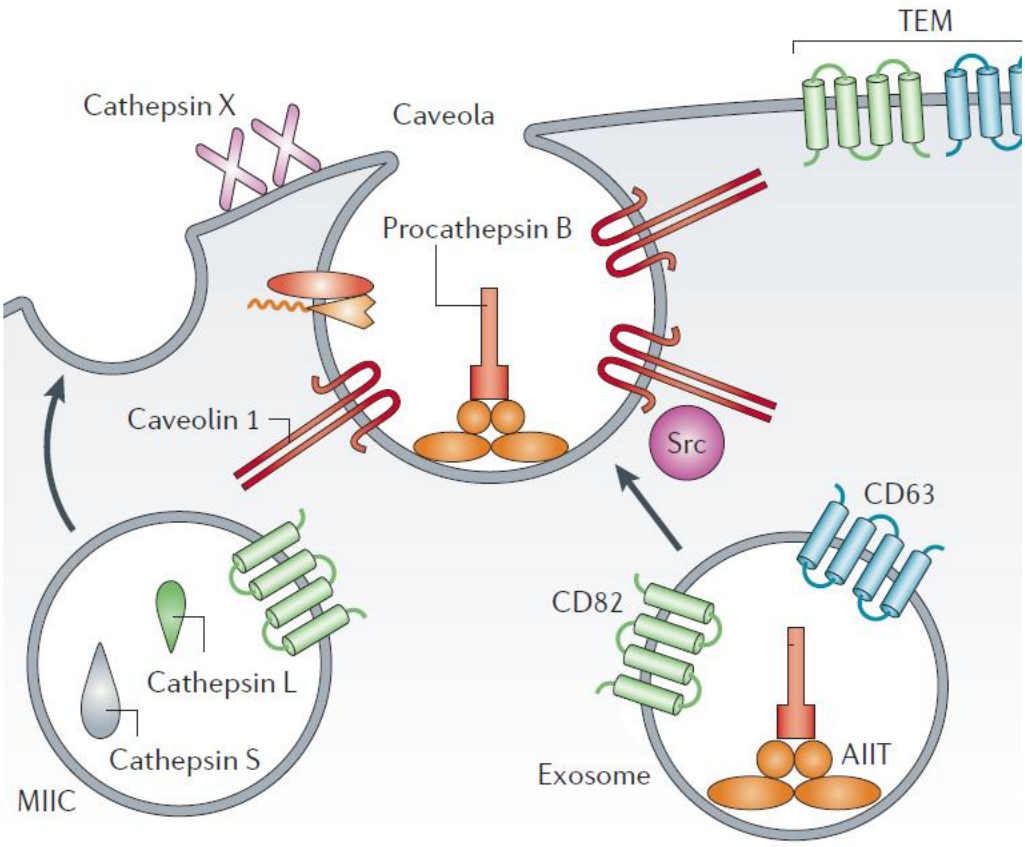

Figure 2.8 - Localization of procathepsin on the tumor cell membrane (Reprinted with permission)[46]

It has also been proposed that the association of cysteine cathepsins with these caveolae in tumor cells and endothelial cells is related to their ability to degrade the extracellular matrix.[46] The caveolae contain both the active and proforms of cathepsin B, the active form stimulated by slight acidification and/or via proangiogenic chemokines such as interleukin 8 in addition to proinflammatory cytokines. The two mechanism proposed to induce the secretion of the active form leading to malignancy are peritumoral acidification and tumor stroma interactions.[46] The caveolae structures are mediated by a direct interaction of procathepsin B with the light chain of the annexin II heterotetramer (AIIT), which binds calcium and phospholipids, is involved in plasminogen activation and has been linked to both endocytic and exocytic vesicular transport.[96] Annexin has been reported to be up-regulated on the surface of tumor cells and in turn, regulates the biogenesis of the multivesicular endosomes, being linked to endocytic and exocytic vesicular transport.[97] In malignancy, cathepsin B is localized from the perinuclear lysosomes to the vesicles at the periphery of the cell (near or on the cell surface) in addition to the out basal surfaces of the tumor cells.[95] Proteolysis adjacent to tumor cells or pericellular proteolysis has been implicated in neoplastic progression.[46]

Cathepsin B –Amino Acid Sequence

The sequence of cathepsin B is a 339 amino acid chain and upon the process of maturation (cleavage of propeptide), becomes a double chain molecule of approximately 254 amino acids in length. The light chain (residues 80-126) is cross-linked via a disulfide bond to the heavy chain (residues 129-333) and is seen in pink. Residues 1-8 (green) make up a signal peptide, residues 9-79 and residues 334-339 make up the pro-peptide (red), all of which are cleaved during processing leaving residues 80-333 (~254

amino acids) as the cathepsin B enzyme (blue). When all the cleaved amino acids are removed the numbering of the sequence changes where previously residue 80 now becomes residue 1. Therefore the active site residues are now Cys29 (prev. Cys108), His199 (prev. His278), Asn281 (prev. Asn298).[89] A comparison between papain and cathepsin B numbering can be seen in appendix A.

Cathepsin B – Structure

Cathepsin B is a bilobal protein of approximately 30 kDa in the mature form (~38 kDa containing the signal and pro-peptide).[89] The disc shaped protein has a thickness of 30 Å, a diameter of approximately 50 Å and is folded into two domains; the left and right domains are seen in their respective orientations (left domain on left and right domain on right) in Figure 2.9. The left hand domain is composed of the amino-terminal half of the

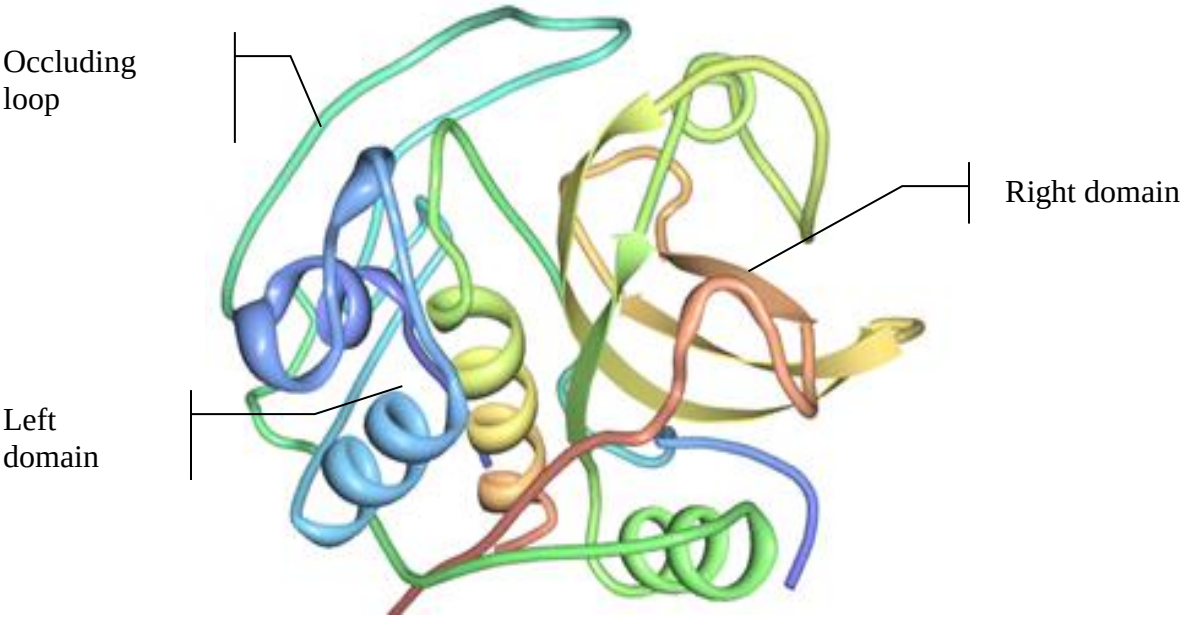

Figure 2.9 - Crystal structure of cathepsin B. Protein Data Bank entry 1HUC (P07585)[89,98,99]

polypeptide chain from residues 11-148 and the last 4 carboxy terminal residues, characterized by a central α-helical structure.[50] This domain contains three α-helices arranged perpendicularly and is largely hydrophobic in nature, containing 18 hydrophobic residues.[100] The right hand domain is composed of the C-terminal domain, being formed by residues 1-10 and the carboxy terminal end of the protein (residues 149-250) and is characterized by a β-barrel with 6 sheets arranged in an anti-parallel motif.[89,63] This domain is enclosed at both ends by α-helices, containing a highly hydrobobic core of approximately 19 aromatic residues. The outer portion of the core consists of charged amino acid residues with three of these extending into the interface between the two domains. [89]

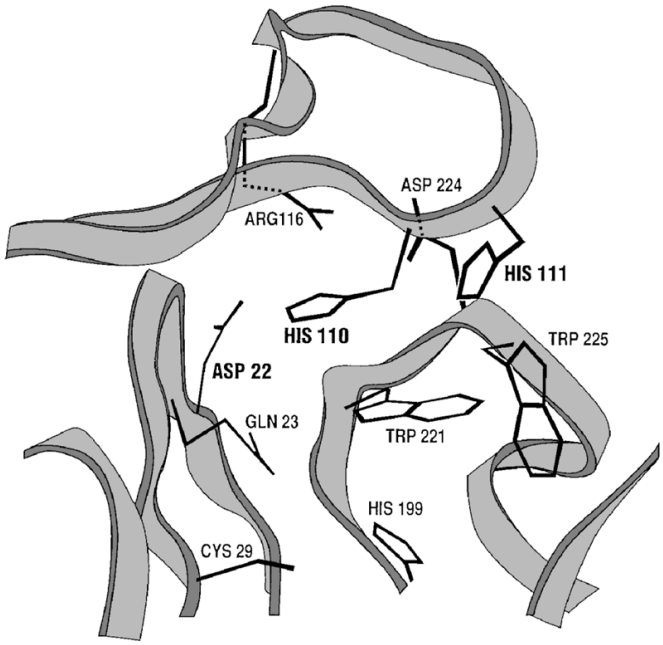

Figure 2.10 - Active site and occluding loop of cathepsin B (reprinted with permission, from [101] © the Biochemical Society)

The two domains interact with each other through an extended polar interface that opens to the V-shaped cleft active site, the ends acting as tethers essentially "clamping"

the domains together and the "rear" being blocked by the occluding loop.[50] At this interface between the left and right domains lies the active site and substrate-binding cleft with the important amino acid residues being Cys29, His199, His110, and His111, the latter two of which are responsible for the exopeptidase activity of the enzyme. The active site of cathepsin B contains a cysteine in the catalytic triad of Cys29, Asn281, and His199 as is seen in Figure 2.10. In the active site, the thiol side chain of Cys29 can form an ion pair with the side chain of His199 over the pH range 4.0-8.5, the cysteine being located on the left domain and the histidine on the right.[102] Cleavage of the substrate peptide bond can then be mediated by the nucleophilic attack of the Cys thiolate group followed by a proton donation by the His as seen in Figure 2.11.[102]

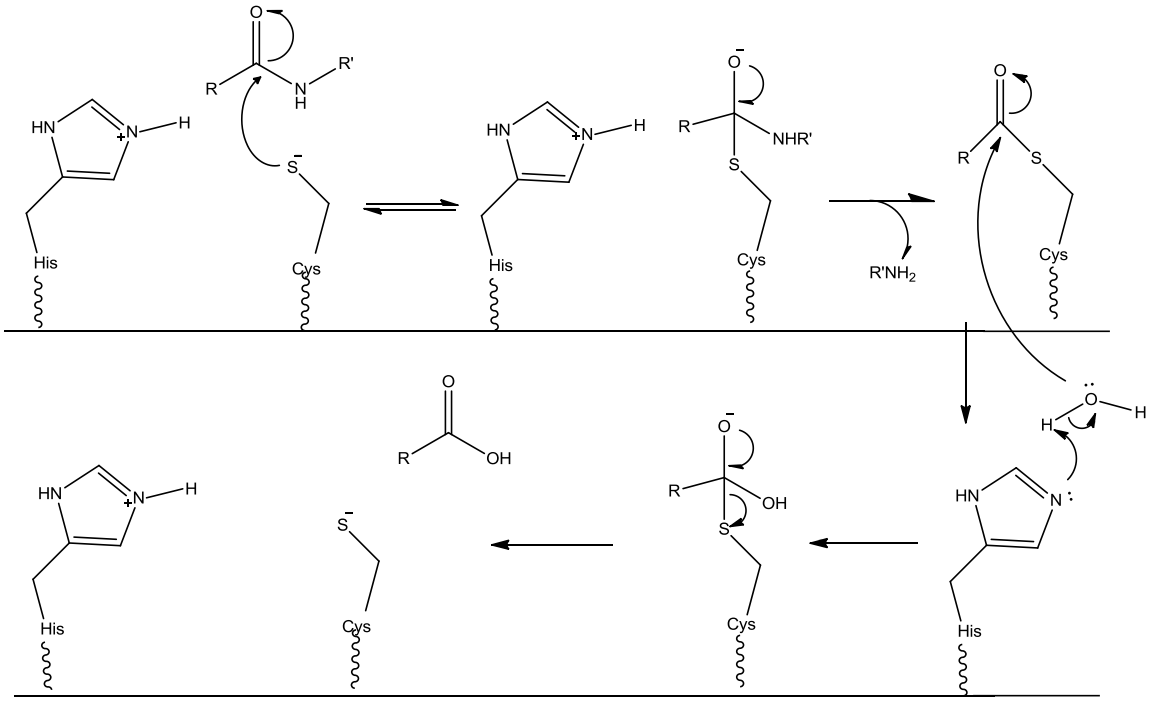

Figure 2.11 - General view of the nucleophilic attack mode of cysteine proteases

As a member of the cysteine protease family, there are multiple cysteine residues that interact to form disulfide bonds. In human cathepsin B there are six total disulfide

bridges formed between the following amino acid residues: 93-122, 105-150, 141-207, 142-146, 179-211, and 187-198 with an additional bridge found in bovine cathepsin B.[103, 89,104] Cathepsin B is unique from many other cathepsins having a dual role depending on the pH, acting as a carboxy dipeptidase at acidic pH and as an endopeptidase at neutral pH.[46,105]The exopeptidase activity is due to an unique occluding loop composed of 18-20 residues, Ile105-Pro126, that restricts active site access, acting as a flexible "flap" which can open and close, Figure 2.12a for location and Figure 2.12b for amino acid interactions.[106,107]

. .

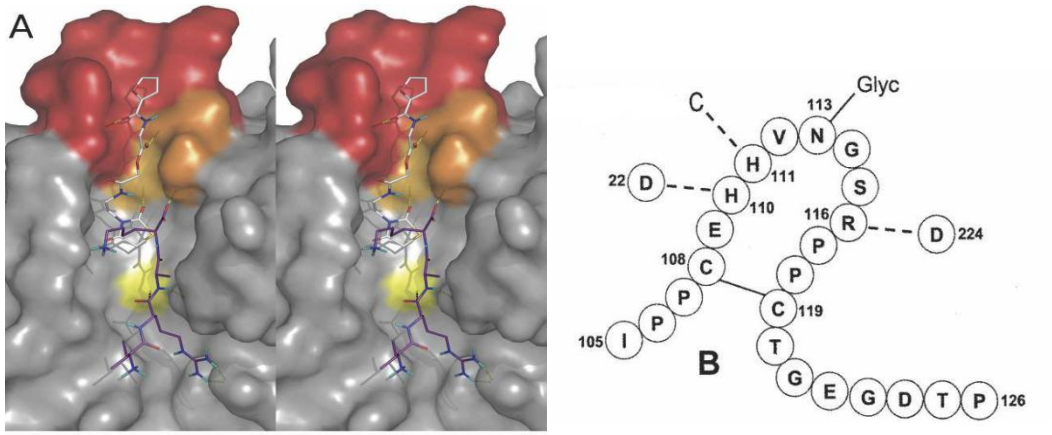

Figure 2.12 - a) Cathepsin B complexed with inhibitor [2-[2-(2,4-dioxo-1,3-thiazolidin-3-yl)ethylamino]-2-oxoethyl]2-(furan-2-carbonylamino) acetate (DOFA), occluding loop in red, His110/111 in orange b) cross linking of amino acids in occluding loop (reprinted with permission) [107]

Figure 2.12a is a stereoview of the inhibitor [2-[2-(2,4-dioxo-1,3-thiazolidin-3-yl)ethylamino]-2-oxoethyl]2-(furan-2-carbonylamino) acetate (DOFA) complexed with human cathepsin B. This three dimensional view illustrates the position of the occluding loop in red, His110 and His111 in orange portion, and the catalytic Cys29 in yellow.[107] The occluding loop is located on the left domain and creates disulfide bonds by cross-

linking Cys108 to Cys119, seen in Figure 2.12b. The covalently closed circular structure begins and ends with an identical Pro-Pro-Cys sequence which has been suggested to help stabilize the ends of the occluding loop.[105] Figure 2.12., in addition to illustrating the active site residues, represents the occluding loop region in human cathepsin B. Here, the Cys29 and His199 act as the catalytic nucleophile and general base while Gln23 stabilizes the oxyanion tetrahedral intermediate of the substrate. In this native form and at low pH, Trp221 and Trp225 form a hydrophobic pocket surrounding active site and two salt bridges between Asp22-His110 and Arg116-Asp224 are created, holding the usually flexible occluding loop in place and blocking access to the active site.[101] With these bonds formed, the histidine residues form the outer boundaries of the S2′ subsite. Upon change to more basic pH and in the inhibitory conformation, the His110 becomes deprotonated, allowing for the loop to freely move and therefore changes the function of cathepsin B from an exopeptidase to an endopeptidase.[105] The two histidine residues account for cathepsin B's preference for carboxypeptidase activity as they can bind the C-terminal carboxylic groups of the substrate. The occluding loop is proposed to contribute to cathepsin B's decreased affinity for potent inhibitors of other papain-like enzymes as deletion or shortening of this flexible structure increased binding to this enzyme.[108]

Cathepsin B Substrate Binding Sites

Cathepsin B contains multiple binding sites that have been defined as S1, S2, S3, S1′, S2′ with outer subsites existing but are less influential.[109] Primed sites refer to the location where the C-terminal portion of the substrate will bind and non-primed sites refer to the N-terminal portion. S designates the locations on the protease where the

inhibitor or substrate will bind and P refers to the substrate residue position. Figure 2.13 is a schematic representation of the binding of a substrate to the active site (A) and the locations of the subsites (B) in relation to the right and left domains of cathepsin B. [68,101,61]. Note that in Figure 2.13, papain numbering is used where Cys25 (shown) is Cys29 for cathepsin B and His159 (shown) is His199 for cathepsin B. The scissile bond is the peptide bond that is cleaved in the enzyme catalyzed reaction.[68] In the P1 position on the substrate, arginine is favored as it renders the substrate more susceptible to cathepsin B in addition to providing more solubility in water. [63,111] The subsites of the enzyme can be more clearly seen in the electrostatic potential surface structure of cathepsin B, Figure 2.14, where red designates negative charge and blue designates positive charge.[109]

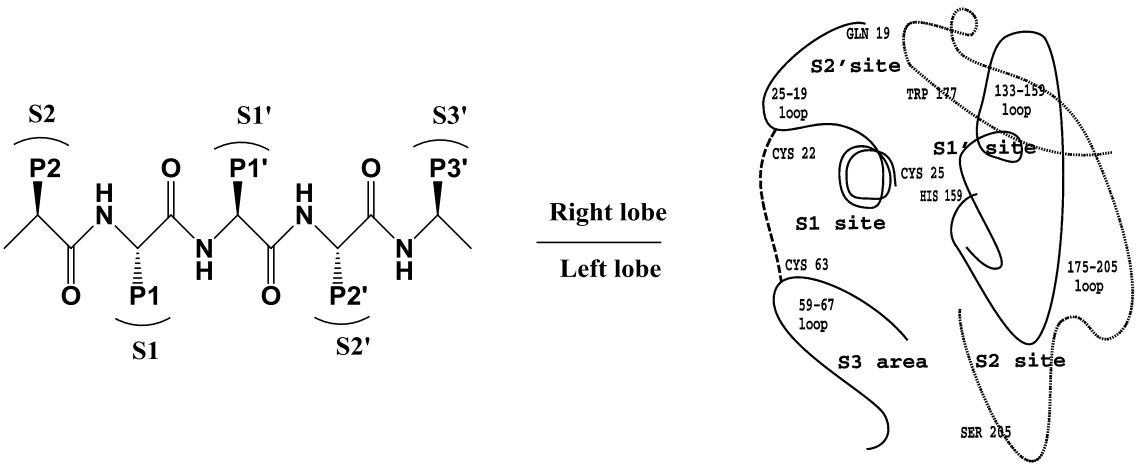

Figure 2.13 - Schematic diagram of substrate binding to active site (recreated and reprinted with permission).[68,110]

Substrates can bind to the active site pockets in an extended conformation, the pockets can be seen by Figure 2.14. This binding supports only three well defined substrate binding sites: S1, S2, and S1′. It is in these pockets that the substrate backbone

interacts with the enzyme by main and side chain interactions, such as hydrogen bonding of residues, the main chain interactions being offered by the occluding loop histidine residues, His110 and His111.[63]

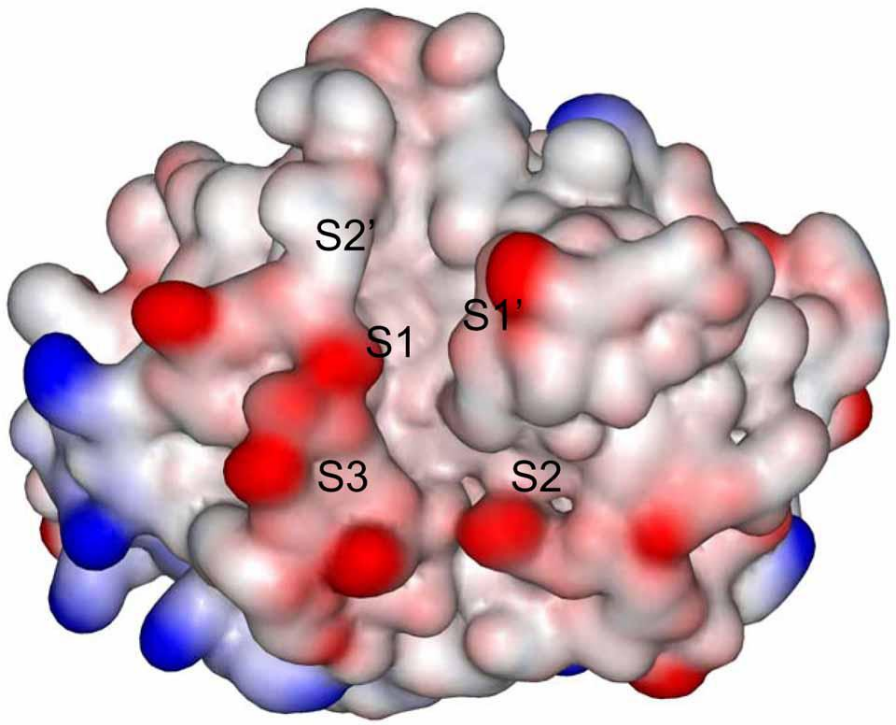

Figure 2.14 – Electrostatic potential surface of cathepsin B substrate binding sites[109]

The S1 and S1′ pockets are relatively deep compared to that of cathepsin S, L and K and are negatively charged due to the residues Glu122 and Glu194, where Glu122 is thought to play an important role in substrate binding.[63] The S2 subsite is a shallow hydrophobic depression that is modified so that it can accept basic residues such as Arg in addition to the standard hydrophobic side chains, such as Phe. The modification includes Glu245 in the S2 pocket, a feature unique to cathepsin B in comparison to other cathepsins, allowing for the binding pocket to accommodate arginine from the substrate.[112] The S2 region forms a pocket where side chain interactions occur only at

position outside of this region, making this subsite a primary determinant for substrate specificity.[112] The S2 subsite is located in a region near the S3 subsite, a shallow wide pocket, and the cleft between the two subsites is deep and narrow with steric hindrance caused by residues Glu245 of the S2 pocket and Pro76 of the S3, therefore limiting substrate length.[109] It must be noted that Glu245 is found only in cathepsin B and not any of the other cathepsins, making this residue a specific feature of the S2 pocket.[63] The occluding loop is located near the S3′ site (not shown in Figure 2.14 but located at the top of the protein near S2′ site) and limits substrate orientation and length due to His110/111's ability to form electrostatic interactions with free carboxylate groups of potential substrates.[111] This interaction of His111 also is a major determinant of cathepsin B's exopeptidase activity. Salt bridges cause the loop to be in the closed position and therefore the His residues block the back entry of the active site by forming an outer boundary around the S2′subsite. His110 specifically interacts with Asp22 through an ion pair stabilized electrostatic interaction.[111] S3 and S4 sites exists but are not generally considered binding sites as is illustrated by the spread of residue positions across the active site cleft on non-primed sites and are more recently referred to as locations where the substrate residues fine their most favorable binding position.[112,63]

Cathepsin B Gene

Cathepsin B is encoded by a gene localized on the human chromosome 8p22.[74] Allelic loss in 8p12-p21 appears to be characteristic of the preliminary stages of human prostate cancer. Cathepsin B is the only cathepsin with a novel amplicon at 8p22-23 where amplification of cathepsin B precedes amplification of other genes in the region resulting in the overexpression in adenocarcinomas of the oesophagus and gastric

cardia.[113];[114] Figure 2.15 is the fluorescent in situ hybridization (FISH) of a normal chromosome using bacterial artificial chromosomes (BAC) mapping where CTSB is cathepsin B and D4 BAC is mapped at chromosome 8p22 and D5 BAC is mapped at chromosome 8p23, indicating unique amplicon.[73]

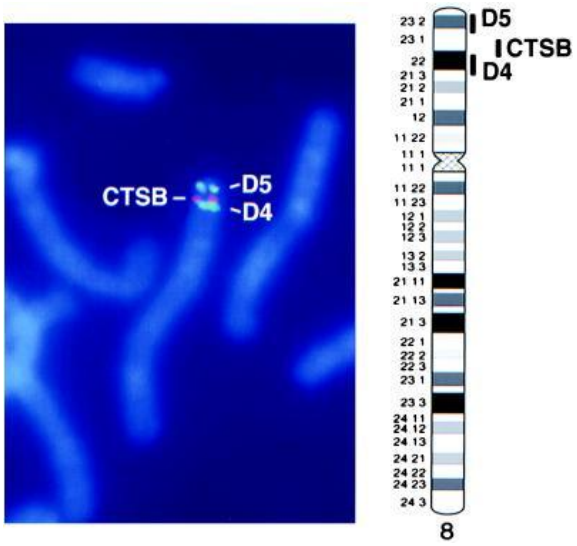

Figure 2.15- Cathepsin B mapped at chromosome 8p22[113](reprinted with permission, © 2013 National Academy of Sciences, U.S.A.)

Protease Inhibitors

As previously mentioned, it is essential that proteases be controlled intracellularly in order to avoid excessive and often destructure proteolysis as these enzymes have many important biological functions. In the cell environment, there is a balance between the proteases and their endogenous inhibitors such as the cystatins and stefins which can be regarded as primary "guardians" of the cell, preventing over-activation for example.[115] The efficacy of protease inhibitors in turn affects the proteolytic cascade. Emergency inhibitors, for example, are primarily used to target proteases expressed in excess that have escaped their appropriate cellular compartment, causing potentially harmful

proteolysis.[116] Cystatins and stefins are grouped into this category and although they are able to distinguish between endo and exopeptidases, they have low specificity for their targets.[117] This characteristic makes it more difficult to bind to exopeptidase enzymes such as cathepsin B which has an occluding loop, a structural feature that requires cystatins to be modified in order to act upon the active site.[115] Within the cell there are also regulatory inhibitors which control or regulate proteases' activity and threshold inhibitors which bind rapidly to proteases to neutralize them in the event that multiple enzymes are accidentally activated simultaneously and endogenous inhibitors are no longer effective. Buffer-type inhibitors, delay-type and pro-inhibitors are all additional types of endogenous competitive inhibitors found in the cell to prevent unnecessary to excessive protease activity.[110,118]

Ideal Inhibitors of Cathepsin B

There have been many studies into the investigation of new inhibitors of cathepsin B over the past two decades and have ranged from natural non-peptidic sources to peptidic compounds.[117] Small molecule inhibitors have generally been of interest due to their size and potential to bind in a substrate-like manner. It is for this and various other reasons that a set of parameters are adapted in order to avoid these potential problems. The ADMET parameters are ideal for a small molecule inhibitor are excellent absorption, distribution, metabolism, excretion, toxicology and in many cases be orally bioavailable, although meeting all these criteria is not expected.[117] A peptidic inhibitor is not ideal in the search for effective inhibitors as the structural and chemical properties of the peptide create an additional challenge of the molecule permeating cellular membranes. Membrane permeant inhibitors, such as nonpeptidic, inhibited invasion of prostate and

melanoma cancer cells only under conditions which reduced intracellularly localized cathepsin B. Select peptidic inhibitors were able to achieve similar results but required long incubation times resulting in endocytosis.[46] This approach would require a deliberate increase in time of the inhibitor and target association and could potentially exacerbate the toxicity of the compounds to surrounding tissues. A review of the literature showed various inhibitors of cathepsin B, divided into peptidic and nonpeptidic inhibitors and further subdivided into reversible and irreversible inhibitors.

Irreversible Peptidic Inhibitors

Epoxysuccinyl Peptidic

Peptidic inhibitors in general display low IC_{50} values against cathepsin B but as previously mentioned, they possess low cell permeability. The most extensively studied class are the irreversible epoxysuccinyl peptides, originating with the discovery of E-64 and continuing with derivatives of the natural compound including CA074 and CA030.[68] The general scaffold and a selection of the epoxysuccinyl inhibitors is seen in Figure 2.16. The IC_{50} values for these compounds are in the low nanomolar range and vary in their selectivity for cathepsin B versus other cathepsins or papain. CA-074 and CA-030 are selective inhibitors of cathepsin B within this series and bind to the S′ subsite in the same orientation as the substrate. In Figure 2.17, a typical binding motif between cathepsin B (seen in light blue) and the inhibitor CA030 (in red) in a vertical orientation is demonstrated in relation to the binding subsites. CA030 interacts with the occluding loop of cathepsin B (shown in green), forming hydrogen bonds between the proline carboxyl group and the histidine positive charge. Also visualized is the oxyanion hole

formed between Gln23 of the enzyme and the oxygen atom on carbon 1 of the inhibitor. The active site thiolate (Cys29) reacts with carbon 2 of CA030 epoxysuccinyl ring resulting in an alcohol formation on carbon 3.[119] In structure activity relationship (SAR) studies for the epoxysuccinyl inhibitors, the most effective inhibitors of this series bind to the S` subsites and interact with the histidine residues of the occluding loop.[68]

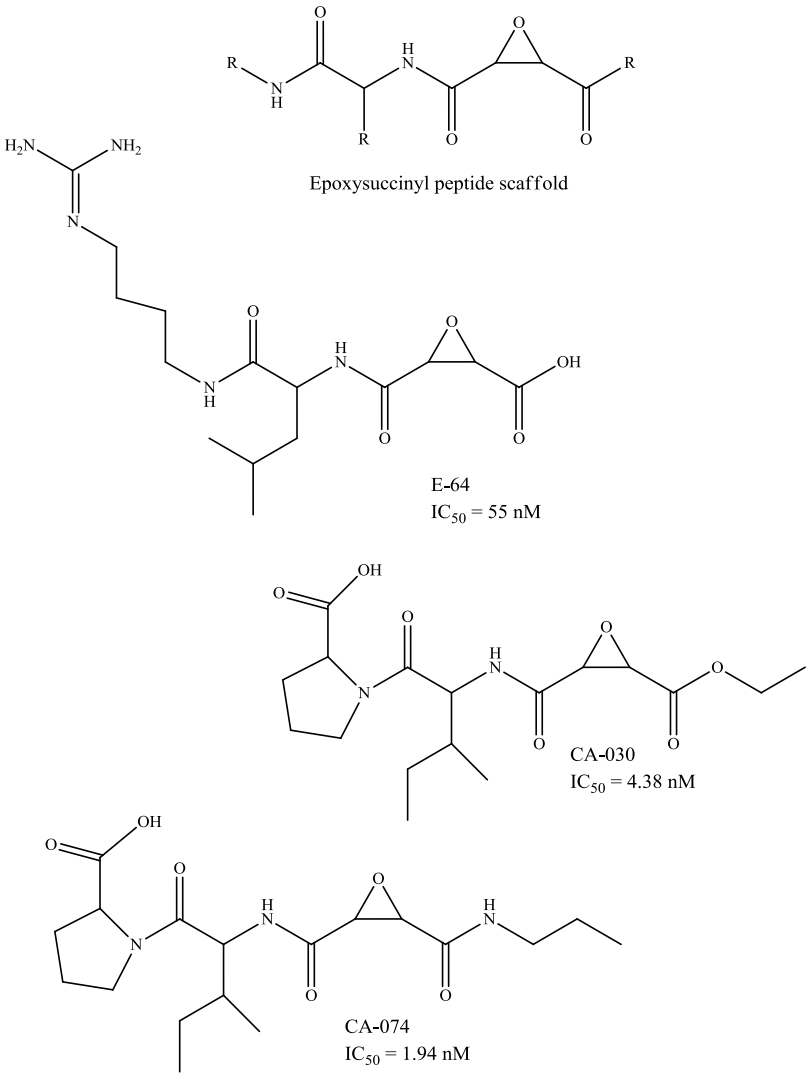

Figure 2.16 – Epoxysuccinyl peptidic inhibitors of cathepsin B

Although an advantage to these membrane impermeant compounds is that they would target only the extracellular or membrane bound cathepsin B, their irreversibility

and covalent binding to the enzyme make them less than favorable.[120] E-64d, a derivative of E-64, reached phase III clinical trials against muscular dystrophy but failed due to adverse side effects such as teratogenicity and hepatic injury.[85]

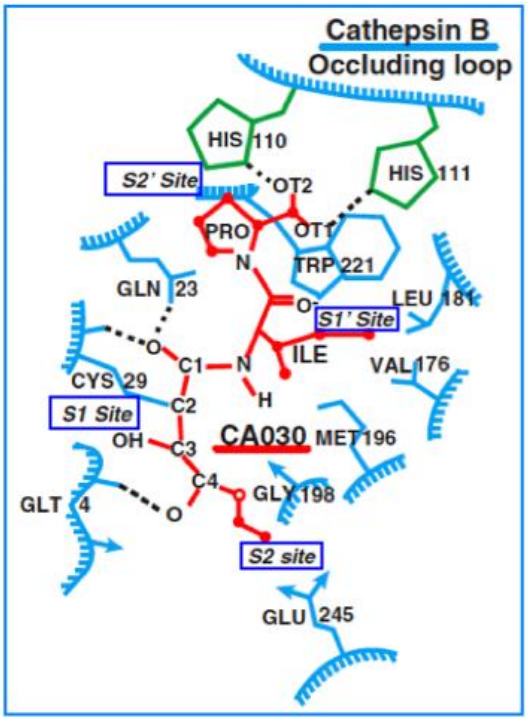

Figure 2.17 - Example of typical binding between cathepsin B and an epoxysuccinyl inhibitor (reprinted with permission)[119]

Aziridine Peptidic Inhibitors

The aziridinyl peptide inhibitors are analogues of the epoxysuccinyl scaffold and interact very similarly with cathepsin B, irreversibly reacting with Cys29 of the active site.[68] The inhibitory ability of these series is very pH dependent as the aziridinyl ring can be protonated on its nitrogen, limiting maximal activity to pH of approximately 4.[68]

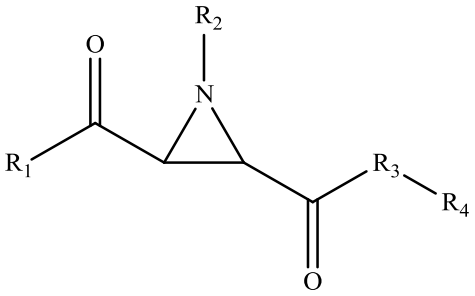

Figure 2.18 – Aziridine scaffold of peptidic inhibitors

Other peptidic and nonpeptidic irreversible inhibitors include the thiadiazole, acyloxymethylketone, and β-lactam series, general scaffolds seen in Figure 2.19. [68,121]

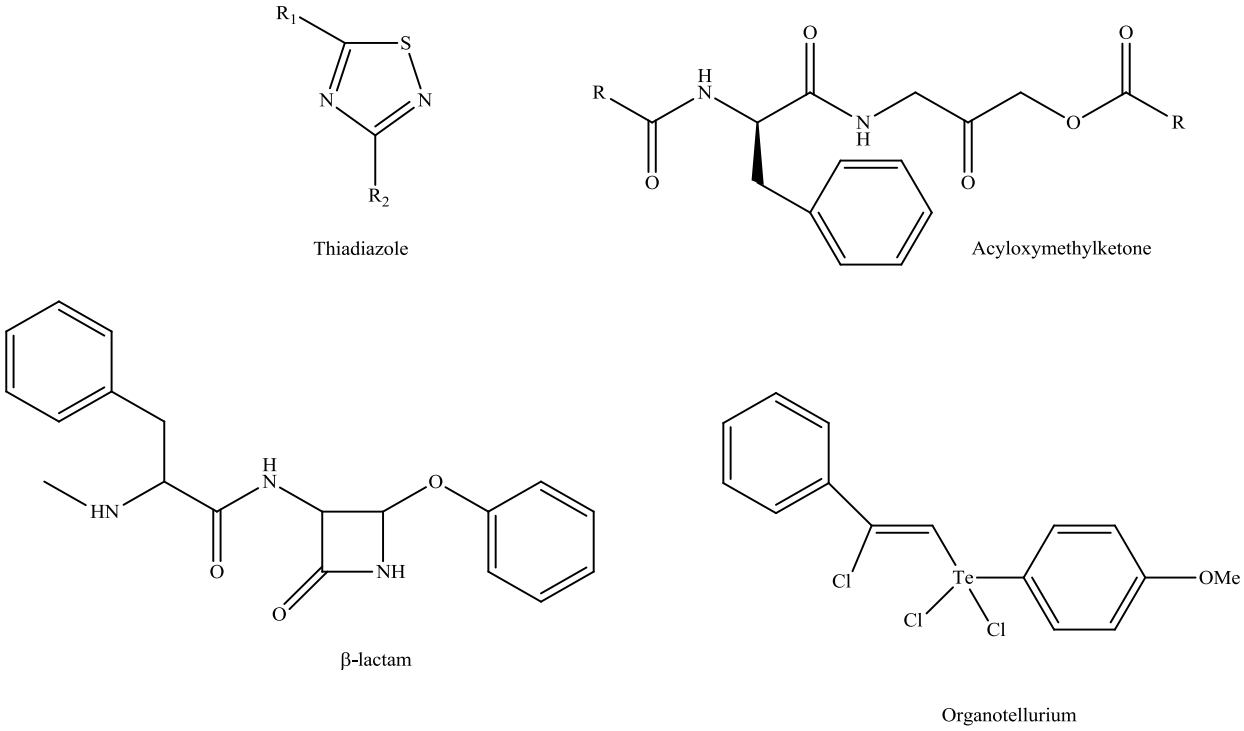

Figure 2.19 –Irreversible inhibitor scaffold

The organotellurium inhibitors, while not peptidic in nature, are generally irreversible and are active only against extracellular cathepsin B due to the high content of reducing agents within the cell. Their high reactivities are associated with tellurium (IV)'s Lewis

acid character and within the cytoplasmic environment, reducing agents such as glutathione, cysteine and NADPH take advantage of the electron pair acceptor, rendering them ineffective.[122,117]

Reversible Peptidic Inhibitors

Inhibitors that are reversible tend to have a lower level of toxicity which is important from a therapeutic view. The attempts made to synthesize reversible tight binding inhibitors of cathepsin B are limited and include scaffolds such as peptide aldehydes, ketones, cyclopropenones, cyclometallated, and nitrile inhibitors.[46,123,111]

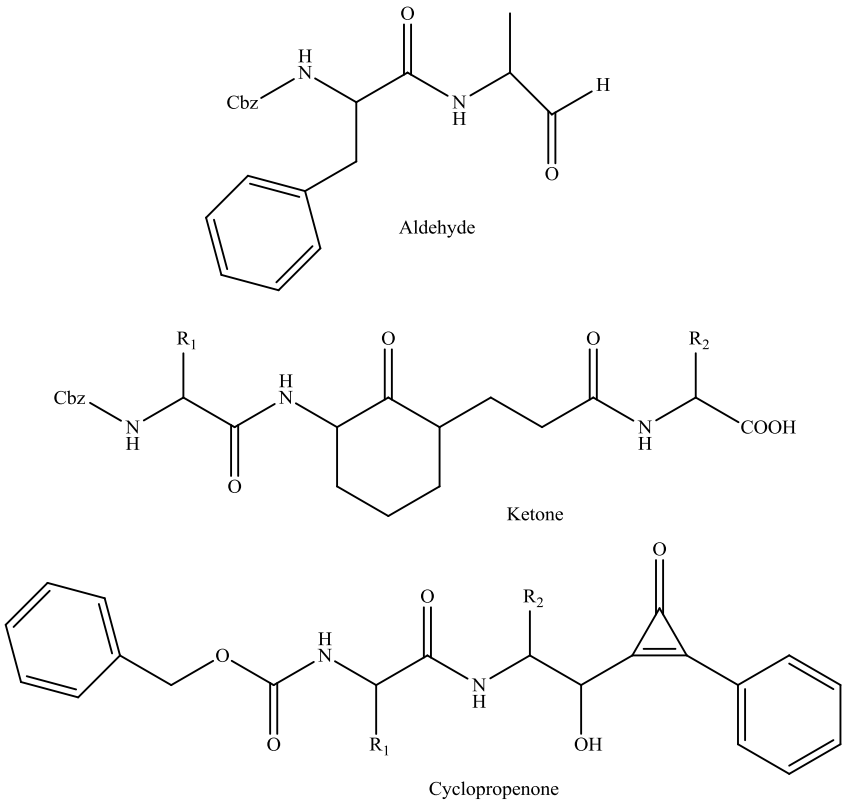

Figure 2.20 – Reversible peptidic inhibitor scaffolds

The ketone and aldehyde moieties, Figure 2.20, react with the nucleophilic thiolate of active site cysteine, giving a reversible hemithioketal adduct which mimics the

tetrahedral intermediate.[124] The mechanism by which these reversible peptidic aldehydes interact with the enzyme is shown in Figure 2.21. While there are few ketones selective

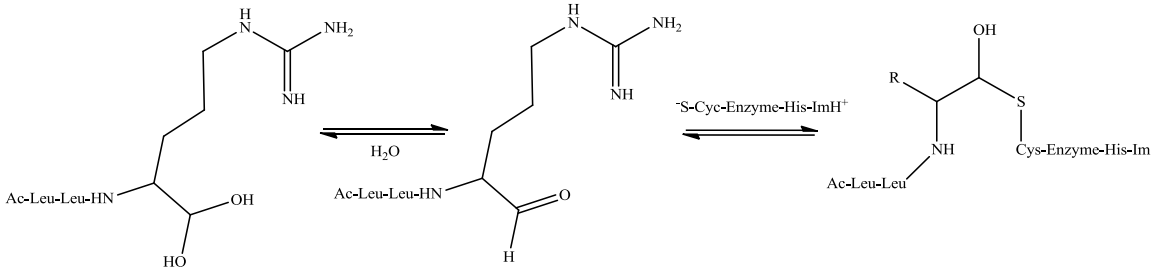

Figure 2.21 - Proposed mechanism of synthetic aldehyde inhibition.[124]

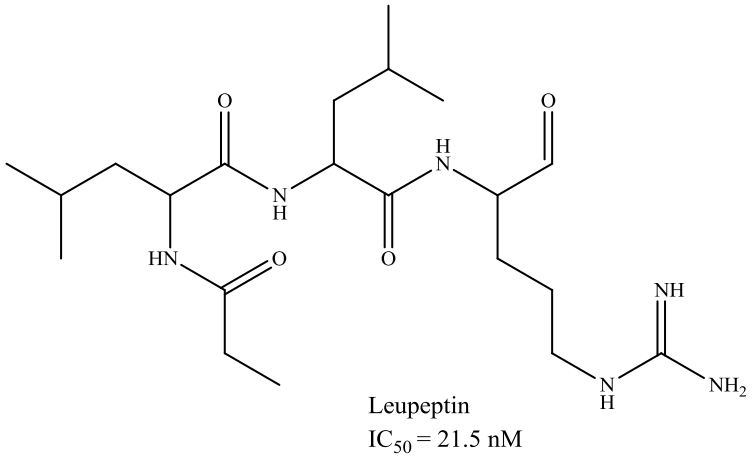

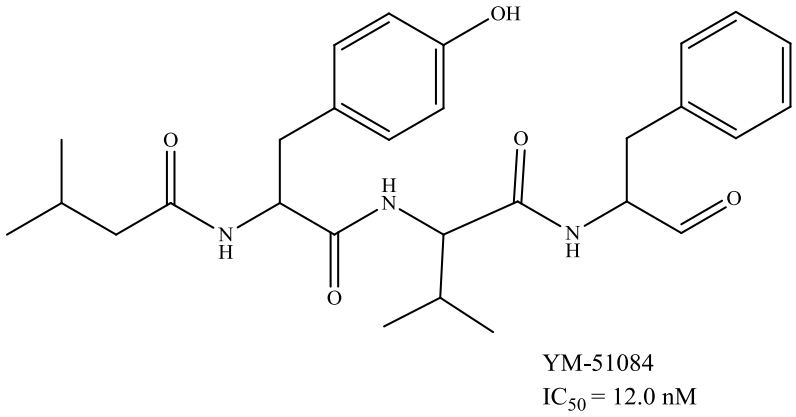

Figure 2.22 – Potent aldehyde inhibitors of cathepsin B

for cathepsin B, studies on the aldehyde analogues provided some potent inhibitors with IC_{50} values in the low nanomolar range.[125,126] Of the aldehydes, active compounds included leupeptin, leupeptin lysinal analogues, and YM-5108 all of which are produced by different streptomyces strains, Figure 2.22.

Nitrile Inhibitors

Nitrile inhibition of cysteine proteases occurs through a reversible thioimidate intermediate stabilized by an adjacent Gln residue. The mechanism of this inhibition is seen in Figure 2.23.

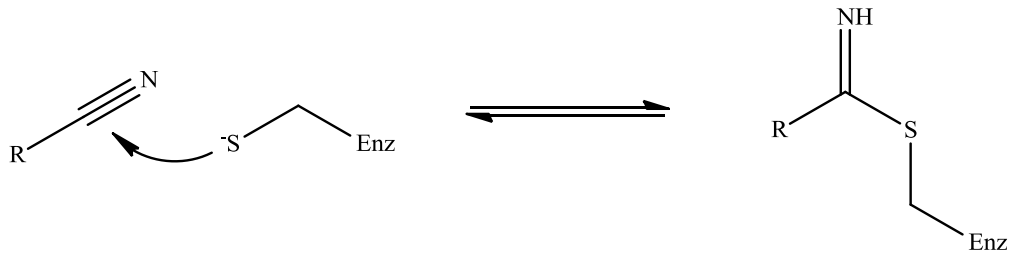

Figure 2.23 – Cathepsin B inhibition mechanism of nitriles

Of the nitrile series, ten dipeptidyl nitrile inhibitors proved to be potent in the low nanomolar range utilizing the carboxylate recognition site in the S2′ pocket of the active site and tethering a carboxylate functional group from the α-carbon to the nitrile.[111] The general scaffold for dipeptidic nitrile inhibitors is seen in Figure 2.24. Slight structural modification of the dipeptidyl nitriles produced N-arylaminonitriles in the target inhibitory range which were selective for cathepsin B in comparison to cathepsins L and S.[46,68]

Nonpeptidic Inhibitors

Nonpeptidic inhibitors appear to be less potent for cathepsin B and very few have been discovered in the low nanomolar range, none of which are within the comparison range. Therefore nonpeptidic compounds with an $IC_{50} < 5\mu M$ are compared.

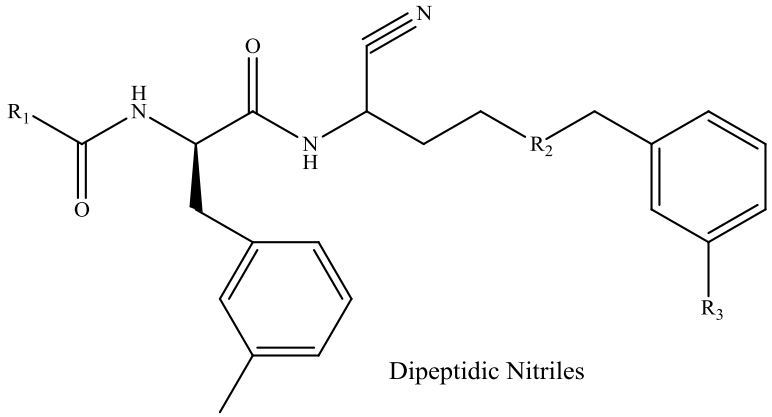

Dipeptidic Nitriles

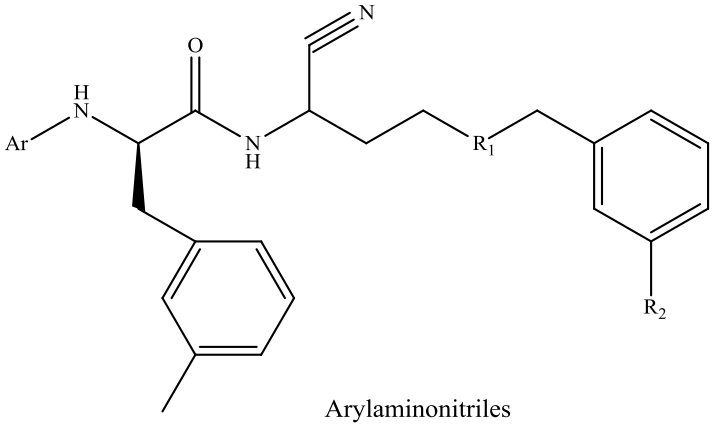

Arylaminonitriles

Figure 2.24 – Nitrile inhibitor scaffold[68]

Of these inhibitors, the pteridine derivative asteropterin isolated from the marine sponge *Asteropus simplexI*, auranofin and its analogues utilize gold (I) complexed to the compounds using a phosphine ligand attached to the gold which confers membrane solubility. The phosphine ligand displaces slowly and possibly mediates therapeutic

effects of the drug. The most potent of the auranofins are competitive reversible inhibitors with IC_{50} values in the range of 204-334 nM, Figure 2.25.[67] Other metals used

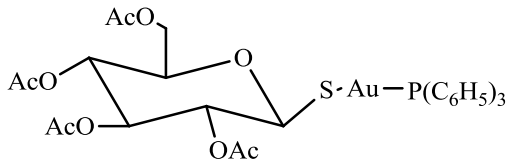

Auranofin derivative

IC_{50} = 0.334 μM

Figure 2.25 – Potent auranofin derivative

in inhibitors include ruthenium (II), ruthenium (III) and osmium which exhibited inhibition in the low micromolar range (2.5-6.5 μM) in contrast to nonpeptidic analogues utilizing iridium and rhodium which were not considered active.[128,129]

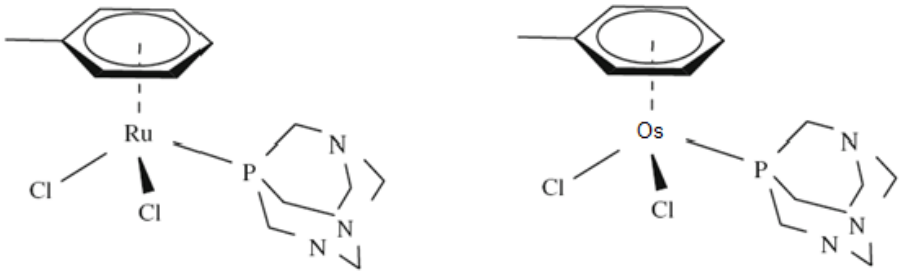

IC_{50} = 2.5 μM IC_{50} = 6.5 μM

Figure 2.26 – Ruthenium and osmium based active inhibitors of cathepsin B (low micromolar range)

Nitroxoline Series

Modifications to the nitroxoline series resulted in effective inhibition of cathepsin B with the most potent compound exhibiting almost twice the inhibition of tumor invasion (MCF-10A cells) *in-vitro* than CA-074. The scaffolds for the nitroxoline inhibitors synthesized are seen in Figure 2.27, the most effective of which inhibited with

a K_i value of 5 μM.[48] This compound was also found to be selective for cathepsin B when compared to cathepsins L and H.

Irreversible Non-Peptidic Inhibitor

Organotellurium (IV) complexes have been found to be inhibitory against cathepsin B binding selectively and irreversibly to the enzyme.[117] These inhibitors work through a proposed mechanism of inhibition involving oxidation of the active site cysteine but are only effective in the ECM as the intracellular matrix contains multiple reducing agents which would render the compounds ineffective.[103] Also in 2008, four phthalic acid derivatives were isolated from seahorse, *Hipppocampus Kuda* Bleeler and although they were not in the comparison range, with IC_{50} values between 130-290 μM, they were considered notable in the natural nonpeptidic reversible inhibitor grouping.[130,131;132]

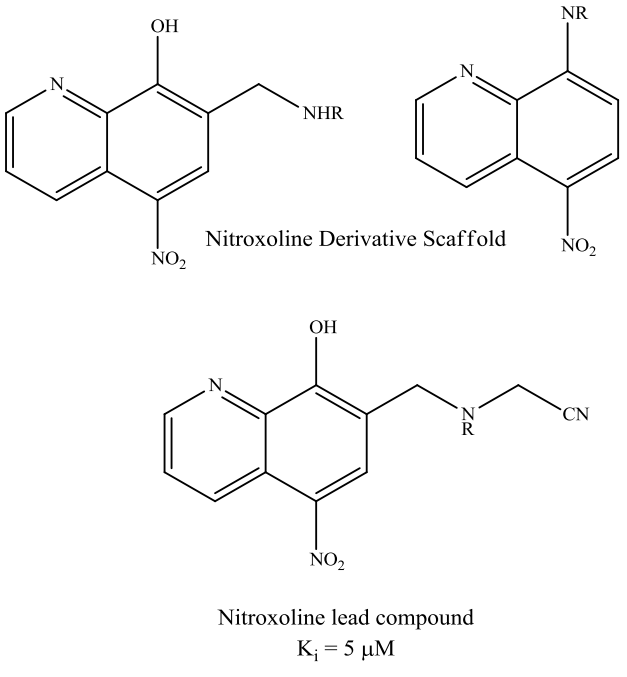

Figure 2.27 – Nitroxoline derivatives as cathepsin B inhibitors

Thiosemicarbazone Moiety for Cathepsin Inhibition

Initial studies have shown small molecule non-peptidic thiosemicarbazone compounds have inhibited the cysteine proteases cruzain (cathepsin L-like enzyme), cathepsin L and cathepsin K in the low nanomolar range.[133,134] A focued library of thiosemicarbazone compound derivatives (Figure 2.28) resulted from a collaborative research project between the Trawick and Pinney laboratories (Baylor University).[51,53,135] This library of nonpeptidic thiosemicarbazone compounds is made up of variations of fused and unfused benzene rings with substituents such as methoxy groups, halogens, alcohols and methyl groups, and has resulted in the discovery of very effective inhibitors of the cysteine proteases cruzain, cathepsin L and cathepsin K. [51-54,54,55] Synthesis of such moieties involves a condensation reaction of a ketone with a thiosemicarbazide to produce various thiosemicarbazones in good yields.[54]

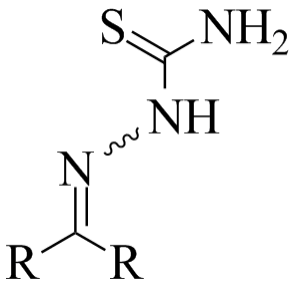

Figure 2.28 – Thiosemicarbazone derivatives

Michaelis Menten Kinetics

Initially, when an enzyme is combined with excess substrate there is a short pre-steady state period where the two components build up to their steady state levels, Figure 2.29 where *k* represents forward and reverse rate constants, E is the enzyme, S is substrate, and P is product. After this initial phase a steady state is achieved where

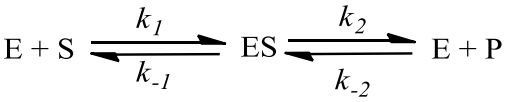

Figure 2.29 - Simple form of enzyme catalyze reaction

the rates of the reaction for these intermediates changes relatively little over time, maintaining a balance between rate of ES formation and ES dissociation. The rate constant, k_1, is assumed to be a rapid reversible step without any chemical changes occurring, only noncovalent interactions holding the enzyme and substrate together.[136] The term k_2 is the rate constant for the conversion of ES complex to product. The steady state kinetics of enzyme substrate interactions is investigated as it provides a degree of enzyme catalytic activity in conditions such as the cell where steady state levels occur. The Michaelis-Menten equation, eq. 1, can be used to determine kinetic parameters in relation to the enzyme and substrate where v_o is initial velocity, [S] is substrate concentration, and V_{max} and K_M are defined in the text. Initially at low concentrations of

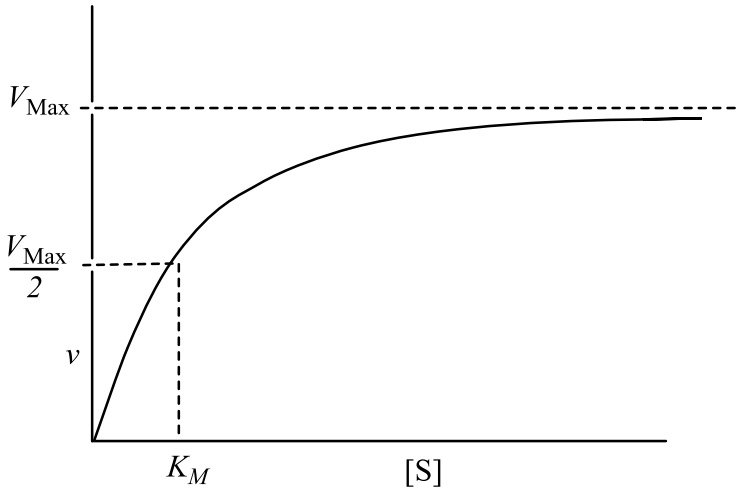

Figure 2.30 – Michaelis-Menten plot of initial velocity of enzyme substrate reaction vs. substrate concentration (theoretical data plotted)

substrate, the velocity increases linearly in proportion to substrate concentration. When [S] is substantially greater than the total enzyme concentration, $[E]_o$, the enzyme active site is said to be saturated and any further increase in [S] will not increase the enzymatic reaction rate. This point is known as V_{max}, seen in Figure 2.30.[137] The V_{max} allows for

$$v = k_2[\mathrm{ES}] = \frac{\boldsymbol{V_{max}[S]}}{\boldsymbol{[S]+K_M}} \qquad \text{Eq. 1 - Michaelis-Menten kinetic equation}$$

the comparison of enzyme obtained from various manufacturers and its activity to current literature values for similarly used enzymes, indicating efficiency of enzyme activity. The Michaelis-Menten constant, K_M, is the concentration of substrate required to produce a reaction rate (velocity) half that of the V_{max}, the relationship seen in Figure 2.30.

Enzyme 1nhibition

In order to evaluate inhibition ability of compounds on the enzyme activity, IC_{50} or K_i values are determined. The IC_{50} is the concentration of inhibitor required to inhibit the activity of the enzyme by 50%. A K_i value is the dissociation constant for the enzyme inhibitor complex [EI]. In the presence of an effective inhibitor, the binding of such a molecule will compete the substrate or alter its binding and therefore decrease the intensity of product formed. This is the theory behind the initial inhibitor efficacy determination. An increase in inhibitor concentration is expected to correspond to a decrease in the product formed. Equation 2 is the equation used to fit data to a sigmoidal dose response curve to obtain an IC_{50} value. In this equation, "bottom" refers to the basal

$$y = \frac{bottom+(top-bottom)}{1+10^{(logIC_{50}-x)(hillslope)}} \qquad \text{Eq. 2 – } IC_{50} \text{ determination equation}$$

response (y-axis plateau) and "top" refers to the maximal response (y-axis plateau) obtained from the reaction curve. The hillslope describes the steepness of the variable slope curves where a value of 1.0 would be standard, greater than 1.0 increasing the steepness of the curve and less than 1.0 decreasing the steepness.(Graphpad Prism Software Guide 5.0) A typical IC_{50} curve is shown in Figure 2.31.

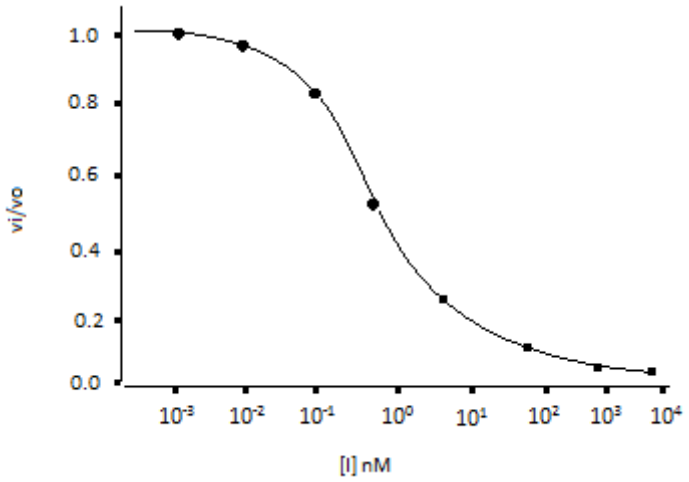

Figure 2.31 – IC_{50} sigmoidal dose response curve

On the y-axis is the fractional activity of the enzyme, a ratio of inhibited rate to uninhibited rate whereas the x-axis is the log of the inhibitor concentration. Although the IC_{50} is more accurately calculated using equation 2, a crude estimation can be made based on the curve where the fractional activity of 0.5 corresponds to an inhibitor concentration on the log scale. An IC_{50} value is dependent on many factors including assay conditions such as substrate concentration, relative to the K_M of that substrate, and pre-incubation time of enzyme and inhibitor, emphasizing the importance of assay conditions.[138]

Enzyme Catalysis Inhibition

There are three types of enzyme inhibitors: irreversible, rapidly reversible and slowly reversible. Irreversible inhibitors, act by binding to the enzyme without the potential of release. This form of inhibition is so tightly bound that they permanently block the enzyme activity, therefore inactivating it. Due to the toxicity of some compounds, irreversibility is often not preferred for therapeutic approaches. Reversible inhibitors interact with the enzyme by diminishing the activity either by binding to the active site or an alternative site in which a conformational change occurs causing decrease in active site binding of other molecules such as substrate.[139]

Time Dependence

Time dependent inhibitors are either irreversible or reversible. Time dependent reversible inhibitors bind to the enzyme on a time scale that allows for the measurement of an initial velocity followed by a steady state velocity of enzyme catalysis, seconds to minutes as opposed to milliseconds.[137] The change in velocity for these slow binding inhibitors can be observed in some cases within the first 20 seconds but can be faster or slower depending on the inhibitor and therefore the progress of the reaction is monitored for a longer period of time. Figure 2.32 shows the product response obtained by monitoring the change in reaction velocity with a time dependent inhibitor. In Figure 2.32 as the inhibitor concentration increases, there is a decrease in the rate of product formed which is expected of inhibition but also it is evident that the velocities are curvilinear. In Figure 2.32b a single curve is visualized more closely and the initial velocity, v_o, is observed to vary over time and the steady state velocity is observed, v_s.

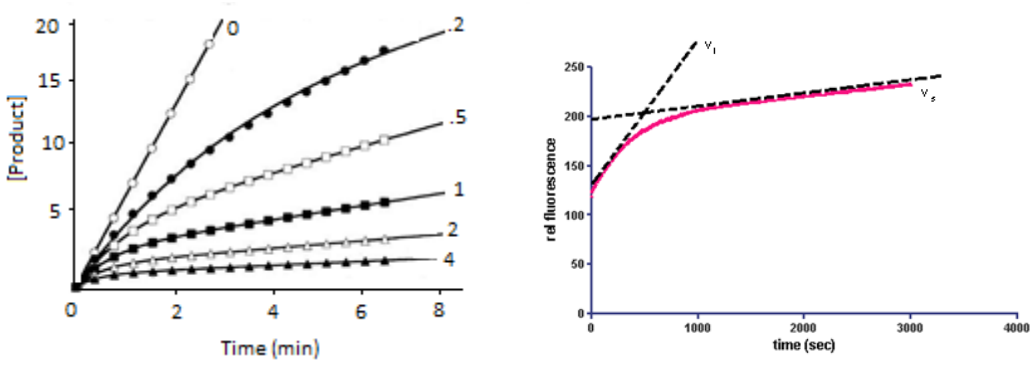

Figure 2.32 – Time dependent inhibition of enzyme activity

$$[P] = v_s t + ((v_o - v_s) * (k_{obs})^{-1} * (1 - \exp^{(-k_{obs} * t)})$$

Eq. 3 – Time dependent equation

The rate constant k_{obs} is associated with the conversion of the initial velocity to steady state. In the case of a non-time dependent inhibitor, the velocity remains unchanged until a significant amount of substrate is consumed.[139] Rapidly reversible inhibitors dissociate from the EI complex quickly whereas slowly reversible dissociate in a slower time frame. The principal for slow-binding inhibition is suggested to be a 1 or 2 step process as shown in Figures 2.33 and 2.34. In a one step process the EI complex dissociates slowly. In a two step process, a non-covalent enzyme inhibitor complex (EI) initially is rapidly formed, followed by a slower step in which EI is transformed resulting in a conformational change to an additional complex (EI*) in which the enzyme is more tightly bound to the inhibitor in a more sTable complex.[137,140] Slow binding can also be due to active site occupancy where one molecule such as water must first be displaced in order for the inhibitor to bind effectively. Either the one or two step mechanisms can describe covalent but reversible enzyme inhibition such as the peptide aldehydes. Although some slowly reversible inhibitors can appear irreversible, their mode of action can be described as slow tight binding in nature.

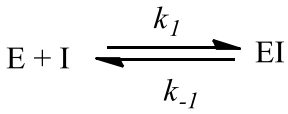

Figure 2.33 – One step mechanism

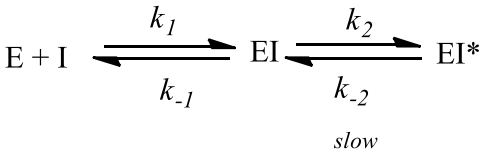

Figure 2.34 –Two step mechanism

When the affinity of an inhibitor for the enzyme is so great that the formation of the enzyme inhibitor complex leaves the free inhibitor concentration significantly depleted, the inhibitor can be termed tight binding and in which case steady state approximations are invalid.[138] Slow-tight binding inhibitor complexes exhibit relatively slow off rates, k_{off}, but can have slow or fast on rates, k_{on}. The inhibition of these types of inhibitors cannot be described by Michaelis-Menten kinetics and therefore an alternative equation can be applied, the Williams-Morrison equation. The K_I of the inhibitor can be determined by fitting the data to the Williams-Morrison equation, eq. 4, only in the case of time dependent inhibitors.[141]

$$\frac{v_i}{v_0} = 1 - \frac{([E]_T + [I]_T + K_I^{app}) - \sqrt{([E]_T + [I]_T + K_I^{app})^2 - 4[E]_T[I]_T}}{2[E]_T}$$

Eq. 4 – Williams-Morrison equation

In equation 7, v_i/v_0 is the relative velocity of the inhibited enzyme reaction is compared to the uninhibited reaction at a set concentration of substrate, I_T is the total

inhibitor concentration, E_T is the total enzyme concentration and K_I^{app} is the apparent dissociation constant for the inhibitor. Plotting data and fitting to equation 4 is presented in Figure 2.35 where the steepness of the response curve increases with increasingly potent inhibitors. Using the K_I^{app}, the K_I can be determined by solving equation 5.

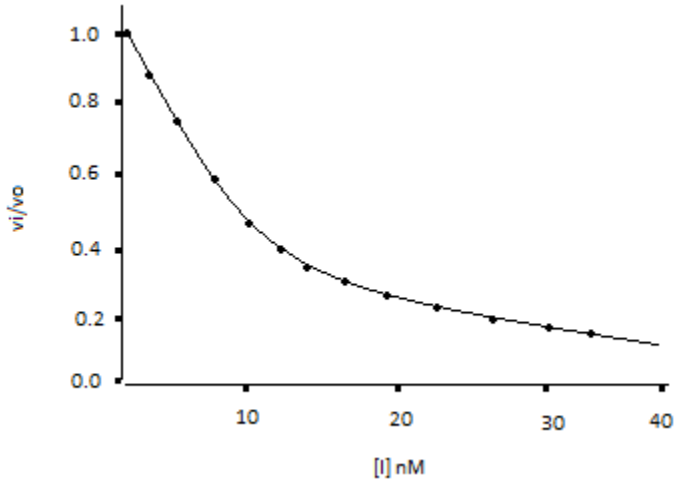

Figure 2.35 - Williams Morrison concentration response plot for tight binding time dependent inhibitor.

Equation 4 does not apply to non time-dependent inhibitors. The Williams Morrison equation also applies to reversible covalent inhibitors.

$$K_I^{app} = K_I \left(1 + \frac{[S]}{K_M}\right) \quad \text{Eq. 5 – } K_I \text{ apparent equation}$$

Rapidly Reversible Modes of Inhibition

There are three basic mechanism of rapidly reversible inhibition of enzyme catalysis: competitive, uncompetitive and noncompetitive (mixed).

Competitive Inhibition

Competitive inhibitors, Figure 2.36, act by directly competing for the enzyme's active site with substrate or substrate-like molecules without affecting the V_{max}. Figure 2.36 is the basic kinetic reaction scheme for a rapidly reversible competitive inhibitor.

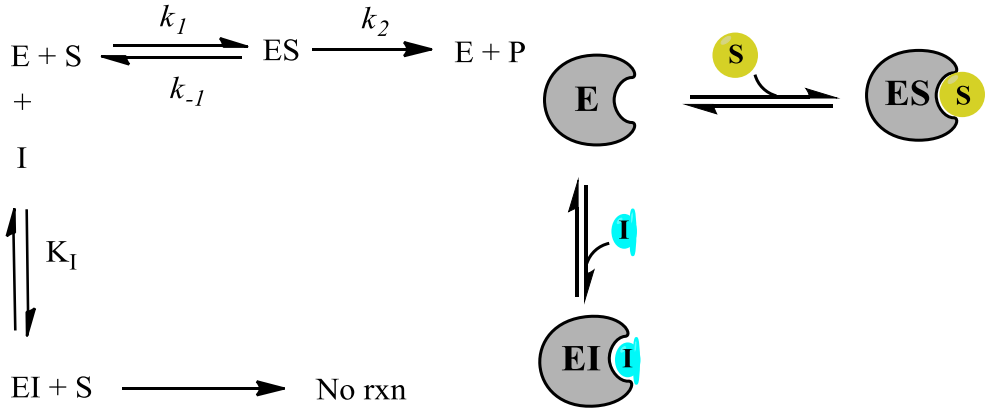

Figure 2.36 – Competitive inhibitor reaction scheme[136,138]

In this reaction scheme, it is assumed that the inhibitor binds to the enzyme and is at rapid equilibrium with the enzyme, therefore rendering the EI complex inactive when available substrate attempts to interact with the enzyme. The presence of a competitive inhibitor alters the Michaelis-Menten equation to include an additional term, α, defined in equation 6 where K_I is the dissociation constant for the enzyme substrate complex. The term α is

$$\alpha = 1 + \frac{[I]}{K_I} \qquad \text{Eq. 6 – Michaelis-Menten α term equation}$$

a function of the inhibitor concentration and its affinity for the enzyme and once inserted into the Michaelis-Menten equation, illustrates how competitive inhibitors affect steady state kinetics, equation 7. When the inhibitor concentration increases, the α term also

increases, increasing the denominator of equation 7 and therefore decreasing the velocity at fixed concentrations of substrate and enzyme. This is apparent in a double reciprocal

$$v = \frac{V_{max}[S]}{[S]+K_M\left(1+\frac{[I]}{K_I}\right)} \qquad \text{Eq. 7 – Michaelis-Menten equation}$$

plot of the inverse velocity vs. inverse substrate concentration for a competitive inhibitor, increasing inhibitor concentration with each curve beginning with the filled squares, Figure 2.37. In Figure 2.37, the point at which the linear lines intersect the y-axis is determined to be $1/V_{max}$, which is constant at all inhibitor concentration for a competitive inhibitor, the point at which they cross the x-axis is defined as $-1/\alpha K_M$, and the slope is the $\alpha K_M/V_{max}$.

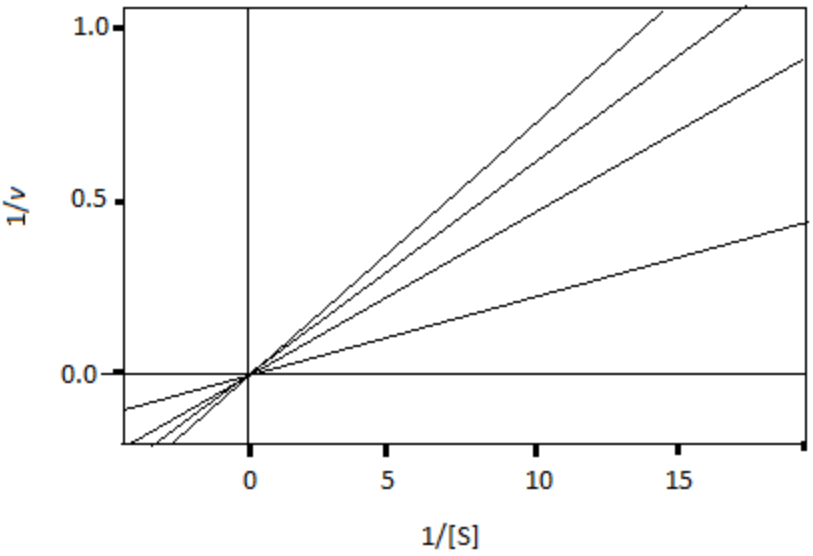

Figure 2.37 – Double reciprocal plot of competitive inhibition

Uncompetitive Inhibition

For an uncompetitive inhibitor, the binding of the compound is directly to the enzyme substrate complex but not to free enzyme. This model, depicted in Figure 2.38, therefore depends on the substrate binding event in order to be effective.

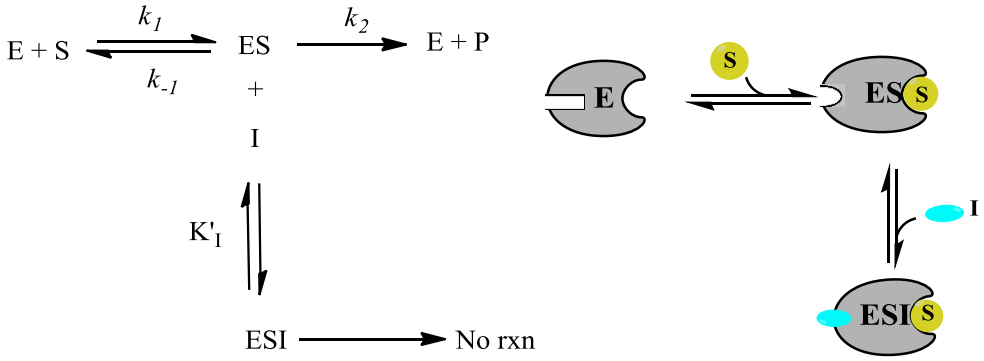

Figure 2.38 – Uncompetitive inhibitor reaction scheme [136,138]

In uncompetitive inhibition, the substrate binding causes a conformational change in the enzyme therefore the structure of inhibitor compound does not necessarily need to mimic the structure of the substrate. This effect of this type of inhibition on the Michaelis-Menten equation is noted in equation 8 and 9. The presence of the α′ term in

$$\alpha' = 1 + \frac{[I]}{K'_I}$$ Eq. 8 – Uncompetitive inhibition α equation

$$v_o = \frac{V_{max}[S]}{\alpha'[S]+K_M}$$ Eq. 9 – Uncompetitive inhibition initial velocity equation

the denominator effects the substrate concentration in this model, therefore as there is an increase in the inhibitor concentration, there is a simultaneous decreases K_M and V_{max}. In Figure 2.39, the double reciprocal plot of velocity vs. substrate is graphed.

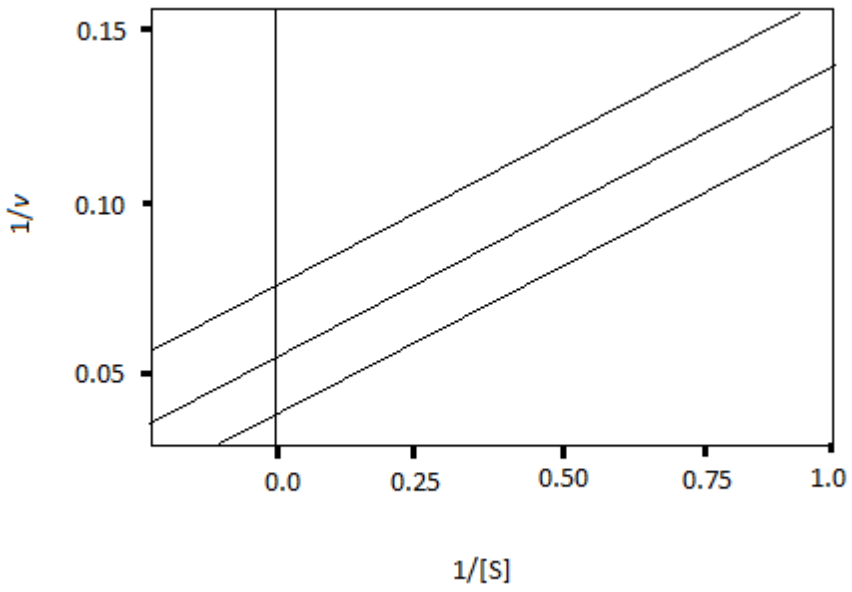

Figure 2.39 - Double reciprocal plot of uncompetitive inhibition

The inhibitor concentration increases horizontally where the point at which the lines cross the y-axis is α'/V_{max} and on the x-axis is - α'/K_M. The horizontal lines of uncompetitive data in this plot are a convenient diagnostic for this type of inhibition. Uncompetitive inhibition has potential in drug design, although not a common mode, as the enzyme activity will decrease as the inhibitor begins to bind and in turn an increase in substrate concentration will occur in the same locale. [142]

Noncompetitive Inhibition

The third modality of inhibition of enzyme activity occurs when the inhibitor binds effectively, with equal or unequal affinity in some cases, to both the enzyme substrate complex and the free enzyme. In noncompetitive inhibition, also referred to as mixed inhibition, the binding events occur at a site distinct from the active site but still

involved in substrate binding and catalysis and can be simultaneous. Figure 2.40 is the schematic for the noncompetitive inhibition model.

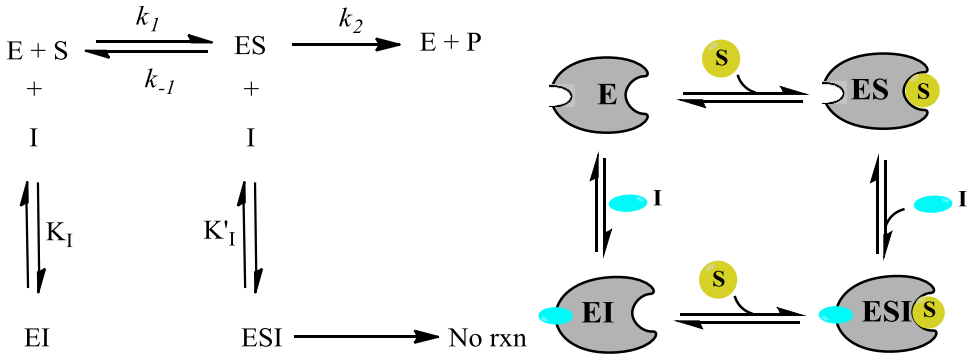

Figure 2.40 - Noncompetitive inhibitor reaction scheme [136,139]

Noncompetitive inhibitors have two distinct dissociation equilibrium constants, one for the binary enzyme inhibitor complex (EI) designated K_I and another for the tertiary enzyme substrate inhibitor complex (ESI) designated K'_I or αK_I. When α is greater than 1, this indicates the preference of the inhibitor for free enzyme; α less than 1 indicates a higher affinity of the inhibitor for the enzyme substrate complex.[139] In contrast to uncompetitive and competitive inhibitor models, noncompetitive inhibitors have differing effects on the Michealis-Menten constants depending on the values of α, summarized in Table 2.1. The effect of noncompetitive inhibition on the Michaelis-Menten equation is illustrated in equation 10. The terms α and α′ in equation 10 allow the inhibitor to be effective at high concentrations of substrate in addition to low concentrations.

$$v = \frac{V_{max}[S]}{\alpha'[S]+\alpha K_M}$$ Eq. 10 – Noncompetitive inhibition Michaelis-Menten equation

A double reciprocal plot of velocity vs. substrate concentration, Figure 2.41, also varies with the value of α. In Figure 2.41, the lines of the inhibited reaction cross at a point other than on the y-axis, a diagnostic determinant. When α = 1 the lines converge at the x-axis, α > 1 the lines intersect above the x-axis, and for α < 1 the lines intersect below the x-axis. The location where the lines converge into each other is defined as $-\alpha/\alpha K_M$, where the lines cross the y-axis defined as α'/V_{max} and the slope corresponds to $\alpha K_M/V_{max}$.

Table 2.1 - Effects of noncompetitive inhibitors on K_M and V_{max} [139]

	α > 1	α = 1	α < 1
K_M	Increases with increasing [I]	No effect	Decreases with increasing [I]
V_{max}	Decreases with increasing [I]	Decreases with increasing [I]	Decreases with increasing [I]

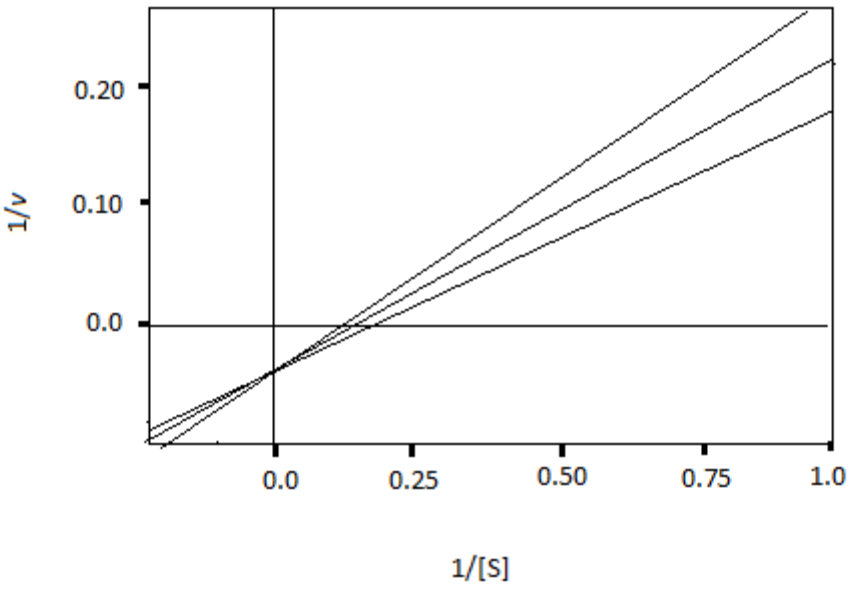

Figure 2.41 - Double reciprocal plot of noncompetitive inhibition

In terms of drug discovery, fewer inhibitors act via the noncompetitive mechanism of action as lead identification of new inhibitors mainly focus on active site directed structures.[139]

CHAPTER THREE

Cathepsin B Materials and Methods

Materials

Human liver cathepsin B was purchased from Sigma (C-8571), Athens (16-12-030102), and Calbiochem (219362). 7-Amino 4-methylcoumarin (AMC) was purchased from Anaspec Inc. (23482). The substrate benzoxycarbonyl-L-arginyl-L-arginyl aminomethyl coumain (Z-R-R-AMC) was purchased from Sigma (C-5429) and Bacchem (I-1135). Dimethylsulfoxide (DMSO) was from Acros (167852500), dithiothreitol (DTT) and ethylenediaminetetraacetic acid disodium salt (EDTA) from Omnipure (3860 and 4010, respectively), and Brij 35 from Sigma (858366). For the assay buffer Na_2HPO_4 (Sigma S-0876) and NaH_2PO_4 (Fisher S369-1) were used. Buffers were filtered through a 0.22 µm PES (polyethylstyrene) low protein binding membrane filter (sterile, Corning 431098) and pH adjusted with 1 M NaOH (BDH H0292) using a Mettler Toledo pH meter. All chemicals except the sodium phosphate were weighed out on a Mettler Toledo AX205 microbalance with an accuracy of 0.01 mg. Sodium phosphate was weighed out on a Mettler Toledo AG204 balance with an accuracy of 0.1 mg. All solutions were prepared with 18Ω ultrapure water that had been gamma irradiated obtained from the Barnstead Diamond purifier. Fluorescence measurements were monitored initially by a Horriba-Jobin-Yvon Fluromax-2 fluorimeter and in later experiments by a Thermo Fluoroskan Ascent FL microplate reader. For microplate assays, Corning 3686 black 96 well plates were used and Starna black walled cuvettes (160 µL) were used in Fluoromax-2 experiments. The final conditions for the cathepsin B assay are 1.25 mM

EDTA, 100 mM sodium phosphate buffer, 60 µM Z-R-R-AMC, 1 nM cathepsin B, 1 mM DTT, 2% DMSO, 0.001% Brij35, and pH 6.8. The experiments were run at 37 °C for optimal enzyme activity. Eppendorf multichannel and single channel mircopipettes were used in preparation and execution of experiments.

Preparation of 0.1% Brij Solution

Brij35 (lot #124K6100, MW 362.55 g/mol) was purchased as a 35% w/v solution; a 0.1% w/v solution was made by taking 28.57 µL of the 35% solution and diluting it up to 10 mL with ultrapure water. This solution was stored at 4 °C.

Preparation of Buffers

A stock solution of 40 mM solution of EDTA was prepared by weighing out 0.744 g of solid (lot #3570335/3577B034, MW 372.24 g/mol) and diluting up to 50 mL with ultrapure water. This solution was kept at 4 °C. A stock solution of 150 mM sodium phosphate buffer was prepared by weighing out 7.402 g of Na_2HPO_4 (lot #120K0125, MW 142.0 g/mol) and 3.033 g of NaH_2PO_4 (lot 021137, MW 137.99 g/mol) and dissolving to approximately 450 mL in a volumetric flask using ultrapure water. The solution was filtered using a 0.22 µM PES low protein binding membrane (Corning) followed by pH adjustment to pH 6.8 with dilute phosphoric acid and brought to a final volume of 500 mL. This solution was kept at 4 °C with a shelf-life of approximately one month.

Assay Buffer 1 (AB1)

For the preparation of 15 mL assay buffer 1, 14.217 mL of 150 mM stock sodium phosphate buffer was mixed with 300 µL 100% DMSO and 483 µL 40 mM EDTA.

Assay Buffer 2 (AB2)

To prepare 5 mL of assay buffer 2, 2.32 mg DTT (Lot #A505256, MW 152.25 g/mol) was weighed out and put into solution with 5 mL assay buffer 1. Solution was vortexed until solid was completely dissolved.

Assay Buffer 3 (AB3)

Assay buffer 3 was used to dilute inhibitors for the assay and was prepared with 9.678 mL 150 mM stock sodium phosphate buffer and 322 µL 40 mM EDTA solution.

Preparation of AMC

A 2 mM stock of 7-amino 4-methylcoumarin (lot AD5760, MW 175.2 g/mol) was made by weighing out 0.3504 mg solid AMC and dissolving via vortex in 1 mL DMSO in a black microfuge tube. The stock solution was stored at -20˚C.

Preparation of Cathepsin B Enzyme Solution

Upon receipt, cathepsin B enzyme was immediately aliquoted into cryo-rated vials at a concentration of 12.76 µM (0.351 mg/mL) and stored in the -80 °C freezer. A 20x dilution of this aliquot was made the day of the experiment by adding 76 µL of cold 0.1% Brij35 to the 4 µL stock on ice, followed by gentle mixing via pipette. Two methods were used to prepare the enzyme from this point, the most current is reported. From the 80 µL of cathepsin B dilution, 6 µL were diluted into 2476 µL assay buffer 2 and stored on ice. Note: this preparation is of the most recent batch of cathepsin B enzyme (Sigma C-8571 lot 046K1292) as each differs slightly in concentration.

Preparation of Inhibitors

Inhibitor dilutions were made with a combination of assay buffer 3 and DMSO in order to keep the concentrations of all components at a set ratio, see Table 3.1 and 3.2.

Table 3.1 - TSC inhibitor dilutions

Inhibitor Solution	Conc (mM)	% DMSO	µL prev sol.	100% DMSO	µl Total	% DMSO
Stock (A)	20	100	-	-	-	100
B	2	100	20	180	200	100
C	0.2	100	20	180	200	100
D	0.02	100	20	180	200	100
E	0.002	100	20	180	200	100
F	0.0002	100	20	180	200	100

Table 3.2 - TSC inhibitor dilutions continued

Inhibitor dilutions at 2% DMSO				
Final Conc (µM)	Conc made (µM)	µL Solution	µL DMSO (100%)	µL AB_3
20	60	1.5 sol A	8.5	490.0
10	30	7.5 sol B	2.5	490.0
5	15	3.8 sol B	6.3	490.0
1	3	7.5 sol C	2.5	490.0
0.5	1.5	3.8 sol C	6.3	490.0
0.1	0.3	7.5 sol D	2.5	490.0
0.05	0.15	3.8 sol D	6.3	490.0
0.01	0.03	7.5 sol E	2.5	490.0
0.001	0.003	7.5 sol F	2.5	490.0

Preparation of Substrate

The substrate stock solution was prepared and stored in dark/black centrifuge tubes or foiled 15 mL falcon tubes. To make an 8.9 mM stock solution, 11.19 mg of Z-R-R-AMC (Bachem Lot # 1007560, MW 621.69 g/mol) was dissolved in 2 mL 100% DMSO and vortexed until dissolved. The stock solution was stored in -20 °C until ready

to use. The day of the experiment, 100 µL of the stock solution was diluted to 180 µM with 4.9 mL ultrapure water in a foiled covered tube.

Table 3.3. Substrate solution preparation

Final Conc (µM)	Conc Made (µM)	Stock used (µM)	µL Stock	µL DMSO	µL H_20
0.4	181.19	8970	20.2	0	979.6
40.0	120.00	181	663.0	6.7	330.3
20.0	60.00	181	331.5	13.4	655.1
6.0	18.00	181	99.4	18.0	882.5

Methods

Cathepsin B Assay

The fluorogenic substrate Z-arginylarginyl-aminomethylcoumarin (Z-R-R-AMC) was used in the enzyme reaction with cathepsin B to fluorometrically monitor the release of AMC (aminomethylcoumarin) via cathepsin B cleavage. The reaction was monitored through the observance of an increase in fluorescence (AMC) at an excitation and emission wavelength of 355 nm and 460 nm respectively (Fluoromax-2 wavelengths were excitation and emission of 355 and 440 nm, respectively). The enzyme was pre-incubated with inhibitor and buffer at 37 °C for 5 minutes followed by addition of substrate, monitoring the fluorometric response for 5 minutes, see Table 3.4 for volumes used in assay. For experiments using the Fluoromax-2, Starna black walled fluorescent-rated microcuvettes were used and were cleaned between experiments with deionized water and dried with a jet of nitrogen gas before and after use. The temperature of 37 °C was achieved via a Neslab RTE-111 water circulator which cycled through the Fluoromax-2 four cell holder. All data analysis was performed using GraphPad Prism 4.03 and 5.0 software.

Table 3.4 – General cathepsin B assay volumes for microplate assay

Solution	Volume (µl)
Enzyme solution	50
Substrate solution	50
Assay buffer 3 or Inhibitor solution	50

AMC Standard Curve Determination

To validate the fluorometer at the excitation and emission wavelengths used (355 and 460 nm respectively) and for enzyme activity standardization purposes, an aminomethylcoumarin standard curve was created monitoring the fluorescence of varying concentrations of AMC. Dilutions were made to include at least 5 concentrations of AMC ranging from 20-0.1 µM with 2% DMSO (see Table 3.5).

Table 3.5 - AMC solution preparation

Final Conc (µM)	Conc Made (µM)	µL 2 mM Stock	µL DMSO	µL H_20
20	60	30	10.2	959.8
10	30	15	25.2	959.8
5	15	7.5	32.7	959.8
1	3	3.7	36.5	959.8
0.1	0.3	10 µL of 30 µM	59.4	930.6

Table 3.6 - AMC curve volumes for microplate assay

Solution	Volume (µL)
AMC solution	50
Assay buffer 2	50
Assay buffer 3	50

AMC fluorescence was monitored for 5 minutes and no pre-incubation time was necessary. The assay was performed in triplicate and volumes used are seen in Table 3.6. From the data, a standard curve was constructed with GraphPad 5.0 software of relative fluorescence versus concentration, allowing for an equation of the line and R-squared value to be determined.

Michaelis-Menten Kinetics

To determine the enzyme's effectiveness the K_M was determined, indicating the concentration of enzyme required for half maximal activity of the cathepsin B. Using a previously made stock solution of Z-R-R-AMC in DMSO, a set of at least 5 concentrations were made varying from 120 µM to 6 µM in dark tubes to prevent light exposure. With the exception of the substrate, the final concentration of all components was kept constant to maintain general assay conditions. The assay buffer and enzyme were pre-incubated at 37 °C for 5 minutes after gentle mixing followed by addition of various concentrations of Z-R-R-AMC, for volumes see Table 3.4 (general cathepsin assay volumes Table 3.4). The reaction was monitored at 37 °C for 5 minutes fluorimetrically and run in triplicate. The data were analyzed via GraphPad 5.0 by plotting velocity of the reaction versus the varying substrate concentrations which were fit to the Michaelis-Menten equation (see equation 10). The V_{max} was not determined due to the limitation of this value on the concentration of the substrate. In order to construct a Michaelis-Menten curve for this purpose, it is recommended to use substrate at a concentration of 0.1 to 10x the value of V_{max} which is subject to our limited sample size and therefore not plausible in our case.

Table 3.7 - Michaelis-Menten dilutions

Final Conc (μM)	Conc Made (μM)	Stock used (mM)	μL Stock	μL DMSO	μL H_20
120	360	8.92	40.4	0	959.6
100	300	8.92	33.6	6.8	959.6
60	180	8.92	20.2	20.2	959.6
30	90	8.92	10.1	30.3	959.6
10	30	8.92	3.4	37	959.6

Inhibitor/Compound Hit Determination

To initially determine if the compounds are inhibiting the enzyme at a reasonable concentration, a cut-off was set at 10 μM inhibitor. All compounds were initially screened at a final concentration of 10 μM and if approximately 50% of the enzyme was inhibited, it was considered to be a "hit" and a full IC_{50} value assay was completed. If significant inhibition was not observed, the compound was reported as ≥ 10 μM and no further testing was required.

IC_{50} Determination

The concentration of inhibitor required to reduce the enzyme's activity by 50% is referred to as the IC_{50}. To determine this value, inhibitors were weighed out fresh from solids if available (between 0.5-1.5 mg) using a glass capillary tube to carefully transfer to a 200 μL microfuge tube. The compounds were dissolved in DMSO to generate a 20 mM stock solution, vortexed until dissolved, and kept at -80 °C in attempt to preserve activity and stability. A set of solutions referred to as A-E were then generated from the stock solution into DMSO (see Table 3.1 previously). From the A-E solutions, inhibitor dilutions were made in DMSO and buffer 3 with the final concentration for the assay between 20 μM and 1 nM (lower concentrations if required). The inhibitor solutions were

then incubated with the cathepsin B solution (50 µL inhibitor and 50 µL enzyme) for 5 minutes at 37 °C after gentle mixing. After the pre-incubation time, the Z-R-R-AMC substrate was added (50 µL) and the plate was gently mixed again followed by immediate monitoring via fluorescent microplate reader at 37 °C in volumes according to Table 3.4. The relative fluorescence response versus time was recorded and exported into Graphpad 5.0 for analysis via the sigmoidal dose response (variable slope) equation with a bottom constraint of zero and top constraint of 1, see equation 2.

Advanced Kinetic Analysis - Progress Curves

In order to determine if the most promising inhibitors displayed time dependence in relation to binding to the enzyme, progress curves were performed. The inhibitor (same dilutions used for IC_{50} determination) and substrate (60 µM) were added to the microplate in volumes according to Table 3.4 (general cathepsin b assay volumes). The enzyme was added and immediately the reaction was mixed gently for 2-3 seconds followed by fluorometric measurements taken continuously for 3000 seconds so as to collect the maximum data points. For analysis, a graph was constructed of relative fluorescent units (RFU) versus time. A deviation from linearity indicated time independence of the inhibitor binding to the enzyme.

Preincubation Time Dependence

The IC_{50} values previously were all performed at 5 minute pre-incubation periods. To determine if pre-incubation time of the inhibitor and enzyme affected the IC_{50}, various times were tested. In this experiment, the enzyme and inhibitor were allowed to pre-incubate at 37 °C for 0, 5, 15, 30, 60, 120 minutes followed by addition of substrate at a

final concentration of 60 µM, monitoring the release of AMC fluorometrically. See Table 3.4 for volumes used. The final concentration of inhibitor was in the range of 0.01-10 µM (according to the IC_{50} procedure) and enzyme at 1 nM. The pre-incubation times versus IC_{50} values were plotted and trends were observed.

Reversibility

Reversibility of the inhibitor was investigated through an experiment in which the enzyme at 100x was pre-incubated at 37 °C with inhibitor at 20 µM for 30 and 60 minutes. Initial concentrations and volumes used for the enzyme-inhibitor incubation is seen in Table 3.8 and were made in a 100-200 µl tube. After incubation, the pre-incubated solution was added to the microplate followed by rapid dilution with substrate in assay buffer with the final concentration of 60 µM substrate, see Table 3.9 for volumes.

Table 3.8 – Reversibility assay volumes enzyme-inhibitor incubation

Solution	Volume (µL)
300x Enzyme solution	3.1
40 µM Inhibitor solution	10
Assay buffer 2	6.9

Table 3.9 – Reversibility assay volumes for microplate assay

Solution	Volume (µL)
Incubated Enzyme-Inhibitor solution	1.5
Substrate solution	148.5

The final concentration of inhibitor, enzyme, and DMSO are 0.2 µM, 1 nM, and 2% respectively. The reaction was then observed at 37 °C for 4 hours and data plotted as relative fluorescent units versus time in seconds.

IC_{50} Substrate Concentration Dependence (Competitive vs.Non. etc)/K_I Determination

The effect of substrate concentration on IC_{50} was determined by generating IC_{50} value data at various concentrations of substrate: 0, 6, 20, 40, 60 µM, see Table 3.10.

Table 3.10 - Serial dilutions for varying substrate concentration

Final Concentration (µM)	Stock Used (µM)	µL stock	µL 100% DMSO	µL H_2O
60.00	8970.00	80.27	0	3920.00
40.00	180.00	2666.67	26.67	1306.67
20.00	120.00	2000.00	40.00	1960.00
6.00	60.00	1200.00	56.00	2744.00
0	0	0	80.00	3920.00

The experiment was completed as is noted in IC_{50} determination and a graph was constructed of IC_{50} vs. substrate concentration. The data was transformed into a Lineweaver Burk plot of 1/v vs. 1/s where "v" is velocity of reaction and "s" is the substrate concentration. This plot indicated whether the inhibitors were competitive, non-competitive, or un-competitive based on the orientation of the data crossed the x and y-axis. Analysis of data to determine K_I was performed with GraphPad Prism 5.0 using a Nonlinear Morrison Plot for time dependent compounds with the following constraints: [Cathepsin B] = 0.002 µM, [Z-R-R-AMC] = 60 µM, and a K_M value from the

corresponding Michaelis-Menten Curve. For non-time dependent inhibitors, classical inhibition kinetics were used to determine the K_I.

CHAPTER FOUR

Cathepsin B Results and Discussion

Cathepsin B and cathepsin L are cysteine proteases that belong to part of the papain subfamily.[143,138] The two enzymes have significant sequence homology of the proenzymes (approximately 29.9%) although there are distinct differences in structural homology.[144] They share key structural similarities. Both enzymes are synthesized as inactive proforms which can be converted to their active form via release of an N-terminal proregion followed by autoproteolytic cleavage.[145] The maturation pattern is analogous for cathepsins L and B. Both cathepsins L and B are 22-25 kDa and are formed by two domains with a central helix prominent on the left domain and a β-barrel motif on the right domain. The V-shaped cleft formed at the interface of the two domains contains the active site residues, a catalytic triad conserved by the two enzymes composed of Cys, His, and Asn. Although cathepsin B can function as both an endo and exopeptidase, cathepsin L is solely an endopeptidase. Another difference is the occluding loop which lies over the active site cleft and is in closed orientation at acidic pH, a feature not seen in cathepsin L, adding to the specificity of cathepsin B. Substrate specificity for the two enzymes is somewhat similar as both enzymes have a deep hydrophobic subsite.[146] The S_2 subsite is a primary determinant of specificity for cathepsins L and B; cathepsin L prefers hydrophobic residues in this position whereas cathepsin B is modified with a glutamic acid residue that accommodates basic residues in the binding pocket.[112] The S_1 subsite for L is not as selective as the S_2 site for cathepsin L but in cathepsin B, there is a preference for non-bulky residues in this position. Considering the similarities of these

enzymes, a focused library of thiosemicarbazone derivatives containing a number of effective inhibitors of cathepsin L was tested for inhibitory activity against the related enzyme cathepsin B.

The Cathepsin B Catalyzed Enzyme Reaction

A fluorogenic method were used to monitor the reaction of cathepsin B and the substrate Z-R-R-AMC. Cathepsin B catalytically cleaves the fluorescent product, AMC, from the substrate, Figure 4.1. The release of AMC was monitored fluorometrically at an excitation and emission wavelength of 355 and 460 nm, respectively. The peptide bond

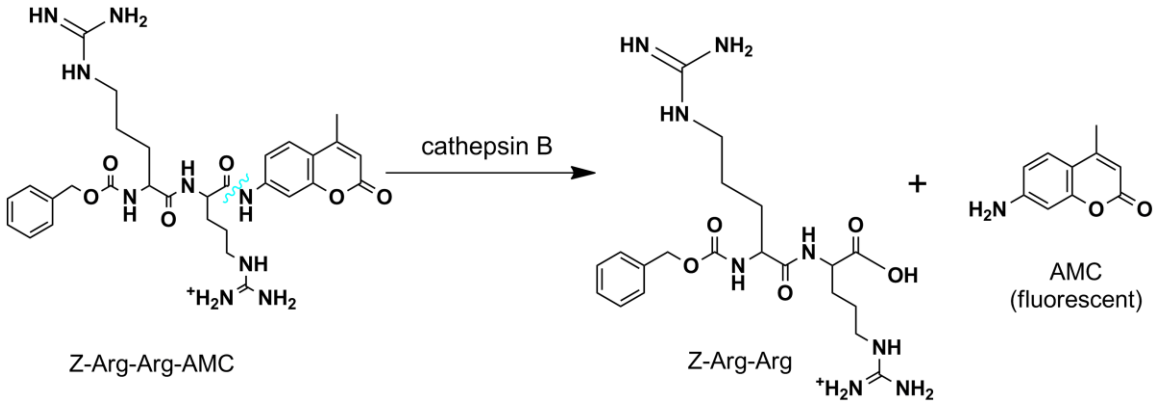

Figure 4.1 – Cleavage of AMC from substrate Z-R-R-AMC via cathepsin B

cleaved by cathepsin B is shown in teal and the fluorescent product aminomethylcoumarin (AMC) is formed. Detection level depends on fluorophore intensity and on instrument sensitivity. In these experiments two instruments were utilized, one with a higher sensitivity allowing for lower substrate concentration and another, a microplate reader, which in effect required a ten-fold increase in substrate concentration for equivalent detection.

Method Development

A search of literature resulted in a multitude of assay conditions for cathepsin B enzyme assays therefore an excel file was compiled and the most frequently used conditions were then tested for optimization. Initial work was performed on Fluoromax2 instrumentation and began with slit width and excitation wavelength. The literature reported wavelengths between and excitation of 355 and 380 nm, therefore wavelength was tested concurrently with slit width which was varied from 2.5 to 5 nm. Scans were run to obtain an entire spectrum to visualize maximal fluorescence response for AMC, the product of the enzyme reaction, without reaching the detection limit of the instrument (approximately 4 E-6 cpm). Buffer was used as the blank. Fluorescence at a slit width of 5 nm and at approximately 355 nm excitation wavelength maximized the emission at 440 nm. In further testing where higher AMC concentrations were used a slit width of 2.5 nm was optimal in obtaining maximal signal without the risk of self- quenching. Conditions also tested to optimize the cathepsin B assay included concentrations of reducing agents (dithiothreitol, DTT), buffer type (sodium phosphate and sodium acetate), EDTA, detergent (Brij) and DMSO. DTT was used as a reducing agent to prevent disulfide bonds from being formed in the active site thereby rendering it irreversibly inactive. The buffer was used to resist changes in pH and as a medium for assay components. EDTA was used as a general chelating agent to remove free metal ions present in solution, binding them and preventing them from affecting the enzyme's active site. Brij30 was used to prevent aggregation of the enzyme and also appeared to stabilize the enzyme. DMSO was used to increase the solubility of the thisemicarbazone compounds. A pH of 6.8 was chosen as it was basic enough to open the occluding loop opening, making the active site available for

substrate and/or inhibitor binding. The enzyme solution was determined to be stable at 1 nM for up to 2 hours at 37 °C by monitoring the fluorescence in the presence of substrate over time, where the slope continually increased at the same rate indicating it did not lose activity. DTT was varied in concentration (2, 4, 8 mM) simultaneously varying the pre-incubation of the enzyme in buffer (0, 5, 15, 30, 45 minutes). Buffer used initially was 130 mM sodium potassium phosphate buffer with 1 and 4 mM EDTA at pH 6.8. The results of the optimization indicated that the following conditions were ideal for cathepsin B assays in our hands: 1 nM cathepsin B, 0.01% Brij 35, 2.7 mM DTT, 2 mM EDTA, 130 mM sodium potassium phosphate buffer, 6 µM Z-R-R-AMC, 2% DMSO, excitation and emission wavelengths of 355 and 440 nm (respectively), a slit width of 5 nm, 5 minute incubation of enzyme at 37 °C and a 5 minute run at 37 °C. The conditions of the assay were converted to a microplate based format and the assay was modified again based on a recent article using similar instrumentation.[147] The conditions were tested for stability, similarity of results using previous conditions and ease of use. These conditions found to be effective with the microplate based format are as follows: 1 nM cathepsin B, 0.001% Brij, 1 mM DTT, 1.25 mM EDTA, 100 mM sodium phosphate buffer pH 6.8, 60 µM Z-R-R-AMC, 2% DMSO, excitation and emission at 355 and 460 nm (respectively), 5 minute incubation of enzyme at 37 °C and a 5 minute run at 37 °C. Compounds were all tested in at least triplicate and compared to control curves in the absence of compounds, therefore normalizing the assay each time.

AMC Curves

Aminomethylcoumarin standard curves were run to ensure the fluorimeter and microplate fluorimeter were working correctly and to normalize the fluorescence data for the enzyme assays. AMC is liberated in the enzyme reaction when cathepsin B

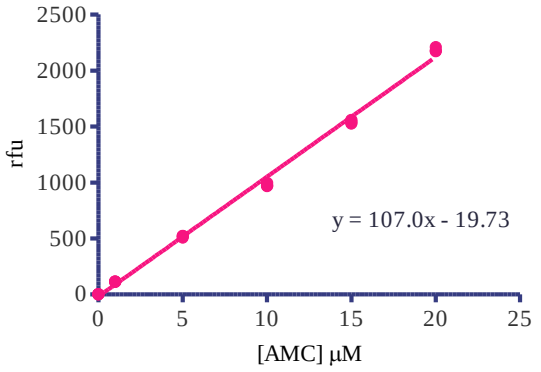

Best-fit values	
Slope	107.0 ± 1.609
Y-intercept when X=0.0	-19.73 ± 18.00
X-intercept when Y=0.0	0.1844
1/slope	0.009348
95% Confidence Intervals	
Slope	103.6 to 110.4
Goodness of Fit	
R square	0.9964

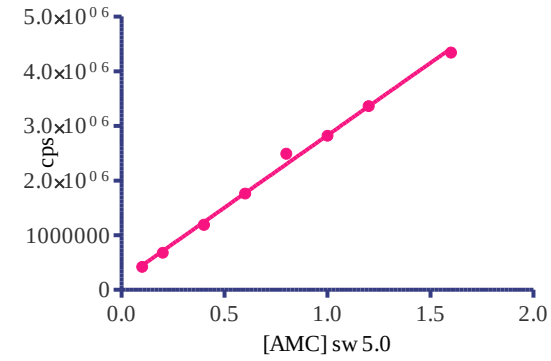

Best-fit values	
Slope	2.646e+006 ± 64885
Y-intercept when X=0.0	180211 ± 57167
X-intercept when Y=0.0	-0.06810
1/slope	3.779e-007
95% Confidence Intervals	
Slope	2.488e+006 to 2.805e+006
Goodness of Fit	
R square	0.9964

Figure 4.2 – AMC standard curve determination on fluorescence microplate reader (left) and Fluoromax2 (right) fluorimeter

hydrolyzes the substrate, Z-R-R-AMC, releasing the fluorescent product. From the equation of the line obtained from the AMC standard curve graphing concentration of AMC vs average fluorescent units, the enzyme assay units are expressed as the amount of AMC released per unit time.

Michaelis-Menten Curves

Michaelis Menten kinetics was performed upon arrival of new enzyme periodically upon long term storage of current stock to ensure activity had not decreased significantly. The literature value of K_M of cathepsin B varies depending conditions used, therefore an assay using the most similar conditions was chosen. The Michaelis Menten equation, equation 12, shows the dependence of the parameters K_M and V_{max} on the concentration of substrate. When creating a Michaelis-Menten curve, it is optimal to use concentrations of substrate 0.1 to 10 times that of the reported K_M. The substrate chosen

$$v = k_2[ES] = \frac{V_{max}[S]}{[S] + K_M}$$

Eq. 12 - Substrate dependence on Michaeli-Menten parameters equation

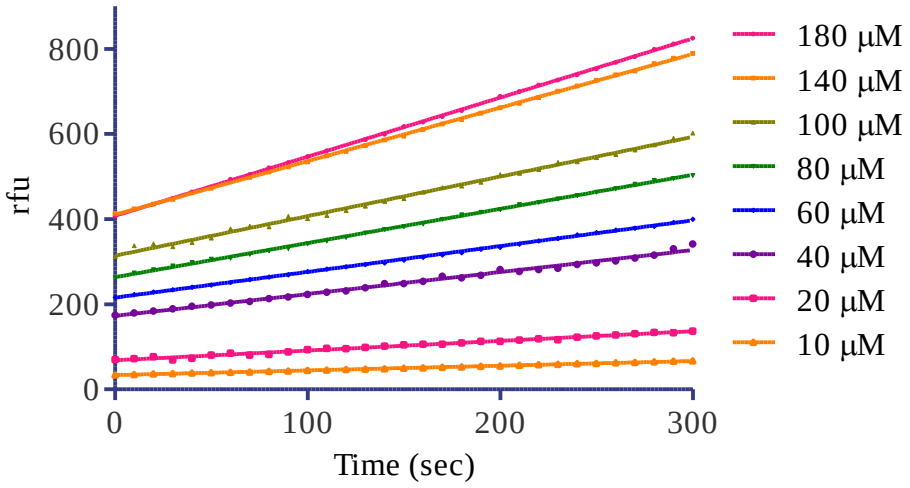

Figure 4.3 – Relative fluorescence response over time varying substrate concentration, Michaelis Menten fit

for these experiments has a relatively high K_M, making it difficult to construct a complete curve due to solubility and high concentration of substrate. This fact also contributes to the sensitivity of the assay to slight variations in the substrate concentration. The value chosen to compare our enzyme with was from Boris and Turk [148] who used the following conditions: 5 mM DTT, 1 mM EDTA, 0.1% PEG (polyethylene glycol), 100 mM sodium phosphate, pH 6.0, 37 °C, and the substrate Z-R-R-AMC. The K_M in this paper is 212 μM with a k_{cat} of 67 s^{-1}. The reaction rates were obtained by monitoring relsease of product, AMC, as a function of time as seen in Figure 4.3.

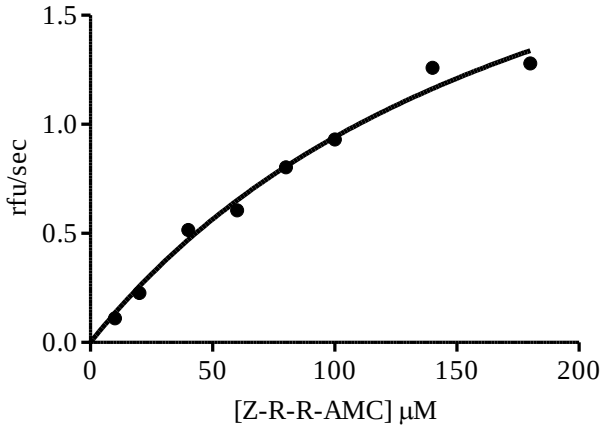

	Slope
Michaelis-Menten	
Best-fit values	
Vmax	2.831
Km	200.8
Std. Error	
Vmax	0.4378
Km	49.00
95% Confidence Intervals	
Vmax	1.760 to 3.902
Km	80.85 to 320.7
Goodness of Fit	
Degrees of Freedom	6
R square	0.9861
Absolute Sum of Squares	0.01842
Sy.x	0.05541
Constraints	
Vmax	Vmax > 0.0
Km	Km > 0.0
Number of points	
Analyzed	8

Figure 4.4 – Michaelis Menten kinetics of cathepsin B from Michaelis-Menten kinetic fits of data collected (and shown), the K_M for is 200.8 μM, within agreement with Turk's literature value of 212 μM.[148]

IC_{50} Determination

Figure 4.5 is the experimental design rational for determining inhibitor effectiveness against cathepsin B. Initially the inhibitory activity of compounds (synthesized by the Pinney laboratory) was determined at a 10 µM cut-off, stage 1. If the compound inhibited the enzyme's activity by 50% or more, a full IC_{50} was determined in stage 2. An IC_{50} is the concentration of inhibitor required to reduce the activity of the enzyme by 50%.

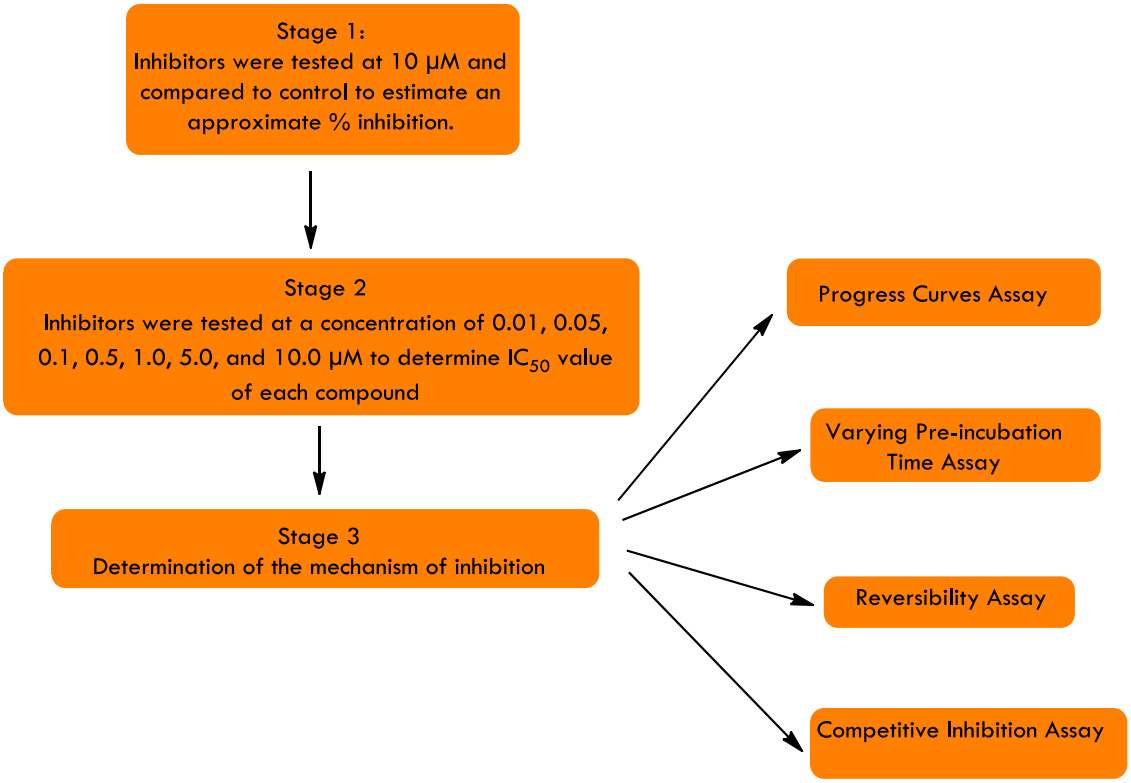

Figure 4.5 – Strategy and experimental design rational for determining inhibitor effectiveness

The enzyme substrate reaction was monitored in the absence and presence of inhibitor at varying concentrations and the resulting rfu vs time graphs were analyzed. The normalized slope, which represented the velocity of the reaction, was plotted versus

the concentration of the inhibitor present in a logarithmic scale. The data was fit to a sigmoidal dose response curve, equation 2, with constraints of the top of the curve set to one and the bottom set to zero. The hillslope is this case is a measure of teepness of the curve where the increase in value indicates an increase in steepness. Of the most potent compounds, the mechanism of inhibition was investigated in stage 3. The library of compounds investigated contained small molecular weight derivatives of the thiosemicarbazone moiety, as seen in Figure 4.6. A number of ketone precursors were also investigated, Figure 4.6.

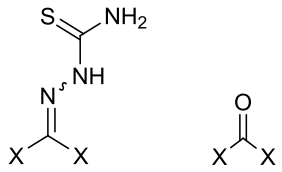

Figure 4.6– Common moieties shared among compounds tested for cathepsin B activity; thiosemicarbazone (left) and ketone (right) moiety.

Table 4.7 contains representative scaffolds of compounds tested against cathepsin B where x are substituents such as halogens, methoxy, nitro, amino, or hydroxyl groups. For a complete list of the structures tested, see appendix B. More than 174 compounds were tested at a 10 µM concentration. While most demonstrated less than 50% inhibition, six compounds showed promising inhibitory IC_{50} values ranging from 1.2 µM to 9.4 µM. The most potent inhibitors of cathepsin B determined from this library all shared a benzophenone thiosemicarbazone moiety, Table 4.11.is the comparison of the ketone precursor with the substituted thiosemicarbazone (TSC) demonstrated the importance of the unsubstituted TSC moiety, Figure 4.8. The substituted thiosemicarbazone functional group also proved to be inactive when the terminal amine was substituted with a phenyl

ring, a benzyl group or an ethyl group. Further substitution on the dibromobenzophenone thiosemicarbazone in the ortho, meta or para positions with groups such as methoxy or t-butylmethylsilyl ether (OTBS) did not show activity; however, an hydroxyl functional group in the para position elicited activity, compound compound **6**, but was very close to the cutoff point of 10 µM.

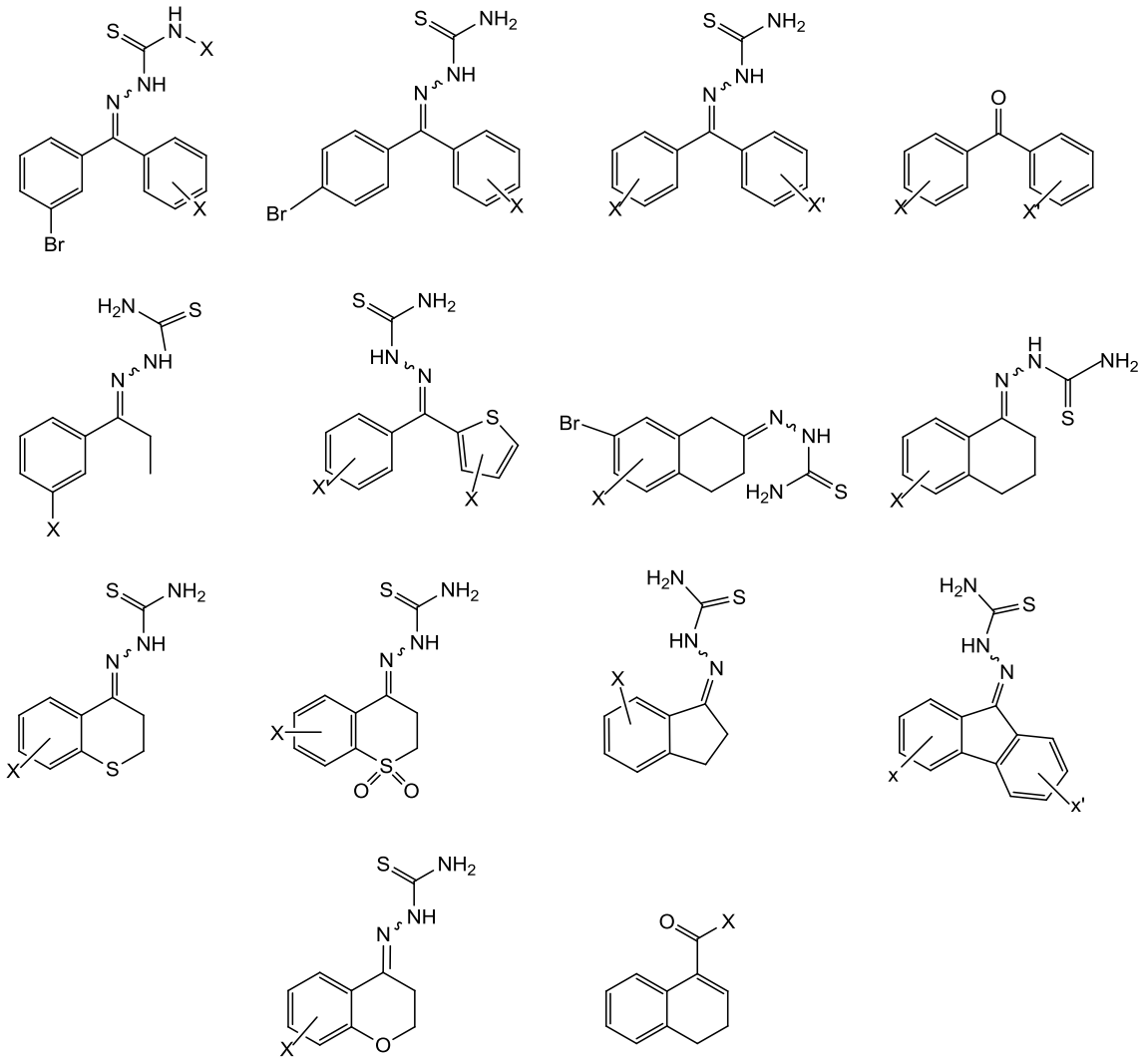

Figure 4.7 – Scaffolds of TSC compounds tested for inhibition against cathepsin B (synthesized by the Pinney laboratory) [51-54,55]

Bromine substituted in the para position on one of the phenyl rings was one feature shared by five of the six active compounds. The trimethoxyphenyl

hydroxymethoxy phenyl moiety, compound **4**, is the most potent of the inhibitors at 1.42 μM. The next most active compounds are compound **3**, compound **2**, and compound **1** with IC_{50}s within the 1-2 μM range. Compound **5** has an IC_{50} approximately three times that of the best inhibitor in this series at 5.691 μM. IC_{50}s were done in at least triplicate and representative graphs are shown in Figures 4.9-4.11.

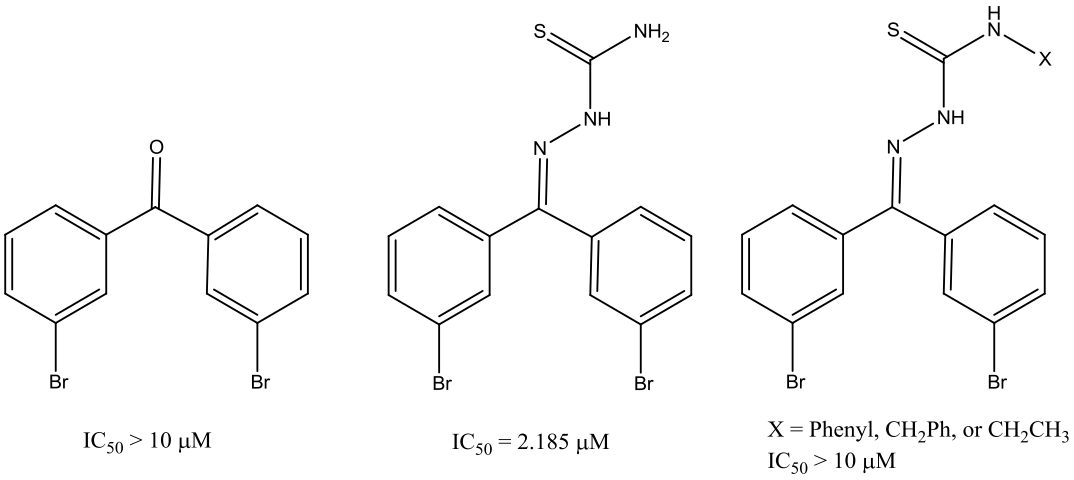

IC_{50} > 10 μM

IC_{50} = 2.185 μM

X = Phenyl, CH_2Ph, or CH_2CH_3
IC_{50} > 10 μM

Figure 4.8 – Thiosemicarbazone "warhead" effect on inhibition

Table 4.11 – IC_{50} values for inhibitors of cathepsin B*

Structure	Compound	IC_{50}
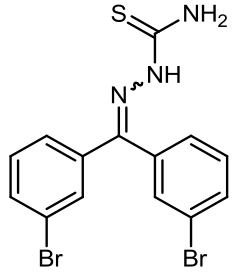	**1**	2.185 ±0.189 μM
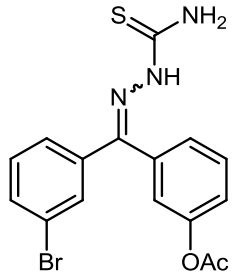	**2**	1.600 ±0.171 μM

Table 4.11 (continued)

Structure	Compound	IC_{50}
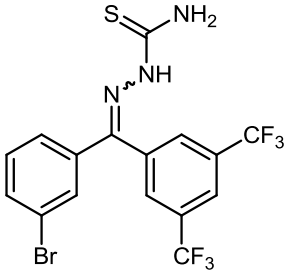	**3**	1.585 ±0.103 µM
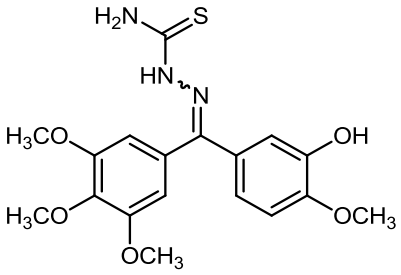	**4**	1.424 ±0.144 µM
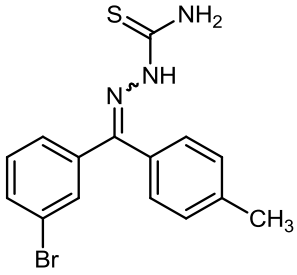	**5**	5.691 ±0.579 µM
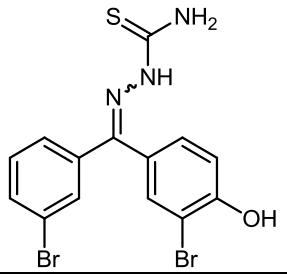	**6**	9.493 µM

*Compounds synthesized by the Pinney laboratory[51-54,55]

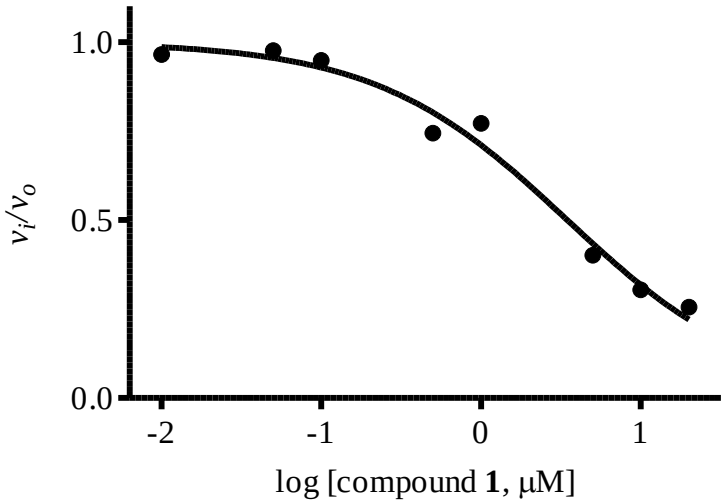

	slope
Sigmoidal dose-response (variable slope) [2]	
Best-fit values	
Bottom	= 0.0
Top	= 1.000
LogEC50	0.5398
HillSlope	-0.7219
EC50	3.466
Std. Error	
LogEC50	0.05576
HillSlope	0.06671
Goodness of Fit	
Degrees of Freedom	6
R square	0.9833
Constraints	
Bottom	Bottom = 0.0
Top	Top = 1.000
Number of points	
Analyzed	8

Figure 4.9 – IC_{50} curve for compound **1**

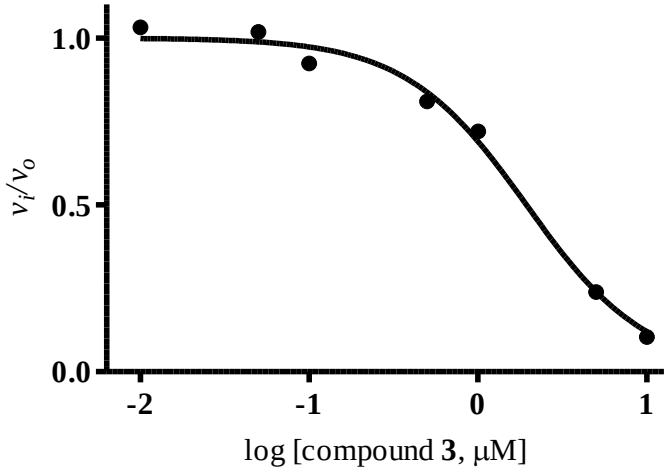

	Slope
Sigmoidal dose-response (variable slope) [2]	
Best-fit values	
Bottom	= 0.0
Top	= 1.000
LogEC50	0.2862
HillSlope	-1.211
EC50	1.933
Std. Error	
LogEC50	0.03858
HillSlope	0.1020
Goodness of Fit	
Degrees of Freedom	5
R square	0.9925
Constraints	
Bottom	Bottom = 0.0
Top	Top = 1.000
Number of points	
Analyzed	7

Figure 4.10 – IC_{50} curve for compound **3**

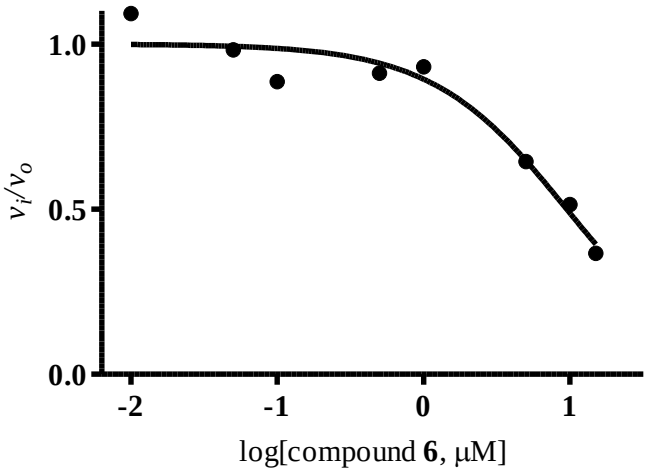

	Slope
Sigmoidal dose-response (variable slope) [2]	
Best-fit values	
Bottom	= 0.0
Top	= 1.000
LogEC50	0.9774
HillSlope	-0.9455
EC50	9.493
Std. Error	
LogEC50	0.06789
HillSlope	0.1907
Goodness of Fit	
Degrees of Freedom	6
R square	0.9495
Constraints	
Bottom	Bottom = 0.0
Top	Top = 1.000
Number of points	
Analyzed	8

Figure 4.11 – IC_{50} curve for compound **6**

DMSO Effects

To solubilize many of the small molecular weight compounds the solvent dimethylsulfoxide (DMSO) was used. DMSO acts a good polar medium that translates well into clinical models within specific concentrations. In enzyme assays, the concentration is kept as low as reasonably possible to avoid toxicity to the animal models

in future studies in addition to limiting the thermal response caused by high concentrations of DMSO in the injection site. These factors led to studies investigating the effect of DMSO on the enzyme activity and on the IC_{50} of the inhibitors. It has been previously reported that DMSO in concentrations in excess of 5% caused an inhibition of cathepsin B activity, unlike other cathepsins whose activities were not affected by the solvent or were stabilized.[149] Enzyme activity was monitored in the presence of 0.8% and 2% DMSO and comparing the velocities of these two graphs there was not a significant difference, within 10%. For the dibromobenzophenone thiosemicarbazone, the IC_{50} was determined at various concentrations of DMSO. In other cathepsins, the increase in this solvent lowered the IC_{50} of this compound; therefore a similar effect was expected for cathepsin B. The IC_{50} for compound **1** against cathepsin B did not significantly change with changing DMSO concentration when 0.8% and 2% DMSO was tested. The IC_{50} values remained within 10% of each other, within the standard error accepTable for this type of data. It is concluded that while the activity of cathepsin B can be affected by greater than 5% DMSO, the IC_{50} of compound **1** and the enzyme's activity are not significantly affected by low DMSO concentrations variation.

Advanced Enzyme Kinetics

Of these six active compounds, the four most potent compounds, compound **1** were further tested to determine the mechanism of inhibition via advanced kinetic methods.

Progress Curves

To assess the time dependence of the inhibition, the reaction rates were monitored as a function of time. For this experiment, various concentrations of inhibitor were plated with 60 μM substrate Z-R-R-AMC. Reactions were initiated by the addition of the enzyme to the inhibitor substrate mixture without preincubation followed by immediate fluorescence measurements for 3000 seconds. The components were added in the sequence noted in order to observe the initial interactions of the enzyme with the inhibitor. The progress curves can be described by equation 14 where P is product formed, v_s is the steady state velovity, t is time in seconds, v_o is the initial velocity and k_{obs} is the rate constant associated with the conversion of the initial velocity to steady state. For time dependent curves, a change in slope over time should be observed where

$$[P] = v_s t + ((v_o - v_s) * (k_{obs})^{-1} * (1 - \exp^{(-k_{obs} * t)}) \quad \text{Eq. 14}$$

the inhibition increases as the reaction progresses. This is due to the initial velocity of enzyme catalyzed substrate cleavage followed by a change to a steady state velocity. The inhibitor binding rate varies but should be observable using this technique. In this study, it was found that two of the inhibitors (compound **1** and compound **2**) were time dependent while the other two were not time dependent (compound **3** and compound **4**) except at the highest concentrations, 10 μM. For compound **1** and compound **2**, an increase in fluorescence is seen in the early time points of the curve which is referred to as the initial (v_i) followed by a change to the steady state velocity (v_s), characteristic of time dependence. Progress curves for compound **3** indicate the inhibitor is not-time

dependent except at the highest concentration, 10 µM. This higher concentration of both compound **3** and compound **4** suggests a different mode of inhibition.

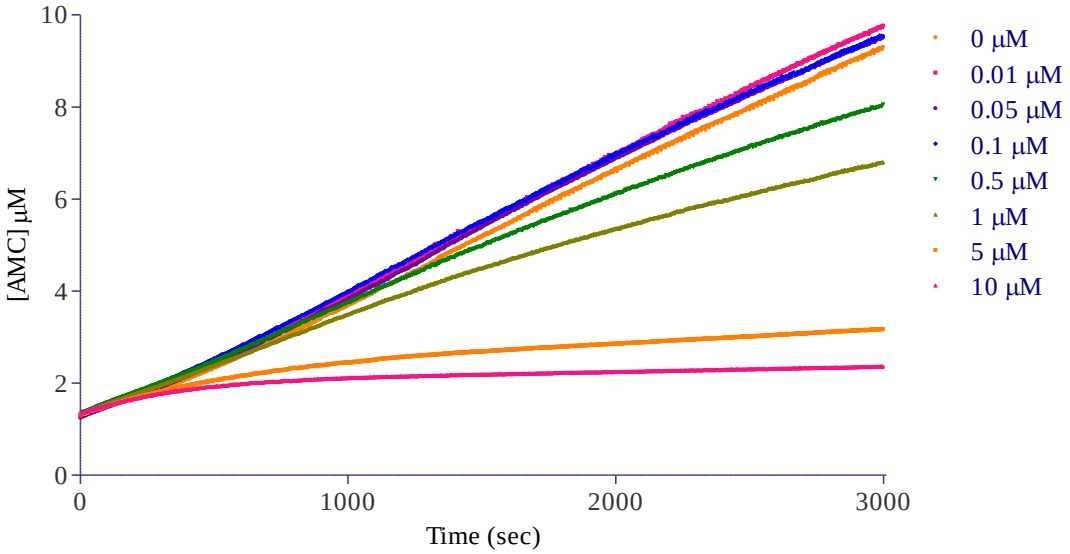

Figure 4.12 – Progress curves and data for the compound **1** inhibition of cathepsin B, fit to equation 14

Table 4.12 – Graphpad Prism 5.0 data analysis compound **1**

Analysis parameters	10 µM compound **1**	5 µM compound **1**
v_o	0.736	0.809
v_s	0.0004679	0.0008585
k_{obs}	0.45±0.07	0.52±0.09
R^2	0.7938	0.9310
Points analyzed	500	500
Constraints	v_o v_s $k_{obs} > 0$	

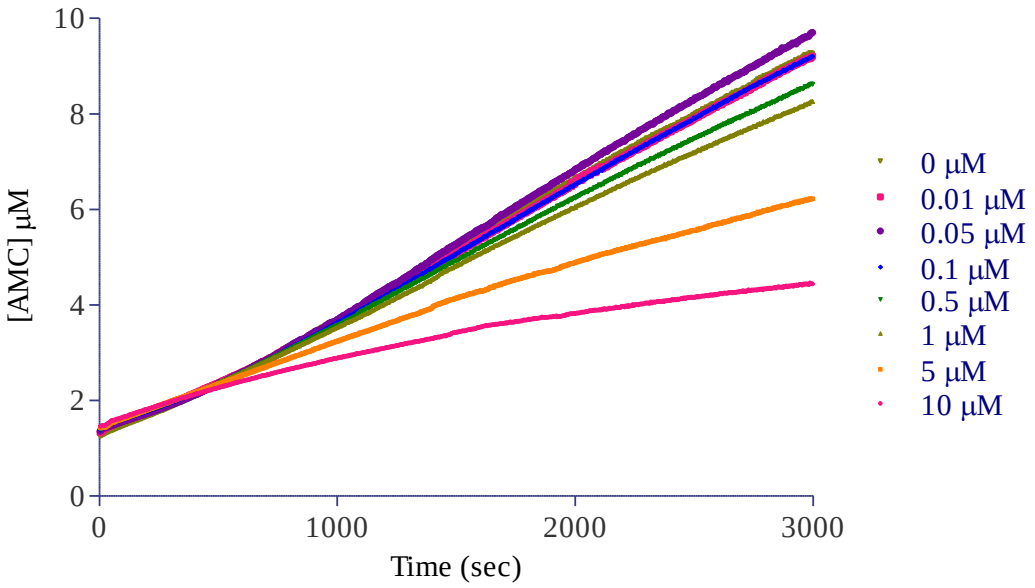

Figure 4.13 – Progress curves and data for the compound **2** inhibition of cathepsin B, fit to equation 14

Table 4.13 – Graphpad Prism 5.0 data analysis compound **2**

Analysis parameters	10 µM compound **2**	5 µM compound **2**
v_o	1.188	~2.110
v_s	0.001263	0.001796
k_{obs}	0.74±0.09	~1.46±0.19
R^2	0.9923	0.9998
Points analyzed	500	500
Constraints	v_o v_s $k_{obs} > 0$	

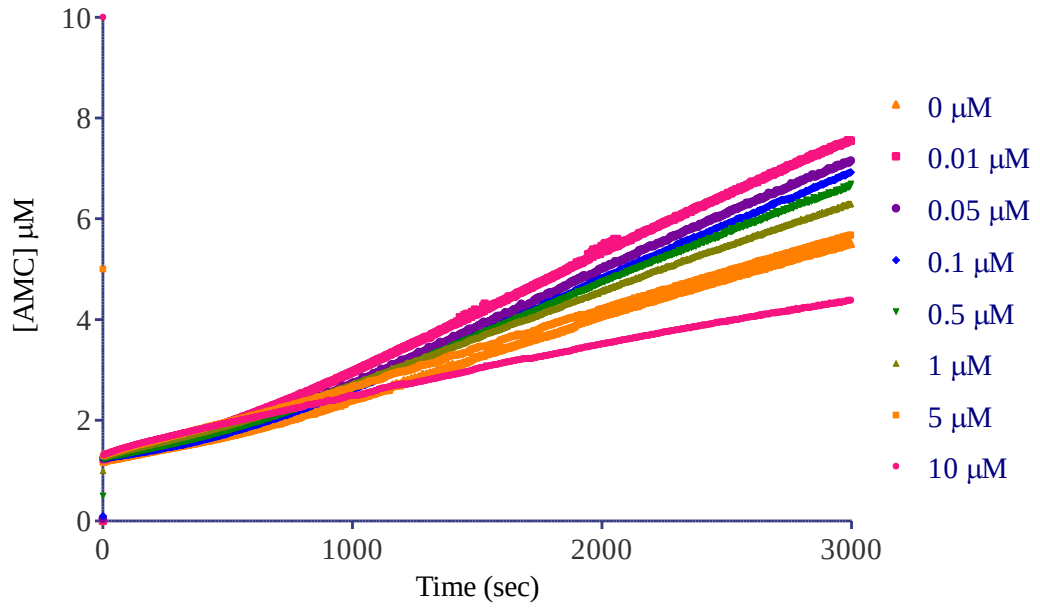

Figure 4.14 – Progress curves for compound **3** inhibition of cathepsin B

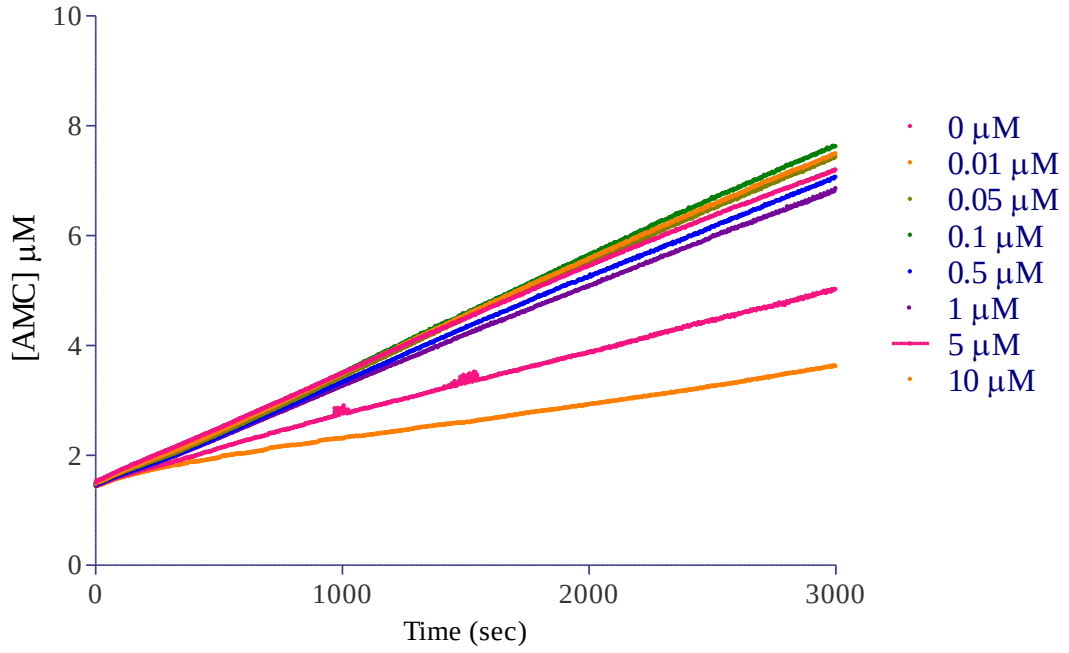

Figure 4.15 – Progress curves for compound **4** inhibition of cathepsin B

Reversibility Studies

To determine if the inhibition of the time dependent compounds (**1**-**2**) was reversible or irreversiblem the enzymatic activity was measured after an extended preincubation of compound and inhibitor followed by rapid and large dilution with the substrate. The compounds at 10-20 µM were preincubated with 200 nM enzyme for 1 hour at 37 °C. The reaction mixture was diluted with substrate for a final concentration of components being 1 nM enzyme, 0.2-0.1 µM inhibitor, and 60 µM substrate. The reaction was then followed fluorometrically immediately after substrate addition for 4 hours at 37 °C. The length of preincubation time with excess inhibitor attempts to allow for saturation of the enzyme with the inhibitor, reducing the event of free inhibitor remaining which could cause an erroneous response indicating reversibility. If the compound exhibits reversible behavior, an increase in enzyme activity would be seen upon comparison between control and inhibited slopes. Figures 4.16-4.19 illustrate the recovery of the enzyme activity after the aforementioned rapid dilution. For a reversible inhibitor, the curve will be curvilinear, increasing in velocity over time. Here, there is an initial phase followed by an increase in velocity for all the reactions. These velocities (slopes) were calculated for 0-200 seconds, 0-500 seconds, 200-1000 seconds, and 500-1000 seconds for the inhibited and uninhibited (control) reactions. For the time dependent inhibitors compound **1** and **2**, reversbibility was observed. Recovery of enzyme activity was measure at 2000 seconds for each graph. When compared to the control, compound **1** recovered approximately 13% of the enzyme's activity and compound **2** recovered 34%. For the other two inhibitors, compound **4** and compound **3**, reversibility was also

observed at high concentrations of inhibitor. When compared to the control, compound **3** recovered approximately 19% of the enzyme's activity and compound **4** recovered 28%.

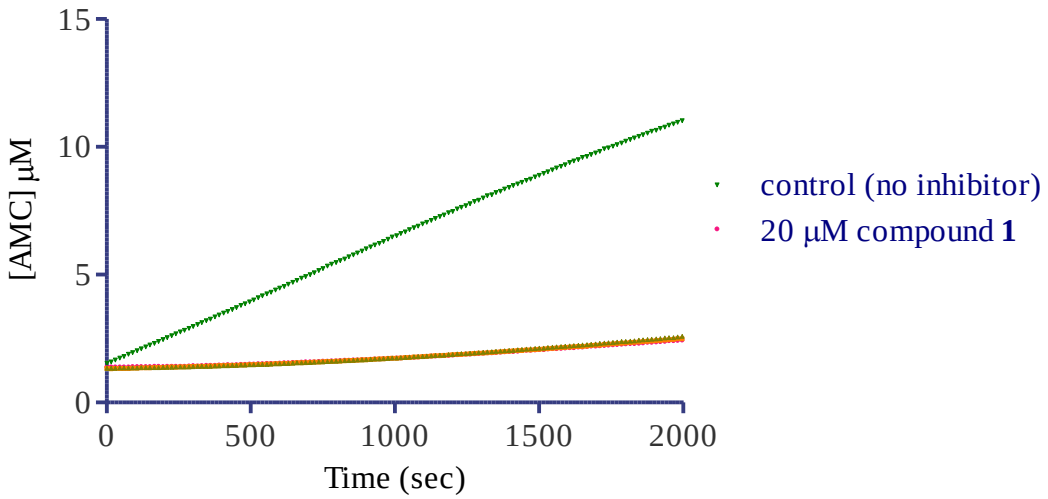

Figure 4.16 – Reversibility studies of dibromobenzophenone thiosemicarbazone, compound **1**

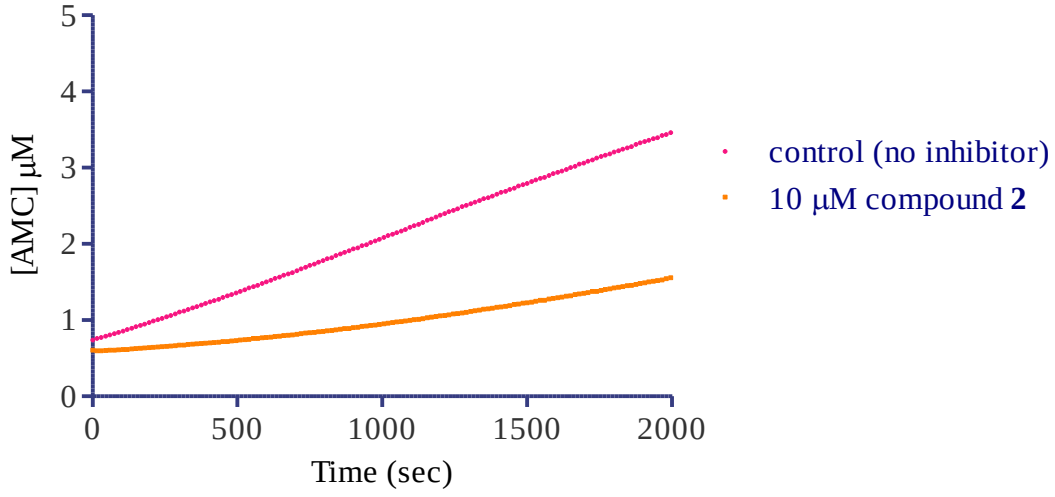

Figure 4.17 – Reversibility studies of monobromo-paraacetatephenone thiosemicarbazone, compound **2**

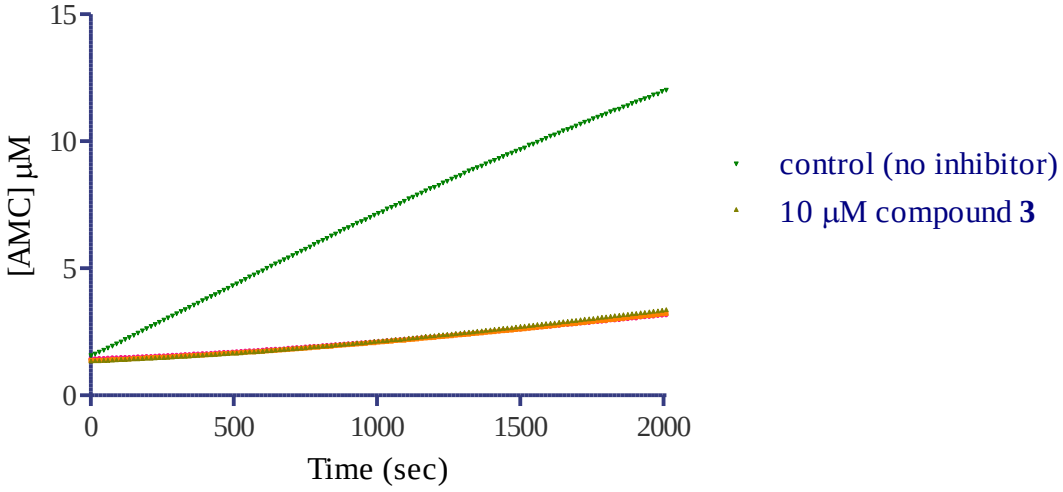

Figure 4.18 – Reversibility studies for the bromo-di-trifluoromethylbenzophenone thiosemicarbazone, compound **3,** preincubated at 10 µM, a concentration that showed some time dependence

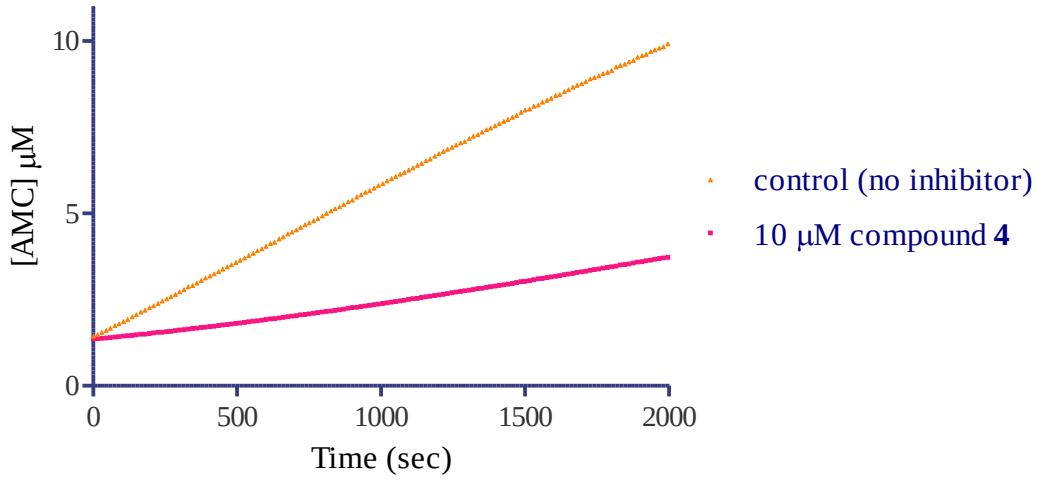

Figure 4.19 – Reversibility studies of trimethoxy-methoxyhydroxylbenzophenone thiosemicarbazone, compound **4,** preincubated at 10 µM, a concentration that showed some time dependence

Preincubation Time Dependence

Time dependence of inhibitor binding is tested by varying the preincubation time of the inhibitor and enzyme at 37 °C. The curves for compound **1** and compound **2**, Figure 4.20-4.21, illustrate that up-to a preincubation time of 60 minutes, longer incubation of inhibitor with enzyme is proportional to a decrease in IC_{50}.

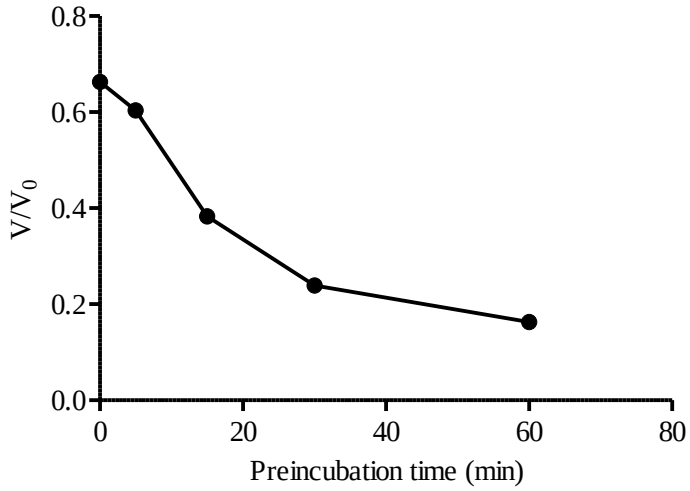

Figure 4.20 – Compound **1** (1 µM) and enzyme preincubation effect on IC_{50}

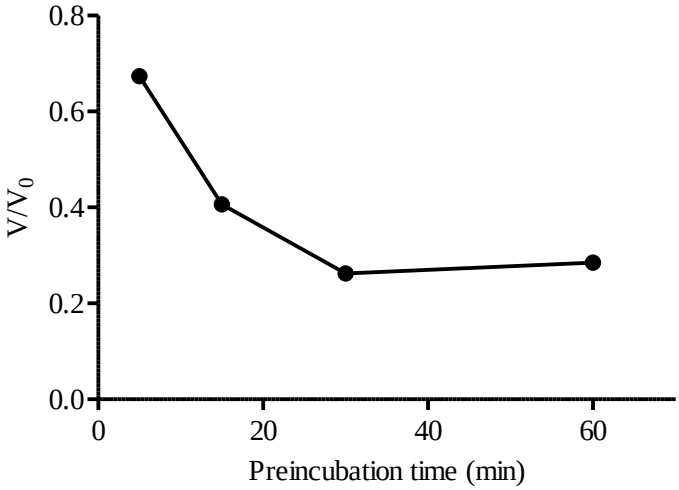

Figure 4.21 – Compound **2** (5 µM) and enzyme preincubation effect on IC_{50}

For compound **3** and compound **4**, there is no indication of a loss of activity as a function of time at lower inhibitor concentrations. This further supports these previous data that indicate compound **3** and compound **4** are non-time dependent inhibitors at concentration less than 10 μM.

*Mode of Inhibition for Tight Binding Inhibitors: Compound **1** and Compound **2***

Tight binding inhibitors are expected to be competitive. This was shown for compound **2** as the IC_{50} increased with increasing substrate concentrations. The inhibitors tested thus far have all displayed reversible inhibition, therefore the mode of inhibition was then studied. Here, the IC_{50} of each the compounds was analyzed as before with 5 minute preincubation varying substrate concentration to a final concentration of 6, 20, 40 and 60 μM. The inhibitory ability of the compounds at the various substrate concentrations was evaluated by plotting the IC_{50} vs. substrate and noting the trend.

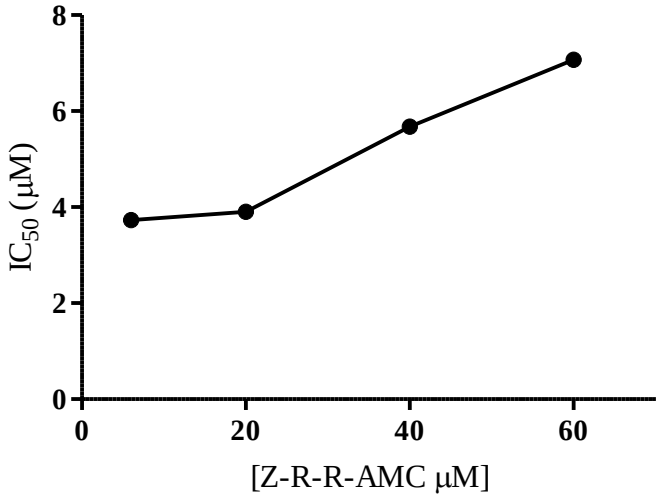

Figure 4.22 – Substrate concentration effect on compound **2** IC_{50}

In compound **1** and compound **2** the graphs follow a general pattern of increasing IC_{50} with increasing substrate, indicating the compounds are competitive with respect to substrate. This also indicates the compounds bind to the active site of the enzyme, therefore possibly blocking the substrate binding and eventual cleavage.

K_I Determination for Tight Binding Inhibitors: Compound 1 and Compound 2

For time dependent compounds, the Williams Morrison equation, equation 15, can be used to determine the binding constant for the inhibitor to the enzyme, the K_I at a specified preincubation time. In equation 15, v_i/v_0 is the relative velocity of the inhibited

$$\frac{v_i}{v_0} = 1 - \frac{([E]_T + [I]_T + K_I^{app}) - \sqrt{([E]_T + [I]_T + K_I^{app})^2 - 4[E]_T[I]_T}}{2[E]_T} \qquad \text{Eq. 15}$$

enzyme reaction compare to the uninhibited reaction at a set concentration of substrate, I_T is the total inhibitor concentration, E_T is the total enzyme concentration and K_I^{app} is the apparent dissociation constant for the inhibitor. This dissociation constant for the enzyme inhibitor constant is indicative of inhibitor potency independent of substrate concentration, unlike IC_{50} values. For non-time dependent inhibitors, the Morrison equation cannot be applied and therefore these must be analyzed by classical lineweaver-burk plots. For compound **1**, a representative graph is seen in Figure 4.23. The Morrison fit gave an average K_I^{app} of 0.7547 µM with a standard error of 0.1441 and an R^2 goodness of fit of 0.9797. This data was collected in triplicate over three separate experiments and 8 of the 9 sets of data were used in the data analysis. The low K_I of the dibromo analogue indicates tight binding of the compound to cathepsin B's active site,

the tightest of the four compounds analyzed in this study. Compound **2** analysis by the Morrison equation gave a K_I of 2.120 µM ± 0.02879 with an R^2 value of 0.9861

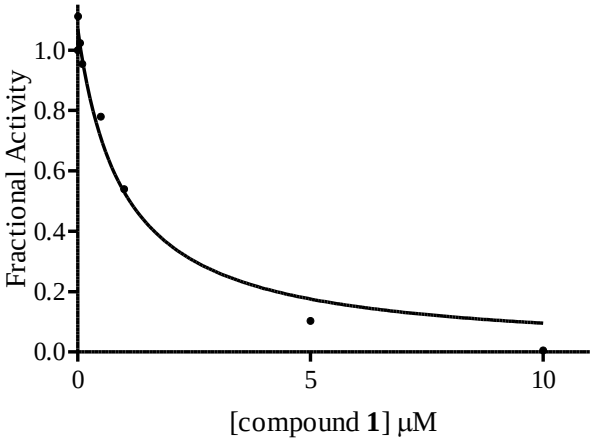

Morrison Ki	
Best-fit values	
Vo	1.071
Et	= 0.0020
Ki	0.7547
S	= 60.00
Km	= 200.8
Std. Error	
Vo	0.03724
Ki	0.1441
Goodness of Fit	
Degrees of Freedom	6
R square	0.9797
Constraints	
Et	Et = 0.0020
S	S = 60.00
Km	Km = 200.8
Number of points	
Analyzed	8

Figure 4.23 - Williams Morrison K_I analysis of compound **1**

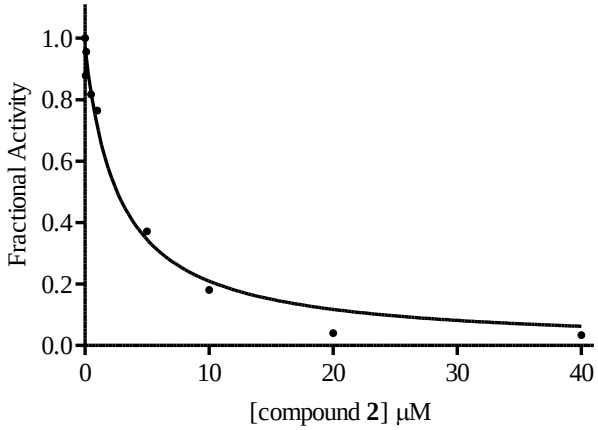

	Slope
Morrison Ki	
Best-fit values	
Vo	0.9708
Et	= 0.0020
Ki	2.120
S	= 60.00
Km	= 200.8
Std. Error	
Vo	0.02879
Ki	0.3355
Goodness of Fit	
Degrees of Freedom	7
R square	0.9861
Constraints	
Et	Et = 0.0020
S	S = 60.00
Km	Km = 200.8
Number of points	
Analyzed	9

Figure 4.24 - Williams Morrison K_I analysis of compound **2**

Mode of Inhibition for Compounds 3 and 4 for Concentrations Less than 10 µM

The inhibition of cathepsin B by compound **3** and compound **4** was not time dependent at concentrations less than 10 µM so their mechanism of inhibition was investigated using equations for rapidly reversible inhibitors. The equations used are seen below.

$$K_{M\,obs} = K_M\left(1 + \frac{[I]}{K_I}\right)$$ Eq. 16- – Graphpad classical competitive inhibition fit

$$v = \frac{V_{max}[S]}{K_M\left(1 + \frac{[I]}{K_I}\right) + [S]}$$

Eq. 17 - Graphpad classical competitive/noncompetitive inhibition y value

$$V_{\max inhib} = \frac{V_{max}}{(1 + \frac{[I]}{K_I})}$$

Eq. 18 – Graphpad classical noncompetitive inhibition fit

$$V_{\max app} = \frac{V_{max}}{\left(1+\frac{[I]}{\alpha K_I}\right)} \qquad K_{\mathrm{M}\,app} = \frac{K_M}{\left(1+\frac{[I]}{\alpha K_I}\right)} \qquad v = \frac{V_{\max app}[S]}{K_{M\,app}+[S]}$$

Eq. 19 – Graphpad classical uncompetitive inhibition fit

$$V_{\max app} = \frac{V_{max}}{\left(1+\frac{[I]}{\alpha K_I}\right)} \qquad K_{\mathrm{M}\,app} = \frac{K_M\,(1+\frac{[I]}{K_I})}{\left(1+\frac{[I]}{\alpha K_I}\right)} \qquad v = \frac{V_{\max app}[S]}{K_{M\,app}+[S]}$$

Eq. 20 – Graphpad classical mixed inhibition fit

The K_M, V_{max} and K_I values used in equations 16-20 were all shared and greater than zero. The values for these terms were fit by Graphpad prism in all three models of inhibition as suggested by the software, except for the K_M value which was set at 200.8 µM. For compound **4**, fits of each mode of inhibition to the data suggested competitive inhibition as the best fit, seen in Table and Figure 4.25.

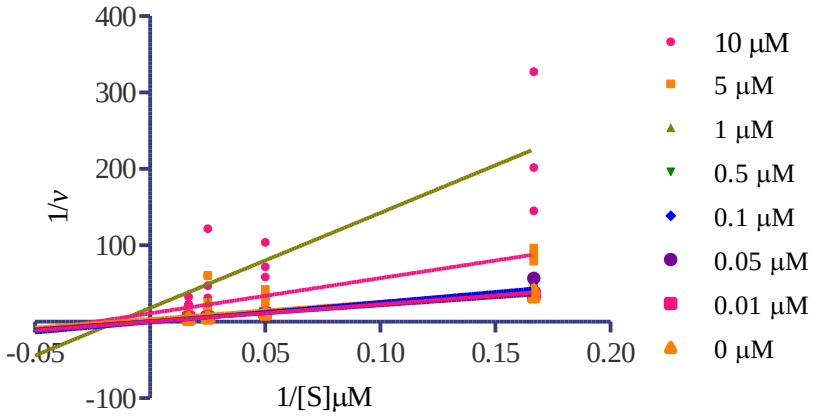

Figure 4.25 – Compound **4** data fit to Lineweaver Burk Graphpad Prism 5.0 competitive enzyme kinetics inhibition equation

The Table of data fit analysis in Table 4.15 indicates the compound fitting the competitive model based on the following parameters: "deviation from the model", global shared fit R^2 value and standard error of the K_I. Although the best fit was

Table 4.14 – Graphpad Prism 5.0 data fit analysis for compound **4**

Competitive inhibition	Global (shared)
Best-fit values	
Ki	1.886 µM
Vmax	1.038 µM s^{-1}
Std. Error	
Ki	0.1933
Vmax	0.01735
Goodness of Fit	
R square	0.9381
Constraints	Km = 200.8 Ki > 0.0 and shared Vmax > 0.0 and shared
Number of points analyzed	14
Deviation from Model	Not Significant

determined to be competitive, the noncompetitive fit did not significantly deviate from the model, therefore further experiments would be necessary to unequivocally prove the mode of compound **4**. The fit parameters can be seen in the K_I determination section below for the compound compound **4**.

K_I Determination for Rapidly Reversible Inhibitors at Concentrations less than 10 µM: Compound 3 and Compound 4

Compound **3** and compound **4** required Lineweaver burk analysis due to their non-time dependent nature. Figure 4.26 and 4.29 are the velocity vs substrate concentration plots for each compound and figure are the double reciprocal plots of these data.

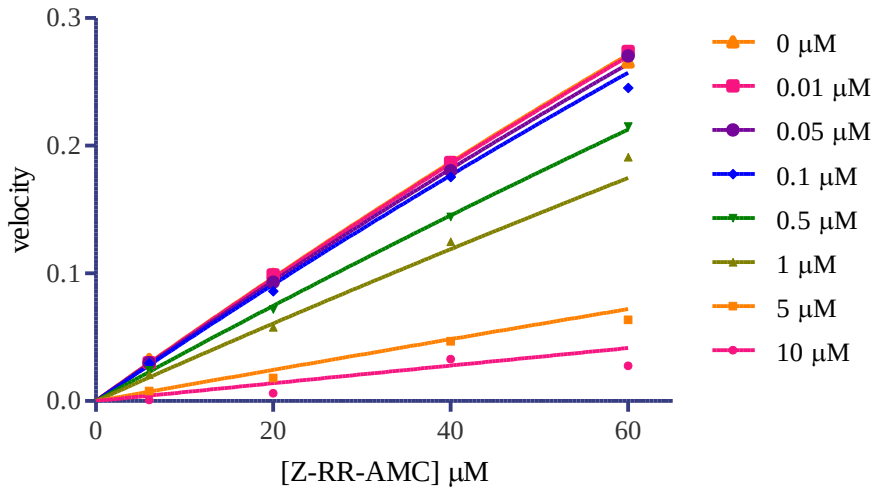

Figure 4.26 – Competitive inhibition plot for compound **3**

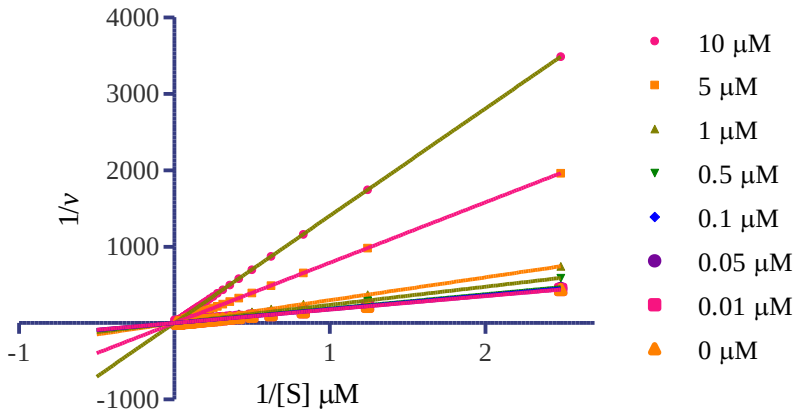

Figure 4.27 - Lineweaver burk analysis of compound **3**

Table 4.15 – Competitive fit parameters for compound **3**

Global Parameters from Graphpad Prism	Competitive inhibition kinetics fit - compound **3**
K_I	1.420 µM ± 0.09344
R^2	0.9437
K_M	200.8 µM
V_{max}	1.152
Constraints were K_I and V_{max} are shared (equation to determine); K_M shared and set	

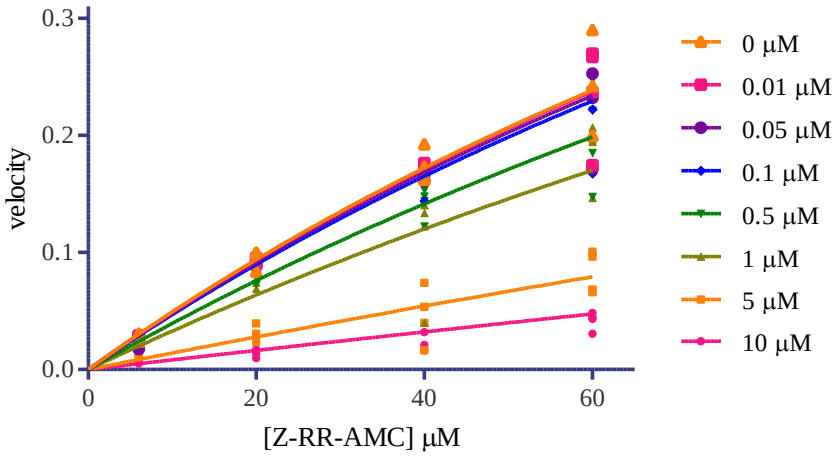

Figure 4.28 – Competitive inhibition plot for compound **4**

Fitting the data to the Graphpad Prism equation for competitive inhibition, equation 17, the K_I and supporting parameters were determined, see Tables 4.14-4.17. Both compounds exhibited similar dissociation constants, 1.42 µM ±0.0934 for compound **3** and 1.913 µM ± 0.1981 for compound **4**. The double reciprocal plot of compound **3** also supports the competitive nature of this compound with the intersecting lines conversing at the y-axis ($1/V_{max}$).

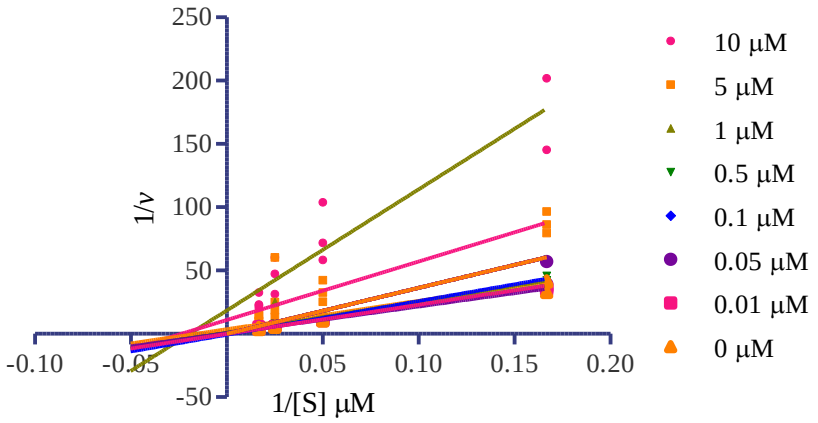

Figure 4.29 - Lineweaver burk analysis of compound **4**

Table 4.16 – Competitive fit parameters for compound **4**

Global Parameters from Graphpad Prism	Competitive inhibition kinetics fit - compound **4**
K_I	1.913 µM ± 0.1981
R^2	0.9389
K_M	200.8 µM
V_{max}	1.037
Constraints were K_I and V_{max} are shared (equation to determine); K_M shared and set	

Advanced Kinetic Analysis Summary

In summary, Table 4.17, of the four inhibitors tested for mode of inhibition, two (compound **1** and compound **2**) were time dependent, competitive, reversible slow tight

binding inhibitors (K_I^{app} = 0.7547 and 2.120 μM, respectively) of cathepsin B with IC_{50} values in the range of 1.60-2.82 μM. The remaining two compounds (compound 3 and compound **4**) were not time dependent but upon further analysis were found to also be competitive (in the case of compound **3**), rapidy reversible inhibitors (K_I = 1.420 and 1.913 μM, respectively) with IC_{50} values of approximately 1.42-1.58 μM. Further

Table 4.17 – Summary of kinetic data for cathepsin B inhibitors[51,135]

Compound	IC_{50} μM	K_I μM	Time dependence	Reversibility	Mode of inhibition	Suggested binding nature
1	2.82	0.7547	Yes	Reversible	Competitive	Slow tight binding
2	1.60	2.120	Yes	Reversible	Competitive	Slow tight binding
3	1.58	1.420	No*	Reversible	Competitive	Rapidly reversible
4	1.42	1.913	No*	Reversible	Competitive	Rapidly reervsible

*Some time dependence was observed at 10 μM

analysis of compound 4 is also needed due to the unique nature of the progress curves at higher concentrations which appeared to exhibit time dependence. The compounds found to be inhibitors of cathepsin B activity were also tested against cathepsin L by colleagues.The majority of the compounds were in the low nanomolar range, exhibiting greater activity for cathepsins L than B. A notable exception is compound **4** with an IC_{50} of 3.60 μM for cathepsin L and 1.42 μM for cathepsin B, indicating a slight selectivity for the latter enzyme. All of the active inhibitors reported here have the potential for therapeutic use targeting both cathepsins L and B. The general trend of efficacy is seen in Table 4.18 where compound **1** was the most potent for both enzymes, inhibiting cathepsin L with an IC_{50} of 16.7 nM and cathepsin B with an IC_{50} of 2.185 μM.

Compound **3** and compound **2** were also potentially good compounds targeting both cathepsins with low IC_{50} values. A review of literature, indicates nonpeptidic inhibitors of cathepsin B have higher IC_{50} values than those reported for cathepsin L. This may be due to the dual activities of cathepsin B and the occluding loop.[68]

Table 4.18 – Comparison of inhibitor potency for cathepsins B and L [51,135]

Compound	Cathepsin B IC_{50} µM	Cathepsin L IC_{50} µM
1	2.185	0.0167
2	1.600	0.1508
3	1.585	0.0960
5	5.691	2.156
4	1.424	3.600
6	9.493	0.1261

CHAPTER FIVE

Introduction to Vascular Disrupting Agents

Tumor Vasculature

Targeting tumor vasculature for cancer and tumor therapy is an emerging field in which the network of blood vessels produced by the metastatic cells are disassembled or inhibited from further growth. Often, one vessel supplies oxygen and nutrients to an entire tumor system, supporting its survival and providing a mode for the spread of metastatic cells. The angiogenic switch is required for the tumor to grow beyond a certain size, illustrating the importance of angiogenesis and vasculature in tumors.[56];[57] Tumor vasculature is fundamentally different from normal vasculature. It is highly disorganized, has an incomplete underlying basement membrane and abnormally high permeability. [150] The development of the disorganized blood vessels originates in part from aggressive growth of neoplastic cells and pro-angiogenic factor overexpression.[151] The discontinuous vessels are often fluid engorged, making them uneven and leaky.[151] The increase in permeability results in vascular content accumulation causes irregular osmostic pressure, leading to vascular content accumulation and also irregularly shaped vessels which can cause inadequate oxygen supply.[151] Many times, there is little distinction between arterioles and venules and an increase in vascular shunts where blood can flow directly from the arteriole to the venule.[152] This blood flow through tumor capillaries can be sluggish, stationary or in some cases reverses direction.[153] The tumor environment is frequently nutrient starved, under oxidative stress and acidic.[154] Hypoxia is a reduction of oxygen which is a characteristic feature of advanced solid tumors, often

associated with poor prognosis in patient outcome in various cancer types[155] Although it can be associated with cell death (necrosis and apoptosis) and restrained cell proliferation and differentiation, it can also produce cellular changes leading to a phenotype that is aggressive and resistant to traditional anti-cancer therapeutic strategies.[151,155] Cell cycle distribution and quiescent cell count are altered under sustained hypoxic conditions, changes that alter the cells' response to drug treatment and radiation.[156] Normal endothelial cells (with the exception of those in the recovery/repair phase) are relatively quiescent upon comparison to tumor cells which exhibit increased activity and response to angiogenic cell signaling. Tumor endothelial cells also are commonly aneuploid in character, having an abnormal number of chromosomes.[152] This abnormality is suggested to be due to factors produced by the tumor microenvironment including loss of tumor suppressors or DNA check points creating this genetic instability.[152] Functional differences include the over expression of proteins or components in growth and survival pathways. Hypoxic cells secrete multiple angiogenic factors, such as vascular endothelial growth factors (VEFG) which is a class of proteins that increase vascular permeability, promote angiogenesis and contribute to endothelial cell survival in blood vessels.[157]; [153] Exploiting the differences in normal and cancerous cells allows for more directed therapy. This promising therapeutic approach would lead to disruption and ultimate termination of the tumor cells fed from the targeted blood vessel with the unlikely event of acquired resistance due to the genetic stability and low mutational rate of endothelial cells.[158,159] Agents to cut off the blood supply include vascular disrupting agents (VDAs) and antiangiogenic agents (AIAs). [160]Figure 5.1 illustrates the effects of AIAs vs VDAs on tumor blood flow and core and periphery cells.[159]

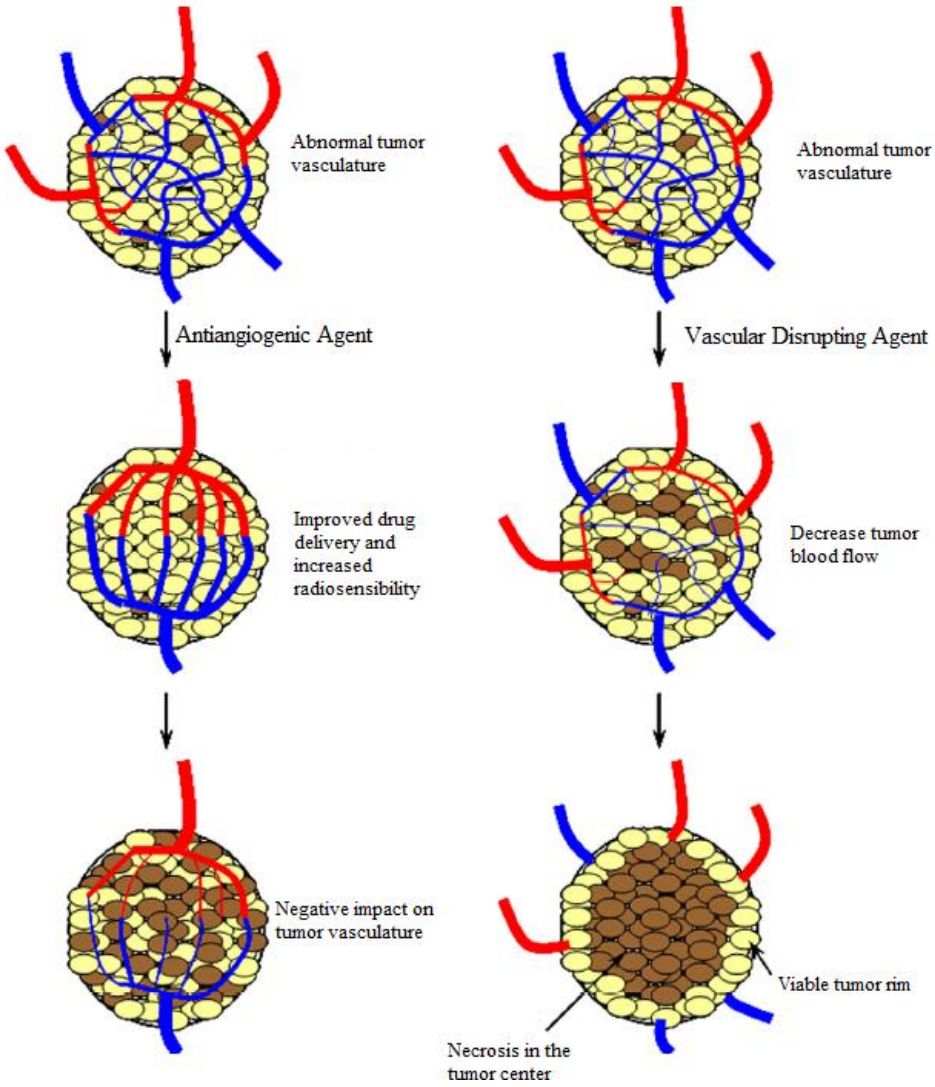

Figure 5.1 – Tumor response to antiangiogenic agents and vascular disrupting agents; cream ovals are viable cells and brown are dying or dead cells. (reprinted with permission)[57]

Vascular Disrupting Agents

Vascular disrupting agents (VDAs) are molecules that disturb the abnormal established network of blood vessels produced in tumors, ultimately leading to tumor necrosis, but often leaving the viable rim intact, Figure 5.1. One important class of VDAs bind to the structural protein tubulin and inhibits its polymerization.[161] Despite the promise of VDAs, none of these agents have been approved by the FDA. They would

VDA	Company	Stage of clinical development	Indication	Combination	Status
Flavonoid					
DMXAA (ASA404)	Novartis	Phase II	NSCLC[a]	Carboplatin, paclitaxel	Stopped
			SCLC[b]	Carboplatin, paclitaxel	
			Prostate cancer	Docetaxel	
			Urothelial carcinoma	Docetaxel	
		Phase III ($1800\ mg/m^2$)	NSCLC[a]	Docetaxel	
			NSCLC[a]	Carboplatin, paclitaxel	
Tubulin binding					
CA-4-P (fosbretabulin)	OXiGENE	Phase I/II	Anaplastic thyroid cancer	Radiotherapy	Ongoing
		Phase II	Anaplastic thyroid cancer		
		Phase II	Ovarian cancer	Carboplatin, paclitaxel	
		Phase II	Solid tumors	Carboplatin, paclitaxel	
		Phase II	NSCLC[a]	Carboplatin, paclitaxel, bevazicumab	
		Phase II	Epithelial ovarian, fallopian tube or primary peritoneal carcinoma	Bevazicumab	
		Phase II/III ($60\ mg/m^2$)	Anaplastic thyroid cancer	Carboplatin, paclitaxel	
AVE8062 (Ombrabulin)	Sanofi-Aventis	Phase II	Ovarian cancer	Carboplatin, paclitaxel	Ongoing
		Phase II	NSCLC[a]	Taxane, platinum	
		Phase III ($25\ mg/m^2$)	Soft tissue sarcoma	Cisplatin	
CA-1-P (OXi4503)	OXiGENE	Phase I			Ongoing
TZT-1027 (Soblidotin)	Daiichi	Phase II	Soft tissue sarcoma		Ongoing
		Phase II	NSCLC[a]		
ZD6126	AstraZeneca/Angiogene	Phase II	Renal cell carcinoma		Stopped
			Colorectal cancer	Oxaliplatin, 5-fluorouracil, leucovorin	
NPI-2358	Nereus	Phase I/II	NSCLC[a]	Docetaxel	Ongoing
EPC2407 (Crinobulin)	EpiCept	Phase I/II	Anaplastic thyroid cancer	Cisplatin	Ongoing
CYT997	YM Biosciences	Phase I/II	Glioblastoma	Carboplatin	Ongoing
		Phase II	Multiple myeloma		
BNC105	Bionomics	Phase I/II	Renal cell carcinoma	Everolimus	Ongoing
MN-029	Medicinova	Phase I			Stand by

Figure 5.2 – Current status of VDAs in clinical trials; NSCLC: non-small cell lung cancer, SCLC: small cell lung cancer (reprinted with permission) [57]

cause rapid morphological changes upon reversible binding to tubulin that leads to the catastrophic disintegration of pre-existing tumor vasculature without significantly harming normal tissue and may be rapidly metabolized or excreted.[56] Specificity of these VDAs is not completely understood although some theories include a) immature vasculature associated with tumors have a discontinuous endothelial lining leading to increased susceptibility of collapse b) sluggish and inconsistent blood flow of tumor vasculature increasing risk damage, and c) varying rates of interactions of actin with tubulin, post-translational tubulin modifications and endothelial-cell proliferation. [162] The current status of VDAs recently in clinical trials is seen in Figure 5.2, many of which are

being tested in combination with other drugs in an effort to improve clinical results.[57] Figure 5.3 shows the selected structures of the VDAs in recent clinical trials.

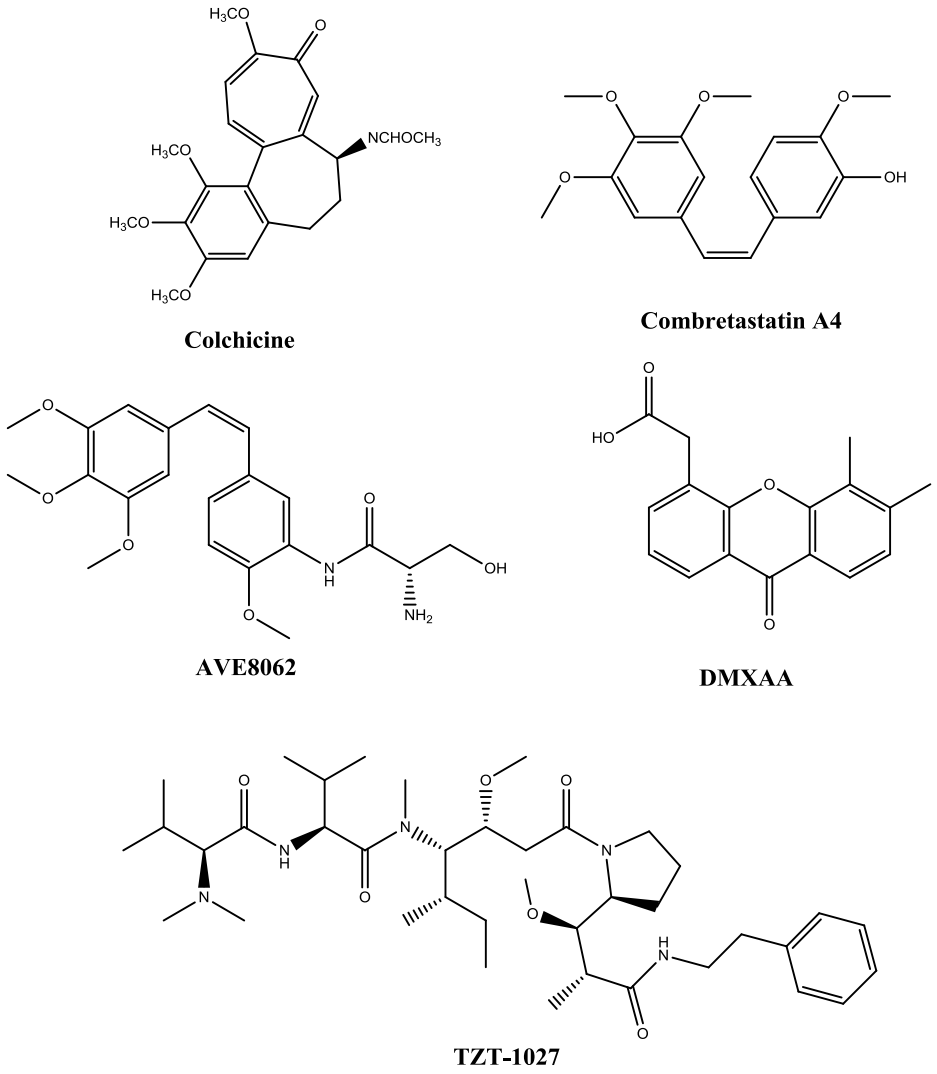

Figure 5.3 – Colchicine and selected VDAs in recent clinical trials

The DMXAA (5,6-dimethylxanthenone-4-acetic acid) series caused rapid reorganization of the actin cytoskeleton and selective shutdown of tumor blood flow but were stopped in phase II and III clinical trials due to unfortunate results indicating poor patient survival.[56] Some of the most well studied VDAs are the combretastatins which

share structural similarities to colchicine but with a reversible affinity for the colchicine binding site. Colchicine is a known binding agent to the structural protein tubulin but due to high toxicity, is not used in clinical settings. Combretastatin A-4 (CA4), trade name ZYBRESTAT (forbretabulin), specifically targets the microtubule depolymerization by strongly inhibiting polymerization by binding to the colchicine site of tubulin and exhibits pronounced cytotoxicity against selective cancer cell lines.

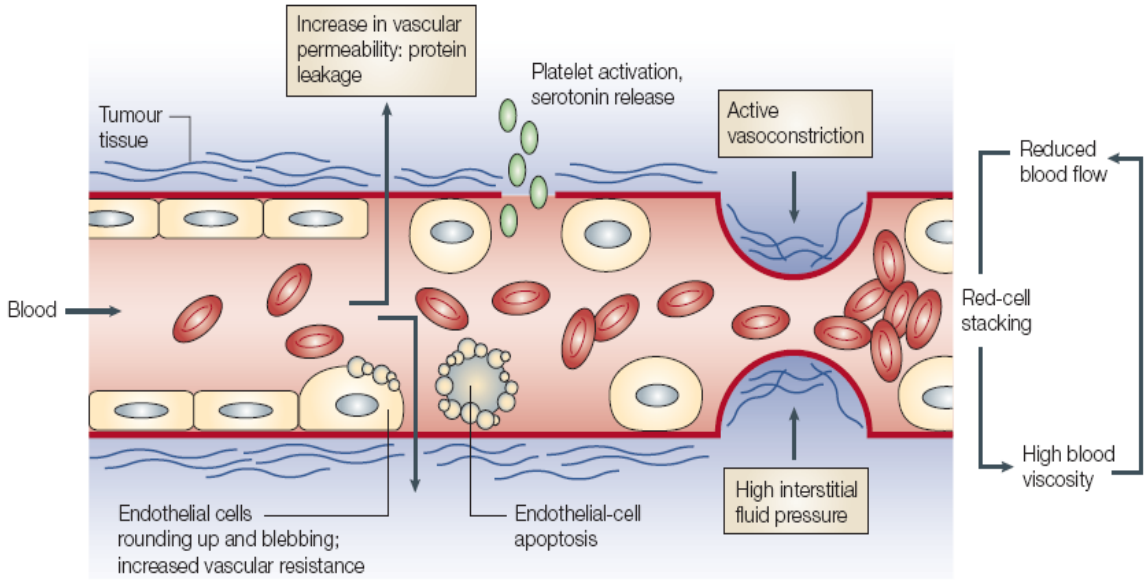

Figure 5.4 – VDA shutdown of pre-existing vasculature (reprinted with permission)[56]

Figure 5.4 illustrates the general mechanism of known VDAs such as combretastatin-A4 phosphate. In this scheme, after treatment with drug (VDAs), vascular shutdown begins with disruption of cytoskeleton elements and blood vessels become leaky and structurally compromised. The cytoskeletal elements that maintain cell-cell adhesions are affected and cells begin to round up, entering into apoptosis where blebbing often occurs, in turn increasing interstitial pressure. This process restricts blood flow and in combination with other factors such as macromolecular permeability and

platelet activation, leads to the eventual shutdown of the vasculature.[56]The structural simplicity of the combretastatins has led to many analogues which have been evaluated in SAR studies and is one of the few drugs that are currently undergoing clinical trials.[163,164] Ombrabulin (AVE8062) is also a combretastatin, modeled after CA4, which shuts down blood perfusion and causes necrosis. Combination therapy was required with this compound as after treatment alone with AVE8062, the viable rim of tumor cells remained, although the rim was narrow.[165] Oxi4503 was studied without combination as this prodrug of CA1 proved to be more potent than CA4P, delaying growth and regression as a single agent.[166] This compound also directly attacked the remaining viable rim cells. TZT1027 was also able to eliminate cancer cells without additional agent assistance and was cytotoxic against tumor cells in addition to having potent anti-vascular effects.[166]

Angiogenesis Inhibiting Agents

Newly formed blood vessels are involved in feedback loops, forming cycles thru which proangiogenic cytokines and growth factors, such as VEGF, are released therefore enabling further angiogenesis.[157] Angiogenesis inhibiting agents (AIAs) target growth of neovasculature and are an attractive target for drug therapy and in some cases clinical trials are being using AIAs with VDAs. These agents focus on interfering with various steps in the process of growth and survival of the newly forming cells often binding to various signaling molecules, therefore inactivating downstream pathways and eventually blocking angiogenesis. Drugs that have been approved by the FDA for this mode of chemotherapy include Avastin (bevacizumab) which acts as a monoclonal antibody to specifically recognize and bind VEGF for inhibition of VEGF receptor activation and

Votrient (pazopanib) used to treat renal carcinoma via interfering with the protein tyrosine kinase activity, Figure 5.5. Two AIAs using a mechanism involving the

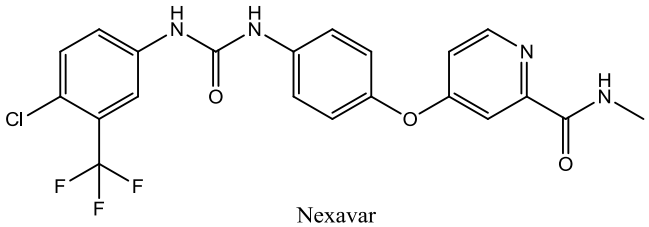

Nexavar

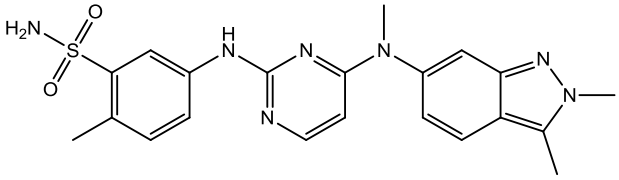

Votrient

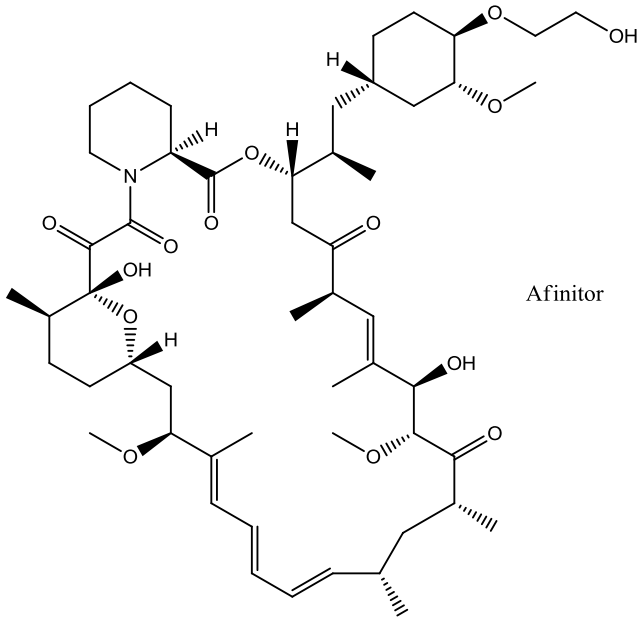

Afinitor

Figure 5.5 – Antiangiogenic agents approved by the FDA

prevention of new blood vessel growth through the termination of cell division are Nexavar (sorafenib) used to treat advanced kidney and liver cancer and Afinitor (everolimus) which treats HER2 negative and HR positive advanced breast cancer.[167]

Modes of Targeting

Standard chemotherapy can include the administration of one or many chemotoxic agent(s) to damage rapidly dividing cells, reducing the tumor burden on many patients while simultaneously damaging normal tissue and impairing pathways such as the reduction of the immune response.[167] Targeted therapy for cancer treatment is ideal in that it reduces side effects of potentially toxic drugs and is more effective per dose unit as more agent is delivered to the target rather than surrounding cells and tissue. These modes of therapy specifically interact with molecules or processes key to the cells' survival and growth throughout tissue. Effective targets would include pathways or molecules that are only present in the carcinogenic cells and absent in normal cells, ensuring drug delivery or action in the desired location. Increasingly more effective, and more common, would be a target that is present in both healthy and cancerous cells but in a higher concentration in the unhealthy cells. This targeting method allows for the termination of normal cells but at a significantly lower rate which could be altered via drug dosage adjustment in some cases. An additional mode of targeting targets a pathway or protein found on both cancer and normal cells where the healthy cells would regenerate and the carcinogenic cells would be permanently destroyed.

Cytoskeleton Components

The cytoskeleton is a dynamic three dimensional structure unique to the eukaryotic cell that is responsible for both movement and stability. It is composed of three well-defined filamentous structures which make up an interactive network: microtubules, microfilaments, and intermediate filaments. Each of these filaments is a polymer of protein subunits that are held together by non-covalent bonds.[168] Endothelial cells line the inner surface of all vessels and regulate permeability of the vascular walls, controlling the transfer between circulating blood and tissue fluids.[113] The endothelial cytoskeleton plays a vital role in maintaining endothelial barrier function as it increases vascular permeability in addition to reorganizing to change the shape of the blood vessels, where a balance between contracting and stretching forces generated by cytoskeleton proteins are a part of normal functioning of the endothelial barrier.[169] Microtubules are a major component of the cytoskeleton and are stiff, hollow, cylindrical structures composed of α,β-tubulin heterodimers, having a wall thickness of 25 nm and an outer diameter of approximately 4 nm.[168] They are distributed throughout the cell cytoplasm assisting in the determination of shape of the cell and also are thought to play a role in maintaining organization. These dynamic polymers play crucial roles in a large number of cellular functions and are components of a diverse array of structures including the mitotic spindle during cell division and the core of cilia and flagella in addition to being involved in direct intracellular trafficking of vesicles, proteins and organelles.[170] There are differences in microtubule stability depending on location, where cytoskeleton and mitotic spindle sites are extremely sensitive to disassembly whereas mature neurons, centrioles, and clilia are much more sTable.[171] The microtubule network

depolymerization and polymerization cycle is vital in the construction of a functional mitotic spindle and often cells arrested in mitosis eventually undergo apoptosis.[172] Therefore disrupting microtubule dynamics with depolymerizing or microtubule disrupting agents has the possibility to seriously affect membranous organelle locations bringing movement of these elements to a halt, making microtubules a major target of anticancer therapy as tumor vasculature is a requirement for tumor growth.[168]

Microtubule Polymerization/Depolymerization

Microtubules are formed in a process called nucleation, localized in the centrosomes, where α/β tubulin three dimensional subunits tightly bind non-covalently, with each globular subunit approximately 55 kDa in size. These subunits have binding sites for two molecules of GTP, one tightly bound at the N-site and one readily exchangeable via hydrolysis with free GTP at the E-site. In a process known as elongation, the heterodimers can assemble head-to-tail in the presence of additional GTP creating a protofilament with specific structural polarity. Typically, 12-13 of these protofilaments will twist upon themselves to give the pipe-like structure of the microtubule, seen in Figure 5.6.[2] The noncovalent interactions between adjacent protofilaments are thought to be involved in maintaining microtubule structure. The positive end exposes the β-subunit while the negative end of the microtubule exposes the α-subunit, the negative end being capped so elongation of the structure occurs from the positive direction and in turn the protofilament is asymmetric with the entire polymer having polarity.[168] The polymerization dynamics of microtubules consists of the gain and loss of a short region of tubulin-GTP or tubulin-GDP-inorganic phosphate at the ends of the microtubules, known as a GTP cap which stabilizes the molecule (Figure 13b).[162]

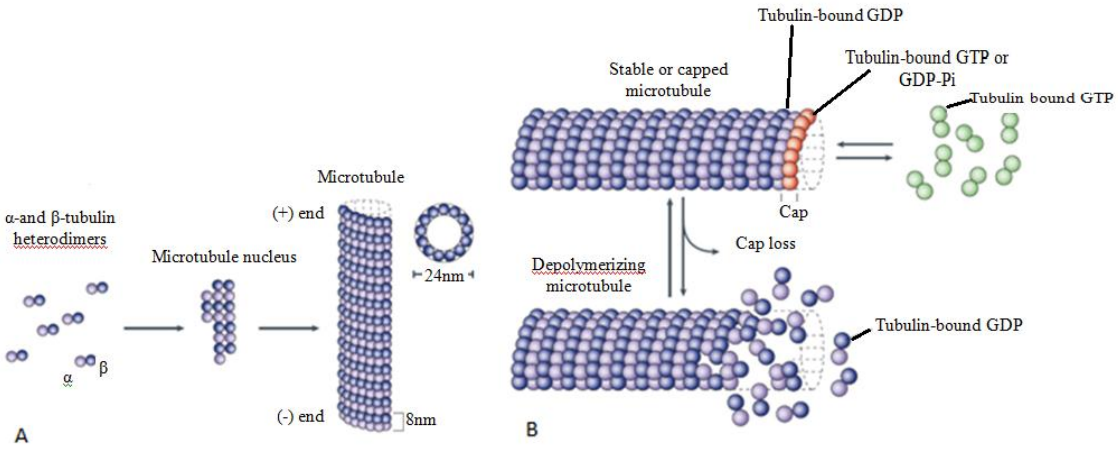

Figure 5.6. Microtubule polymerization/depolymerization (reprinted with permission)[162]

The cap is created when tubulin-bound GTP is hydrolyzed at the E-site to tubulin-GDP and Pi simultaneously (or very quickly thereafter). Upon the loss of the cap (dissociation of the inorganic phosphate), tubulin-bound GDP can dissociate causing depolymerization of the microtubule.[162]

Binding Sites/Depolymerization Agents

The binding of compounds to microtubules and tubulin is the target of many anticancer drugs currently in developmental and clinical phases and can be divided into two groups: polymerization promoters and polymerization inhibitors.[172,173] Colchicine is the most well studied of the inhibitors and disrupts polymerization of microtubules involved in cell division, destabilizing them and therefore interfering with tubulin dynamics.[174] This disruption has proved clinically useful for designing anticancer agents although the dosage required for depolymerization utilizing colchicine is too close to the maximum tolerated dose.[2,150] Figure 5.7 illustrates tubulin with the specific binding sites

that are used in drug research: taxol, colchicine, and vinblastin, each of which accommodates compounds of very different structures.[175]

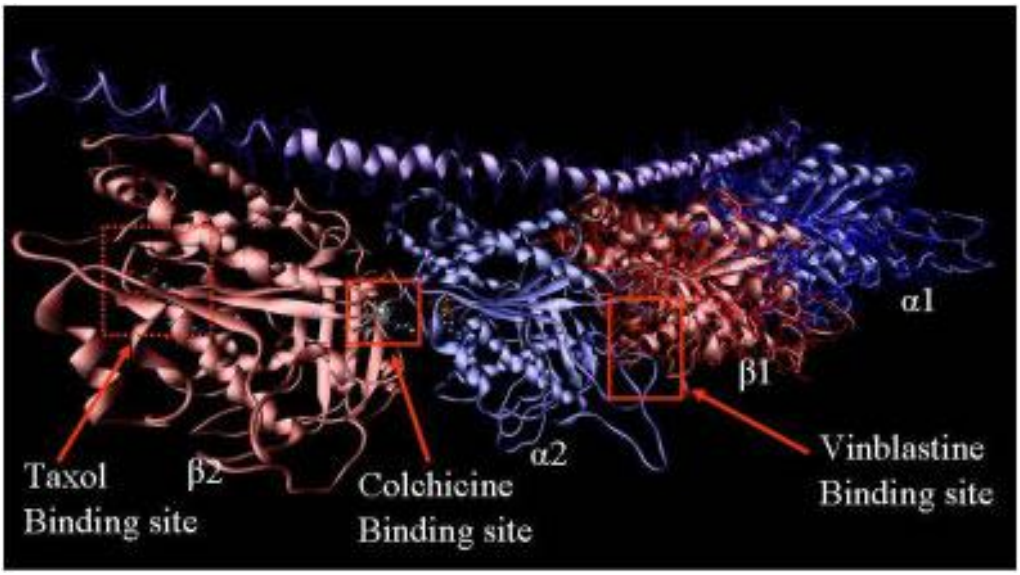

Figure 5.7. Tubulin binding sites of three microtubule inhibiting agents (reprinted with permission) [177]

The taxol binding site is located in the ß2 subunit of tubulin, the vinblastin site at the interface between the ß1 and α2 subunits and the colchicine binding site is at the interphase of the α2 and ß2 subunits.[176]A closer view of DAMA (*N*-deacetyl-*N*-(2-mercaptoacetyl)) colchicine bound to tubulin at the colchicine binding site is seen in Figure 5.8. DAMA colchicine was used in this study to allow for the establishment of the location of the N-acetyl group and to unambiguously define the orientation of colchicine in its asymmetric electron density.[178] In Figure 5.8, the DAMA colchicine binds to the binding site which is surrounded by S8 (residues 313-320) and S9 (residues 351-356), T7 loop (residues 244-251) and helices H7 (residues 224-243) and H8 (residues 252-260). [156, 173, 172, 167] When bound, colchicine also interacts with the T5 loop (residues 173-182)

of the adjacent α-subunit in addition to the β-subunit, allowing for stabilization of the tubulin heterodimer.[179] At low concentrations, colchicine inhibits microtubule dynamics

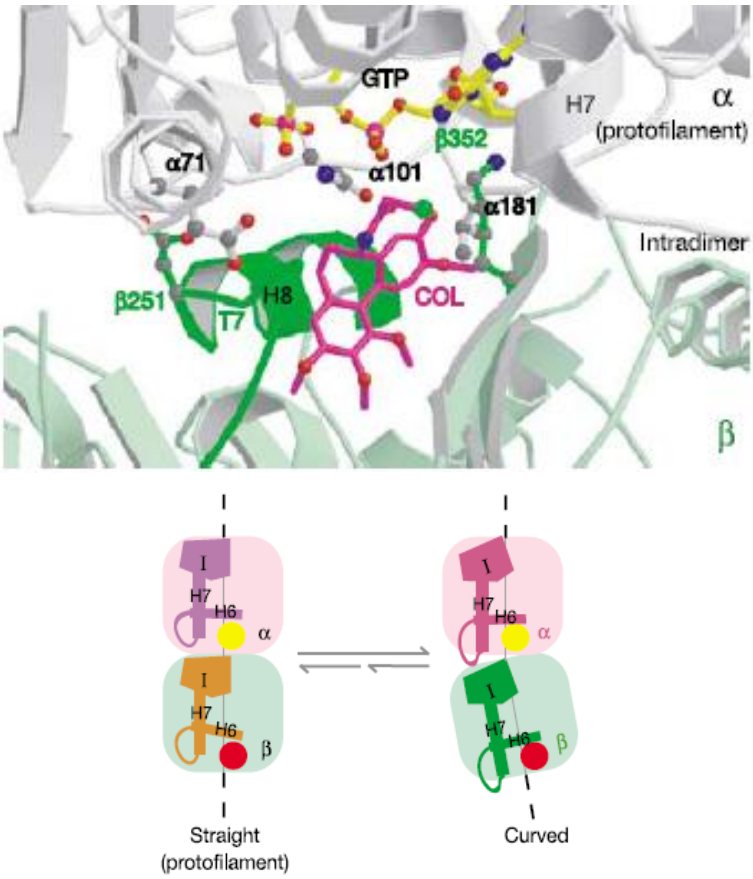

Figure 5.8. DAMA colchicine bound tubulin and straight vs. curved form of the protofilament (reprinted with permission) [178]

and growth is hindered but at high concentrations of bound colchicine, microtubules depolymerize. Microtubule stability is reliant on lateral and longitudinal interactions between adjacent subunits, therefore when colchicine binds, the lateral contacts of the subunit of the newly formed end of the protofilament are displaced leading to a bent conformation. In Figure 15b, the typical conformation of linear tubulin is prohibited due to the steric hindrance of the colchicine molecules with the subunit, preventing the α-

subunit from binding. As the drug concentration increases, more lateral contacts are absent and the proportion of the lateral to longitudinal contacts will increase thus destabilizing the ends of the microtubule followed by disassembly.[178] [180] Depolymerization of microtubules via colchicine binding activates the small guanosine nucleotide triphosphatase, RhoA, which is an intracellular coordinator of the cytoskeletal rearrangement of microtubules.[150] RhoA-GDP is found in all eukaryotic organisms and regulates many aspects of intracellular actin dynamics, participating in pathways that affect cell proliferation, apoptosis, adhesion, motility, and vesicular trafficking.[181] It regulates molecular events by cycling between inactive GDP-bound form and active GTP-bound form. RhoA-GDP is activated by guanosine nucleotide exchange factors (GEFs) that promote the exchange of free GTP for bound GDP.[150;182,183] In the active state (GTP-bound), Rho binds specifically to the Rho-binding domain (RBD) of Rhotekin to control downstream signaling cascades. In the proposed mechanism (fig 16) for vascular disruption of tubulin-binding agents, depolymerization of microtubules leads to the MAPs (microtubule associated proteins) being released which in turn activates RhoA. [150] In Figure 5.9, the vascular disrupting agent passes through the endothelial cell membrane to the microtubules. Upon contact, the microtubules release MAPs which in turn begin depolymerization of the vasculature releasing alpha, beta tubulin dimmers and oligomers and also proteins which activate guanine nucleotide exchange factors (GEFs). The GEFs then activate RhoA-GDP (inactive form) to RhoA-GTP (active form) by the release of GDP. The active RhoA-GTP can now activate RhoA kinase and other downstream effectors which eventually lead to the rearrangement of the cytoskeleton and vascular collapse.[150]

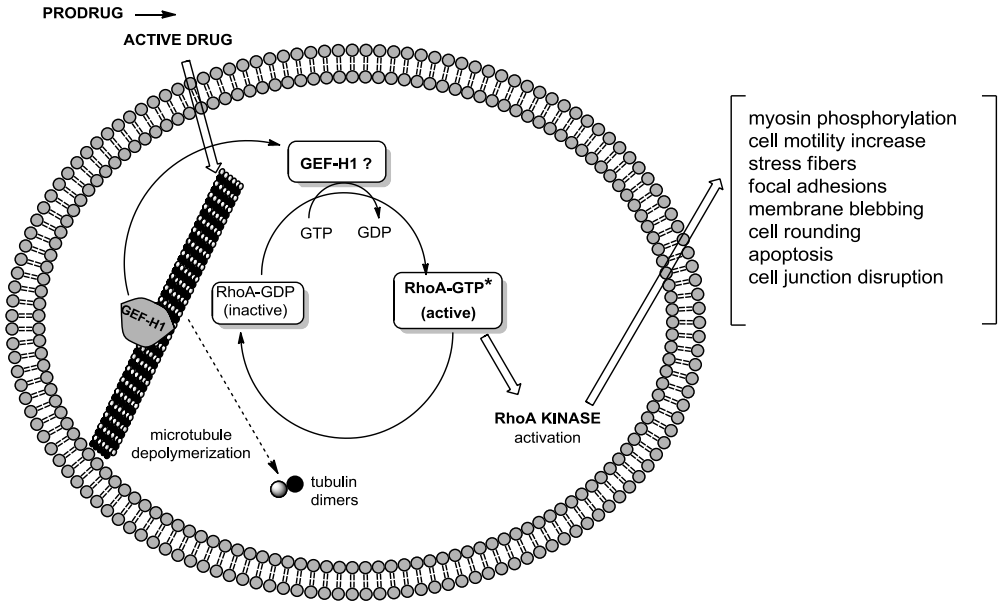

Figure 5.9. Proposed mechanism for vascular disruption by tubulin binding agents (Reprinted with permission by Dr. M. L. Trawick and Dr. K. G. Pinney) [150,184]

Cancer Cell Line Characterization

Many carcinogenic cells are aneuploid. The breast cancer cell line MDA-MB-231 is derived from human metastatic mammary tissue and is epithelial-like. These adherent cells are epidermal growth factor (EGF) and transforming growth factor α (TGFα) positive and are anueploid with chromosome counts near triploid range.(ATCC) The phenotype of MDA-MB-231 cells is spindle shaped, forming long and thin cell in culture although it is characteristic of this cell line to have some cells rounded up. Figure 5.10 is a photomicrograph of the cell line in culture. The breast cancer cell line cell size is approximately100 µm for attached cells. Doubling time is the period required for cells to double in population in cell culture. The doubling time for MDA-MB-231 cells is 24-30 hours. [185];[186]

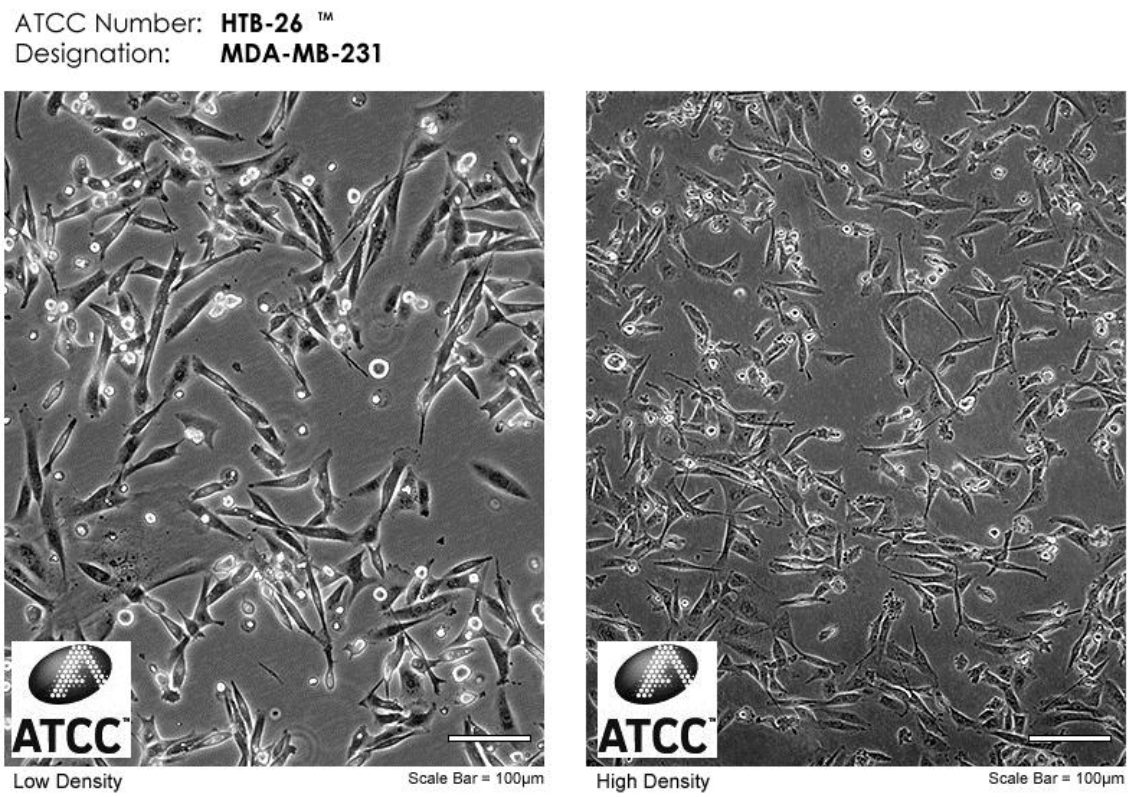

Figure 5.10 – MDA-MB-231 cells in culture (reprinted with permission)

MDA-MB-231 cells are triple negative breast cancer (TNBC), lacking estrogen receptors (ER-), progesterone receptors (PR-) and HER2. This triple negative indicates that the cancer growth is not estrogen and progesterone dependent and therefore the cell line does not respond to hormonal therapies such as tamoxifen. TNBC is often more aggressive and difficult to treat with an increased change of re-occurrence and metastasis.(nationalbreastcancer.org) Approximately 10-15% of all breast cancers are triple negative and often have poor patient outcome upon comparison to other breast cancer subtypes and therefore is a good model in the search for anticancer agents.[187]

CHAPTER SIX

Tubulin Materials and Methods

Materials

Tubulin was purified from bovine calf brain purchased from H & B packing in Waco, Texas. The following chemicals were purchased from Sigma: GTP - Guanosine 5′-triphosphate sodium salt hydrate (G8877), glycerol (G5516), EDTA - ethylenediaminetetraacetic acid disodium salt dihydrate (E5134), MES - 2-(N-Morpholino) ethanesulfonic acid hydrate (M5287), 2-(*N*-Morpholino) ethanesulfonic acid sodium salt (M3058), EGTA - glycol ether diamine tetraacetic acid (E4378), magnesium chloride hexahydrate (M2670), sodium chloride (S9888), 2-mercaptoethanol (M7154), ATP – adenosine 5′-triphosphate disodium salt hydrate (A2383), colchicine (C9754), and Na_2HPO_4 (S-0876). Glutamic acid (16245-453) was purchased from USB chemicals. Coomassie Blue Bradford reagent (1856209), bovine serum albumin standards (23209), and Halt protease inhibitor cocktail-EDTA free (87785) were purchased from Thermo fisher. The Active Rho pull-down and detection kit was purchased from Pierce (16116) and contained the following components: 5.5 mg/ml GST-Rhotekin RBD (solution in 50 mM Tris-HCl, pH 7.2, 150 mM NaCl, 0.5% Triton X-100, 5 mM $MgCl_2$, 1 mM DTT, protease inhibitors and 10% glycerol), 50% slurry of glutathione agarose resin in 0.05% sodium azide, 100 mM GDP, 10 mM GTPγS, SDS sample buffer (125 mM Tris-HCl, pH 6.8, 2% glycerol, 4% SDS (w/v) and 0.05% bromophenol blue), lysis/binding/wash buffer (25 mM Tris-HCl, pH 7.2, 150 mM NaCl, 5mM $MgCl_2$, 1% NP-40 and 5% glycerol), spin cups, and collection tubes. Also purchased from Pierce was PVDF

membrane (88518). The blender used for the purification of tubulin was Waring brand. The following were purchased from Biorad: RC-DC protein determination assay kit (500-0119) (containing reagent A alkaline copper tartrate solution, reagent B folin reagent, reagent S surfactant solution, and RC reagent I and II), Transblot semi-dry electrophoretic device (170-3940), Transblot electrophoretic transferall wet transfer device (170-3930), Power Pac 300 power source. Dri-bath heating mantle 16500 was from Thermolyne. Circulating temperature controlled water baths were RTE-111 models from Neslab. DMSO was purchased from Acros (127790010). Ethanol was purchased from Amresco (E402-4L). Ethylene glycol used in the water baths was purchased from Beckman Dickenson (BDH1125-44P). Black walled microcuvettes were purchased from Starna cells (16.160-Q-10/Z15) and cuvette cleaner was purchased from Hellmanex (CH2631/BC). Potter elvehjem homogenizers (5 and 50 mL) were Pyrex brand. An Agilent 8453 UV-vis was used for all measurements in the ultraviolet/visible range. The ultracentrifuge used was a Beckman Coulter Optima LE-80K with a Ti-45 Beckman rotor and 70 mL centrifuge polypropylene tubes and adaptor with 3 and 5 mL tubes. The oven was from Thelco Precision Scientific. Filtration devices used for radioactive experiments (Millipore) was used in conjunction with a vacuum pump (Millipore WP6122050). Tritium bound (ring C, methoxy-^{3}H) colchicine (250 μCi) was purchased from Perkin Elmer (NET189250UC) and Ecoscint H scintillation fluid was purchased from National Diagnostics. GF/A glass fiber filters (1820-025) were from Whatman and a LS6500 Beckman Coulter liquid scintillation counter. For cell culture purposes, HUVECs (human umbilical vein endothelial cells ATCC number CRL-1730) and MDA-MB-231 (human breast cancer cells ATCC number HTB-26) were purchased from ATCC and cultured in

T-75 (BD BioCoat) or 6 well plates (Corning 3978XX1) and were grown in Thermo NAPCO 8000 WJ incubators at 37 °C for 5% CO_2 and 95% bulk air. For HUVECs, cultures plates were coated with sterile 0.1% gelatin solution (Sigma G9391). Biosafety hoods were SterilgardIII Advance, medium used was Dubelco's Modified Eagle medium (DMEM – Cellgro 10017CV) and Medium 200 (Gibco M200-500), PBS was purchased at 10X from Rockland Scientific (MB008), and trypsin EDTA (2553CL) was purchased from Cellgro. The following were all obtained from Gibco: TN trypsin neutralizing reagent (R002-100), TE trypsin EDTA reagent (R001-100), fetal bovine serum (FBS) (16000-077), and amphotericin B (30003CF). Gentamycin was purchased from Teknova (93626). Cells were visualized with a Zeiss Axiovert 40 CFL microscope at 40x and 20x magnification. A Beckman Coulter Z1 particle counter was used to count cells in ZPak solution (8320312). Coulter Clenz (Beckman 8546929) was used as a cleaning agent for the cell counter in between use. Cell culture techniques utilized an Eppendorf 5810R 15 Amp centrifuge with a swinging bucket rotor (A-4-81) and an aerosol tight rotor (FA-45-30-11). An Eppendorf minifuge was used outside of cell culture facilities. For flow cytometry experiments, a Beckman Dickenson FACScalibur flow cytometer was used. Flow cytometry experiment vials were purchased from BD Falcon (5ml-12mm x 75mm), BD FACSFlow sheath fluid (342003), RNase A from Omega Bio-Tek (AC117), and propidium iodide solid from Sigma (P4170). Calibration beads for flow cytometry were also purchased from Beckman Dickenson (Calibrite beads: 340497, 340487 and 345036). For western blot assays RhoA protein (101594) and anti-RhoA (rabbit) antibody (68826) were purchased from Abcam. Secondary peroxidase-conjugate AffiniPure goat anti-rabbit IgG (H+L) antibody (111-035-003) was purchased from Jackson Immuno

Research. ECL Prime Western blotting substrate (RPN2232) and the miniVE electrophoresis vertical gel apparatus (80-6418-77) was obtained from Amersham-GE Healthcare Life Sciences. Simplyblue Safestain (LC6065), MES 20x SDS running buffer (NP0002) and 4-12% Bis Tris electrophoresis gels (1.5 mm/15 wells) were precast (NP0336BOX) and purchased from Invitrogen. Bovine serum albumin fraction V (BSA) was purchased from Omnipur (2930). Amicon ultra concentrator tubes (UFCS01096) with 10K limit were used to concentrate samples. Phosphate buffered saline (PBS) was from Rockland Immunochemicals (MB-008). Impulse heat sealer was purchased from American International Electric, gel pouches (heat sealable) were purchased from Thermo (GP2-100), tween 20 from Amresco (0777-1L), black boxes were from Licor BD Biosciences, liquid nitrogen from Praxair, shaker from Thermo (2314), phospho myosin light chain antibody from Cell Signaling (3674S), and phospho focal adhesion kinase antibody from Invitrogen (700255). The imager used to image chemiluminescent western blots was kindly borrowed from the Baylor Molecular Biosciences Facility and was an Ultralum Discovery system with a CCD camera equipped with UltraQuant 5.0 software. Strip PCR tubes, falcon tubes, pipette tips, and 1.5 mL microfuge tubes were all purchased from VWR. Solids were weighed out on a Mettler Toledo AG204 balance with accuracy of 0.1mg or on a Mettler Toledo AX205 microbalance with an accuracy of 0.01mg. All solutions were prepared with 18Ω ultrapure water that had been gamma irradiated and obtained from the Barnstead Diamond purifier.

Methods

Tubulin Purification –Solutions

A 6 cycle process was performed to produce purified tubulin from bovine calf brain. For solution preparation for the purification, 1 M glutamate at pH 6.6 was made by weighing out 18.72 g of L-glutamic acid sodium salt monohydrate (MW 187.13) and dissolving in 100 mL of ultrapure water, adjusting the pH to 6.6 with 1 M hydrochloric acid, followed by filtration through a Corning 0.33 micron filter. A 0.8% isotonic saline solution (w/v) was prepared by dissolving 8 g of sodium chloride (MW 58.44) in 1 L of ultrapure water. For 200 mL of 10X stock solution A, the following were weighed out: 15.35 g of MES acid (MW 213.2), 17.8 g MES base (217.2), 0.76 g EGTA (MW 380.4), 0.07244 g EDTA (MW 372.2), and 0.4066 g $MgCl_2$ (MW 203.3). The solids were dissolved upto 200 mL of ultrapure water and the pH was checked to ensure pH of 6.4. Once dissolved to 1X, the final concentrations of solution A are 0.1 M MES pH 6.4, 1 mM EGTA, 1 mM $MgCl_2$, 1 mM 2-mercaptoethanol, 0.1 mM EDTA, 0.1 mM GTP. On the first day of the tubulin preparation, 50 mL of 10X stock solution A was taken and the following were added: 26.2 mg GTP (MW 523.2), 35.1 µL 2-mercaptoethanol (MW 78.13), 147.3 mL glycerol (MW 92.09, density 1.25 g/mL) and up to 500 mL ultrapure water-this solution was labeled Solution A with Glycerol. A stock solution of 100 mM ATP was made by weighing out 27.5 mg ATP (MW 551.1) and dissolving in 50 µL of water. A stock solution of 100 mM GTP was made by weighing out 26.2 mg GTP (MW 523.2) and dissolving in 50 µL ultrapure water.

Tubulin Purification – Procedure

One Ti45 rotor was pre-cooled at 4 °C while another was placed in an oven at 37 °C. The respective centrifuge tubes were also placed with the rotors. Freshly slaughtered calf brain was obtained from a local slaughterhouse the morning of the experiment and was packed on ice with 0.8% isotonic saline solution for transport. Upon arrival at the Baylor Science Building room B311 (cold room), the brains were removed and blood vessels, clots, meninges, and brain clots were removed and the cleaned brain was rinsed in saline. The tissue was weighed and approximately 200 g was added to an ice cold Waring blender followed by 0.75 mL/g of solution A with glycerol (for 200 g tissue, 150 mL solution A with glycerol was added). The solution was homogenized at medium speed for approximately one minute, checking for homogeneity after blending. The homogenate was divided into 6 pre-cooled 70 mL polycarbonate tubes and was weighed with caps to ensure balance in the rotor. The samples were centrifuged at 32,000 rpm at 2 °C for 1.07 hours. Supernatant was decanted and volume was measured in a beaker. Based on this volume, ATP and GTP were added to a final concentration of 1 mM ATP and 0.3 mM GTP while the beaker was warmed in a water bath at 37 °C for 1.5 hours, swirling occasionally to mix. At this point the solution became cloudy, indicating polymerization has occurred, a sample of which was save and frozen for protein concentration determination. The supernatant was then quickly weighed out into 3 polycarbonate tubes (pre-warmed) and centrifuged at 32,000 rpm at 37 °C for 1.07 hours. A sample of this supernatant was saved as the first warm supernatant and the remaining supernatant was decanted onto ice immediately after centrifugation was complete to ensure a warm decant. The pellets were homogenized on ice in a cold Potter-Elvehjem

tissue homogenizer in 12 mL cold solution A (cold depolymerization). All efforts were maintained to work quickly as possible at the given temperature, minimizing loss of integrity and volume of the protein sample. The suspension was kept on ice for 30-45 minutes and then weighed into cold centrifuge tubes with 5-10 mL adaptors if volume was low and centrifuged at 24,000 rpm for 2 °C for 30 minutes in a cold rotor. The supernatant from this spin step was homogenized in approximately 6 mL of cold solution A and re-centrifuged at 24,000 rpm for 2 °C for 30 minutes. A third homogenization was now performed on the cold supernatant with cold solution A and solution was re-centrifuged at 24,000 rpm at 2 °C for 30 minutes in a cold rotor. The cold pellet was set aside as MAPS A (microtubule associated proteins) and the supernatant volume was recorded. ATP and GTP were added for a final concentration of 1 mM and 0.3 mM and glycerol was added to a final concentration of 4 M. The current solution was incubated for 1 hour at 37 °C in a water bath with occasional swirling. The warm mixture was centrifuged at 32,000 rpm at 37 °C for 1 hour after which the supernatant was decanted and the pellet was homogenized in approximately 3-6 mL of solution A and left on ice for 30-45 minutes. The cold mixture was centrifuged at 24,000 rpm at 2 °C for 30 minutes, the supernatant of which was now at 2 cycle tubulin. The 2 cycle tubulin was adjusted to 27.5 mg/ml protein if needed with solution A and the following added: 1 mM GTP, 2 mM DTT, and 1.6 M Mes pH 6.0 (1.36 M base component and 0.242 M acid component). The product was incubated at 37 °C for 1 hour followed by centrifugation at 39,000 rpm at 37 °C for 1 hour. The high Mes supernatant was decanted while the mixture remained warm and this supernatant was labeled as the high Mes supernatant and frozen in liquid nitrogen. The remaining warm pellets were homogenized in 5 mL of cold

1 M glutamate and left on ice for approximately 2 hours, followed by centrifugation at 39,000 rpm at 2 °C for 1 hour. The glutamate soluble supernatant was removed and GTP was added to a final concentration of 1 mM, this solution was incubated at 37 °C for 1 hour. The cold pellet was saved as MAPS B. After incubation, the tubulin mixture was centrifuged at 39,000 rpm at 37 °C for 40 minutes, decanting while maintaining temperature and homogenizing pellet in a cold homogenizer with 2.5 mL 1 M glutamate to cold depolymerize. The homogenate was left on ice for 1 hour followed by a clarify spin at 39,000 rpm at 2 °C for 40 minutes. GTP was again added to a final concentration of 1 mM and the supernatant was allowed to incubate at 37 °C for one hour. Centrifugation at 39,000 rpm at 37 °C for 40 minutes was performed to recover polymerized tubulin and the pellets homogenized in 3 mL of 1 M glutamate on ice overnight producing 3 cycle tubulin. Clarifying the homogenate, a 40 minute spin at 39,000 rpm at 2 °C was performed retaining the supernatant and adding GTP to a final concentration of 1 mM. A fourth polymerization was done by incubating the GTP-rich supernatant for 1 hour at 37 °C followed by recovery with a 40 minute spin at 39,000 rpm at 37 °C. Pellet was homogenized in 1 mL of 1 M glutamate and UV spectroscopy was used to determine exact concentration. Tubulin was diluted to approximately 5-10 mg/mL and left on ice for 1 hour followed by the final clarification spin at 39,000 rpm at 37 °C for 40 minutes. The supernatant was carefully stored on ice and visually inspected for signs of cloudiness which indicate polymerization. 1.5 mL cryovials were placed on ice for approximately one hour and tubulin was aliquoted into vials which were then flash frozen in liquid nitrogen to ensure protein stability. The end product is six cycle purified bovine tubulin. At each step, the supernatant or pellet to be discarded was tested for

protein concentration via Bradford protein assay and an electrophoresis gel was run on various tubulin cycles to ensure purity.

Tubulin Protein Determination – Bradford Assay

A Bradford assay was utilized to determine an approximate protein concentration of tubulin. The Bradford reagent was brought to room temperature prior to the experimental set up. The Agilent UV-vis 8453 was turned on and allowed to warm up (including lamps) while standards were being made, at least 15 minutes. In this assay, a set of 5 standards of bovine serum albumin were made from a 2 mg/ml stock solution, as is seen in Table 6.1. For each sample, 25 µl of protein (unknown or standard) was placed in a black 1.5 ml microfuge vial and 1.225 mL of Bradford was added and mixed by inversion. Tubes were allowed to incubate at room temperature for 10 minutes and were transferred and run in disposable plastic cuvettes (Plastibrand 759075D) at 595 nm.

Table 6.1 - BSA standards for Bradford assay

Concentration (mg/ml)	Total protein	BSA standard (µl)	Water (µl)	Bradford reagent (µl)
Blank (no protein)	-	-	25.0	1225
0.2	5 µg	2.5	22.5	1225
0.4	10 µg	5	20.0	1225
0.6	15 µg	7.5	17.5	1225
0.8	20 µg	10.0	15.0	1225
1.00	25 µg	12.5	12.5	1225
1.2	30 µg	15.0	10.0	1225
1.4	35 µg	17.5	7.5	1225

Tubulin Protein Determination – UV

The primary method to accurately determine the concentration is based on a method from *Biochemistry* vol. 35, 6, 1996, pg 2009. In this procedure, a Hamilton syringe was used to aliquot volumes of purified tubulin and dilute it in 1 M glutamate on ice. This volume was then placed in a pre-cooled black walled glass cuvette and under nitrogen gas to reduce condensation, the temperature was maintained at 4 ℃ via circulating water bath. A 1 M glutamate solution was used as a blank. The measurements were taken on an Agilent UV-vis 8453 at 255 and 278 nm. Between samples, the cuvettes were thoroughly cleaned with Hellmanex cuvette cleaner, rinsed with copious amounts of deionized water, and blown dry with house nitrogen gas.

Tubulin Polymerization Assay Set-Up

The final conditions of the assay are 0.8 M glutamate, 1 mg/ml tubulin, 4% DMSO, and 0.4 mM GTP. The volumes in the cuvettes were 160 µl Glutamate/tubulin mixture, 32 µl GTP, and 8 µl DMSO. Water baths were turned on approximately 1 hour before experiment began, one to 38˚C and the other to 0˚C. The Agilent 8453 was turned on and lamps turned on approximately 45 minutes to 1 hour before experiment began and log book was logged into. Eight Starna cuvettes (160 µl) were cleaned (part # 16.160.Q.15) and placed in multicell holder of UV-vis. The cold water bath was connected to the multicell holder and house nitrogen gas was turned on 15 minutes prior to placing cuvettes in holder to prevent condensation from forming. The wavelength was set to 350 nm. 10 mM GTP was made: 10.3 mg solid dissolved in 1.968 mL ultrapure water (kept on ice); this was diluted to 2.5 mM by taking 250 µl of 10 mM and diluting with 750 µl of ultrapure water. 10 mg/ml of 5 or 6 cycle tubulin (-80˚C) was thawed on

ice (~30-45 min) and diluted to 1.25 mg/ml with 1 M glutamate. The program was set up as follows.

Setting Up the Time Based Measurement Program

On the desktop, open the Ascent uv-vis software. Select “time and calculation parameters” from the “setup” option on the “time and calculation” box on the left of the screen. Select “multicell (8-cell)” followed by “setup” from the “sampling” option and

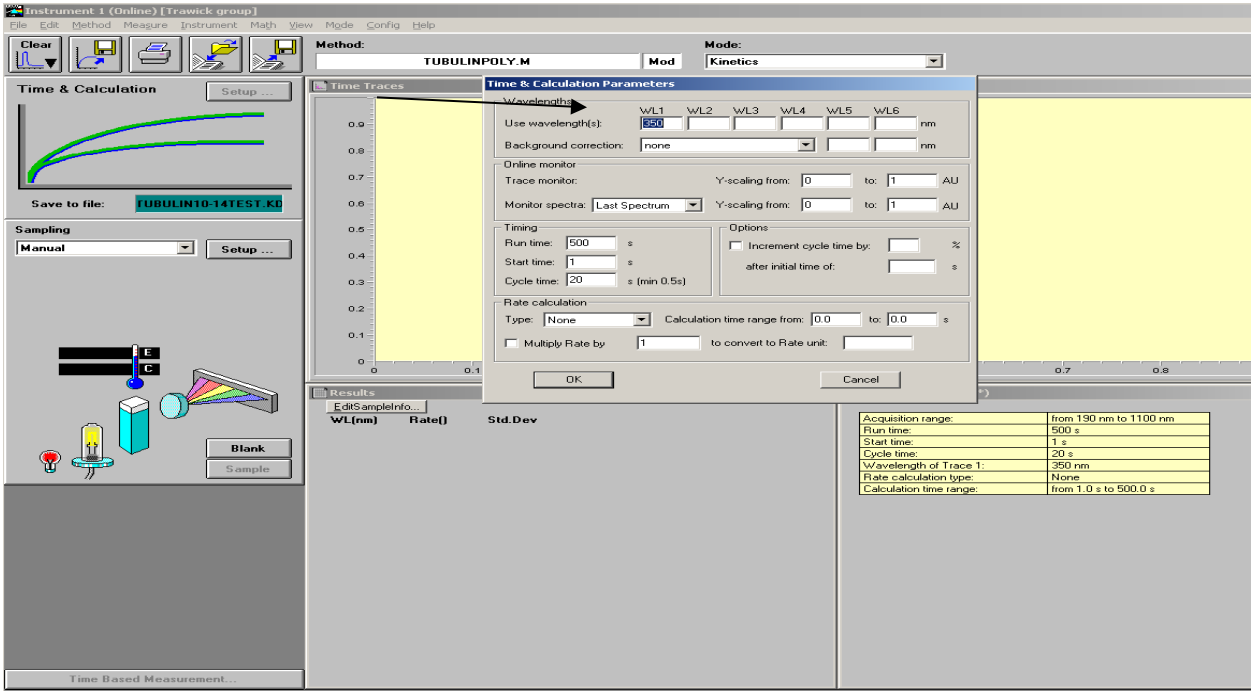

Figure 6.1 – Time based measurement screen 1

enter in which cells are blanks and which are samples. In the “sampling” option, click the “blank” button. There is an option to run a zero cell to account for differences between cells, to do this, go to the “view” tab and click on “zero cell spectra”. When ready to begin reading of samples, click the “time based measurement” bar at the bottom left of the screen, save the file if prompted, then click the “start” button located on the bottom left of the screen (the “time based measurement” bar changed into a “start” and “abort”

bar) When sampling is complete, the data will appear on a graph, to look at any one set, click on the data point on the graph (not on the results/text window).

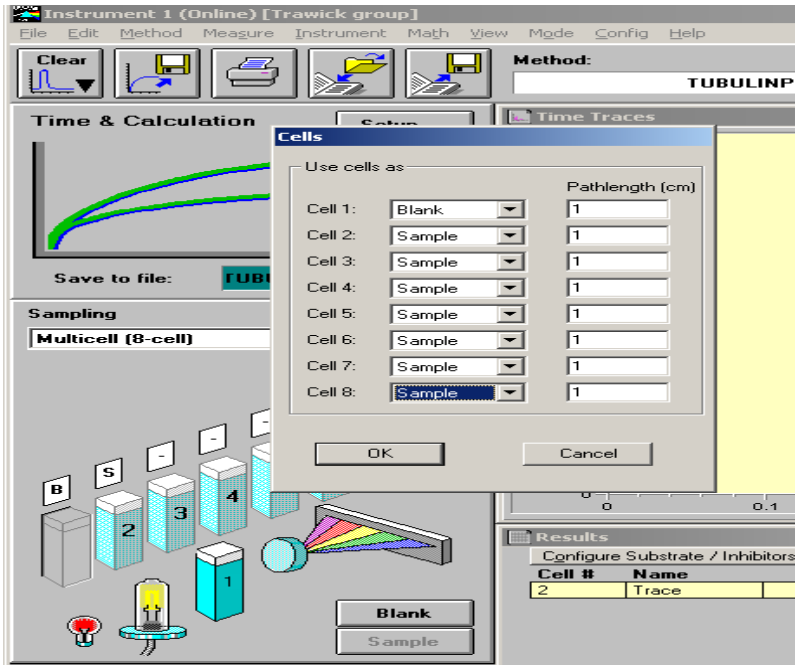

Figure 6.2 – Time based measurement screen 2

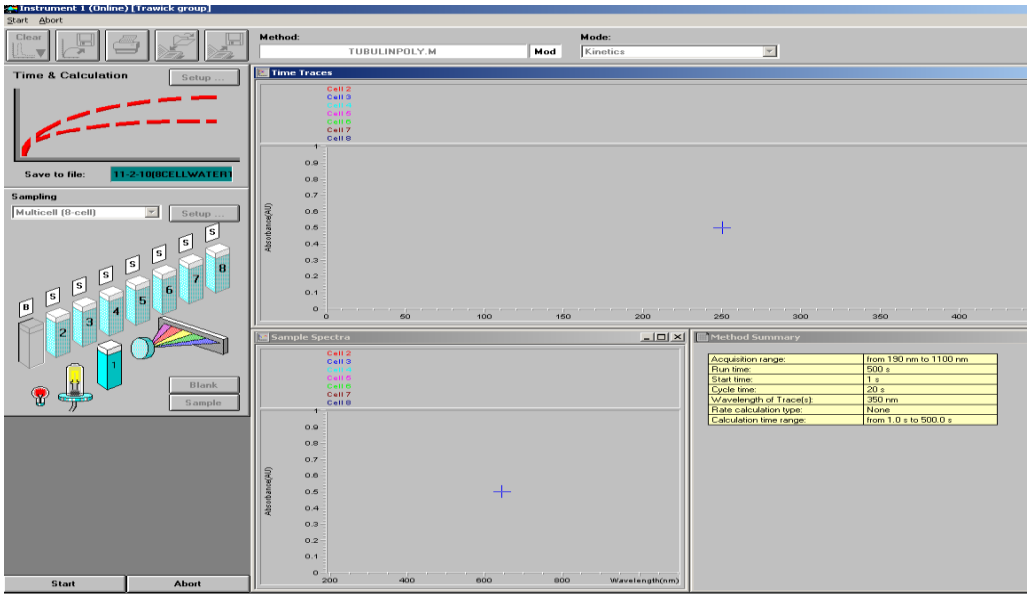

Figure 6.3 – Time based measurement screen 3

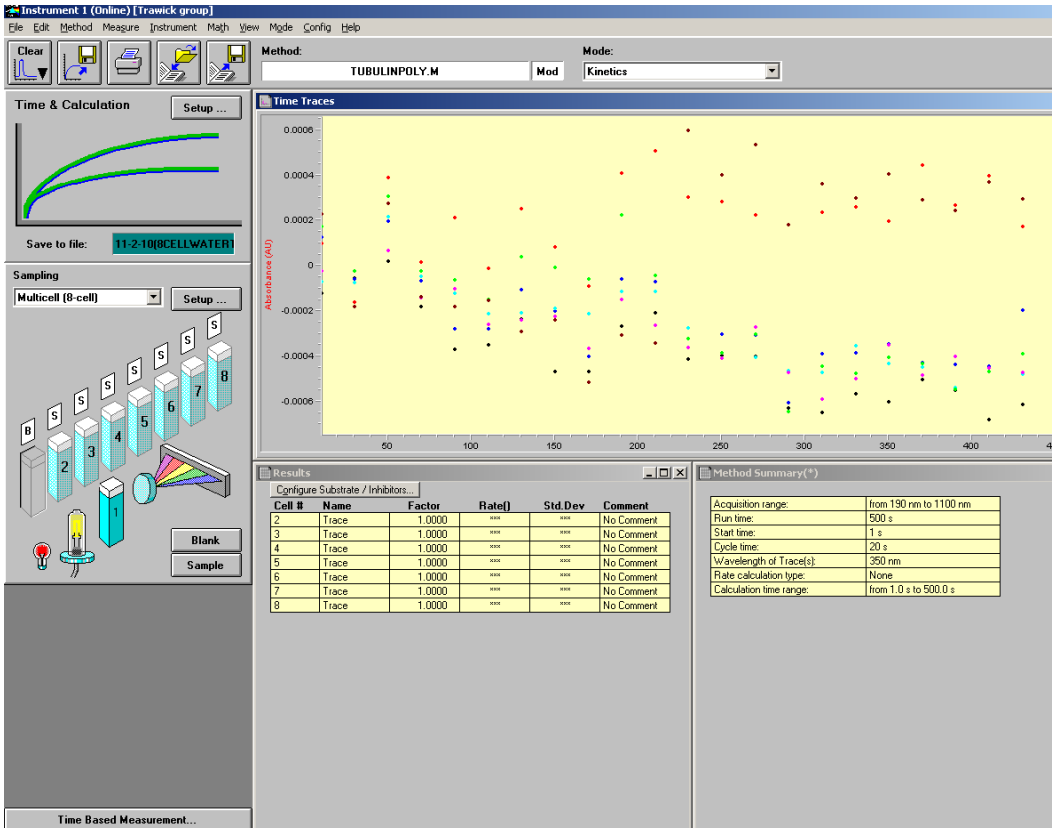

Figure 6.4 – Time based measurement screen 4

Data was retrieved using the following method. Select the data (only one set at a time) on the graph by clicking on a data point. Select “file”/”export selected data”/”CSV” and safe to USB drive. Save remaining data as before. Remove USB and open on another computer for data analysis using Excel. Open Excel viewing “all files”, choose data file “text import wizard” and choose “delimited”/“next”/ “delimited comma”/”next”/”finish”. Data will appear in tabular form and analysis can proceed in Graphpad Prism5.0.

Tubulin Polymerization Water Bath Optimization

Water baths were optimized to increase temperature during warm polymerization with the quickest rate but not allowing the temperature to ever rise above 31˚C. Points

were tested following the initial 37˚C switch (from the cold depolymerization step), time = 4.5, 3, 2, 1 minutes for changing temperature of water bath to 30.75˚C. A temperature probe was placed in the glutamate in the cuvette to monitor temperature and temperature was recorded every 2 seconds until the temperature plateaued. The optimal time was

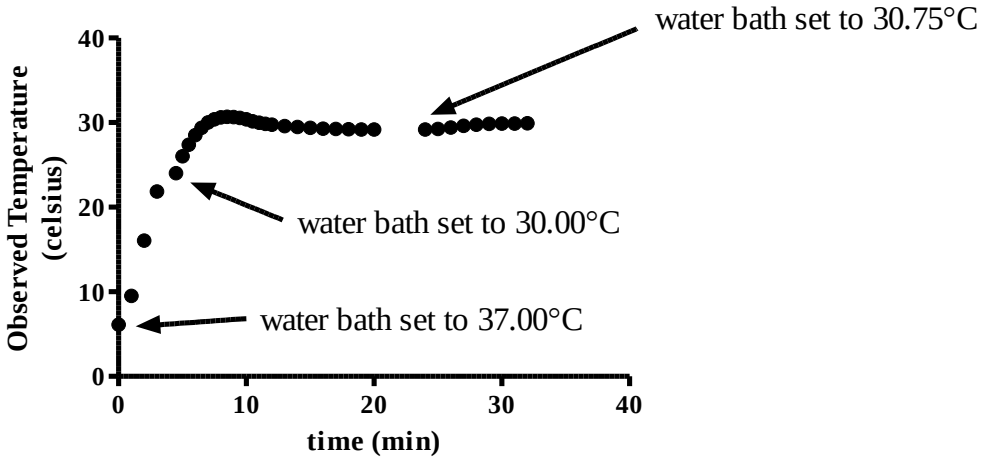

Figure 6.5 – Water bath optimization for polymerization assay

found to be 1 minute, therefore the procedure reads:"Once cuvettes are in holder and have equilibrated to temperature for 8 minutes, the instrument began reading the cuvettes at ~5.8˚C (water bath set to -5.00˚C) for 100 seconds. After this time, the water baths were switched to the 37˚C bath for 1 minute, followed by decreasing the warm water bath to 30.75˚C."

Tubulin Polymerization

A turbidometric assay was used to monitor the polymerization of tubulin in a cooled 200 µl black walled cuvette. Final conditions are seen in Table 6.2. Tubulin was thawed on ice from liquid nitrogen storage to maintain integrity and all other solutions except for DMSO and DMSO-inhibitors were also kept on ice. Cuvettes were allowed to

cool for at least ten minutes in the multichannel cell holder that was connected to a water bath set to 0 °C. Tubulin, DMSO or inhibitors, and glutamate were placed in the cold cuvettes (8 µl inhibitor or DMSO, 160 µl glutamate-tubulin mixture). 32 µl GTP was added and the mixtures were mixed by gentle pipetting and then placed back into the cuvette holder. The bag surrounding the multicell holder was sealed and the nitrogen was adjusted to a gentle stream to prevent condensation. The software was preset to run kinetics for 3200 seconds starting at time = 0 seconds and cycle time of 10-20 seconds. The instrument collected data for 2 minutes and 40 seconds while the cuvette holder was attached to the cold water bath at which point the water baths were quickly changed to the 37 °C water bath for 1 minute, followed by adjusting the set temperature of the warm water bath to 30.75 °C. At this point the reaction was allowed to proceed for 40 minutes and 40 seconds at the desired temperature. After the designated time, the water bath flowing into the cuvette holder was quickly switched back to the cold water bath for the remainder of the 3200 seconds. Tubulin polymerization was monitored in the presence of varying concentrations of inhibitor (0, 0.5, 1.0, 1.5, 2.5, 3.5 µM) with an incubation time of 15 minutes at 30˚C and 15 minutes on ice. The conditions for this assay are in Table 6.2:

Table 6.2 – Final assay condition for inhibition of tubulin polymerization assay

Tubulin Polymerization Assay Conditions	
Assay Component	Concentration
6 cycle Tubulin	1.0 mg/ml
Glutamate	0.8 µM
Inhibitor	0, 0.5, 1.0, 1.5, 2.5, 3.5 µM
DMSO	4%
GTP	0.4 mM

Each experiment contained one blank (0.8 M glutamate), one to two controls (tubulin, glutamate, GTP, and DMSO) and 6 inhibitor concentrations (tubulin, glutamate, GTP, inhibitor).

Radiometric Binding of Tubulin

To determine if the lead compounds bound to the colchicine binding site of tubulin, radiolabeled colchicine was used in a competitive binding assay. Final concentrations for the assay were 100 mM glucose-1-phosphate, 1 mM GTP, 1 M glutamate, 1 mM $MgCl_2$, 0.5 mg/ml BSA, 0.1 mg/ml tubulin, 2.5% DMSO, 5 µM colchicine (~0.25 µCi/sample). The wash buffer used was 10 mM sodium phosphate/10 mM $MgCl_2$ pH 7.0. Tritiated colchicine was diluted 1:20 with 200 µM cold colchicine for the experiment with an expected counts per minute (CPM) of approximately 260,000 on the liquid scintillation counter. The 200 µM colchicine solution was diluted from a 40 mM stock made by dissolving 15.97 mg solid colchicine (MW 399.44) in 1 mL of 100% DMSO and stored in the -20 °C. Inhibitors were weighed out and dissolved in 100% DMSO. To 0.2 mL strip PCR tubes, 5 µl of inhibitor or DMSO was added, 100 µl reaction mixture (glucose, $MgCl_2$, BSA, GTP), and 90 µl tubulin glutamate mixture. These tubes were capped and allowed to sit on ice for 30 minutes after which 5 µl of tritiated colchicine was added. Samples were mixed by inversion and allowed to warm at 37 °C for 1 hour in the dark followed by transfer to ice for a final 30 minutes. The filter apparatus was set up as in Figure 6.6 connecting the apparatus to the trap flask before connecting to the vacuum pump. All the processes involving radioactive material was performed in the specified tritium hood in a radioactive isotope approved area. Three

GF/A filters were placed over each mesh grating in each of the 12 positions on the sampler and the cover was applied to ensure their seal. For each 12 samples, three

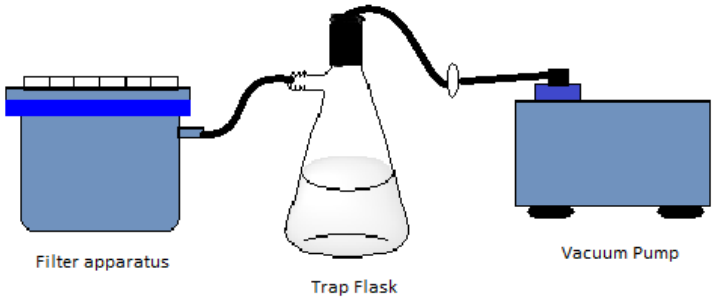

Figure 6.6 – Filtration apparatus setup for radiometric binding assay

positive controls (tubulin, reaction mixture, DMSO, and hot colchicine) and three negative controls (glutamate without tubulin, reaction mixture, DMSO, and hot colchicine) were run. GF/A filters were pre-wetted with 1 mL of cold wash buffer and allowed to gravity filter. Then, 180 µl of each cooled sample was added to the pre-wetted filter and allowed to sit approximately one minute before adding another 1 mL of cold wash buffer. The vacuum was then activated with the pressure reading at 50-70 mPa to ensure proper suction and seal on the sampler. While the vacuum was running 6 washes of 3 mL cold wash buffer were pipetted onto the filters with the final wash allowed to filter for approximately 5-10 minutes to ensure all the excess liquid was removed. Once filtered, the vacuum was turned off and the apparatus dismantled. The filters were removed with tweezers and placed directly into the bottom of glass scintillation vials containing 20 mL EcoScint H scintillation fluid which were capped and inverted gently 3 times to ensure homogenaety. Vials were allowed to sit for 48 hours after which the

maximal cpm could be achieved in a timely manner. Samples were run on a Beckman Coulter LS6500 detecting tritium for 20 minutes or until the error was less than 0.5%. All material that had potentially come in contact with radioactive chemicals was wiped clean with radiac-wash and was swipe tested for residual radioactivity against 3H, 32P, and 14C where an elevated level is 3 times that of the blank swipe. All samples were run in triplicate in three separate experiments.

Flow Cytometry

To determine the compounds' effect on the cell cycle, flow cytometry was performed. Human breast cancer cells (MDA-MB-231) and human umbilical vein endothelial cells (Huvec) were culture in ATCC suggested media with FBS and antibiotics. MDA-MB-231 cells were used between passage 3 and 17 and HUVECs were used between passage 2 and 4. Cells were grown to confluency and split with trypsin or trypsin-like solution. Cells were counted on the Beckman Coultier Z-series cell counter by taking 200 µl of homogenous cell suspension and pipetting it into 19.8 mL Z-Pak saline solution in cell counting vials. The cell counter was allowed to equilibrate after initiating and then flushed twice with Z-pak saline solution. The cell sample was inverted twice before placing on the counter stage and counts were taken to exclude particles less than 8 µm as the cell sizes are greater than this exclusion. The samples were counted in duplicate and the cells per ml was averaged and recorded. The suspension was diluted to plate 200,000 cells per well of a 6 well plate or 100,000 cells per ml. Cells were plated and allowed to adhere for 48 hours in the case of MDA-MB-231 cells and 24 hours in the case of HUVECs. Huvec cells were plated on 1% gelatin coated plates. After the adherent time, medium was replaced with fresh medium containing various concentrations of

inhibitors in DMSO or appropriate vehicle control. For a typical experiment there were two controls and four concentrations of inhibitor. The incubation time with inhibitor was 48 hours and 24 hours, for MDA-MB-231 cells and HUVECs, respectively. Pictures were taken with a digital camera attached to a microscope at 40X and 20X before harvesting the cells to note any phenotypic changes present. Media was then removed and placed in a 15 ml conical vial while the plates were trypsinized for 5 minutes in the 37 °C incubator. After incubation, the trypsin was neutralized and cells were removed via gentle pipetting with a 1 ml pipette. Suspension was transferred to the corresponding 15 ml conical vials containing previously transferred media fractions and a 1X PBS wash was applied to the wells to detach and wash any remaining cells and was collected in the corresponding 15 ml conical vial. Vials were centrifuged at 2,000 rpm for 5 minutes after which the supernatant was carefully removed and 1 ml 1X PBS was added. Vials were gently vortexed to break up the pellet formed and were centrifuged again at 2,000 rpm for 5 minutes. The supernatant was removed and the PBS addition and centrifugation was repeated. At this point, once the PBS was added the solution should contain little if any residual color from the media. Samples were vortexed again to break up clumps and maintain homogeneity and 50 µl aliquots were taken and placed in 19.95 ml Z-Pak saline solution and counted as previously mentioned. The values obtained were multiplied by 4 as the volume counted was one fourth less than what is required for cells per ml. The cell counts were recorded for trend analysis. Cells were then vortexed again in conical vials to re-suspend and 1 ml ice cold 70% ethanol was added drop-wise as the vials were being vortexed to avoid clumping. The samples were place at room temperature for 30 minutes before being stored in the fridge overnight which greatly reduced clumping during

analysis. After overnight storage at 4 °C, the samples were centrifuged again at 2,000 rpm for 5 minutes and the ethanol solution was poured off (instead of pipetting which could disturb the pellet), allowing tubes to rest inverted to remove excess ethanol. RNase A was diluted from 25 mg/ml solution to 20 µg/ml by a dilution of 80 µl into 100 ml with 1X PBS. To make a 20 µg/ml propidium iodide (PI) solution (MW 668.4), 1.5 mg of solid PI was weighed out and dissolved in 75 mL of ultrapure water. This solution was kept covered with foil as it is light sensitive. To the ethanol free tubes, 1 ml 1X PBS in addition to 1 ml RNase A was added to each tube followed by vortexing, ensuring the absence of clumps. To the tubes, 1 ml propidium iodide solution was added followed by brief vortexing, covered with foil and placed at 4 °C for 2 hours. During the staining time, the flow cytometer was turned on and allowed to warm up approximately 15 minutes before the computer was started. Once on, the FACSflow software was opened and calibration was performed. Figure 6.7 overviews the flow cytometer instrument procedure.

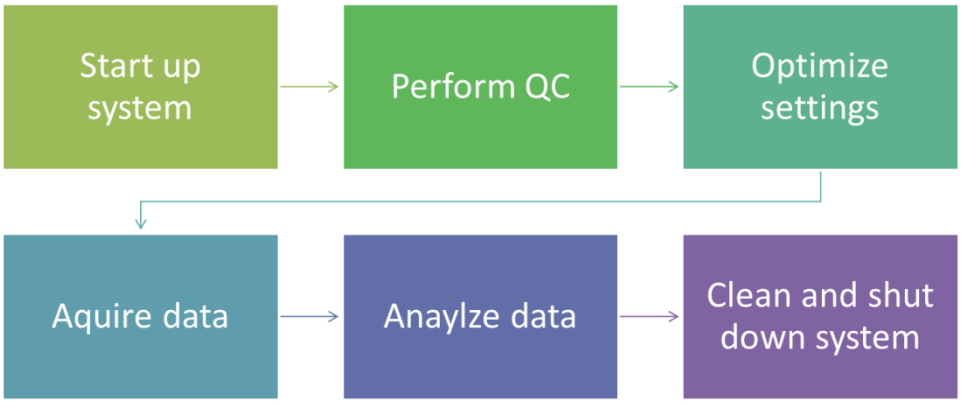

Figure 6.7 – Flow cytometer instrument procedure scheme

Flow Cytometer Calibration

Two flow tubes were set up, one with 1 ml deionized water (tube A) and the other with 3 ml (tube B). To tube A, one drop of well mixed/vortexed unlabeled beads was added. To tube B, one drop of each unlabeled, FITC (fluorescein isothiocyanate), PE (phycoerythrin), and PerCP (peridinin chlorophyll protein) beads was added. Initially an operator set up window opened, seen in Figure 6.8. Pressing accept allows the

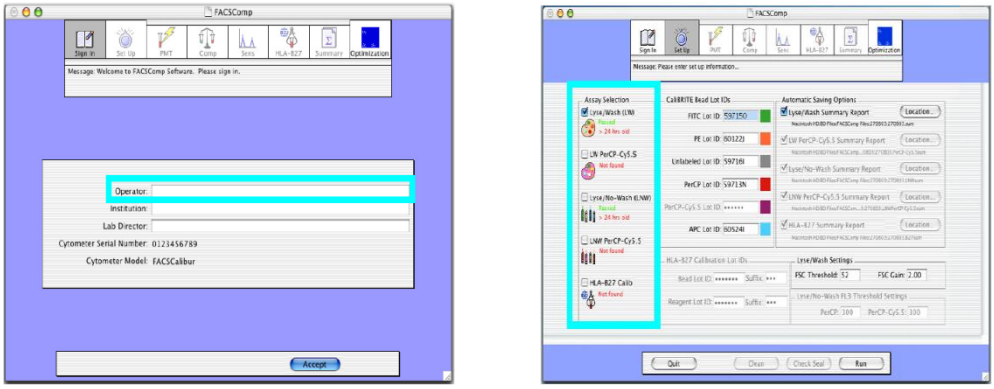

Figure 6 8– FACSCalibur set up screen 1-2 (courtesy and © Becton, Dickinson and Company, reprinted with permission)

progression to the next window in which lysis wash assay settings were chosen and lot numbers of calibrate beads were entered. Selecting run progresses to an optimize window, followed by a prompt to load tube A in septum on low or medium flow rate. Figure 6.9 illustrates how the unlabeled beads and labeled are detected. Once tube A has completed, tube B is prompted to be run and the following screens will optimize the photomultiplier tubes and analyze events and event rate. Once calibration is complete, a summary sheet window will appear and summarize the bead and instrument quality and its pass or fail status. If any parameters failed, the standards were made again and run

until complete passing was achieved. Cytometer sip was cleaned with Beckman Coulter Clenz before beginning samples.

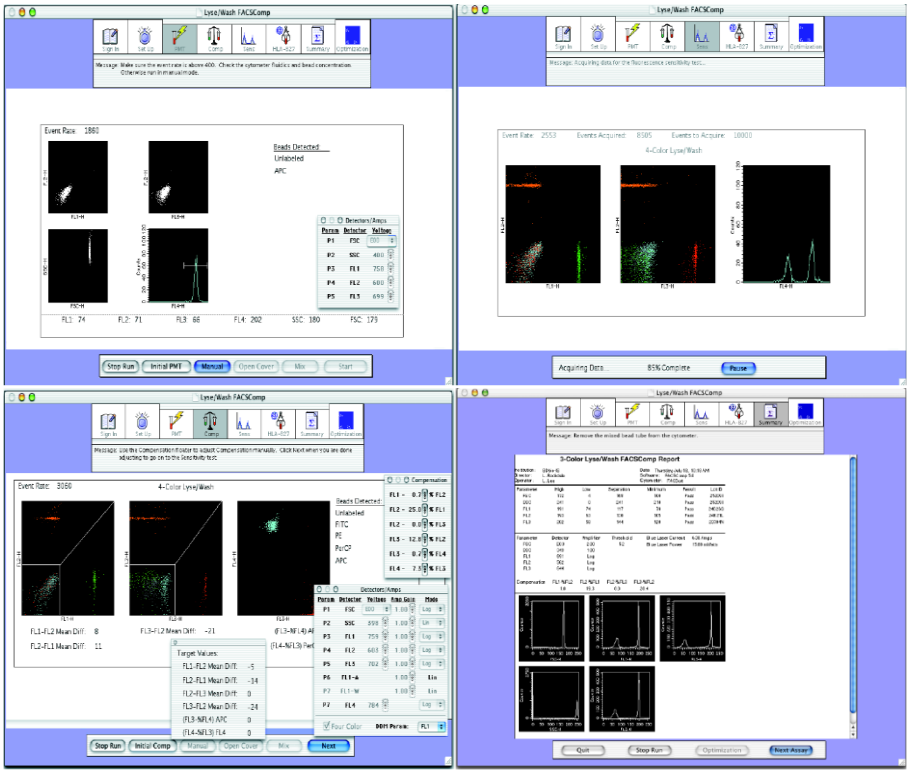

Figure 6.9 FACSCalibur set up screen 3-4 (courtesy and © Becton, Dickinson and Company, reprinted with permission)

Optimization of Conditions for Specific Cell Line

To optimize conditions for the cell line, a sample was prepared without inhibitor. Initially, CellQuest Pro software was opened and computer was connected to the cytometer. The acquisition window and browser were opened. A new analysis window was opened and an acquisition histogram and acquisition dot plot graph was created plotting FSC (forward scatter) vs SSC (side scatter) and FL1 vs FL2 and FL2 vs FL3. With the acquisition placed in set-up, the sample was run at low or medium flow rate.

While running, the counter window was opened to observe flow rate. Data can be visualized during collection on the histograms created. FSC, SSC, FL1, FL2, and FL3 were adjusted under detectors/amps option to maximize the population into the correct fluorescent laser, shown in Figure 6.10.

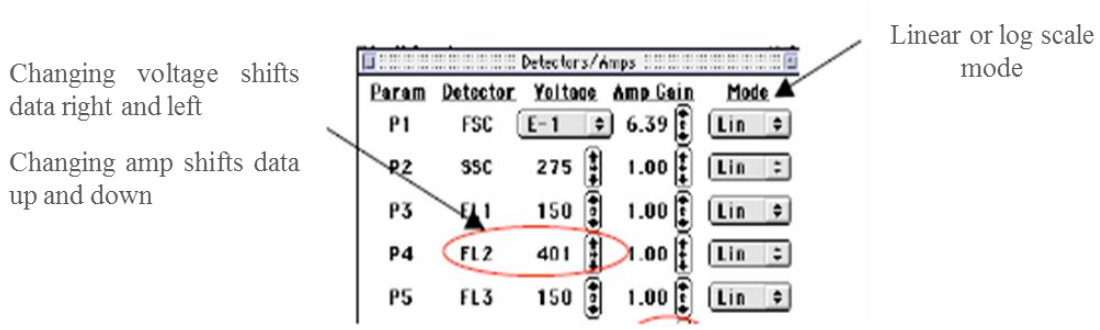

Figure 6.10 – Instrument settings optimization (courtesy and © Becton, Dickinson and Company, reprinted with permission)

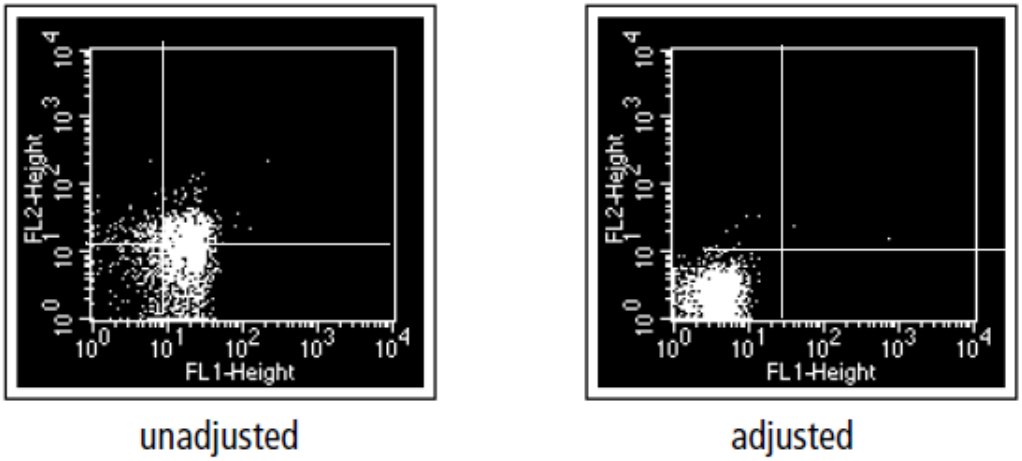

Figure 6.11 – FACSCalibur optimization: unadjusted sample vs adjusted using parameters in Figure 6.10 (courtesy and © Becton, Dickinson and Company, reprinted with permission)

From the FSC vs SSC graphs, gates can be made to exclude certain populations of cells which was not done in these experiments.Acquisition and storage settings were also

set up to acquire all events collecting 10,000 events or 20 minutes. Optimized settings were then saved by selecting cytometer > instrument settings > then save. This file was saved in the following location for auto-sampler usage: BD application > worklist manager > CellQuest experiment folder.

Running Samples with Loader/Auto-Sampler

Samples were placed in manually one at time or in a multi-sample loader and sampled as set up in program. For working with the loader/auto-sampler, the worklist manager software was launched and settings were chosen from previously optimized files. All volume from stained samples was placed in BD falcon flow tubes after vigorous vortexing. Samples were loaded into the round auto-sampler and sample information was added into the worklist and rack ID assigned. Samples were run on medium or high flow rate, monitoring the event rate. A summary report of sample status was printed out and saved for records. At the end of each run, the flow was cleaned with 10% bleach for 1 minute on high flow followed by 5 minutes at regular flow, followed by the same procedure with deionized water. Samples were analyzed, comparing data against controls from histograms of counts vs FL2-H. Response from the FL2-H laser corresponds to propidium iodide intensity, indicating DNA content and histograms were created from data which were segmented into apoptotic, G1, G2/M, S and aneuploid phase. Using histogram percentages, relative events were plotted in Graphpad Prism5.0 for analysis.

Tubulin Cell Signaling of RhoA

Generating Cell Lysate

Breast cancer cells MDA-MB-231 and HUVECs were allowed to grow until 50-80% confluency (depending on experiment) and media was changed with the addition of compound/inhibitor. The compound was allowed to incubate with the cells for 1-4 hours after which the media was removed and the plates were placed on ice. A 1X PBS wash was applied and allowed to pool in a corner of the flask as the flask was placed at an angle on the ice. The PBS was removed after approximately one minute and 1 ml cell lysis buffer with protease inhibitor was added and cells were immediately scraped with a cell scraper into one corner of the flask while still remaining on ice. Lysate was collected and placed in a 1.5 ml microfuge tube on ice and centrifuged at 16,000 rcf for 15 minutes at 2 °C. The spun samples were then placed on ice and supernatant was removed into a new iced tube. A small aliquot was removed for RC DC protein determination while the remaining lysate was flash frozen in liquid nitrogen if not used immediately to preserve GTPase activity.

RC DC Protein Determination

The RC DC assay allows for protein concentration determination in the presence of detergents and reducing agents. Here, 25 µl of protein sample or BSA standard was placed in a 1.5 ml centrifuge tube and 125 µl reagent I was added, the solution vortexed, and allowed to sit for 1 minute. 125 µl of reagent II was then added, tubes vortexed, and centrifuged in a minifuge at 14,000 rpm for 3-5 minutes. Supernatant was removed by placing tube upside down on an absorbent pad and allowing the liquid to draw out. At this point, white precipitate was seen on the bottom of the microfuge tube (protein), indicating the procedure was progressing. A working reagent solution was then made with 5 µl reagent S to every 250 µl reagent A. To the supernatant-free tubes, 127 µl

working reagent was added and samples were vortexed and allowed to sit 5 minutes or until the precipitate was dissolved. 1 ml of reagent B was added to each tube, vortexed, and incubated at room temperature for 15 minutes. 200 µl of each solution was placed in a well of a clear 96 well plate and the plate was read at 640 nm on a uv-vis microplate reader. A standard curve was generated and from the equation of the line, concentration of the lysate were determined. Once the protein determination had been performed, the pull down assay was begun and the frozen lysates were quickly thawed and diluted with lysis buffer to 1 mg/ml.

Positive and Negative Control Treatment

For the negative and positive controls, 500 µg protein was placed in a 1.5 ml microfuge tube and 10 µl 0.5 M EDTA was added to achieve a final concentration of 10 mM. EDTA was prepared by weighing out 1.86 g solid ethylenediaminetetraacetic acid disodium salt dihydrate (MW 372.24) and dissolving it in 10 ml ultrapure water. The positive control was treated with a non-hydrolyzable GTP analogue to prevent the Rho A from becoming inactive and the negative with excess GDP to keep the Rho A mainly in the inactive form. Lysates containing EDTA were vortexed and 5 µl of 10 mM GTPγS (final concentration of 0.1 mM for positive control) and 5 µl of 100 mM GDP (final concentration of 1 mM) were added and vortexed. Samples were incubated at 30 °C in a heating mantel for 15 minutes with constant agitation on a shaker. To terminate the reaction, samples were placed on ice and 32 µl of 1 M $MgCl_2$ for a final concentration of 60 mM and the sample was vortexed. To make 1 M $MgCl_2$, 2.03 grams of $MgCl_2$ (MW 203.3) was weighed out and dissolved in 10 ml ultrapure water.

Affinity Precipitation of Active Rho A

A spin cup was placed in each collection for each sample and 100 µl of well mixed agarose beads in 50% slurry was added to each spin cup. The tubes were centrifuged for 1 minute at 6,000 x g at 2 °C and flow through was discarded. 400 µl of the cold lysis buffer (containing the protease inhibitor) was added to each spin cup and the tubes were inverted gently to wash the beads, followed by centrifugation for 1 minute at 6,000 x g at 2 °C and flow through was discarded again. To each cup, 70 µl GST-Rhotekin RBD (400 µg) was added while tubes remained on ice. Up to 700 µl lysate was then added to each spin cup on ice and the tubes were capped and vortexed. The tubes were placed in an ice bucket on a shaker and incubated with constant gentle agitation for 1 hour to allow the rhotekin to bind the active Rho A. After incubation, the cold samples were centrifuged for 1 minute at 6,000 x g at 2 °C and flow through was discarded. Spin tubes were transferred to new collection tubes and 400 µl lysis buffer with protease inhibitor was added. Tubes were gently inverted and centrifuged for 1 minute at 6,000 x g at 2 °C and flow through was discarded. The wash step was repeated two additional times while maintaining all samples on ice. Each spin cup was again transferred to a new collection tube and 50 µl reducing agent was added for a final concentration 200 mM. Reducing agent was prepared by mixing 2.5 µl β-mercaptoethanol to 50 µl 2X SDS sample buffer. Tubes with samples were vortexed and allowed to incubate at room temperature for 2 minutes. Samples were centrifuged 2 minute at 6,000 x g at 2 °C and spin cups were discarded. Flow through samples contained active Rho A and were heated for 5 minutes at 95-100 °C. Samples were concentrated by placing the entire volume of pull down in an Amicon Ultra-0.5 filter seated within a corresponding tube. Samples

were capped and centrifuged in a minifuge for 22 minutes at 14,000 x g at room temperature. Filters were then placed upside-down in new tubes and without capping the tube, centrifuged at 1,000 x g for 2 minutes and RD DC was repeated to obtain the final concentration for gel electrophoresis analysis.

Electrophoresis and Transfer

For each sample, a tube was made up containing 2.5 µl LDS sample buffer and the volume needed to obtain 25-50 µg protein. These samples were heated for 5-10 minutes at 90 °C. Based on concentration of samples, 25-50 µg protein was loaded into each well of a 4-12% bis-tris SDS Page gel. The molecular weight marker used was a fluorescent marker ranging from 12 kDa to 225 kDa and 4-5 µl was loaded onto the gel. Electrophoresis was run on ice with cold 1X MES running buffer for approximately 2-3 hours at 90-100 volts. For the transfer, PVDF membrane cut to the size of the gel was incubated with pure methanol for 5 minutes before being incubated with blotting paper in Towbin buffer at 4 °C. Towbin buffer was made by weighing and dissolving 3.027 g Tris HCl (MW 121.1), 14.41 g glycine (MW 75.07) and 1 g sodium dodecyl sulfate (MW 288.38) in 200 ml methanol and upto 1 L ultrapure water. Final concentrations of Towbin buffer are 25 mM Tris, 192 mM glycine, 20% methanol, and 0.1% SDS. (NOTE: A three buffer system was originally used for the semidry transfer apparatus but optimization required conversion to one buffer system and wet transfer device.) Sandwiches were made for transfer with the wet device in the following order: red electrode, 2 sheets wet blotting paper, 1 pre-wet membrane, bis-tris gel with protein, 2 sheets wet blotting paper, black electrode. After each layer, a roller was used to remove any air bubbles. Transfer was done on ice, with cold Towbin buffer, and an ice pack placed in the transfer

chamber. Transfer time varied but the most effective time was 4 hours at 25 volts with volts constant. Once transfer was complete, the gel was placed in water for a wash step and then into Simply Blue safe-stain to stain for protein. The membrane was placed directly in 3% BSA-TBST and gently rotated for 2 hours to block non-specific proteins. To make 3% BSA-TBST, 3 g BSA fraction V was weighed out and dissolved in 100 ml TBST-taking care to ensure the solid was in solution for at least 30 minutes before use. After blocking the membrane it was washed with TBST buffer for 5 minutes twice. Primary antibodies were made up at dilutions suggested in 3% BSA-TBST and were left on the membrane overnight at 4 °C with gentle shaking. The following day the membrane was washed 5 times for 5 minutes each with TBST. Secondary antibody was diluted from a stock solution to 1:100,000 dilution with 3% BSA-TBST and left to incubate with washed membrane at room temperature for 1 hour. 5 wash steps were performed for 5 minutes each after which the chemiluminescent substrate was made. The substrate was made in a 1:1 ratio in a tube covered with foil. For each membrane, approximately 4 ml of substrate was used. Membrane was placed in a gel pouch and substrate was added. Bubbles were removed so that membrane was completely immersed in solution for 3-5 minutes, following which excess was removed by rolling a pencil or serological pipette over the gel pouch over an absorbent pad. Pouch was heat sealed and immediately imaged using the Ultralum imager equipped with a digital camera for 15-40 minutes depending on sample with binning of 2x2. Blots were analyzed with Ultraquant 5.0 software using the density analysis tool.

CHAPTER SEVEN

Investigative Studies on the Mechanism of Action of Benzosuberenes: Results

Strategy

In a long term collaborative effort between the research laboratories of Kevin G. Pinney and Mary Lynn Trawick, a series of benzosuberenes including compound **7** were designed as combretastatin analogues and were synthesized and evaluated biologically. In previous studies, the benzosuberenes were found to have extremely potent cytotoxicity and therefore the mechanism of action was herein investigated. The combretastins are vascular disrupting agents that have a similar structure to colchicine and bind to the colchicine binding site on tubulin. As not all VDAs are tubulin binding agents, the investigation began with determining whether the benzosuberene compounds interacted with tubulin. Initially a turbidometric assay was performed, monitoring the polymerization of tubulin and its inhibition in the presence of compound. Inhibition of polymerization indicated that the analogues bound to the tubulin subunits and prevented assembly. To determine whether the inhibitors bound at the colchicine binding site or to another site on tubulin, tritium labeled colchicine was utilized in a competitive binding assay. Inhibition of radiolabeled colchicine binding to the colchicine binding site of tubulin indicated preference for binding of the benzosuberene analogues at this location. Since compounds that inhibit microtubule dynamics often affect cell division, the effects of the analogues on cell cycle were determined. Flow cytometry methods allowed for the identification of the cells into their cell cycle phase, demonstrating the effects of the benzosuberene compounds. Accumulation of DNA in various phases indicated inhibition

of cell mitosis or increase in cell death, depending on the sample. The ability of the compounds to modify various targets within tumor development was then investigated through a series of protein purification of cell lysates and imaging, probing for various proteins within the signaling pathway. Cytotoxicity data obtained by Dr. Tracy E. Strecker of the Trawick lab is seen in Table 7.1 for the MDA-MB-231 breast cancer

Table 7.1 – Cytotoxicity of compounds on human breast cancer cell line MDA-MB-231

Cytotoxicity Data for compounds	
Compound	IC_{50} (nM) in MDA-MB-231s
7	0.0416[40]
8	34.8
CA4	43.0[188]
Colchicine	37[189]
9	2.87
10	293
11	10.7
12	
13	43.0
14	40.1
15	0.0508
16	0.0136

*See Table 7.2 for compound structures.
`Compounds synthesized by the Pinney laboratory

cell line The cell line MDA-MB-231 is a mammalian mammary cancer cell line with aneuploid characteristics, at near triploid chromosome counts. These IC_{50} values, also referred to EC_{50} (effective concentration) or GI_{50} (growth inhibition), corresponds to the

concentration of compound required to inhibit growth of the cell line by 50% when compared to a vehicle control.

Purification and Protein Determination

For the experiments performed, a large amount of 5-6 cycle tubulin was required and therefore in house purification of the protein was done. The purification of tubulin from calf brain is based on the polymerization of tubulin protein occurring under warm conditions in the presence of GTP and depolymerization under cold temperatures. Hamel et al. developed a method of purification in the early 1980s removing a number of minor components referred to as microtubule associated proteins (MAPS) for a large scale tubulin purification/preparation. This method was used with minor modifications. Here, high concentration of organic anions, namely MES, and glycerol solutions were utilized to homogenize the crude brain, creating a slurry for initial centrifugation. Samples initially were centrifuged to remove large amounts of lipids followed by various centrifugation cycles selectively polymerizing tubulin induced via high MES concentration (1.6 M) and GTP. EGTA and EDTA were added to chelate available calcium ions which interfere with polymerization of the target protein. Glycerol and sucrose were used in the purification buffer as they have been found to greatly facilitate tubulin polymerization as compared to the absence of these two components. Glycerol was also determined to significantly stabilize the normally labile tubulin subunits during purification.[190] Calf brain was utilized as it was relatively easily obtainable and has previously been shown to contain large amounts of tubulin in comparison to other organs and tissues. [191,192]

Protein Determination

Eight preparations of tubulin purification from calf brain were completed, each of which originated from approximately 400 g of brain tissue and yielded a between 33 to 155 mg of 5-6 cycle tubulin. Protein determination was necessary to quantify the purified product. Various methods are available for this purpose with each having limitations and incompatibilities with components such as detergents or reducing agents. For our purposes, the Bradford protein assay was a convenient method that roughly quantified tubulin protein concentration. Subsequent more accurately determined concentrations were obtained via a UV-vis assay using the wavelengths 278 and 255 nm. The Bradford assay is based on a Coomassie Brilliant Blue acidic solution which results in a spectral shift in maximal absorbance from 465 to 595 nm upon protein binding. Stabilized by hydrophobic and Van der Waals interactions, the anionic form of the dye changes color when the protein's positive charges bind to negatively charged molecules in the dye. The positive charges on the protein are approximately proportional to the number of negative ligands of the Bradford dye. [193] The detection limit of this assay is 1-25 µg/ml and is compatible with most reducing agents and chelators which are present in the tubulin purification samples. A standard curve was generated and using the equation of the line, the concentration of the tubulin samples was determined. It was observed that concentrations above 1.0 to 1.2 mg/ml do not follow a linear trend as is noted by Thermo Pierce. Figure 7.1 represents a typical standard curve of BSA samples using the Bradford protein assay with an R^2 of 0.988. The primary technique to accurately determine protein concentration is based on a method from Harrison *et al.* 1976 and *Biochemistry* vol. 35, 6, 1996, pg 2009.

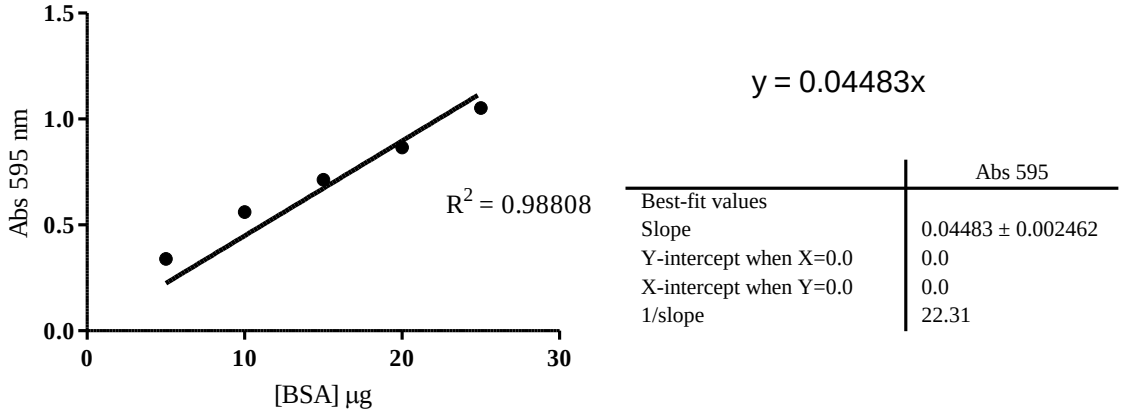

	Abs 595
Best-fit values	
Slope	0.04483 ± 0.002462
Y-intercept when X=0.0	0.0
X-intercept when Y=0.0	0.0
1/slope	22.31

Figure 7.1 – Standard curve for Bradford assay (Bovine serum albumin)

This method calculates the final concentration of the purified tubulin using molar extinction coefficients for tubulin and GTP. From the scan of the tubulin sample, a graph of absorbance vs wavelength was constructed. Due to the baseline of the curve not reaching zero, a new baseline was achieved by extrapolating the portion of the curve 325 nm to 400 nm. From this point, the wavelengths in question were used to determine the absorbance at that point using the newly created baseline. Absorbance value targets were in the range of 0.01 and 1.0. With the data obtained, the concentration was determined using the following extinction coefficients: for tubulin, 1.2 L/g-cm at 278 nM and 0.65 L/g-cm at 255 nM, for GTP, 12.17 x 10^3 and 7.66 x 10^3 M cm at 255 nm and 278 nm respectively. From this point, the OD_{278} and OD_{255} was determined by solving two simultaneous equations for x.

OD278 = absorbance value determined = [extinction coefficient tubulin at 278 nM] (x) + [extinction coefficient GTP at 278 nM] (y)

OD255 = absorbance value determined = [extinction coefficient tubulin at 255 nM] (x) + [extinction coefficient GTP at 255 nM] (y)

For the representative curve seen in Figure 7.2, after incorporating the dilution factor into the equation, the concentration of tubulin is 9.56 mg/ml.

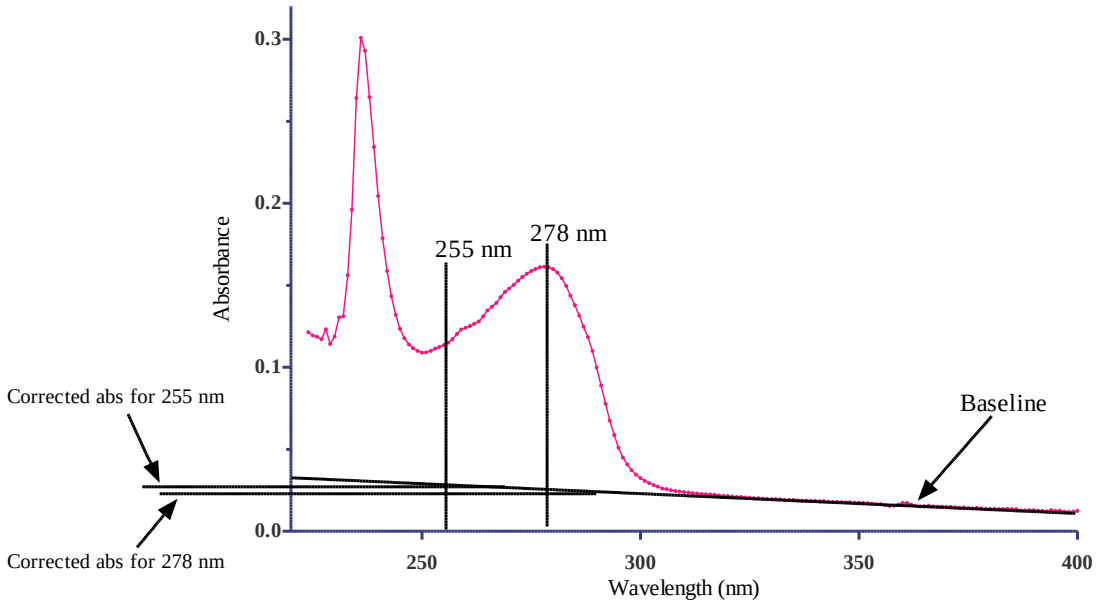

Figure 7.2 – Representative tubulin concentration determination, preparation 5

Gel Electrophoresis of Purified Tubulin

SDS-Page gels were run on purified cycle 5-6 tubulin to verify minimal contamination of other proteins, namely microtubule associated MAPS A and B found at a slightly higher molecular weight than tubulin which is located at approximately 50-55 kDa. Gel electrophoresis is a method that separates proteins as they migrate through an electric field. In this method, SDS (sodium dodecyl sulfate) is added to negatively charge all the proteins available in the sample and which upon heating, denatures the protein and binds. Heating is also performed in the presence of a reducing agent (β-mercaptoethanol) to cleave disulfide bonds, therefore removing the possibility of quaternary or tertiary protein structure formation and facilitating protein denaturation. Once samples have been

loaded onto a gel, an electric field is applied forcing the negatively charged proteins to move from the cathode and towards the anode (positively charged electrode) through the fel which acts as a sieve. Once the protein has been successfully separated, the gel is stained with Simply blue safestain which preferentially stains proteins (dye component is Coomassie Brilliant Blue G-250). Figure 7.3 is a representation of a SDS-PAGE gel (4-12% gradient polyacrylamide) of the various steps during the tubulin preparation. On the far left is the molecular weight marker used to visualize a standard size of protein. Samples of ten and five micrograms of 6 cycle purified tubulin were loaded onto the gel and it is evident due to the lack of excess bands that the sample is pure. Tubulin protein is approximately 50-55kDa in size as seen in Figure 7.3.

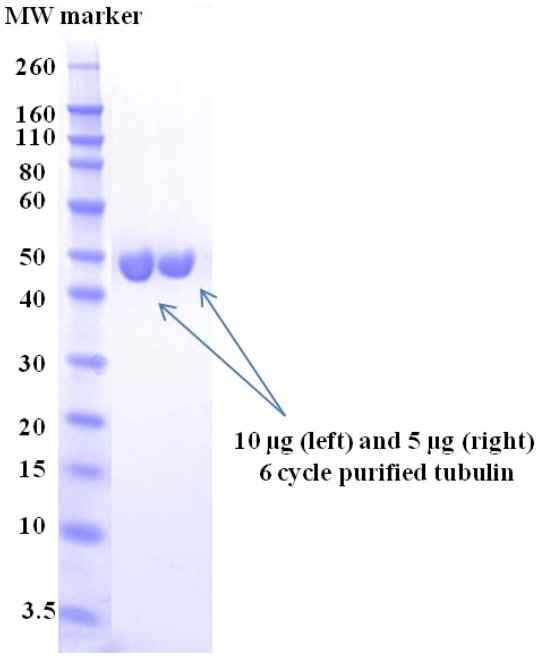

Figure 7.3 – Representative SDS PAGE gel of purified tubulin (6 cycle)

Inhibition of Tubulin Polymerization

In order to observe the effects of the compounds on the growth of the tubulin polymer chain, polymerization ability of the protein was determined by a turbidometric kinetic method, monitoring the reaction via UV-Vis at 350 nm. Tubulin polymerizes in the presence of GTP at warm temperatures and depolymerizes under cold conditions. In this assay used to measure the amount of polymerization which occurred, the increase in absorbance is proportional to the increase in polymerization of the target protein. A representative curve is seen in Figure 7.4 where decreased absorbance indicates no polymerization (no turbidity) and increase in absorbance indicates polymerization (turbidity).

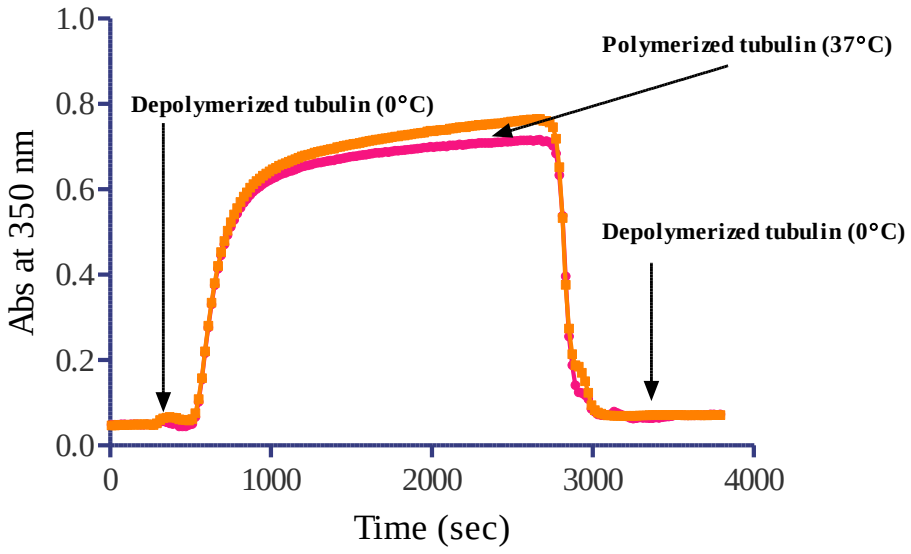

Figure 7.4 – Polymerization of 1 mg/ml 6 cycle tubulin kinetic curve

Inhibition of tubulin polymerization was performed via these same methods where tubulin was monitored in the presence and absence of inhibitors and inhibition was

quantified. From absorbance curves, points were taken at 300 and 1500 seconds for depolymerization and polymerization values, respectively. Using these data points, an IC_{50} curve was constructed and an IC_{50} value was calculated. Inhibition of tubulin polymerization was completed for five compounds, each of which was tested in triplicate in at least two independent experiments. CA4 was previously published and was tested to validate the assay. [150] The IC_{50} values, structures and names are seen in Table 7.2.

Table 7.2 – Inhibition of tubulin polymerization results

Compound	Structure	IC_{50} µM
7	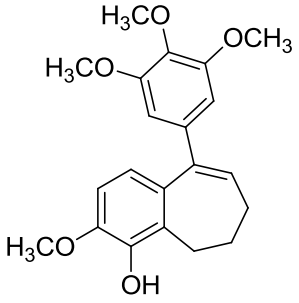	1.0†
8	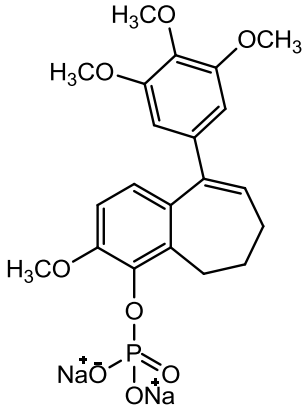	>40 µM[60]
CA4	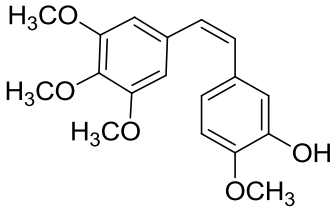	0.81 [150]

Table 7.2(continued)

Compound	Structure	IC_{50} µM
Colchicine	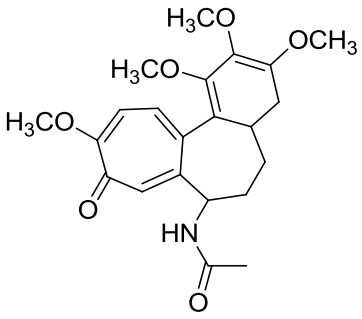	0.92
9	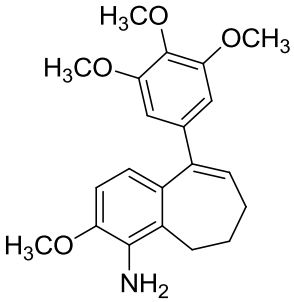	1.3†
10	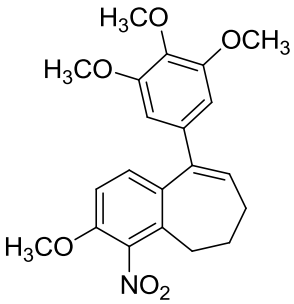	3.2†
11	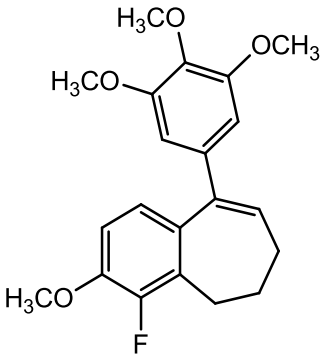	0.89*

Table 7.2(continued)

Compound	Structure	IC_{50} µM
12	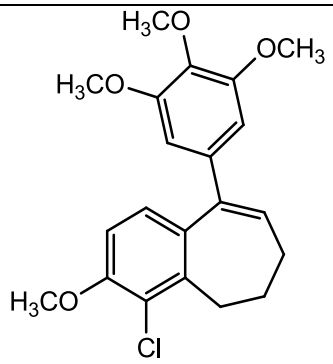	0.93*
13	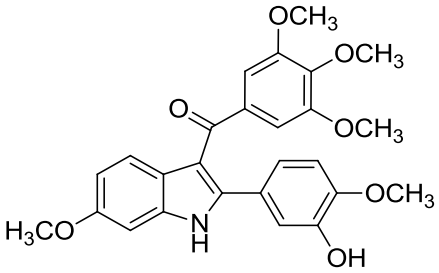	ND
14	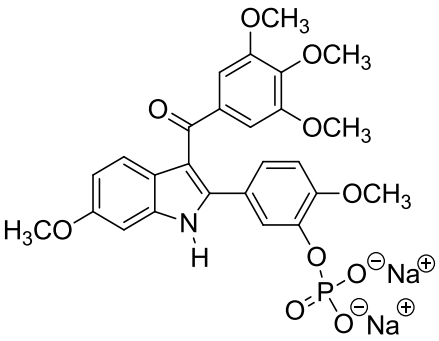	ND
15	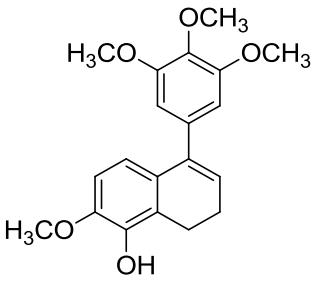	ND

Table 7.2(continued)

Compound	Structure	IC50 µM
16	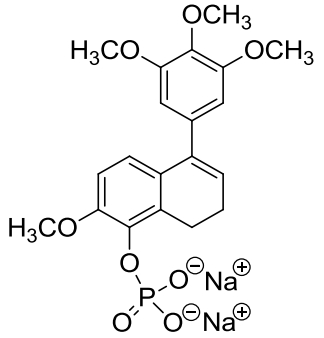	ND
17	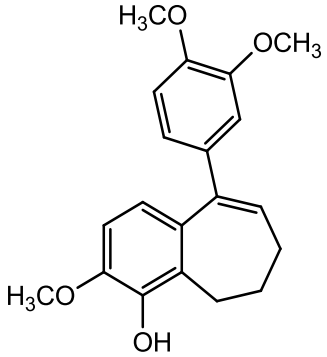	0.74*
18	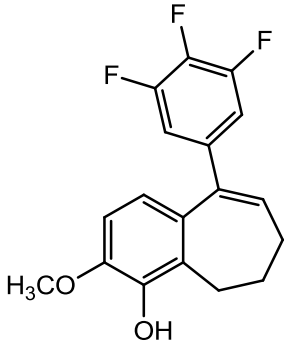	ND
19	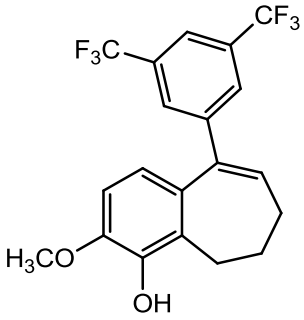	ND

Table 7.2(continued)

Compound	Structure	IC_{50} µM
20	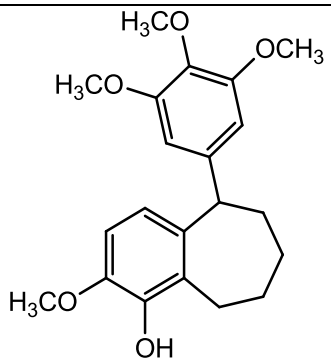	ND
21	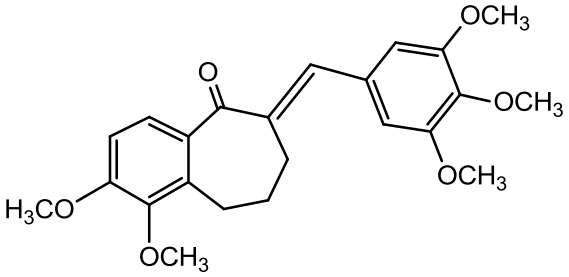	ND

Compounds synthesized by the Pinney laboratory
ND = not determined
†For additional data see ref [60,194]

Other analogues of the benzosuberenes were tested but by Justin Tidmore (compound **11** and compound **12**) and this manuscript has been accepted. Compound **11**, compound **12**, compound **17** and compound **18** were comparable to colchicine and CA4 in regards to IC_{50} value, with values under 1.0 µM. Compound **19** and compound **20** were also below 1.0 µM, inhibiting tubulin polymerization at approximately half the IC_{50} of colchicine. Compound **21** was greater than 10 µM. Compound **7** had potent inhibitory activity for inhibition of tubulin with an IC_{50} of 1.0 µM followed by the amino analog compound **9** with an IC_{50} of 1.3 µM. In comparison, the nitro analog, compound **10**, was more than twice that of the amino moiety. Colchicine and CA4 IC_{50} values were both relatively close to the reported literature values of 1.4 µM and 1.2 µM, respectively. [150];

[195] Therefore, compound **7** did inhibit tubulin polymerization indicating the compound's binding to tubulin with an inhibitory activity comparable to that of CA4.

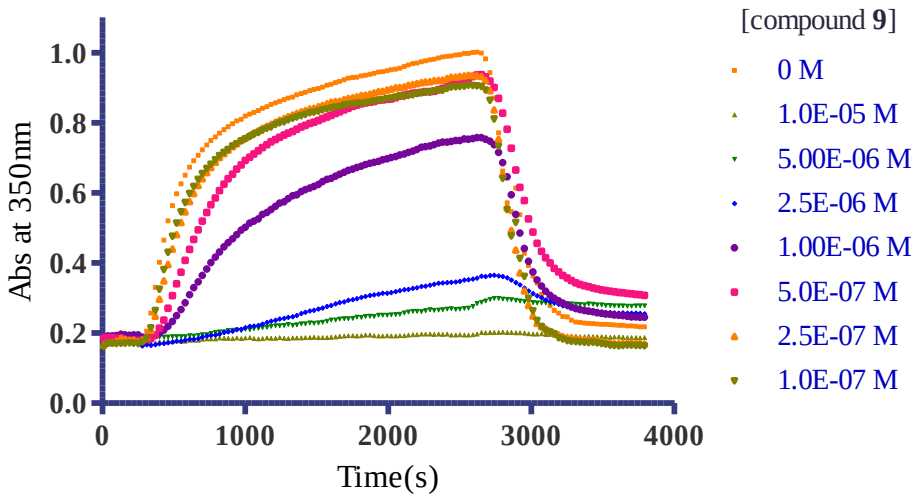

Figure 7.5 – Inhibition of tubulin polymerization by compound **9**, absorbance curves

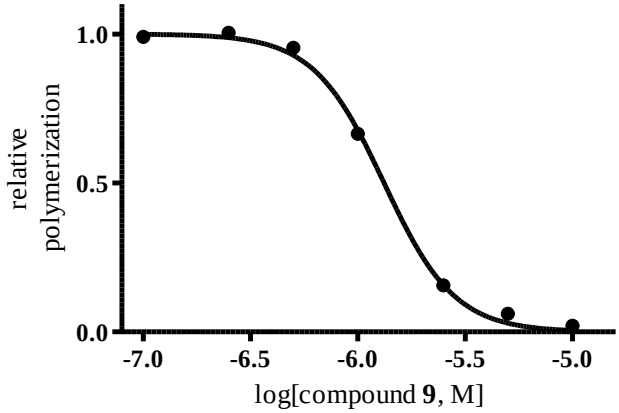

	pol-depol
Sigmoidal dose-response (variable slope) [2]	
Best-fit values	
Bottom	= 0.0
Top	= 1.000
LogEC50	-5.878
HillSlope	-2.635
EC50	1.324e-006
Std. Error	
LogEC50	0.01363
HillSlope	0.1688
Goodness of Fit	
Degrees of Freedom	5
R square	0.9981
Constraints	
Bottom	Bottom = 0.0
Top	Top = 1.000
Number of points	
Analyzed	7

Figure 7.6 – IC_{50} determination of compound **9** on tubulin polymerization

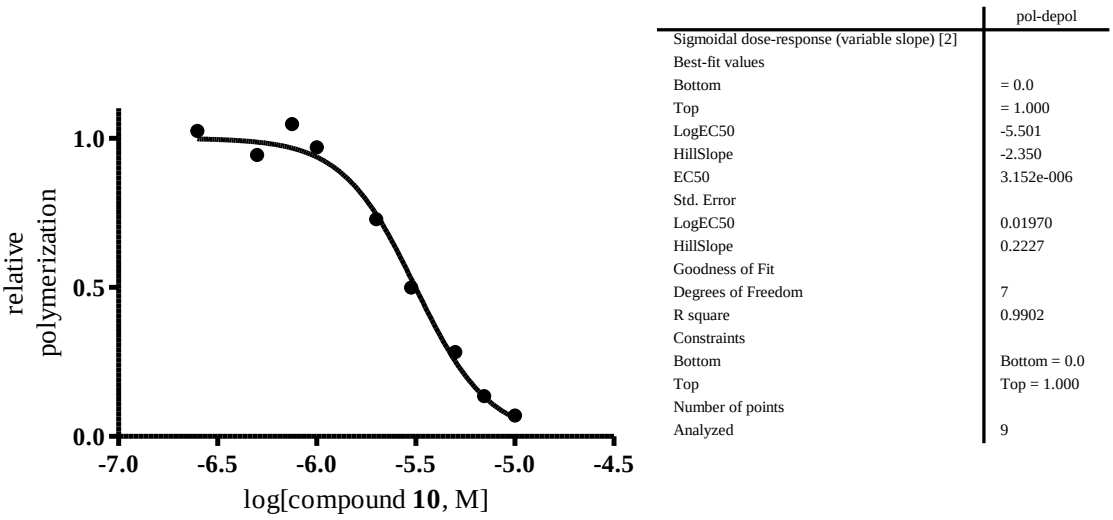

	pol-depol
Sigmoidal dose-response (variable slope) [2]	
Best-fit values	
Bottom	= 0.0
Top	= 1.000
LogEC50	-5.501
HillSlope	-2.350
EC50	3.152e-006
Std. Error	
LogEC50	0.01970
HillSlope	0.2227
Goodness of Fit	
Degrees of Freedom	7
R square	0.9902
Constraints	
Bottom	Bottom = 0.0
Top	Top = 1.000
Number of points	
Analyzed	9

Figure 7.7 – IC_{50} determination of compound **10** on tubulin polymerization

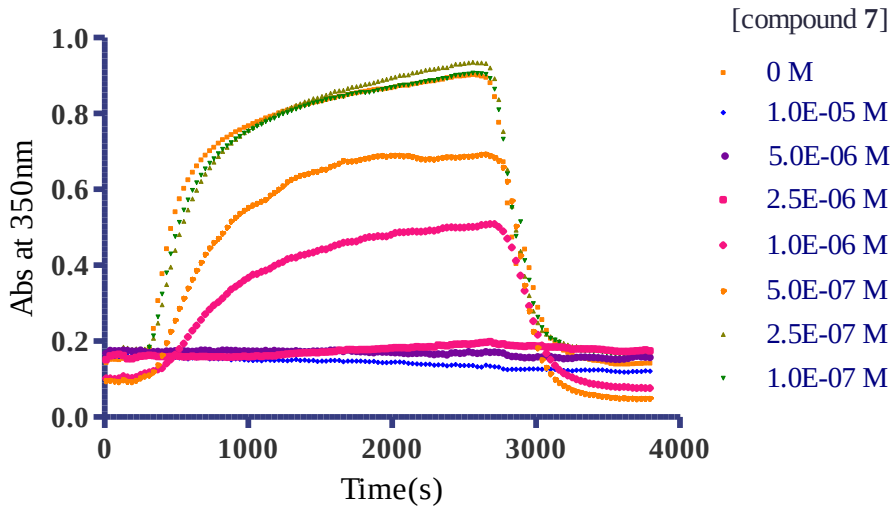

Figure 7.8 – Inhibition of tubulin polymerization by compound **7**

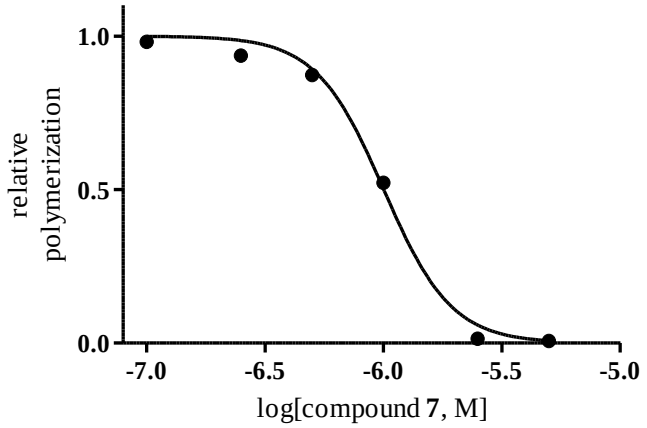

	pol-depol
Sigmoidal dose-response (variable slope) [2]	
Best-fit values	
Bottom	= 0.0
Top	= 1.000
LogEC50	-5.999
HillSlope	-3.036
EC50	1.002e-006
Std. Error	
LogEC50	0.01961
HillSlope	0.4316
Goodness of Fit	
Degrees of Freedom	4
R square	0.9946
Constraints	
Bottom	Bottom = 0.0
Top	Top = 1.000
Number of points	
Analyzed	6

Figure 7.9 - IC_{50} determination of compound **7** on tubulin polymerization

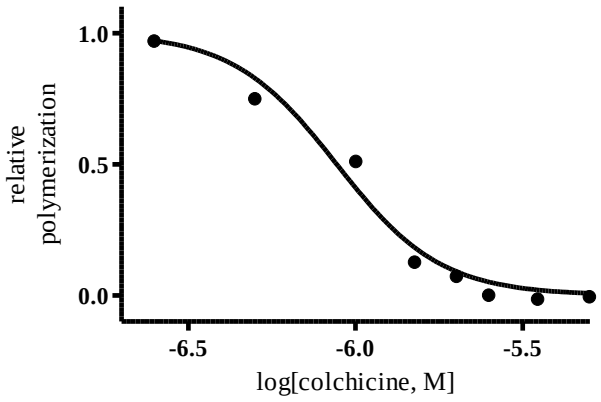

	pol-depol
Sigmoidal dose-response (variable slope) [2]	
Best-fit values	
Bottom	= 0.0
Top	= 1.000
LogEC50	-6.057
HillSlope	-2.793
EC50	8.777e-007
Std. Error	
LogEC50	0.03085
HillSlope	0.4346
Goodness of Fit	
Degrees of Freedom	6
R square	0.9775
Sy.x	0.06294
Constraints	
Bottom	Bottom = 0.0
Top	Top = 1.000
Number of points	
Analyzed	8

Figure 7.10 - IC_{50} determination of colchicine on tubulin polymerization

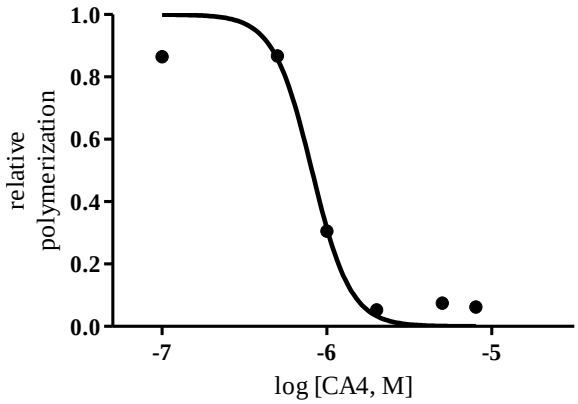

	pol-depol
Sigmoidal dose-response (variable slope) [2]	
Best-fit values	
Bottom	= 0.0
Top	= 1.000
LogEC50	-6.091
HillSlope	-3.731
EC50	8.106e-007
Std. Error	
LogEC50	0.03969
HillSlope	1.068
95% Confidence Intervals	
LogEC50	-6.201 to -5.981
HillSlope	-6.695 to -0.7675
EC50	6.290e-007 to 1.045e-006
Goodness of Fit	
Degrees of Freedom	4
R square	0.9641
Absolute Sum of Squares	0.02797
Sy.x	0.08363
Constraints	
Bottom	Bottom = 0.0
Top	Top = 1.000
Number of points	
Analyzed	6

Figure 7.11 - IC_{50} determination of CA4 on tubulin polymerization

Competitive Binding Assay

There are three characterized drug binding sites on microtubules: the vinblastin, taxol, and colchicine binding sites. The benzosuberene analogues examined in this study are similar in structure to combreastatins which are known to bind to the colchicne binding site. To determine whether the benzosuberene compounds bound to the colchicine binding site of tubulin, a competitive radiometric assay was performed. Here, tritium labeled colchicine was incubated with the compounds and tubulin.

Competitive Binding Assay - Method Development

Although the method followed was published by Hamel et al, some method development was required to determine optimal conditions.[195] Initially conditions used by Hamel were tested in the absence of radiolabeled colchicine to visualize if polymerization would occur. Even using the small concentration of tubulin, 0.1 mg/ml, polymerization

occurred. The conditions are as follows: 0.1mg/ml tubulin, 1 M glutamate, 5% DMSO, 0.5 mg/ml BSA, 100 mM K-phosphate, 1 mM $MgCl_2$, 1 mM GTP. The conditions used in literature for this assay are summarized below and each was tested to optimize the assay. Conditions tested radiometrically included reaction mixture, incubation time for inhibitor and tubulin, wash buffer, wash steps, liquid scintillation counter (LSC) response over time, filter type and count: Reaction mixture was tested per Hamel consisting of 1 M glutamate, 100 mM glucose-1-phosphate, 1 mM GTP, 0.5 mg/ml BSA and no ^3H colchicine initially.[195] As per Hamel, the reaction mixture was also tested in the presence of 1 mM $MgCl_2$ and 0.1 mg/ml tubulin, also not initially containing ^3H colchicine.[162] Finally, the reaction mixture with 1 M glutamate, 100 mM glucose-1-phosphate, 1 mM GTP, 1 mM $MgCl_2$, 0.1 mg/ml tubulin and ^3H colchicine initially added was tested. The last mixture did not contain BSA. Reaction samples were 200 µl in volume and 100 µl vs. 180 µl was tested for filtration. The optimal buffer used for the reaction mixture incubation contained a mixture of glucose 1-phosphate, glutamate, GTP and albumin, an effective combination known to strongly stabilize the colchicine binding of tubulin.[196] For incubation time, conditions used by Hamel, Borisy and Bhattacharyya were compared.[190,195,196] Hamel's method included beginning with all the reagents cold and combined, with the exception of the radiolabeled colchicine, kept on ice for 30 minutes followed by a 3 hour preincubation at 37˚C. At this point, the mixture was cooled on ice for 30 minutes, ^3H colchicine was added, and mixed reaction mixture was incubated for 1 hour at 37˚C followed by a final 30 minutes on ice. The successive temperature changes were assumed to allow for tubulin polymerization/depolymerization cycles. Borisy's method was modified and tested, which included beginning with all reagents cold

followed by ten minutes on ice once mixed. A 1 hour incubation time at 37˚C followed by ten minutes on ice completed this incubation experiment. Last, Bhattacharyya's method was tested which included the cold reagents mixed on ice for 30 minues, a 1 hour incubation at 37˚C, completed by a 30 minute cold period on ice. The initial cooling of the reagents kept the tubulin from polymerizing before the addition of inhibitor which could potentially reduce the protein's polymerization ability. Due to the fact that colchicine binds to tubulin in a two step manner where the initial binding is fast with approximately 60% of the binding occurring, the compounds were allowed to incubate with the tubulin in buffer initially on ice for 30 minutes in the absence of ^{3}H-colchicine.[197]; [198] This pre-incubation was performed in effort to allow for an initial period where the colchicine-like compounds were unhindered by colchicine which binds to tubulin with a K_d between 0.98-1.4 μM.[199,198] Following the preliminary incubation period, radiolabeled colchicine (~260,000 cpm) was added to unlabeled colchicine to achieve a final concentration of 5 μM and the samples were gently swirled. Samples were then incubated at 37ºC in reduced light for 1 hour, followed by 30 minute incubation on ice. The warm incubation was to allow the colchicine to bind tubulin as the extent of binding is temperature dependent, where at 37ºC the extent of colchicine bound is 20x that at 0ºC.[191] Differing literature sources suggested various times for the warm incubation with 10 and 60 minutes being a commonality, therefore these two time points were tested using CA4 as the ligand for comparison. As is seen in Figure 7.12 and Table 7.3, 60 minute incubation gave approximately double the counts per minute, reducing the effect of small variations. This point in conjunction with the previously established data

from of the efficiency of colchicine binding over time, a 60 minute warm incubation step was decided upon.[198] Wash buffer was then optimized using methods from Hamel,

Table 7.3 – Counts per minute at various time points for 10 and 60 minute warm incubation of the reaction mixture with tritiated colchicine

	48 hour time point		72 hour time point	
[CA4] µM	CPM 10 min warm inc	CPM 60 min warm inc	CPM 10 min warm inc	CPM 60 min warm inc
0	5635	10372	5765	10741
1	1196	3383	1216	3411
5	-53	707	-53	700
10	63.5	409.5	80	430

Bhattacharyya, and Borisy.[190,195,196] The first wash buffer was cold 1 mM $MgCl_2$, 100 mM glucose 1 phosphate, at pH of 6.0. An alternative wash buffer contained cold 1 mM GTP, 1 mM $MgCl_2$, 0.5 mg/ml BSA, 100 mM glucose 1 phosphate, 1 M glutamate, at a pH of 7.0. The latter conditions were tested with and without GTP/BSA. Another wash buffer tested was cold 10 mM phosphate, 10 mM $MgCl_2$ at pH 7.0 and the last wash buffer was cold 67 mM Na Phosphate, 100 mM KCl, pH 6.8. The wash buffer was tested extensively as this portion of the assay involved the washing the filters from any unbound radiolabeled colchicine, therefore any left in the filter erroneously would cause a false positive. The number of wash steps tested was an initial 1 ml after the reaction mixture was added to the filter, allowing this volume of gravity filter, followed by either 3 washes of 3 mls each or 6 washes of 3 mls. Determination of optimal number of wash steps was determined to be six individual times as any further washing did not seem to affect the results of the controls. The volume and number of wash steps was determined to be 6 washes of 3 mls. Different filters were tested including DEAE, GF/C, GF/A, GF/F.

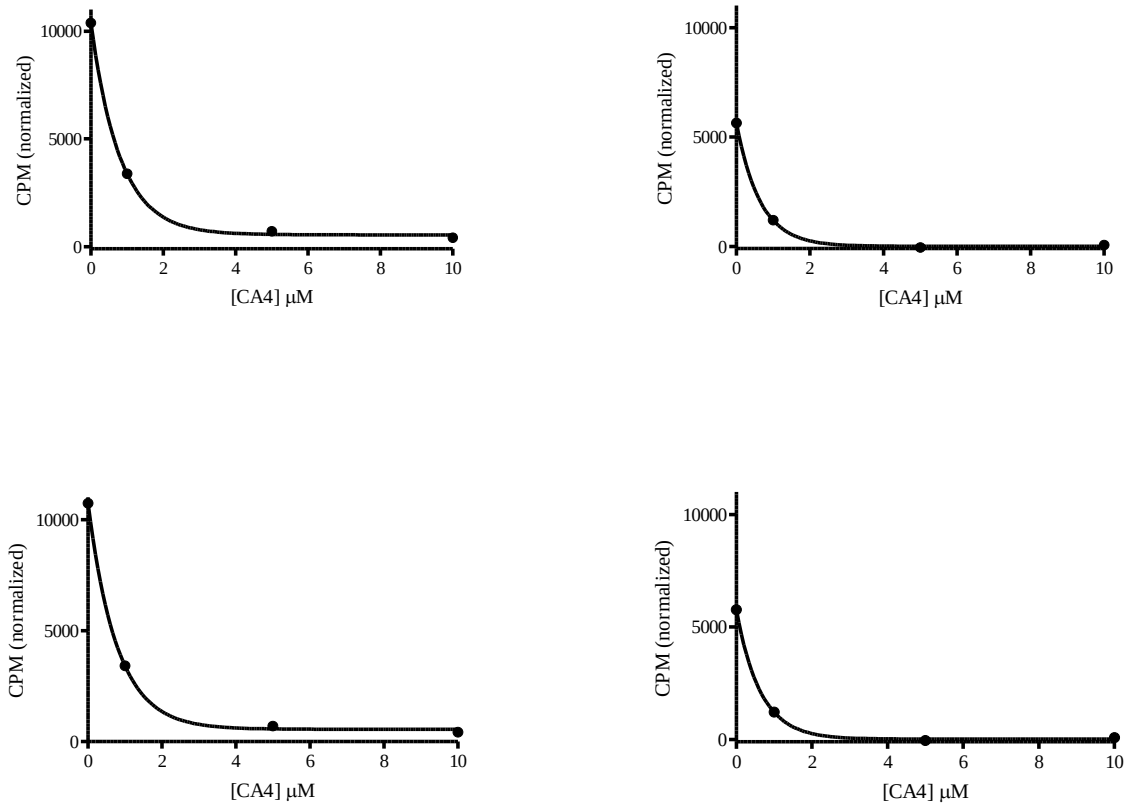

Figure 7.12 – Warm incubation optimization of CA4 for competitive binding assay; top left - binding at 48 hours, 60 minute warm incubation, top right – binding at 48 hours, 10 minute warm incubation, bottom left – binding at 72 hours, 60 minute warm incubation, bottom right – binding at 72 hours, 10 minute warm incubation

One to three filters were layered and suction of the vacuum apparatus was varied as one literature source suggested eliminating the vacuum during wash steps to allow the wash buffer to sit on the filters for a specified time before resuming suction. Samples were filtered based on the theory that the protein bound colchicine would remain trapped in the glass filter paper while the free colchicine and compound would be washed through, allowing for the measurement of signal by the filter paper to indicate the amount of radioactive material bound to tubulin. Filters were chosen based on testing of various filters used in the assay in literature. The majority of methods used a form of glass filters,

therefore GF/A and GF/F were chosen. GF/A filters provide a high flow rate and fine particle retention down to 1.6 µm and are recommended for radioimmunoassay of weak β-emitters. GF/F filters are also high efficiency filters, retaining down to 0.7 µm and is recommended filtration of difficult biochemical solutions. An example of the filter determination data is seen below where an optimal filter type would create reproducible data from the same samples. For the experiments performed with potential colchicine binding site compounds in this body of work, GF/A filters were chosen.

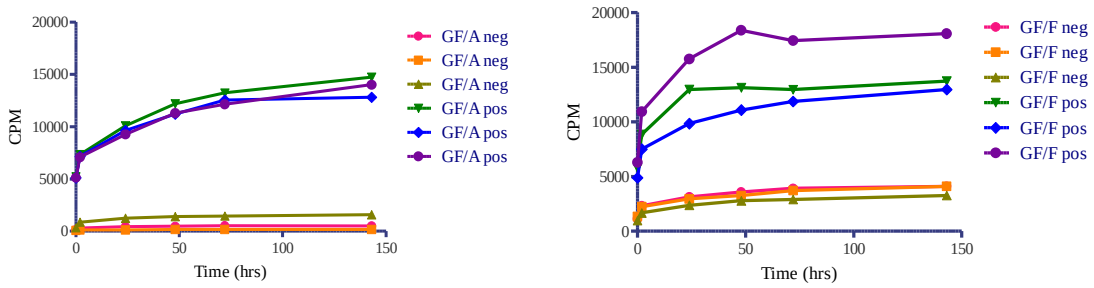

Figure 7.13 – Comparison of response (CPM) over time using GF/A (left) vs GF/A (right) filters

Next, the LSC response over time was observed. Once the filters were placed in the scintillation vials, scintillation fluid was added and the vials were inverted to homogenize the contents. The amount of time the filter needed to be in the scintillation vial with fluid was determined by taking readings with the LSC at the following times until a consistent reading was achieved: 10 minutes, 30 minutes, 240 minutes, 24 hours, 48 hours, 72 hours, 120 hours, 96 hours, 120 hours, 144 hours, and 216 hours. This time was to allow for the radiolabeled colchicine to dissociated from the filter and go into solution for detection. Samples were counted after 72 hours in the scintillation cocktail based on a time based study of positive controls (no inhibitor). The time point chosen

provided sufficiently reproducible data within a relative time frame of 72 hours. The final conditions for the optimized assay were a reaction mixture of 100 mM glucose-1-phosphate, 1 mM GTP, 1 M glutamate, 1 mM $MgCl_2$, 0.5 mg/ml BSA, 0.1 mg/ml tubulin, 2.5% DMSO, and 5 μM colchicine (~0.25 μCi/sample). The reaction timeline was 30 minutes on ice, 1 hour at 37ºC followed by 30 minutes on ice, filtering the sample on 3 GF/A filters. The wash buffer used was 10 mM sodium phosphate/10 mM $MgCl_2$ pH 7.0. The counts per minute (CPM) values obtained from the samples were then used to determine amount of colchicine bound at different concentrations of potentially interfering compound which in turn was utilized to construct IC_{50} plots.

Competitive Binding Assay – Compound Inhibition Results

Graphs of the individual results are seen in Figures 7.14-7.19 and a summary of the results of the compounds tested are seen in Table 7.4. An IC_{50} was determined for compound **7** for competitive binding with radiolabeled colchicines and was found to be 0.36 ±0.0074 μM. CA4 published in the literature which was known to bind to the colchicine binding site was used used for comparison.[60]

Table 7.4 – Inhibition of colchicine binding in radiometric analysis[60,200]

Compound	Inhibition of colchicine binding [compound] = 1 μM	Inhibition of colchicine binding [compound] = 5 μM
7	60%	92%
8	33%	30%
CA4	93%*	97%*
9	65%*	91%*
10	37%*	54%*
11	44%	89%

Table 7.5 (continued)

Compound	Inhibition of colchicine binding [compound] = 1 μM	Inhibition of colchicine binding [compound] = 5 μM
12	50%	80%
17	0%	10%
18	0%	0%
19	15%	27%
20	25%	56%
21	18%	29%

*For additional information see ref [60]

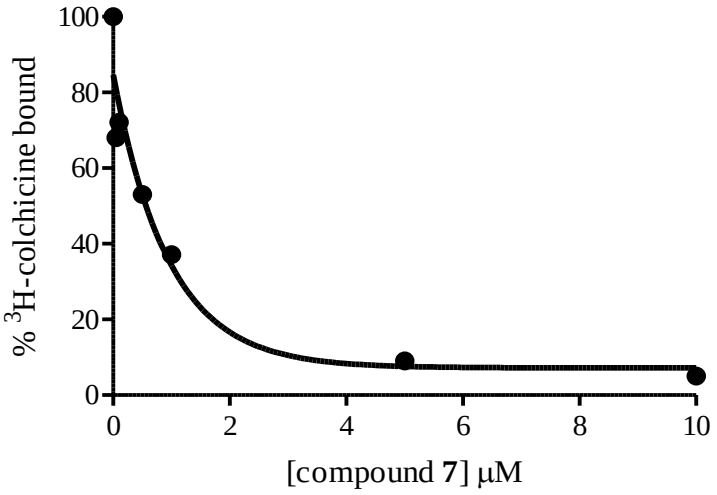

Figure 7.14 – Inhibition of ^{3}H-colchicine binding to tubulin by compound **7**

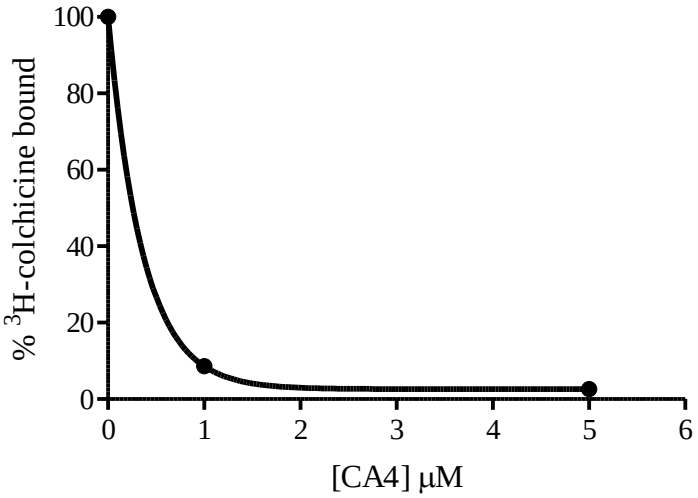

Figure 7.15 – Inhibition of ^{3}H-colchicine binding to tubulin by CA4

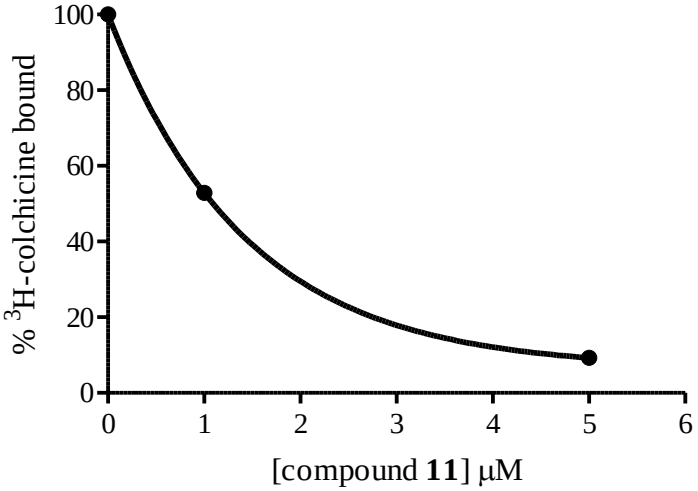

Figure 7.16 – Inhibition of ^{3}H-colchicine binding to tubulin by compound **11**

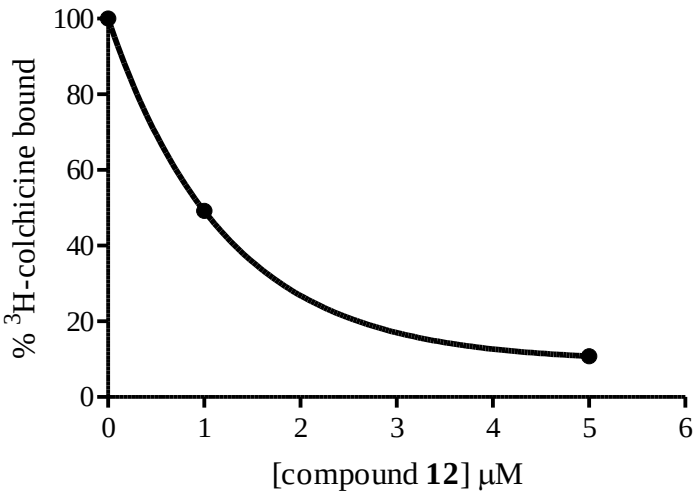

Figure 7.17 – Inhibition of ^{3}H-colchicine binding to tubulin by compound **12**

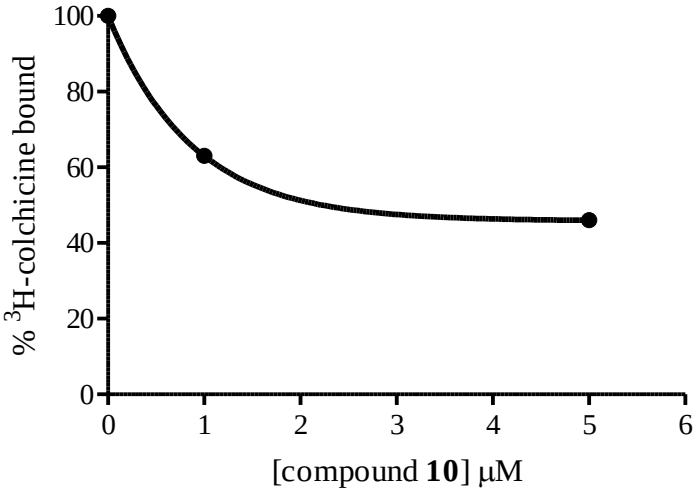

Figure 7.18 – Inhibition of ^{3}H-colchicine binding to tubulin by compound **10**

Among the benzosuberene compounds, compound **7** and compound **9** (the amino analog) displayed excellent binding to the colchicine binding site of tubulin with approximately 92% and 91% (respectively) inhibition of radiolabeled colchicine bound.

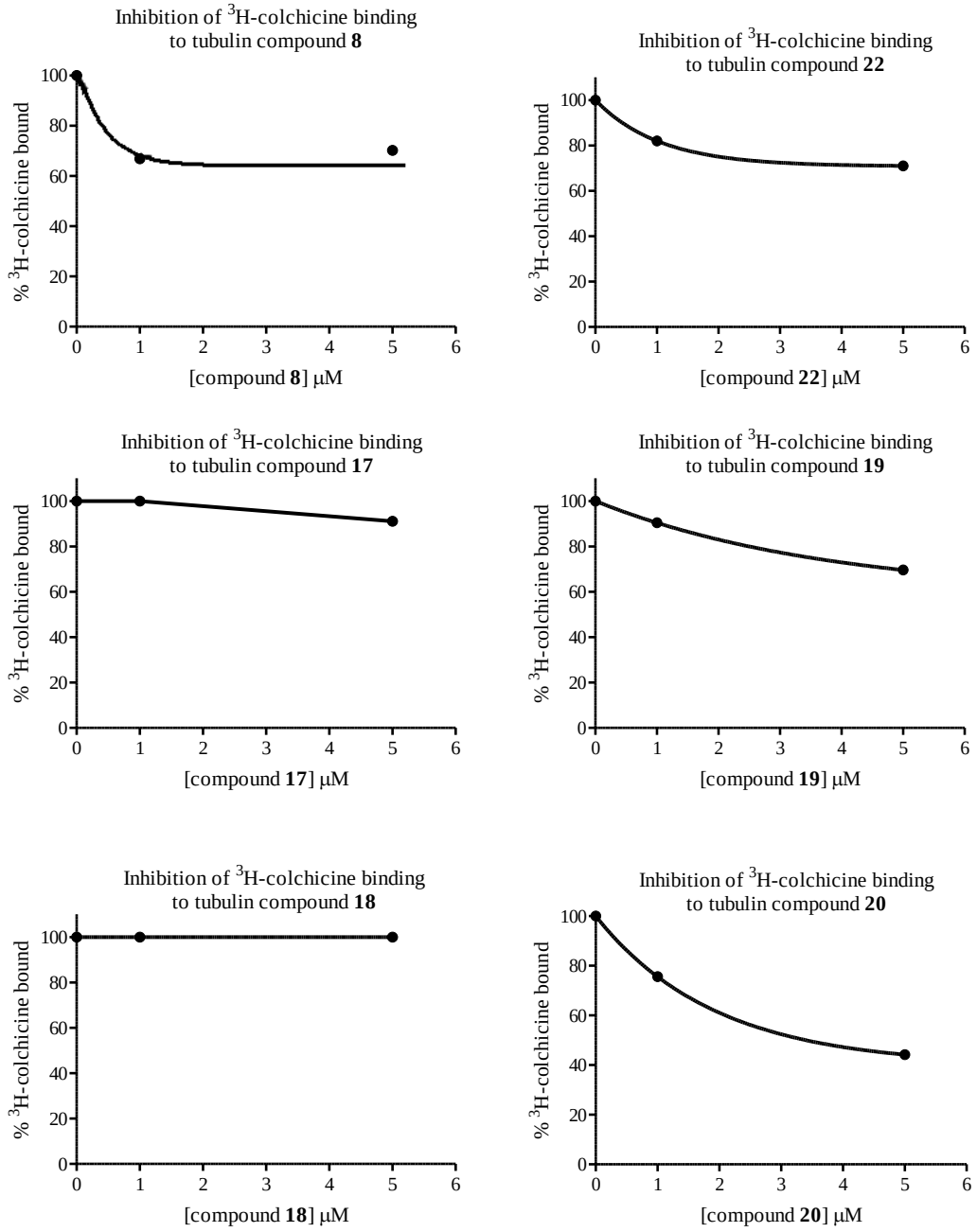

Figure 7.19 – Effects of select benzosuberene analogues on ^{3}H-colchicine binding to tubulin with moderate to low efficacy

Compound **11** and compound **12**, the fluoro- and chloro- analogs, respectively, were almost as effective in binding to the colchicine binding site with 89 and 80% inhibition of

the ^{3}H-colchicine, respectivley. Approximately 50-60% inhibition of binding was seen for compound **20** and compound **10**, the reduced benzylidene analog and the nitro analog, respectively. Compound **21**, compound **17**, and **19** demonstrated approximately 30% inhibition. Lastly, compound **18** did not bind to the colchicine binding site in the given time period, therefore no inhibition is seen.

Flow Cytometry Analysis of the Effects of Benzosuberene Analogues on the Cell Line MDA-MB-231

Tubulin binding vascular disrupting agents affect microtubule dynamics and thus can inhibit formation of the mitotic spindle and thereby mitosis in which the mitotic spindle forms as the cells begin to divide into daughter cells. Therefore effective tubulin binding VDAs can result in blockade cell cycle in the G2/M phase.[57] This result is readily characterized by flow cytometry in which the labeled cells are measured through a fluidically focused stream detected by various lasers. To determine the effect of the compounds on the cell cycle of MDA-MB-231 breast cancer cells, flow cytometry was performed utilizing propidium iodide to stain DNA content of the cells. Propidium iodide (PI) binds DNA in a stoichiometric ratio of 1:1, therefore the DNA content is directly proportional to PI fluorescence. Cells that are further in their cell cycle will essentially have more DNA and therefore a greater fluorescence response. Increase in the area under the curve at various PI intensities (amount of DNA) was calculated and % events of the total 10,000 cell events were determined for each cell cycle phase. MDA-MB-231 cells are aneuploid, meaning that there are an abnormal number of chromosomes present and the peak indicating this variation is seen on the far right of the flow spectra as there is more DNA present. Aneuploidy is often a definitive marker of tumor presence.[201]Table

7.5 is the effective concentration on cell cycle arrest in the G2/M phase. The effective concentration indicates the concentration (in μM) at which the cells shift from the majority being in the G1 phase to the G2/M phase. Structures for compounds found in Table 7.5 can be seen in Table 7.2. The majority of the cells in the vehicle control are in

Table 7.6 – Flow cytometry analysis of cell cycle

Compound	Effective concentration on cell cycle arrest in G2/M phase (MDA-MB-231)
7	0.1-0.01 μM
8	0.1-0.01 μM
CA4	0.005-0.001 μM
CA4P	0.1-0.01 μM
11	0.1-0.01 μM
12	0.5-0.1 μM
13	0.5-0.1 μM
14	0.05-0.01 μM
15	0.005-0.001 μM
16	0.01-0.005 μM

the G1 phase, ranging from 50-70% and upon treatment with an effective inhibitor, a shift is seen essentially blockading the cells in G2/M. Select compounds were tested but due to degradation of a few of the compounds, the testing was inconclusive and therefore results were not reported, most notably compound **9** and compound **10**. Histograms are seen in

Figure 7.20 where the y-axis is the counts (cell events) and the x-axis is the response of the FL2-H laser, being DNA content. Histograms were analyzed and % events in the specified regions was plotted in Graphpad 5.0 allowing for an additional visualization of the effective concentration trend of the compounds. An example of a histogram with peaks labeled is seen in Figure 7.20. In this histogram there are four distinct peaks which.

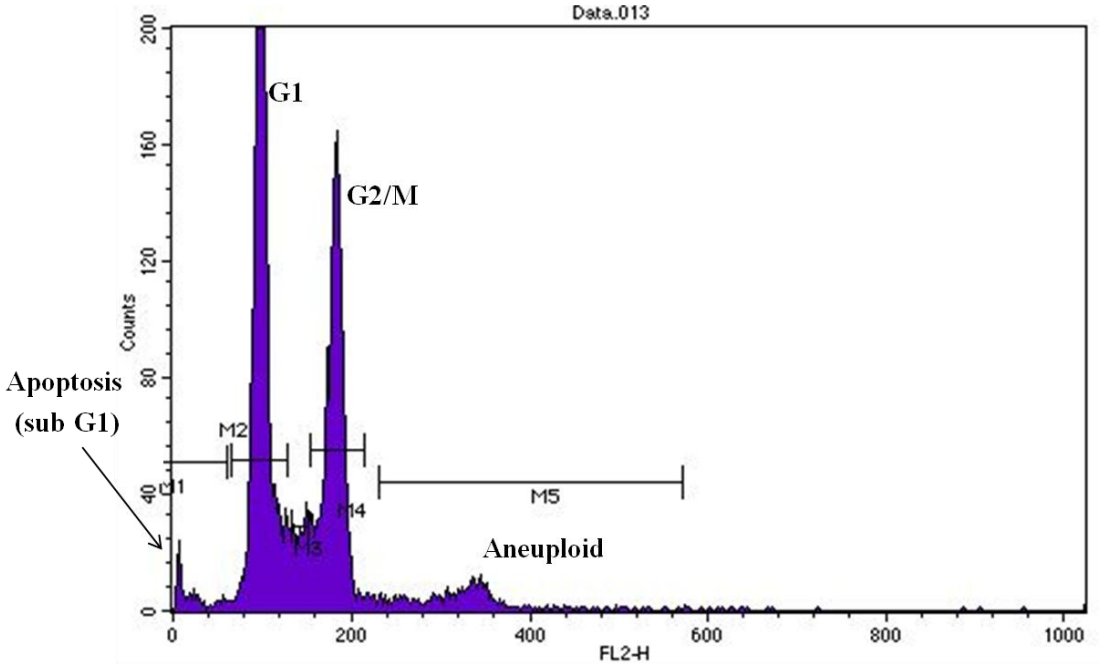

Figure 7.20 – Example of flow histogram with peaks labeled

are labeled In the subsequent tables, the peaks are not labeled as G1 or G2/M, for example, but can be identified by their position along the x-axis. The sub G1 or apoptotic peak is represented by the first gated portion of the graph, ranging from zero to approximately 70 on the FL2H axis, and indicates the portion of the cell sample undergoing apoptosis. The lack of an increasing apoptotic peak with increasing compound concentration suggests that the cells are being blocked later in their cell cycle, reducing the possibility of the drug killing the cells as its primary mode of action in this

case. The G1 peak is the next peak and represents the cells in a “resting state” of cell cycle. The G2/M peak is approximately twice that of the G1 peak as there is an increase in DNA as the mitotic spindle is formed and cells prepare for division. The aneuploid peak is the small peak directly to the right of the G2/M peak and as mentioned previously, is characteristic of this cancerous cell line. Photos were also taken of the cells plated on the 6-well cell culture plates before harvesting for flow and these are seen in Figure 7.21 which follows:

A - Control

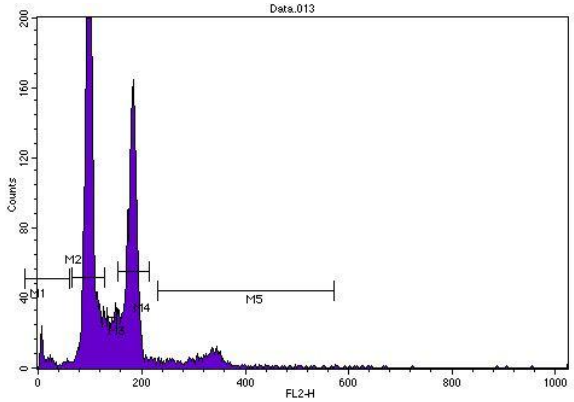

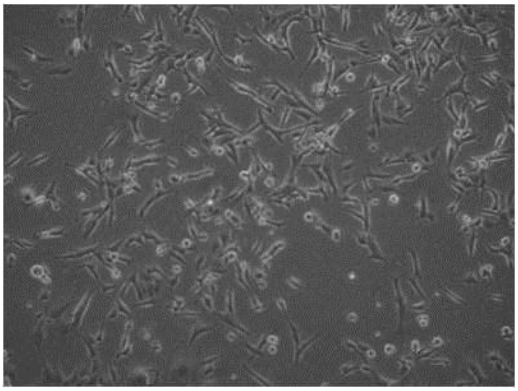

B – 1.0 µM compound **7**

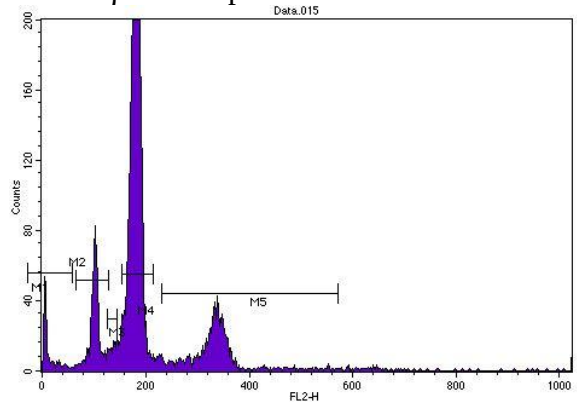

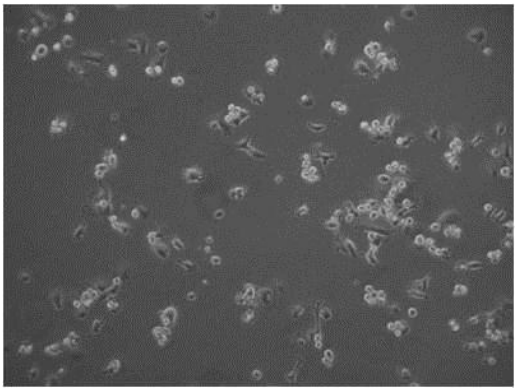

C – 0.5 µM compound **7** Figure 7.21 continues

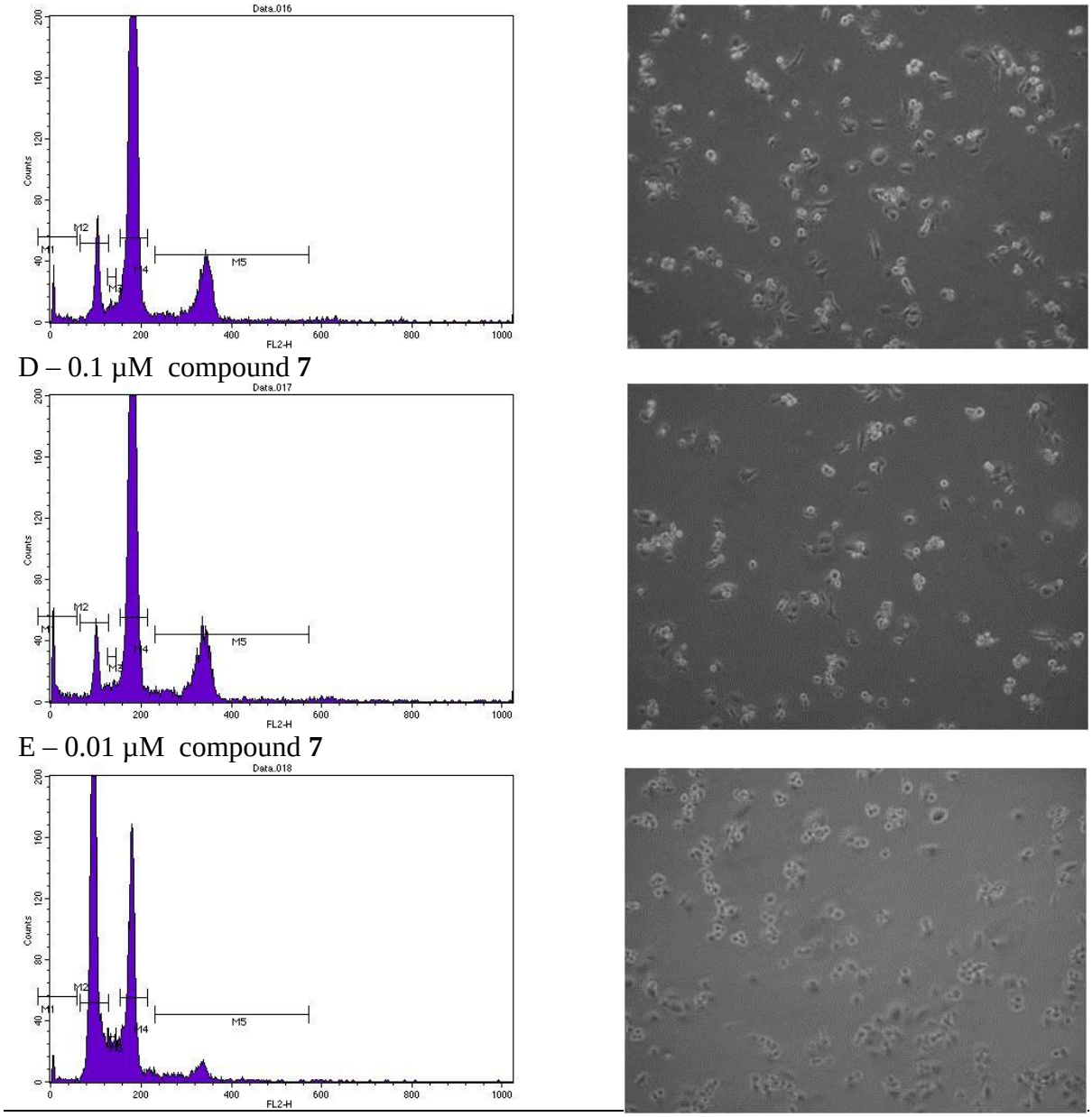

D – 0.1 µM compound **7**

E – 0.01 µM compound **7**

Figure 7.21 - Compound 7 treated MDA-MB-231 cells analyzed by flow cytometry; histograms on left, cells before harvesting on right (20x).

Photos obtained by the microscope on 20x magnification were utilized to provide evidence of a qualitative phenotypic trend among the MDA-MB-231 cells after treatment with the compounds. In many cases, significant rounding up of the cells (in comparison to the controls) was not seen at the higher end of the effective concentration; rounding up

was often observed at the lower concentration also. Figure 7.21 and Figure 7.22 are for the flow cytometry analysis of compound **7**. The effective concentration for this

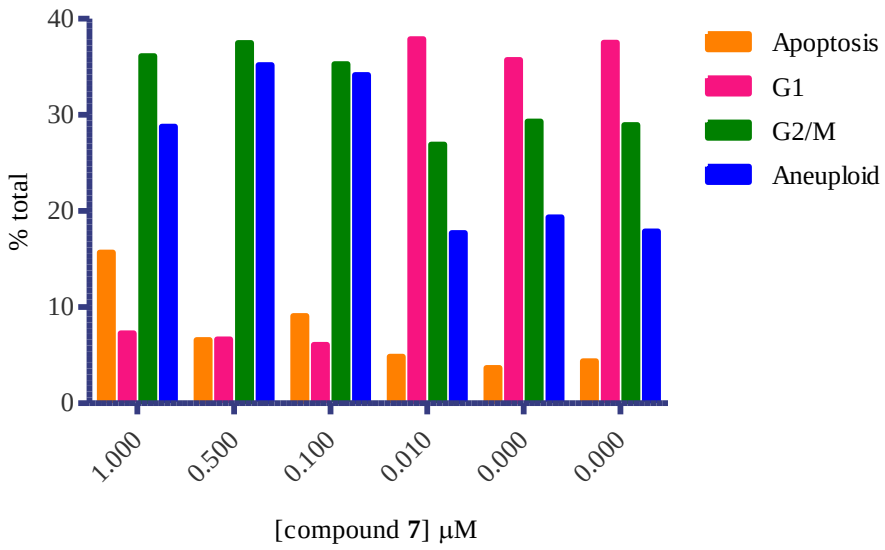

Figure 7.22 – Compound **7** treatment summary of effect on MDA-MB-231 cell cycle arrest after 48 hour treatment

compound is between 0.1-0.01 µM for a 48 hour treatment. Significant rounding up of cells is seen within the effective concentration range. This indicated that blockade in the G2/M cycle does not necessarily correlate completely with a phenotypic rounding up effect of the cells within this cell line. Cells treated with high concentrations of compound **7** appeared to have an increase in apoptosis and aneulpoid when compared to decreasing concentrations and controls. Cell rounding is a characterisitic feature of endothelial cells treated with the VDA CA4 and cell rounding was also observed for benzosuberene treated MDA-MB-231 treated cells. The disodium salt of the phosphate benzosuberene was equally as active as its parent compound and caused rounding up at a different time point.With compound **8**, rounding up was seen at the high concentrations, 1.0-0.5 µM, but at concentrations near the effective concentration of the compound, 0.1-

0.01 µM, the effect was not seen. In cells treated with compound **8**, the cells appeared significantly less rounded up, displaying an attached morphology observed in figure 7.23 below:

A - Control

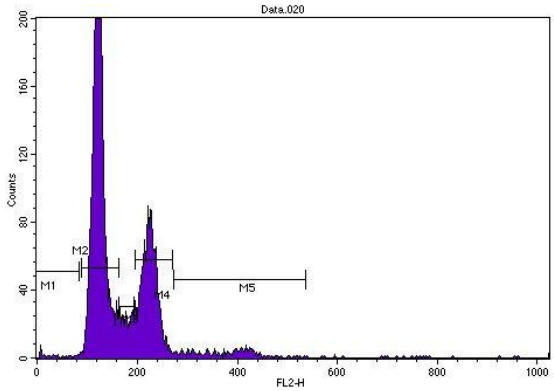

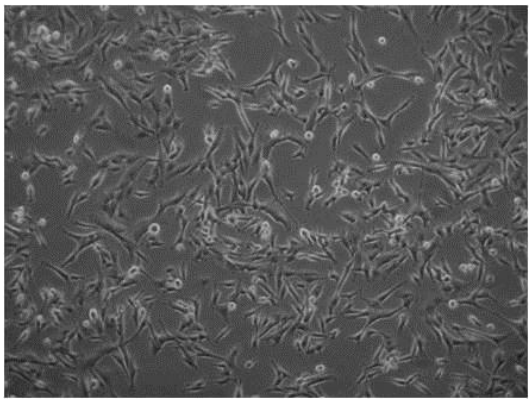

B – 1.0 µM compound **8**

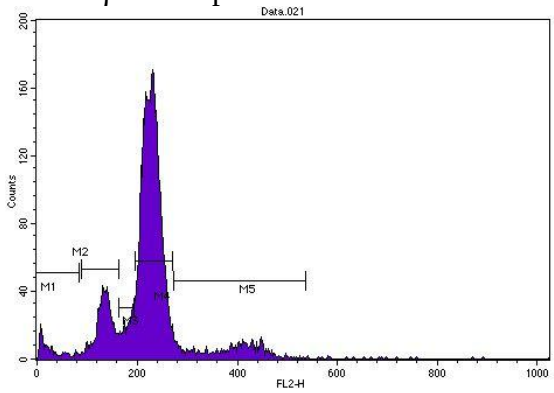

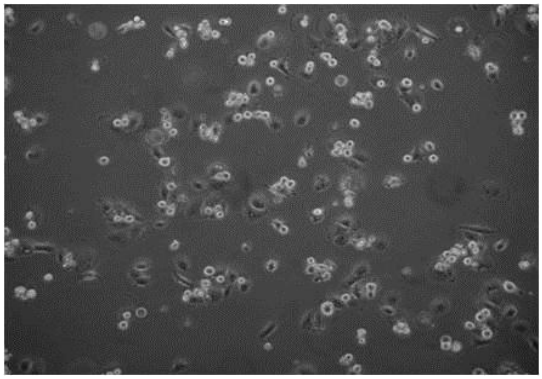

C – 0.5 µM compound **8**

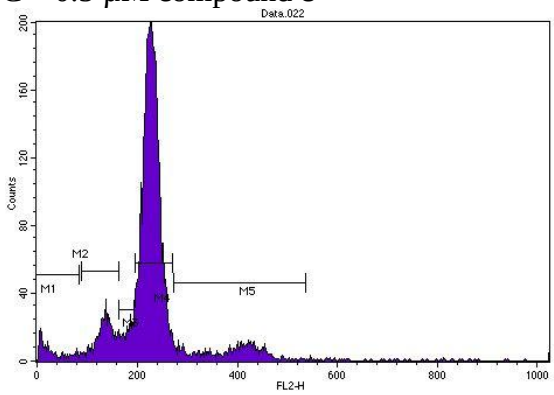

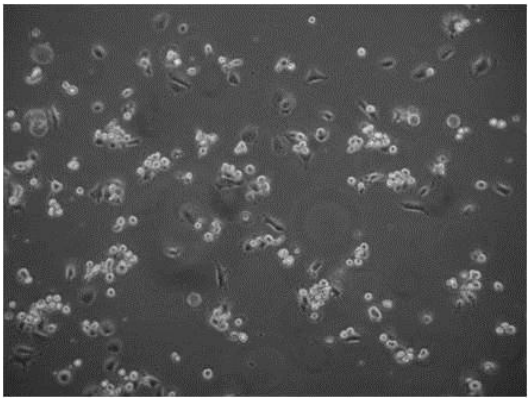

D – 0.1 µM compound **8**

Figure 7.23 continues

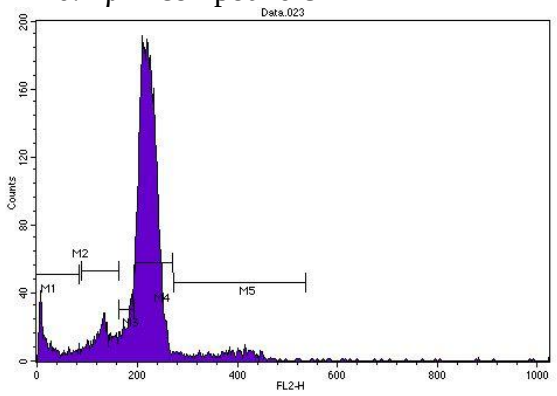

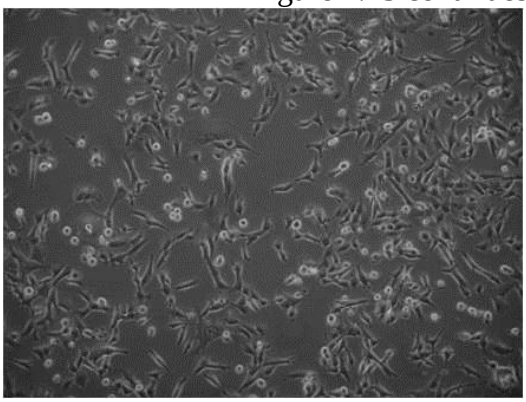

E – 0.01 µM compound **8**

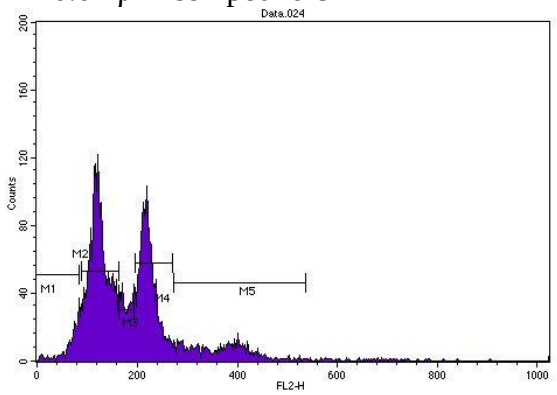

Figure 7.23 - Compound **8** treated MDA-MB-231 cells analyzed by flow cytometry; histograms on left, cells before harvesting on right (20x)

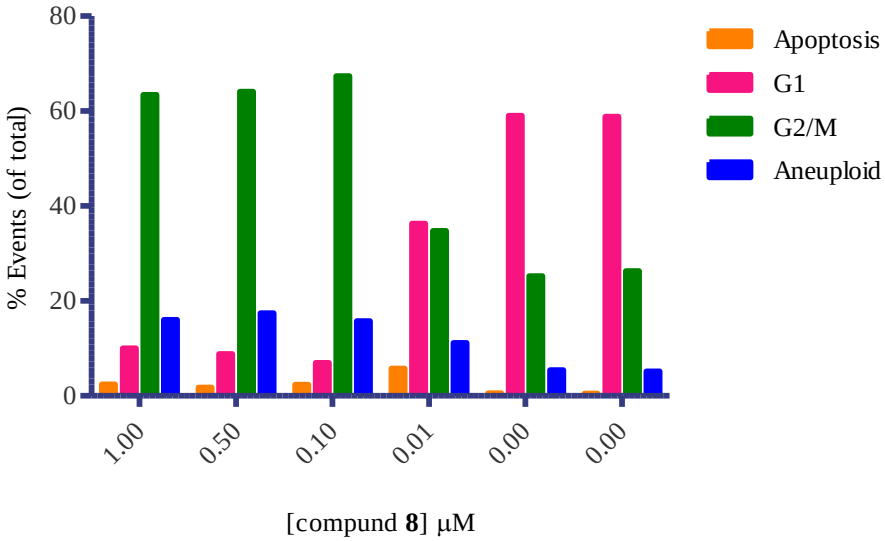

Figure 7.24 – Compound **8** treatment summary of effect on MDA-MB-231 cell cycle arrest after 48 hour treatment

There is no significant difference in apoptosis for the concentration range and the effect on the aneuploid fraction is not similar to the trend seen in compound **7** as little change is seen with respect to concentration of compound. This indicates a different mechanism of action from compound **7**.

Cells treated with combretastatinA4 exhibited rounding up within an effective concentration range of 0.005-0.001 µM. Treatment with the phosphate salt, CA4P, also induces rounding up but at the low end of the effective concentration range, 0.01 µM, the cells appear to be spread out and not in the process of rounding. There does not appear to be significant change in apoptosis for both combretastatin compounds and in the case of CA4P, the aneuploidy fraction is increased in the treated cells when compared to the controls. CombretastatinA4 treated MDA-MB-231 cells are seen in Figure 7.25 below:

A –Control

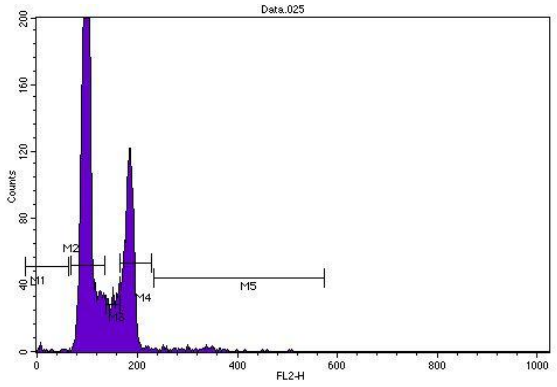

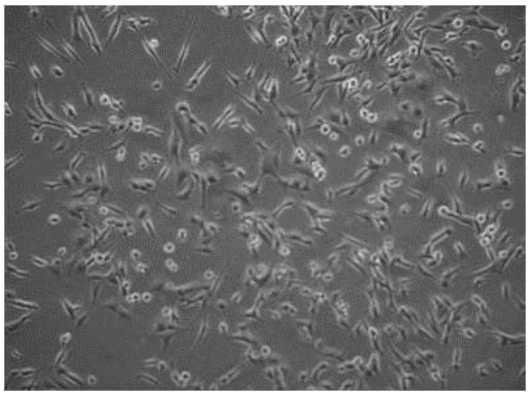

B – 0.01 µM CA4

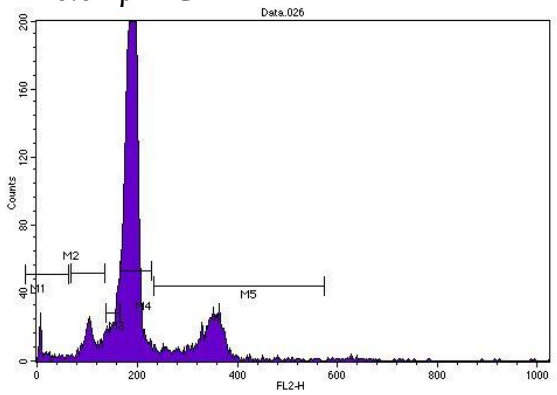

C - 0.005 µM CA4

Figure 7.25 continues

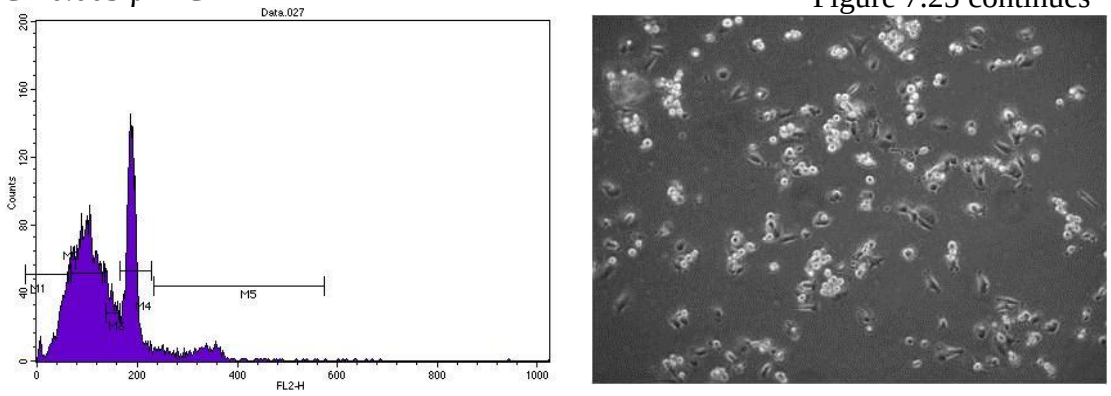

D - 0.001 µM CA4

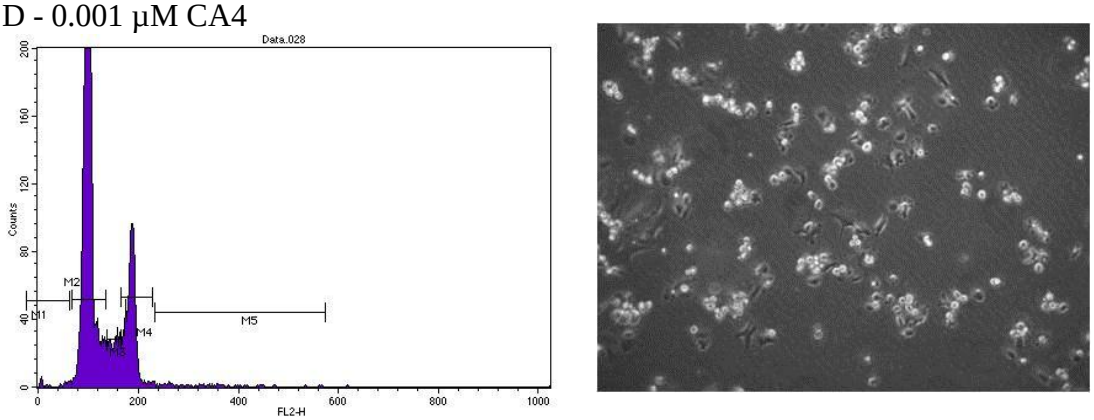

E - 0.0005 µM CA4

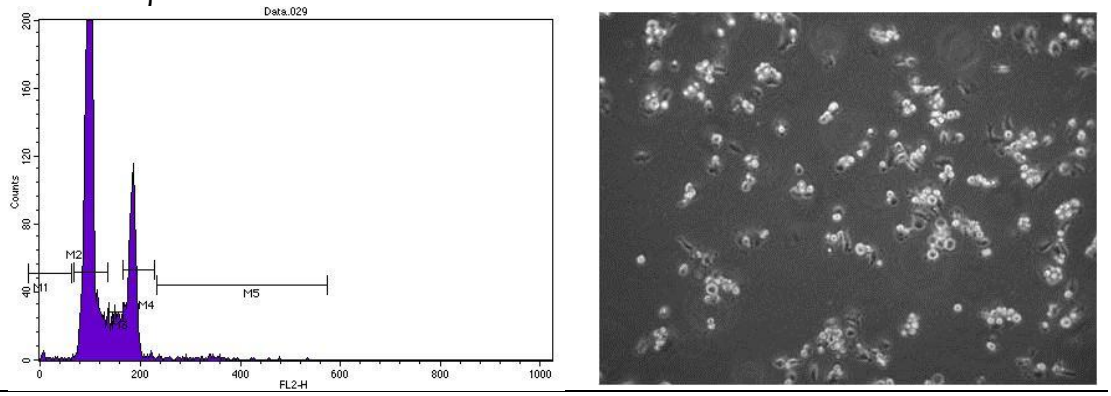

Figure 7.25 – CA4 treated MDA-MB-231 cells analyzed by flow cytometry; histograms on left, cells before harvesting on right (20x)

In samples treated with compound **11**, the chloro analogue, cell rounding was observed below the effective concentrations as is seen in Figure 7.29. The cell pictures indicated cell rounding at 0.1 and 0.01 µM treated samples. For the fluoro analogue, less rounding up occurred within the effective concentration range, Table 7.31. The effective

concentration for compound **12** is between 0.5 and 0.1 µM and cell rounding is observed at 0.5µM but not at 0.1 µM. Aneuploid fractions appear to increase with increasing concentration of both compounds, beginning the increase at the effective concentration of the compound.

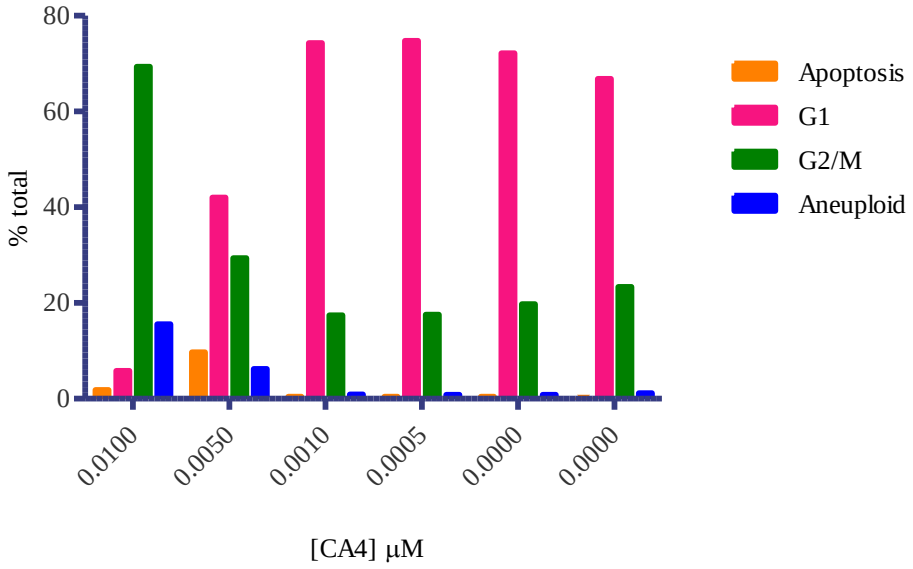

Figure 7.26 – CA4 treatment summary of effect on MDA-MB-231 cell cycle arrest after 48 hour treatment

A - Control

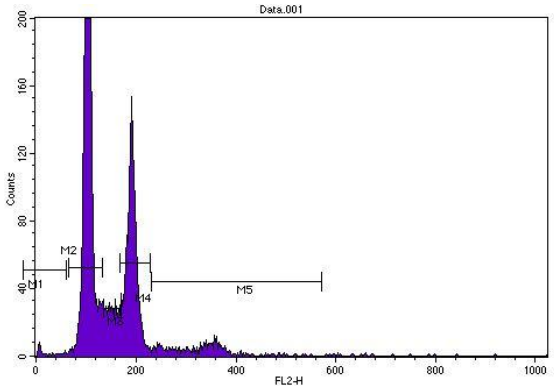

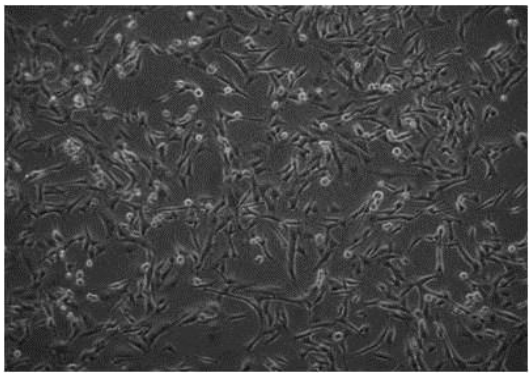

B – 1.0 µM CA4P

Figure 7.27 continues

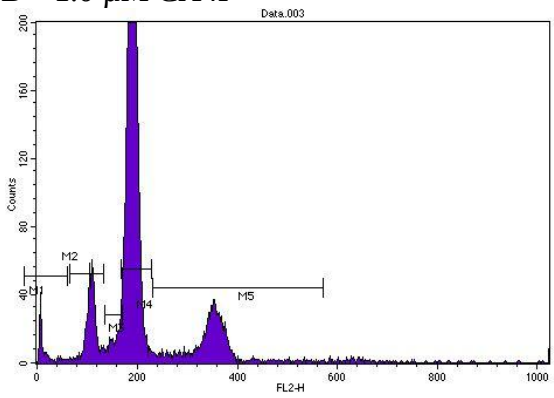

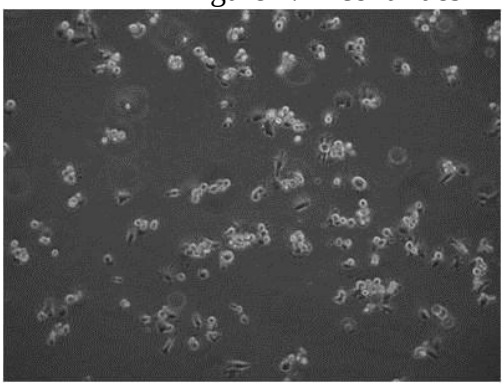

C – 0.5 µM CA4P

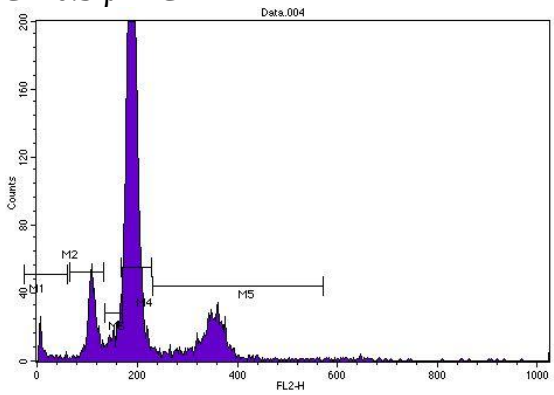

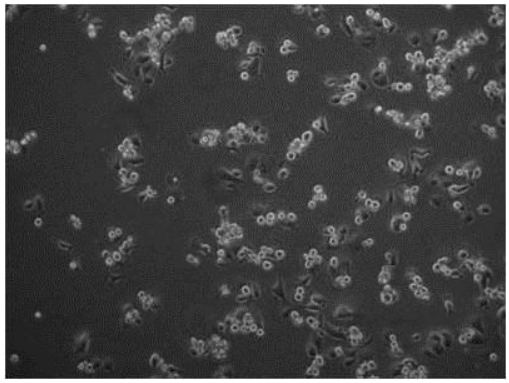

D – 0.1 µM CA4P

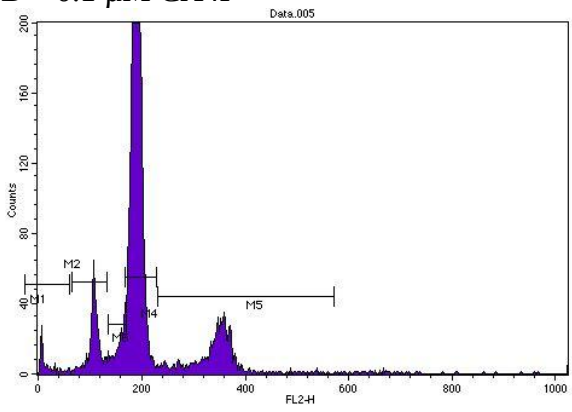

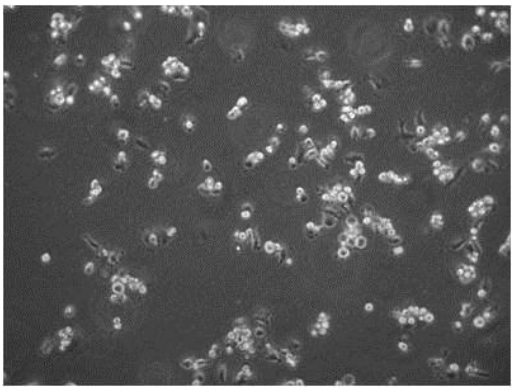

E – 0.01 µM CA4P

Figure 7.27 continues

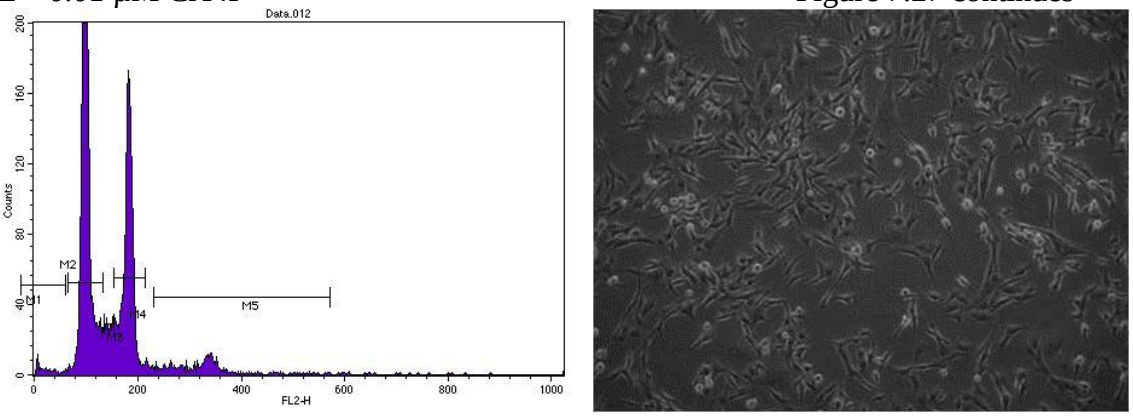

Figure 7.27 - CAP treated MDA-MB-231 cells analyzed by flow cytometry; histograms on left, cells before harvesting on right (20x)

.

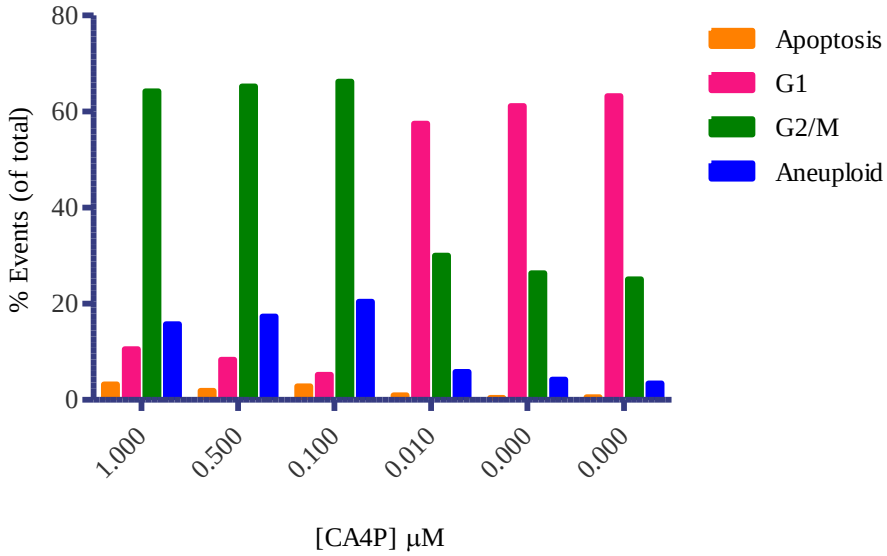

Figure 7.28 – CA4P treatment summary of effect on MDA-MB-231 cell cycle arrest after 48 hour treatment

A - Control

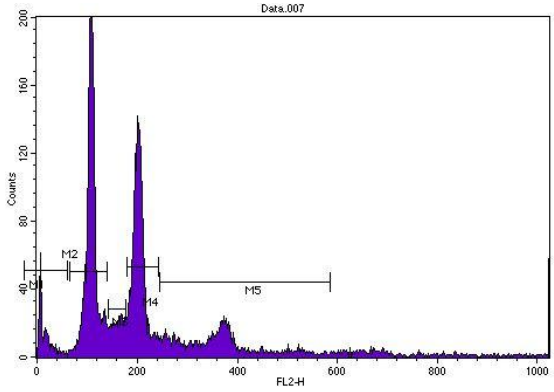

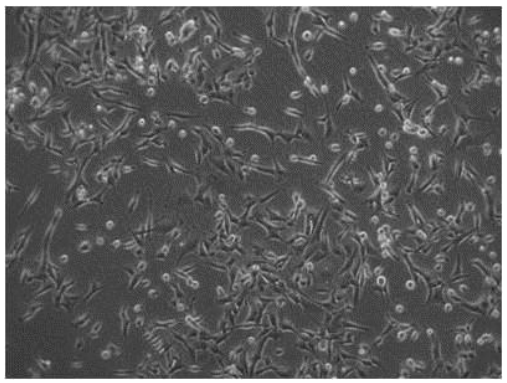

B – 1.0 µM compound **11**

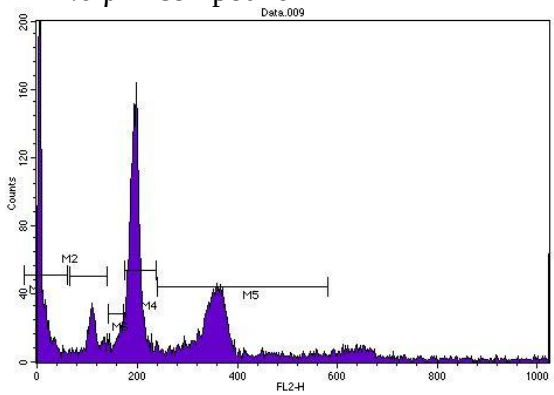

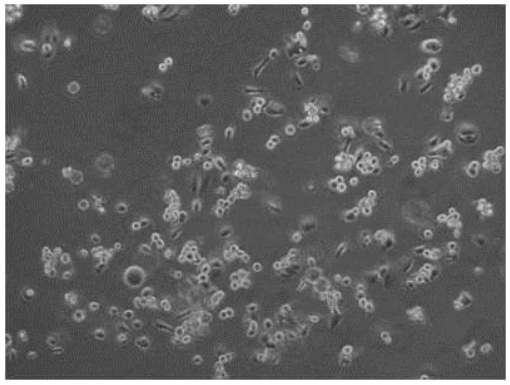

C – 0.5 µM compound **11**

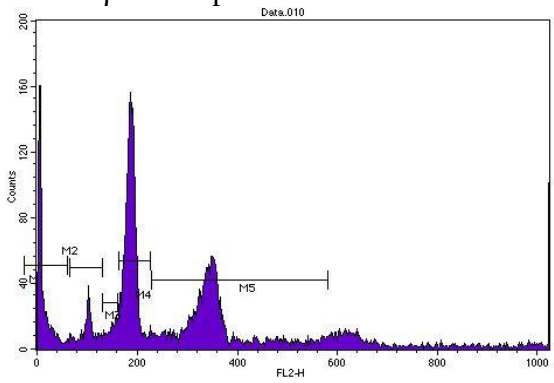

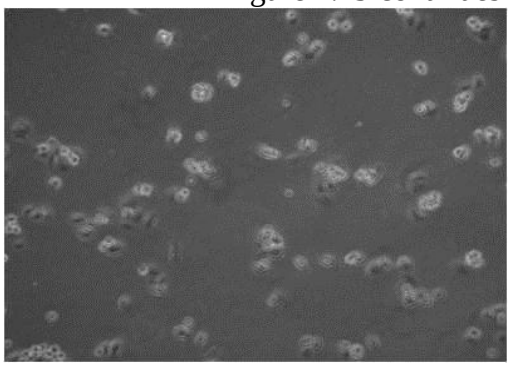

Figure 7.29 continues

D – 0.1 µM compound **11**

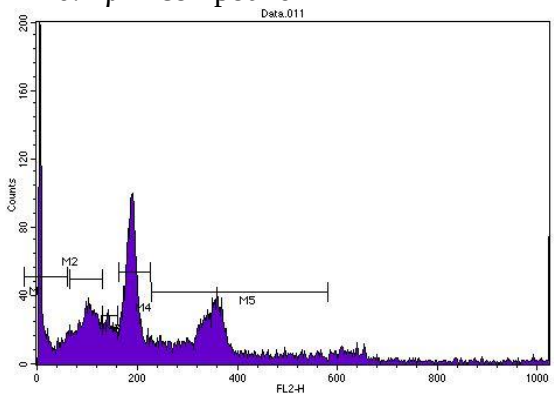

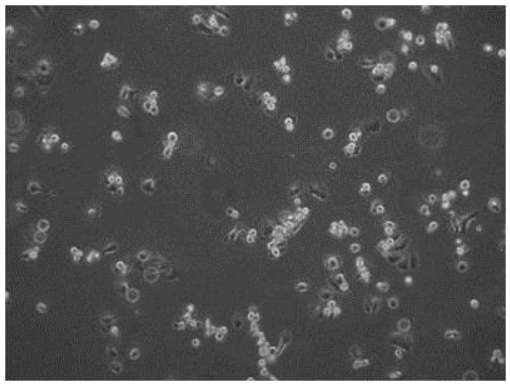

E – 0.01 µM compound **11**

Figure 7.29 continues

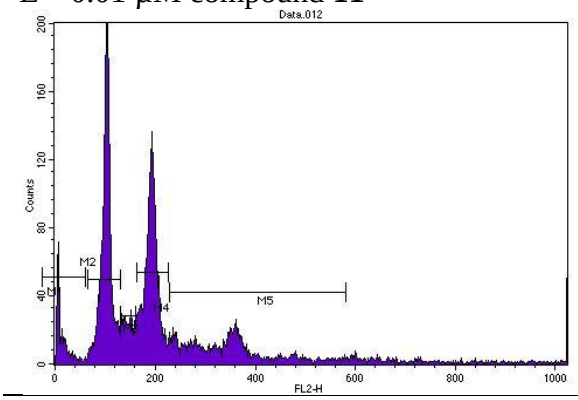

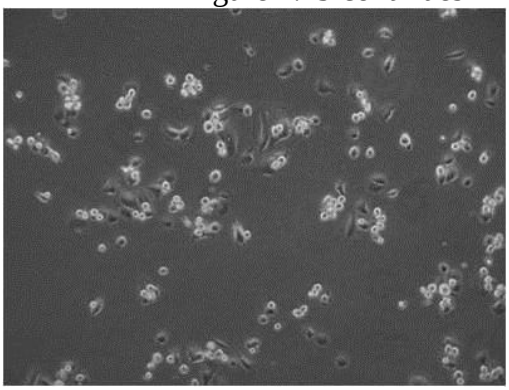

Figure 7.29 - Compound **11** treated MDA-MB-231 cells analyzed by flow cytometry; histograms on left, cells before harvesting on right (20x)

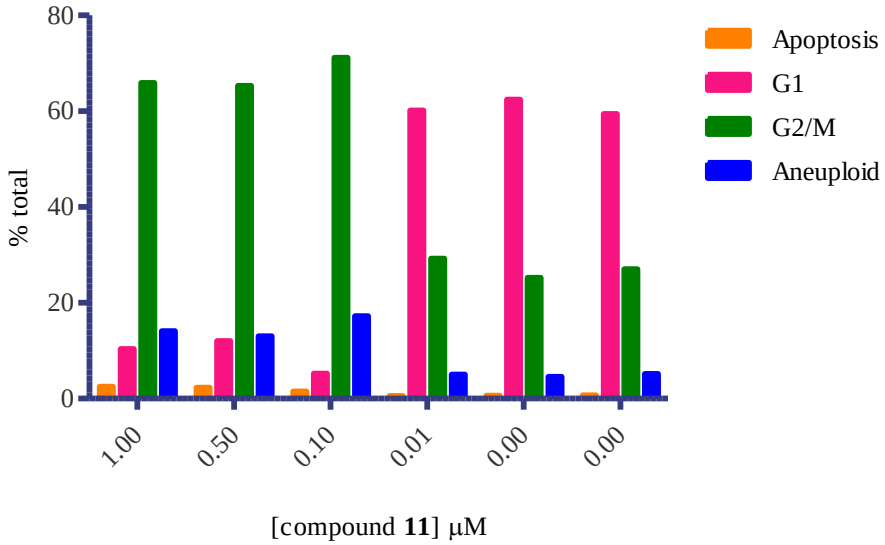

Figure 7.30 – Compound **11** treatment summary of effect on MDA-MB-231 cell cycle arrest after 48 hour treatment

A - Control

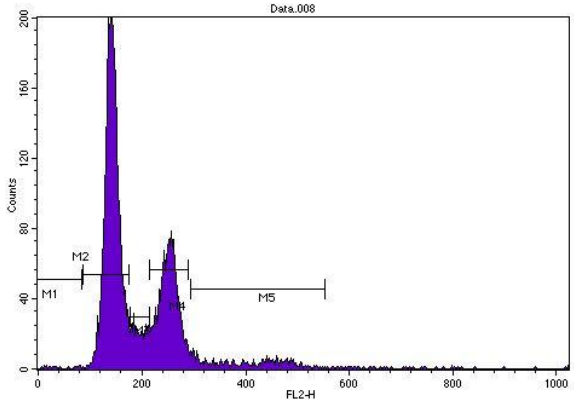

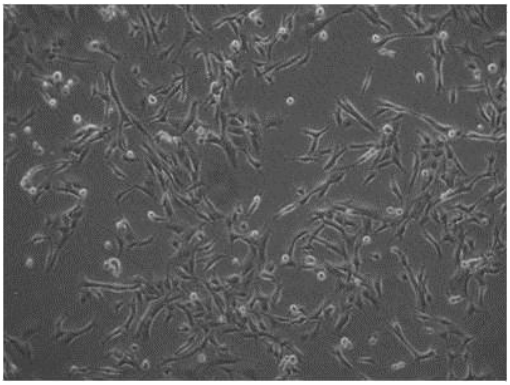

B – 1.0 µM compound **12**

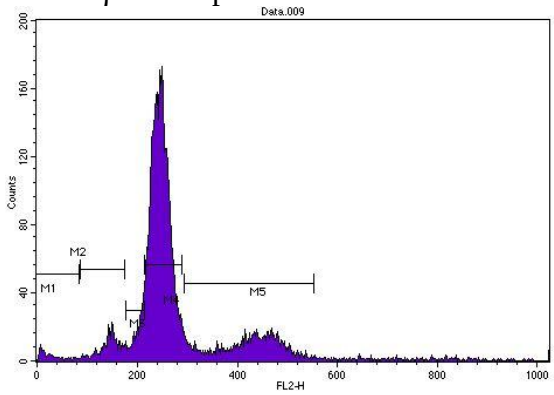

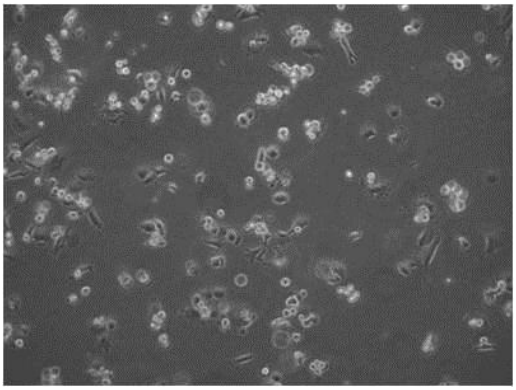

C – 0.5 µM compound **12**

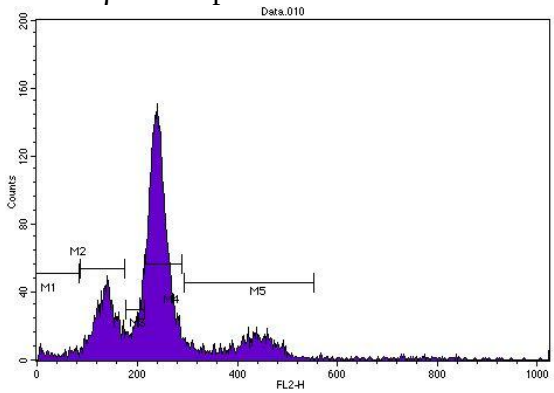

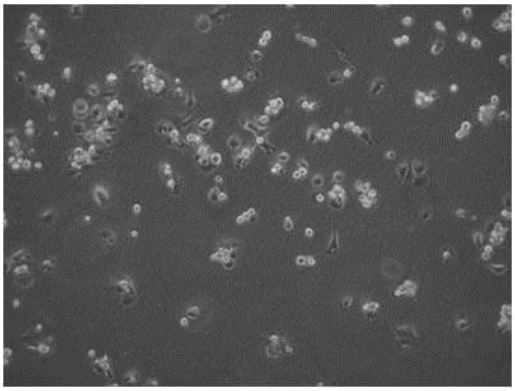

D – 0.1 µM compound **12**

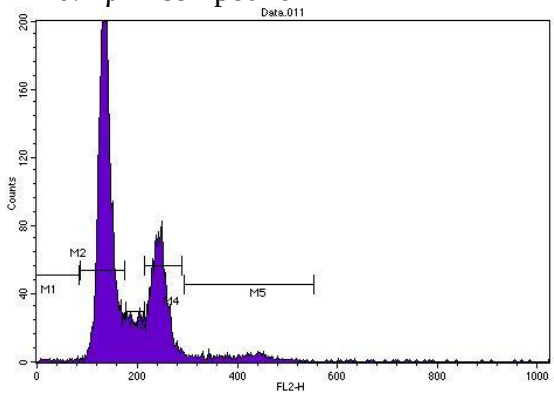

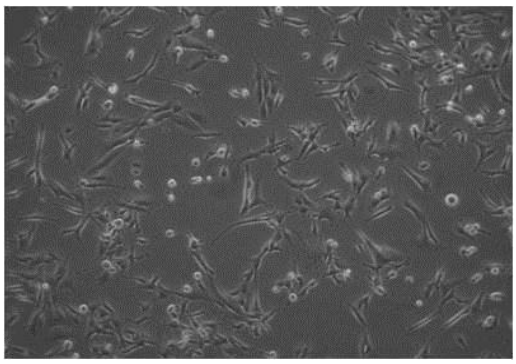

E – 0.01 µM compound **12**

Figure 7.31 continues

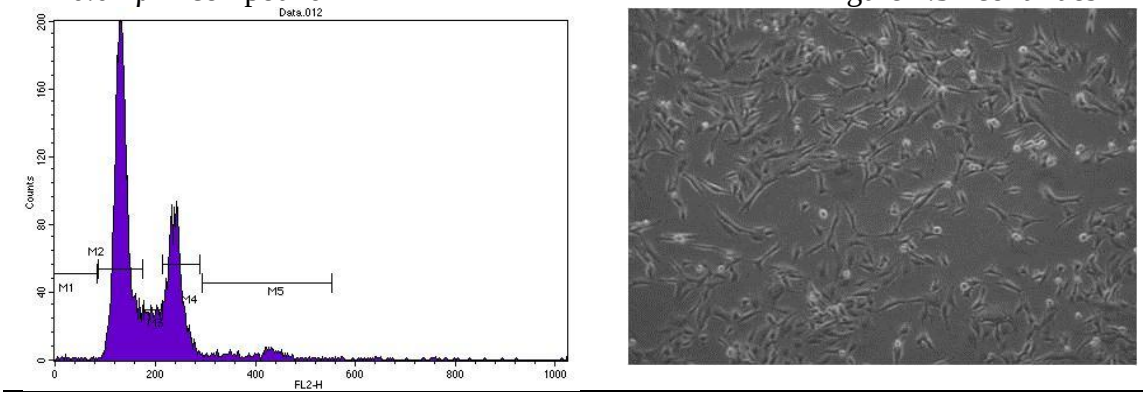

Figure 7.31 - Compound **12** treated MDA-MB-231 cells analyzed by flow cytometry; histograms on left, cells before harvesting on right (20x)

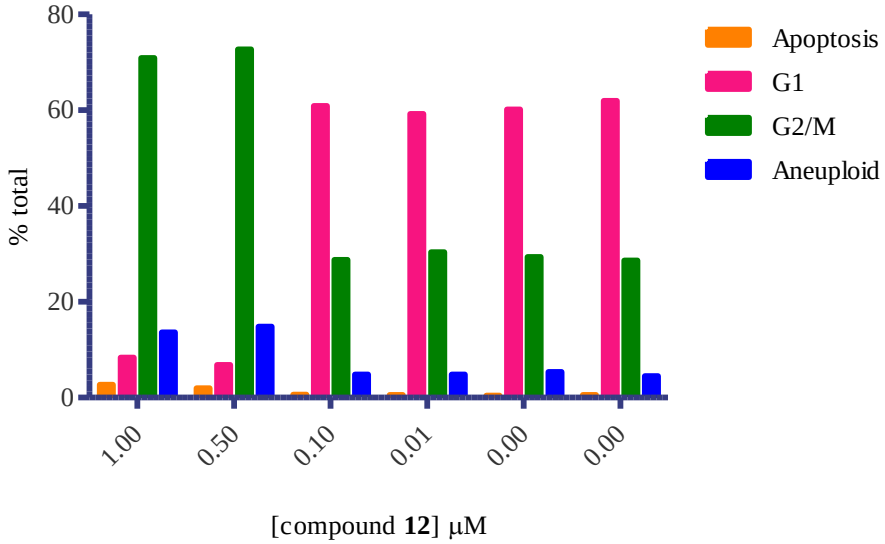

Figure 7.32 – Compound **12** treatment summary of effect on MDA-MB-231 cell cycle arrest after 48 hour treatment

Compound **9** and compound **10**, the nitro and amino analogues, were analyzed but gave inconsistent results. For compound **13**, cells remained attached at concentrations less than 0.1 µM and began to round up at 0.1 µM, completely rounding up by 0.5 µM. The fraction of cells in aneuploid phase increased with increasing concentration of compound. For compound **14**, the rounding up correlated with the effective concentration

and no significant difference was seen in apoptosis and aneuploid phase with increasing compound concentration, bar graph not shown.

A - Control

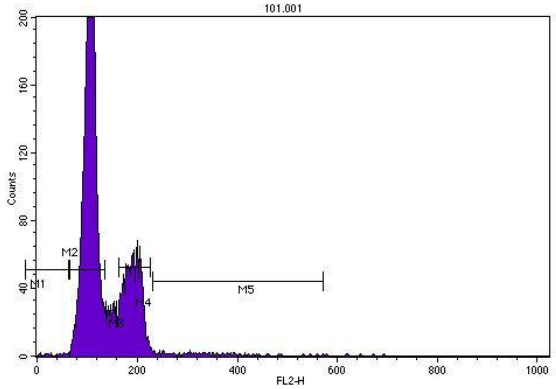

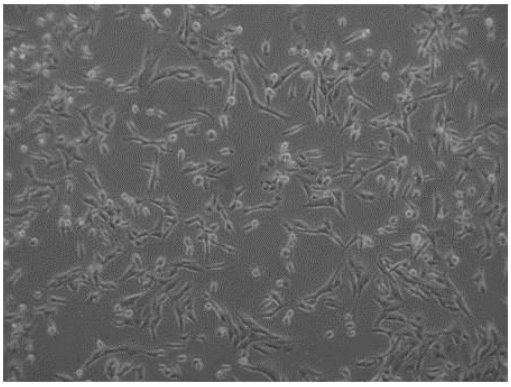

B - 0.5 µM compound **13**

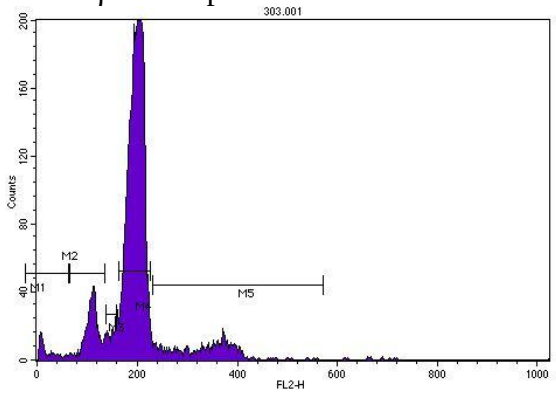

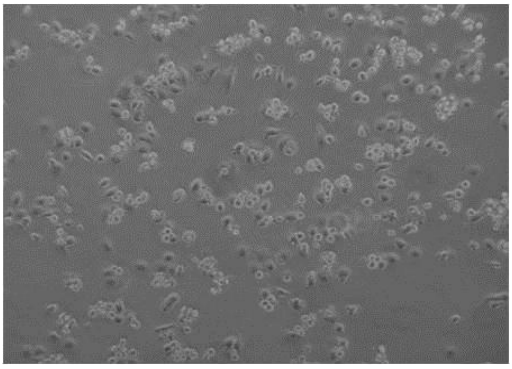

C - 0.1 µM compound **13**

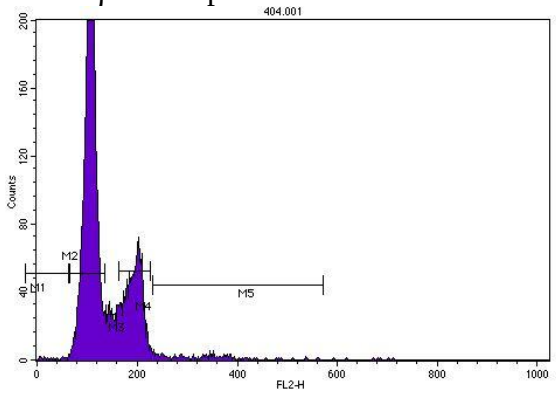

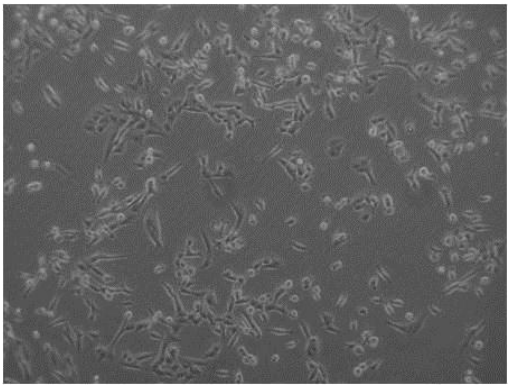

D - 0.01 µM compound **13**

Figure 7.33 continues

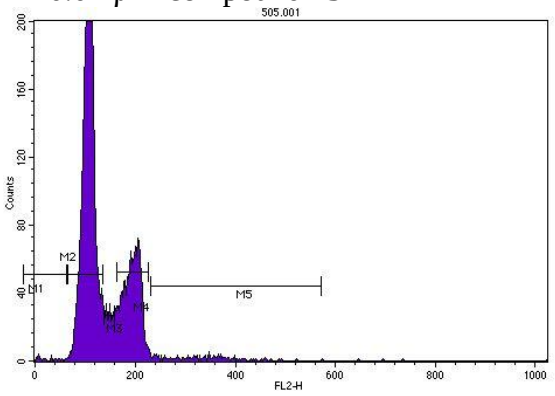

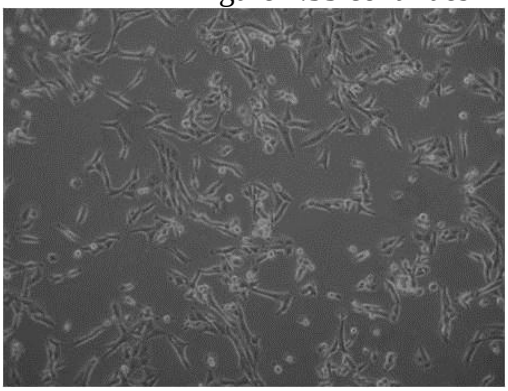

E - 0.001 µM compound **13**

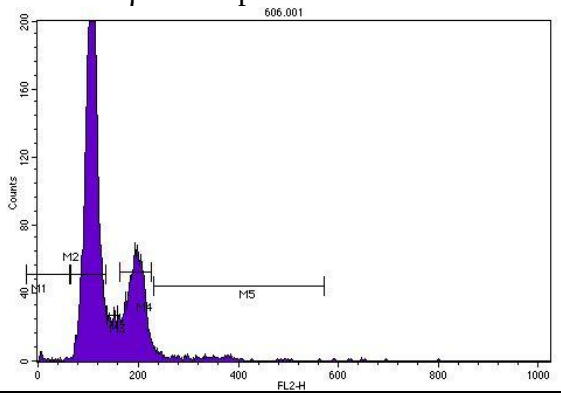

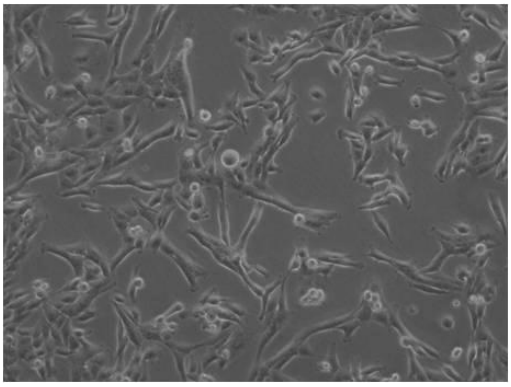

Figure 7.33 - Compound **13** treated MDA-MB-231 cells analyzed by flow cytometry; histograms on left, cells before harvesting on right (20x)

.

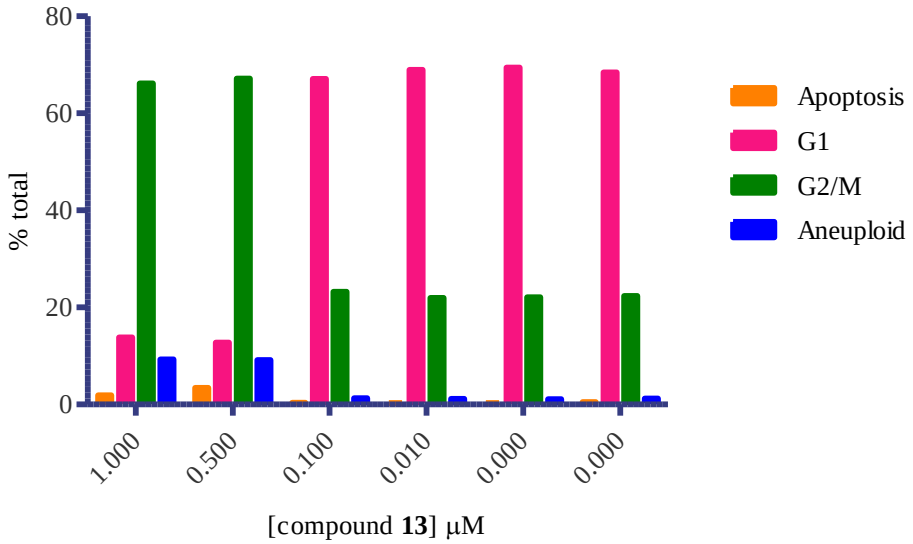

Figure 7.34 – Compound **13** treatment summary of effect on MDA-MB-231 cell cycle arrest after 48 hour treatment

A - Control

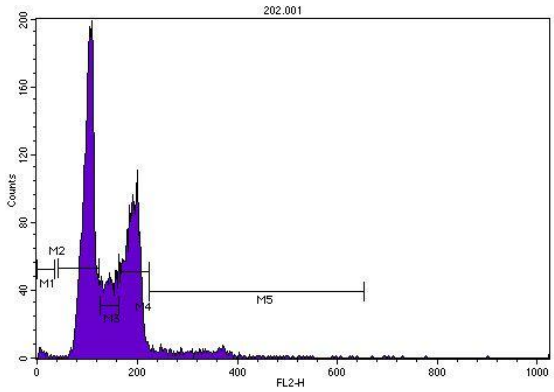

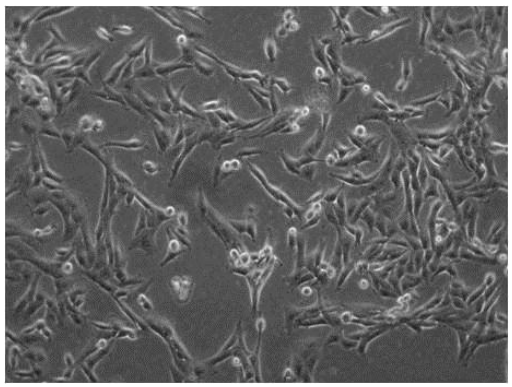

B – 0.1 µM compound **14**

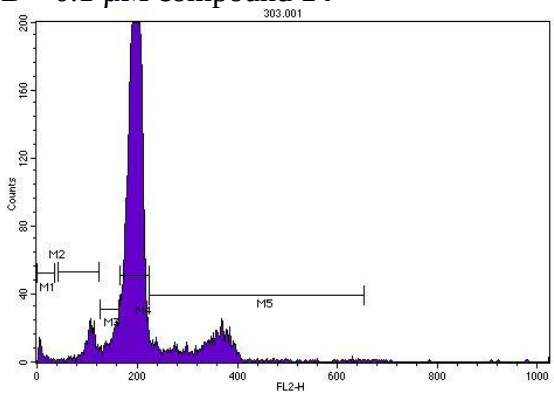

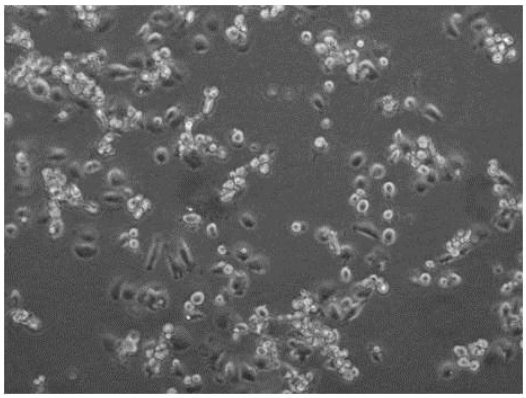

C – 0.05 µM compound **14**

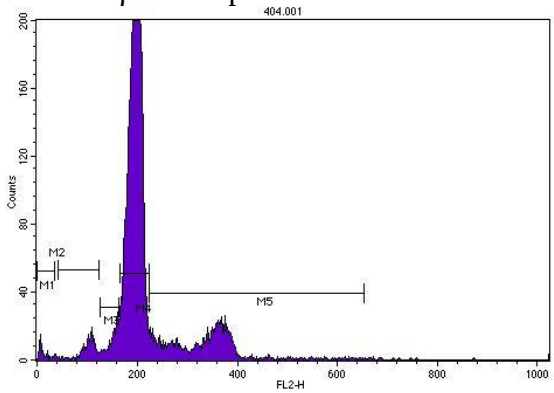

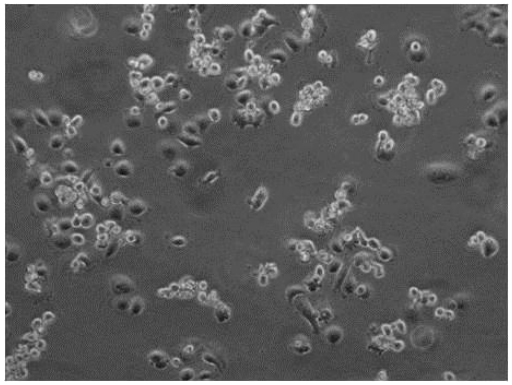

D – 0.01 µM compound **14**

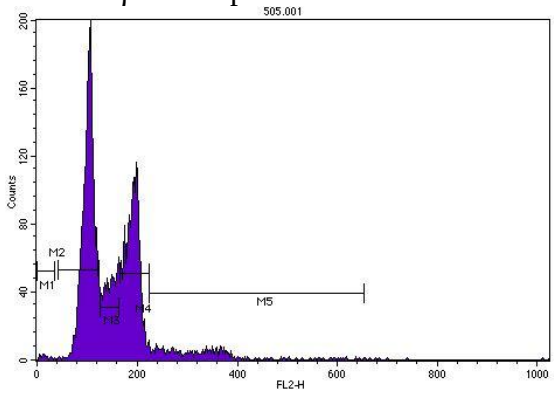

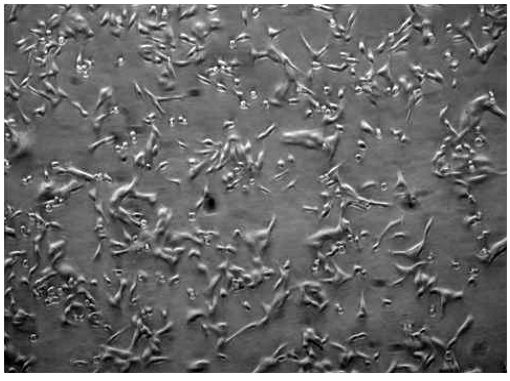

E – 0.005 µM compound **14** Figure 7.35 continues

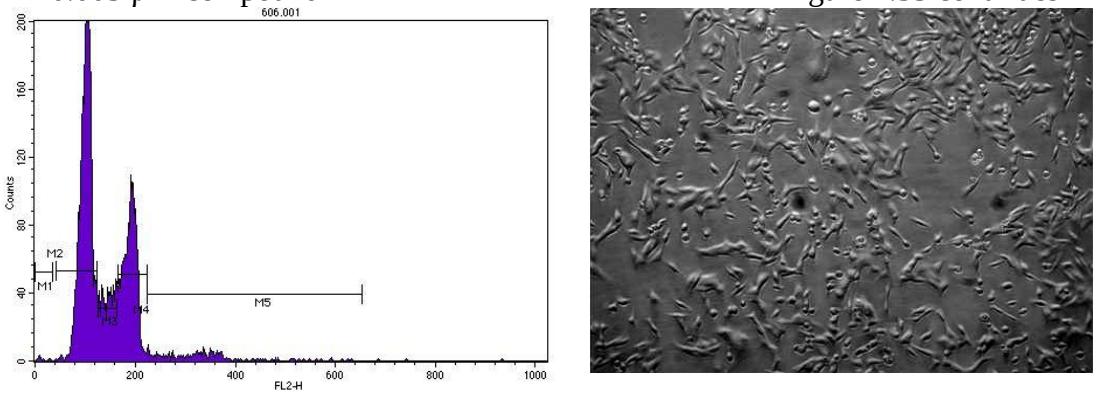

Figure 7.35 - Compound **14** treated MDA-MB-231 cells analyzed by flow cytometry; histograms on left, cells before harvesting on right (20x)

Compound **15** and compound **16** were determined to have effective concentrations of 0.005-0.001 µM and 0.01-0.005 µM but for both compounds, rounding up was still visible at 0.001 µM and 0.005 µM for each treatment, compound **15** and compound **16** respectively. This indicated that blockade in the G2/M cycle does not necessarily correlate completely with cell rounding within this cell line. The percent cells in the anueploid phase followed a similar trend as when treated with other compounds, increasing in proportion to increasing compound treatment concentrations.

A Control

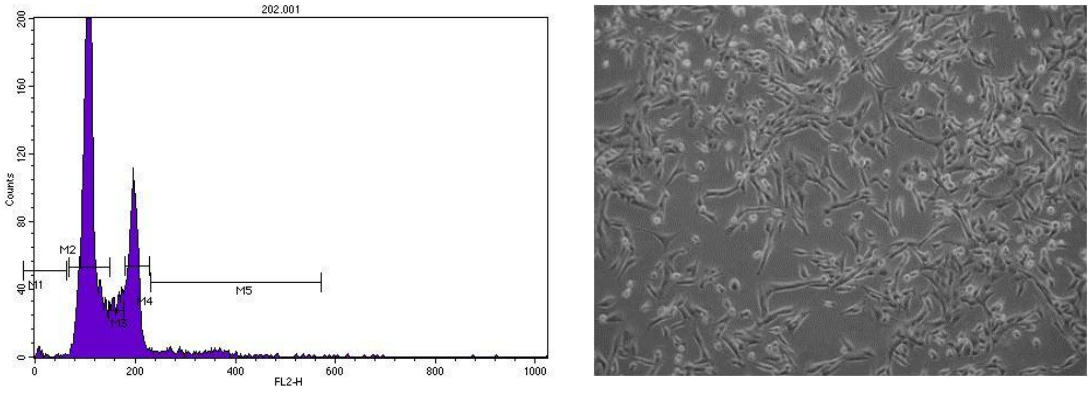

B - 0.01 µM compound **15**

Figure 7.36 continues

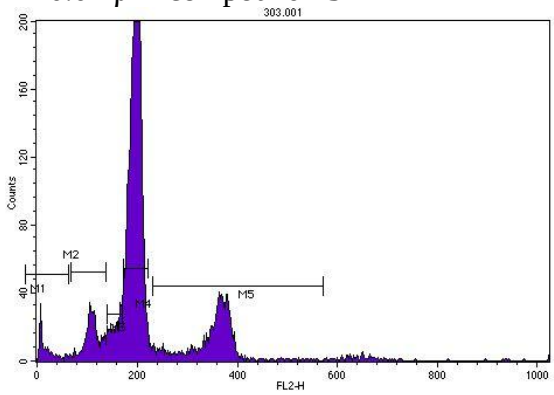

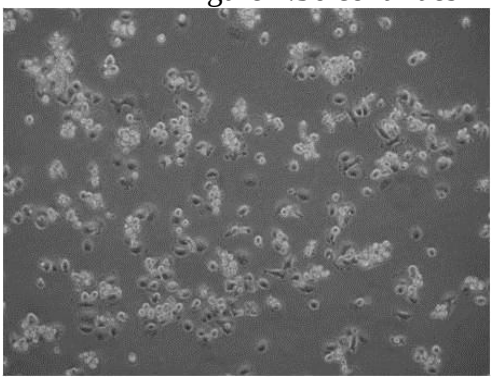

C - 0.005 µM compound 15

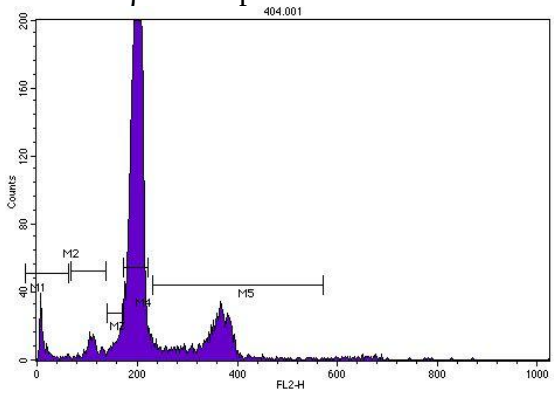

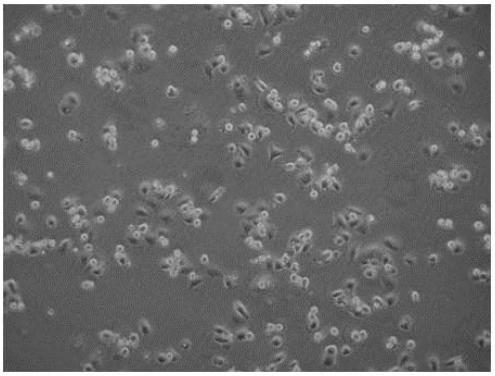

D - 0.001 µM compound 15

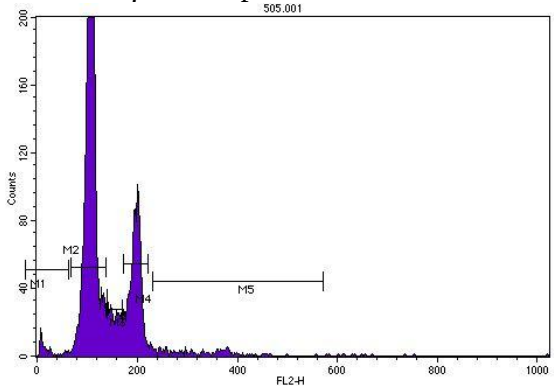

E - 0.0005 µM compound 15 Figure 7.36 continues

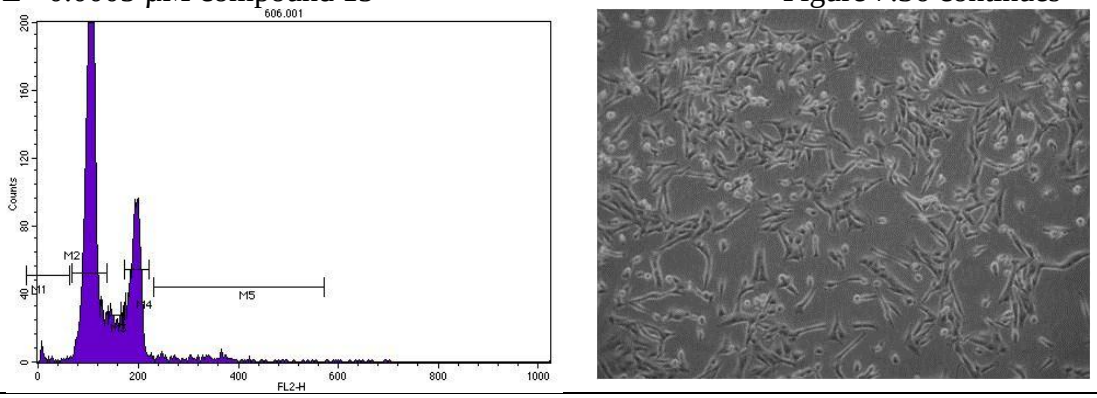

Figure 7.36 - Compound **15** treated MDA-MB-231 cells analyzed by flow cytometry; histograms on left, cells before harvesting on right (20x)

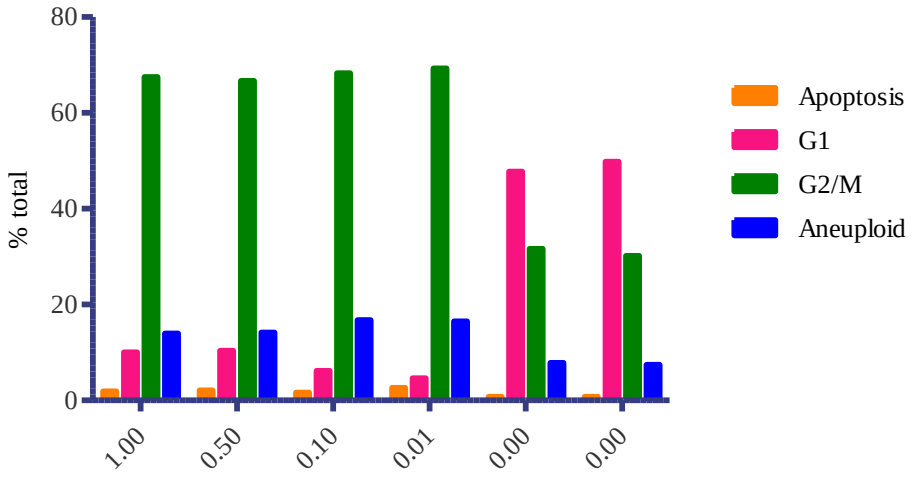

[compound **15**] µM

Figure 7.37 – Compound **15** treatment summary of effect on MDA-MB-231 cell cycle arrest after 48 hour treatment

A Control

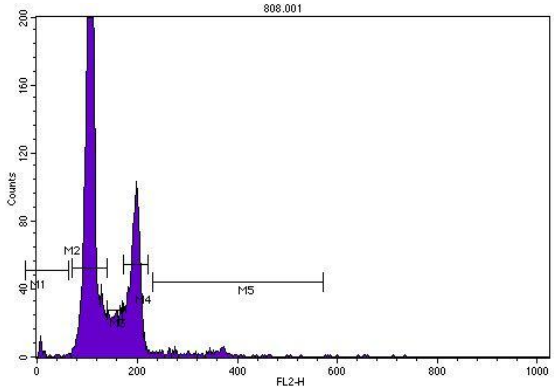

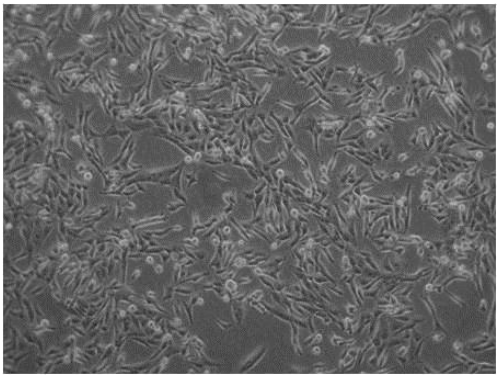

B – 0.01 µM compound **16**

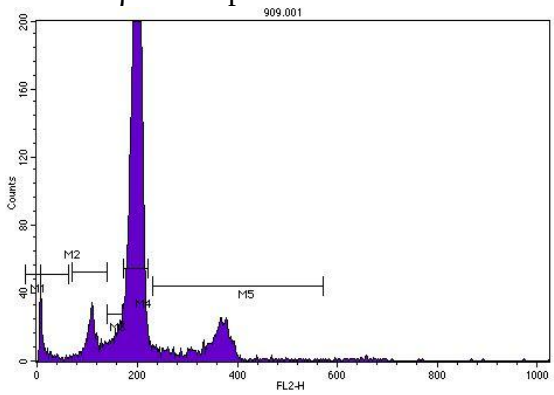

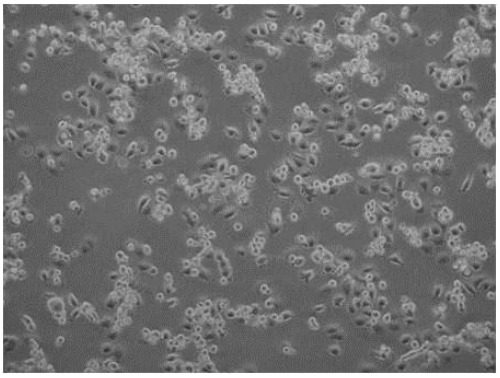

C – 0.005 µM compound **16**

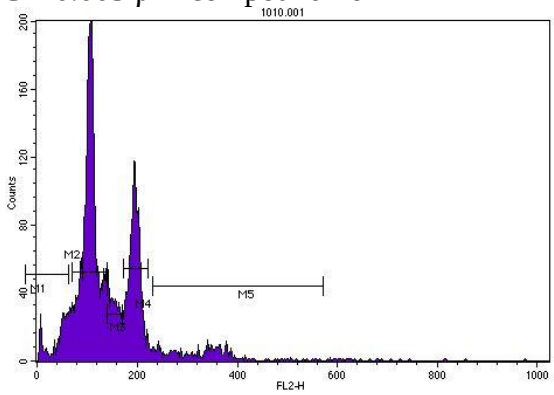

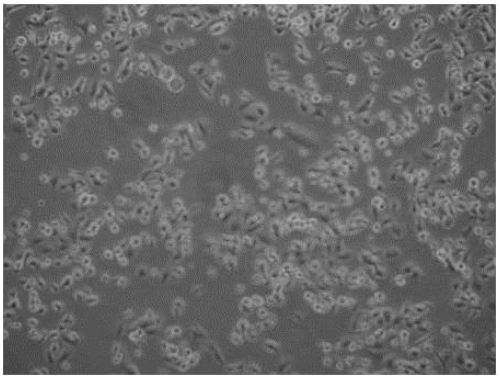

D – 0.001 µM compound **16**

Figure 7.38 continues

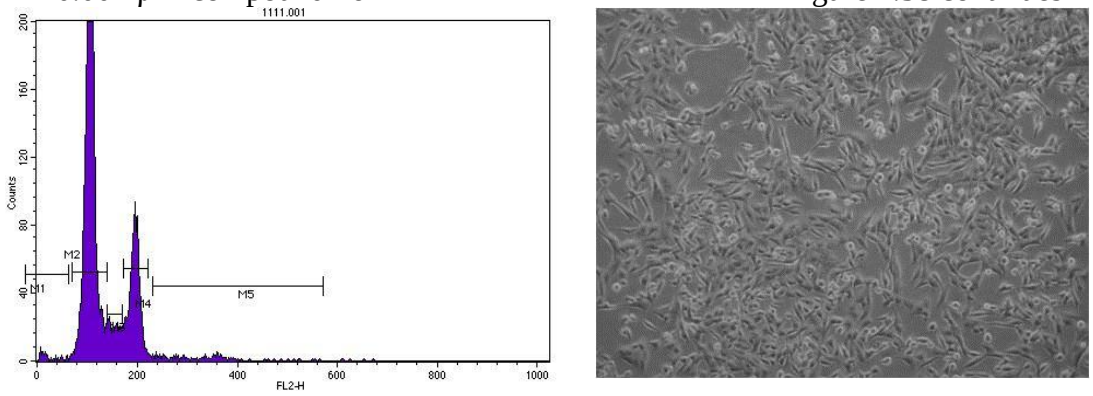

E – 0.0005 µM compound **16**

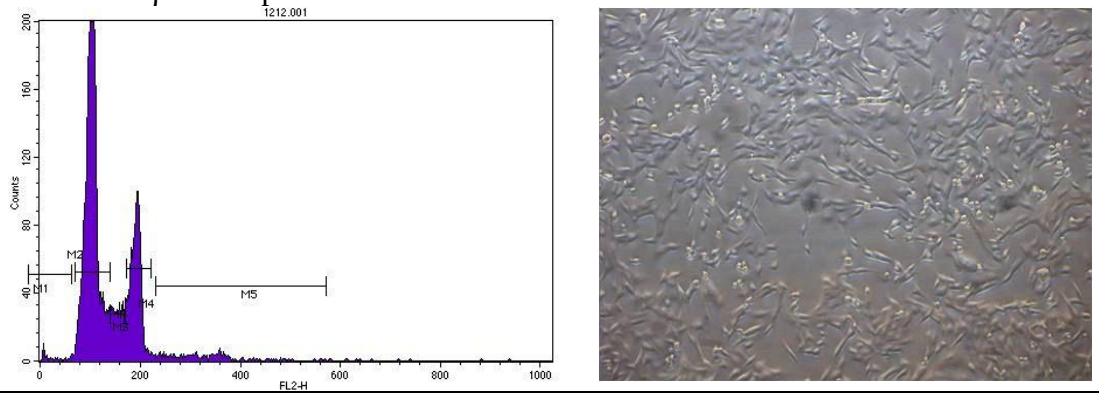

Figure 7.38 - Compound **16** treated MDA-MB-231 cells analyzed by flow cytometry; histograms on left, cells before harvesting on right (20x)

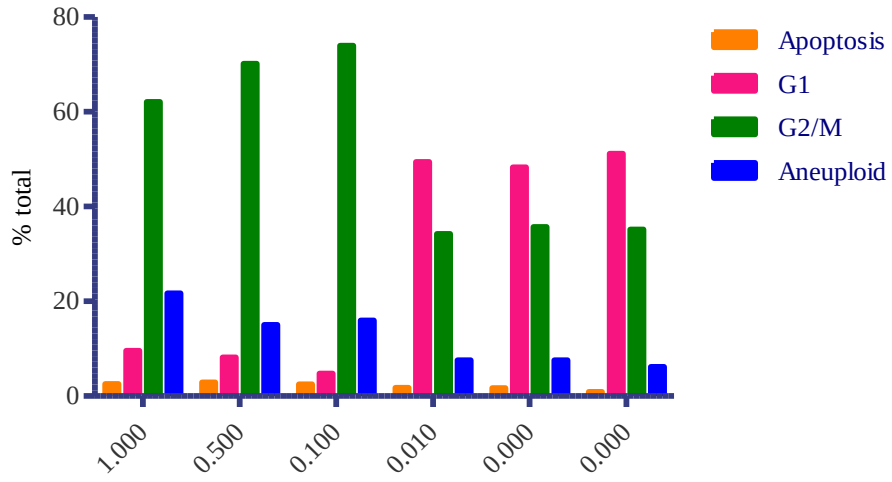

Figure 7.39 – Compound **16** treatment summary of effect on MDA-MB-231 cell cycle arrest after 48 hour treatment

Adherent vs. Nonadherent Cell Study

In previously published literature, pooled cells were separated into adherent and non-adherent fractions for analysis to determine the percentages of cells in each phase of the cell cycle. Cell samples, MDA-MB-231 cells, were prepared by pooling adherent and non-adherent cells in tubes and after washing and centrifugation, analysis. To investigate the percentages of cells in the different cell cycle phases in non-adherent cells versus adherent cells, the individual fractions were separated and analyzed. Non-adherent cells were collected by aspirating off the media of the 6-well plate or 3 cm dish. Adherent cells were the cells that were removed by trypsinization. Both fractions were washed and centrifuged in a similar manner. The vehicle control in this experiment was DMSO treated cells at a concentration equivalent to that in the compound **7** treated sample.

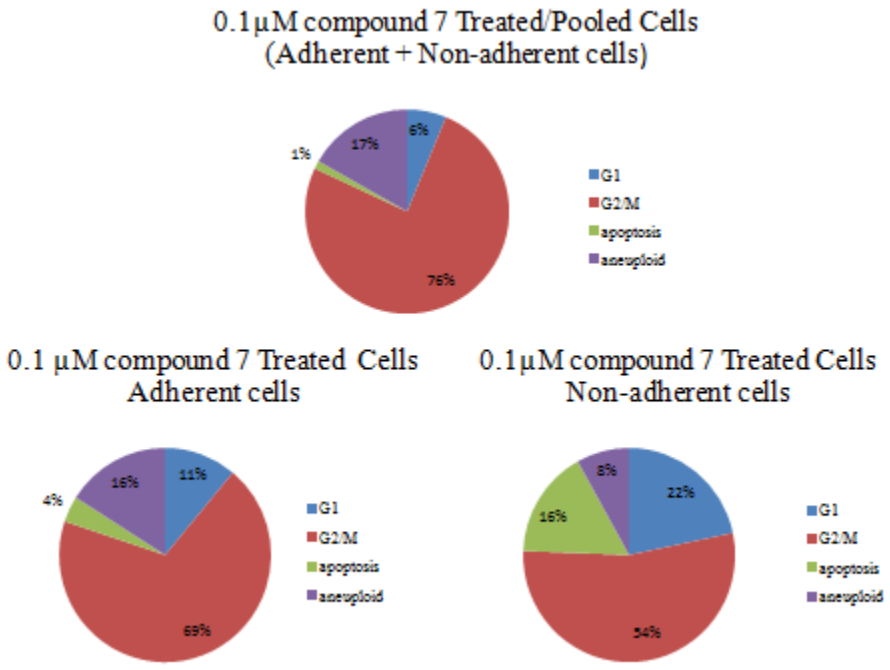

Figure 7.40 – Adherent vs. non-adherent MDA-MB-231 cells in vehicle control (DMSO)

For the total or pooled sample, which contained both adherent and non-adherent cells, the majority of the cells were in the G1 phase at 71% of total events, Figure 7.40. The G2/M phase consisted of 24% of the cells with 4% and 1% in the aneuploid and apoptotic phases, respectively. The adherent fraction analyzed separately was very similar to the pooled cell sample with percentages of cells comparable to those in the adherent and non-adherent cell sample. A difference was noted upon analysis of the non-adherent fraction which showed a shift in the majority of the cell phase. Here, most of the cells were in the apoptotic state, 76%, which can be explained by the fact that most of the non-adherent cells have entered this phase and have begun to round up and detach from the plate. In contrast to the pooled and adherent fractions, the non-adherent vehicle control fraction was only 16% G1 and 7% G2/M. The percent of cells in the aneuploid phase did not significantly change between the non-adherent and adherent fractions. Within this study, MDA-MB-231 cells were treated with 0.1 μM compound **7**, a concentration within the effective concentration range, Figure 7.41. The pooled fraction was composed of largely of cells in the G2/M phase at 76% with only 6% in the G1 phase. A increase in aneuploid phase was seen in comparison to the control cells at 17% when treated with compound **7**. The apoptotic fraction was comparable to the control at approximately 1%. For the adherent and non-adherent cell fraction the majority of the cells were in the G2/M phase with slightly higher percentage in the adherent cell sample. The more significant differences occurred in the G1, anueploid and apoptotic cell cycle phases. In the adherent sample, the percent in G1 was half that in the non-adherent sample and the percent in aneuploid was twice that of the non-adherent cells, 11% and 22% for adherent and non-adherent respectively. The adherent cell sample remained approximately the same in

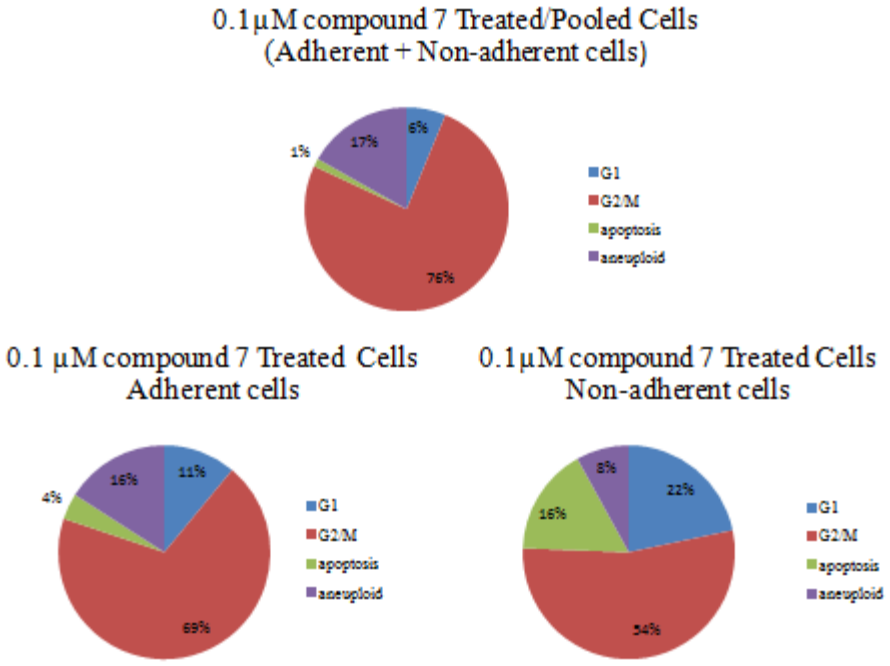

Figure 7.41 – Adherent vs. non-adherent MDA-MB-231 cells treated with compound **7**

percentage of cells in the aneuploid phase in comparison to pooled cells. The non-adherent cells decreased the aneuploid percentage by almost half, 17% in pooled versus 8% in non-adherent. The number of cells undergoing apoptosis increased slightly from the pooled fraction to the adherent fraction and significantly increased in the non-adherent fraction. This trend mimics that of the control and can be explained similarly. Cells treated with compound **8** exhibited similar results to its parent compound where the majority of the cells were in G2/M in all fractions, Figure 7.42. There was an observable decrease in the percentage of cells in aneuploid and an increase in apoptosis upon comparison of the adherent to the non-adherent fractions. The percentage of cells in the G1 phase of the cell cycle in the adherent and non-adherent fractions increased upon comparison to the pooled cells.

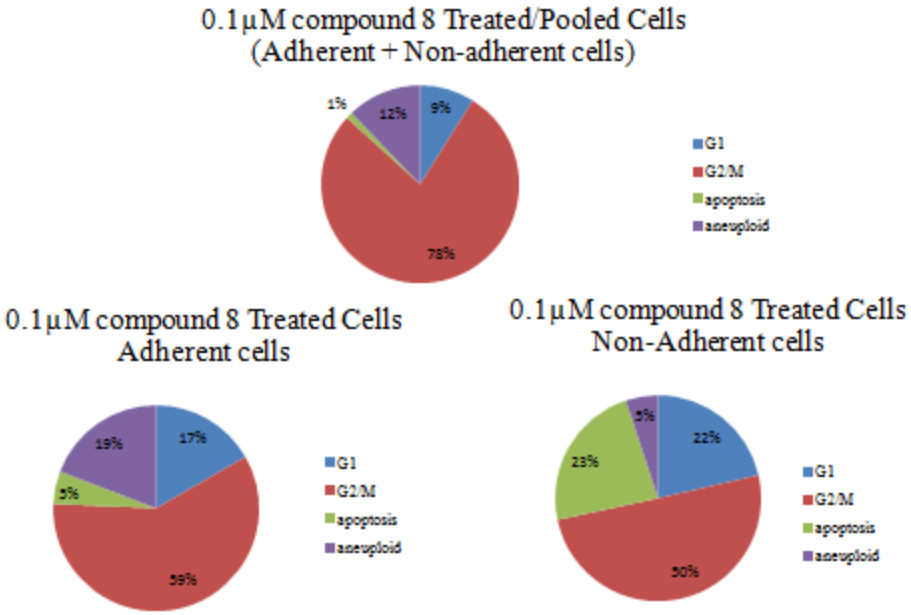

Figure 7.42 – Adherent vs. non-adherent MDA-MB-231 cells treated with compound **8**

Cell Plating Density

Cell number varies in the literature and optimization was done to determine if the cell density affected flow cytometry results of treated and untreated samples. Adequate plating must be achieved as overly sparse plating causes growth to slow and plating at high density can impede growth. Cells, MDA-MB-231, were plated at 100,000 (low density), 200,000 (medium density) and 400,000 (high density) cells per 6 well plate as these concentration. Results indicated neither low nor high density plating had a significant effect on the results although 20X pictures of the samples taken before harvesting indicated that the cells were near 100% confluency, data not shown. At the maximal confluency, cell growth could be retarded or cells could begin to round up and detatch, mimicking the effect of the VDA, therefore interfering with accurate data analysis. It was based on these results that 200,000 cells per 6 well plate was chosen for experiments.

Time-Dependent Assay

In order to further characterize the mechanism of action, a time based study was performed on compound **7** and compound **8**. This experiment observed the cell rounding effects in addition to the cell cycle effects of the cell line MDA-MB-231 over a time course treated with the compounds. The goal was to visualize when the compounds began to affect the breast cancer cell line in terms of cell cycle and cell rounding. Controls were done at every time point for comparison. Here, cells were plated for 48 hours followed by treatment time as noted in Table 7.6. Time 0 was treated with addition of compound or vehicle control followed by removal after approximately one minute. After 48 hour plating time, it was characteristic of this cell line to observe some attachment but given the zero time period, the extended morphology often seen in cells after longer plating time was not seen.

*Compound **7** Time Dependence Study*

The sample at time 0 was not a significant difference in the treated versus vehicle control cells which was expected and is evident in the 20x photographs in Table 7.6. By four hours, the cells in the control sample began to adhere while the treated samples did not. Adherence was consistently less in the treated cells over the time course until 24-48 hours where the treated cells began to adhere to the plate. The delay in adherence would indicate that the cells were affected by the treatment and as seen in the flow histograms, at 0.1 μM compound **7** for 48 hours, significant blockade in the G2/M phase of the cell cycle is seen. Figure 7.43 is the cell count for the harvested cells which further illustrates the blockade effect of the cells in the the G2/M phase as the treated cells did not divide as readily as the untreated.

Table 7.7 – 20X magnification of MDA-MB-231 cells treated with vehicle control (0.22% DMSO) or compound (compound **7**) at indicated times

Treatment time (hr)	Vehicle Control	0.1 µM compound **7**
0	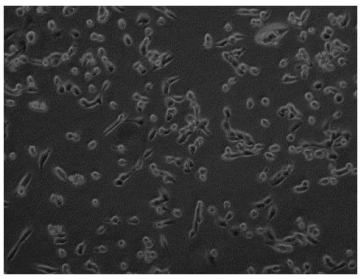	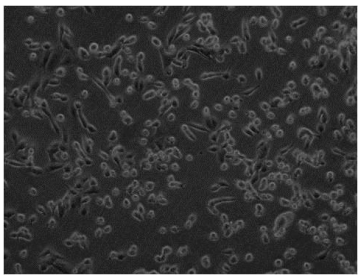
4	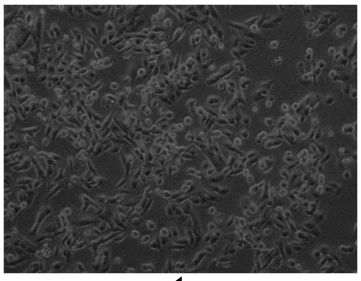	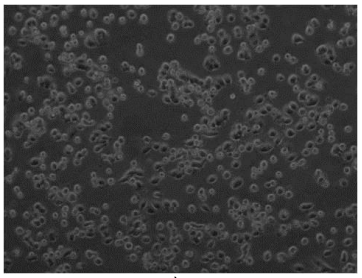
	Initial cell attachment	No cell attachment
8	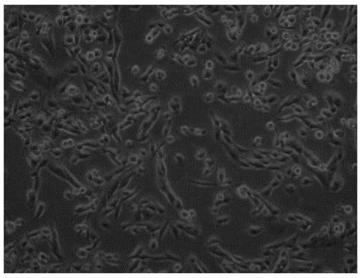	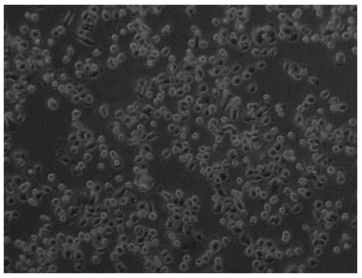
12	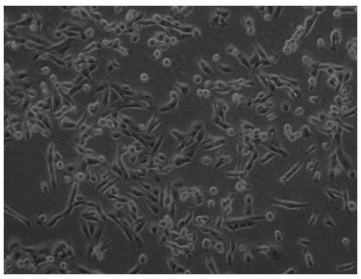	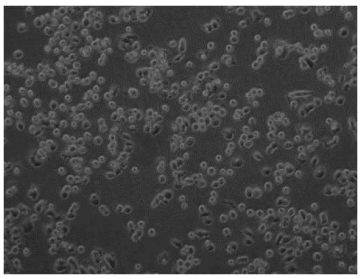

Table 7.6 continues

Treatment time (hr)	Vehicle Control	0.1 µM compound **7**
16	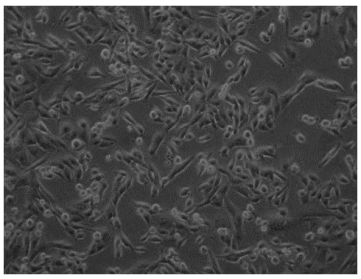	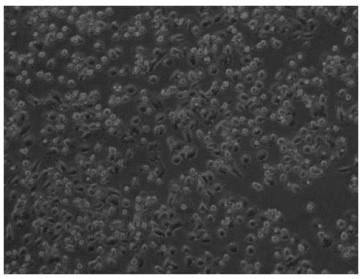
24	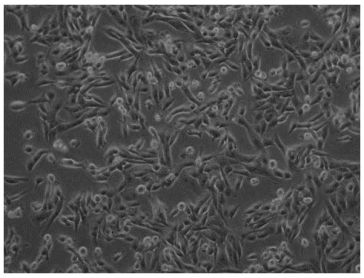	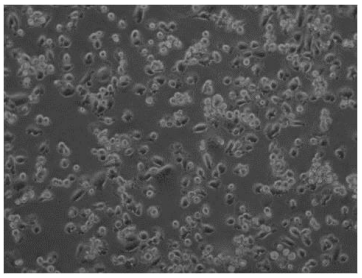 Initial cell attachment
48	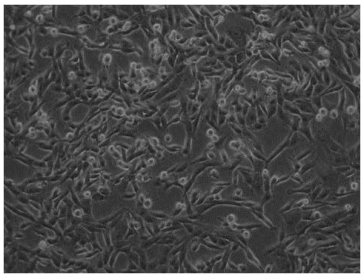	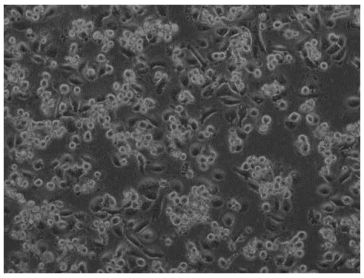 Increased cell attachment
72	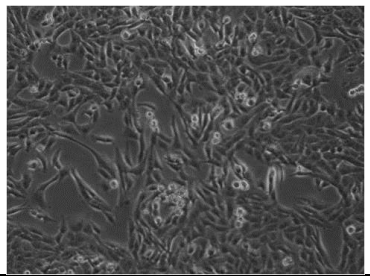	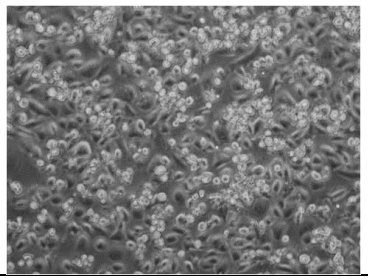

A graph of cell number after treatment for noted times and harvesting is seen in Figure 7.43. The cell number is approximately the same for the control and treated sample up to 16 hours. At 24 hours the vehicle control sample doubles in cell number

while the sample treated with 0.1 µM compound **7** increases slightly in number but does not double. This graph suggests that the benzosuberene compound is preventing

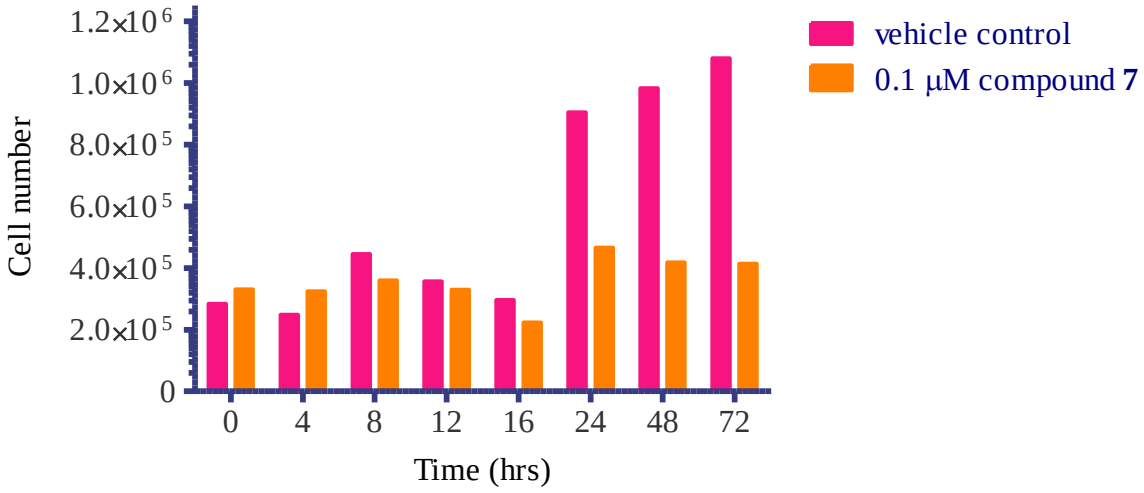

Figure 7.43 – Inhibition of cell growth (MDA-MB-231) after treated at indicated times with vehicle control (0.22% DMSO) and 0.1 µM compound **7**

mitosis from occurring as the cell number is not increasing as is seen in the control. To observe the change in the percentage of cells in the different cell phases, the varying time point samples were harvested, treated with RNAse A, labeled with PI and analyzed via flow cytometry. The percentages in the G1 and G2/M phase was analyzed first as the shift of the majority of the cells in these phases is characteristic of the combretastatins. As seen in Figure 7.44, for the vehicle control treated samples, after approximately 16 hours the percentage of cells in the G1 and G2/M phase reached a plateau, remaining constant through the remaining time course. For the cells treated with 0.1 µM compound **7**, there was an initial decrease in G1 and increase in G2/M, shifting from the majority of G1 to G2/M around the 16 hour time point, Figure 7.45. This shift indicated that at 16 hours, more of the cells were in the G2/M phase than the G1 phase, opposite to what was

seen in the control. The percentage of cells in G2/M then does not change indicating a blockade which would results in a significant decrease or elimination of cell division,

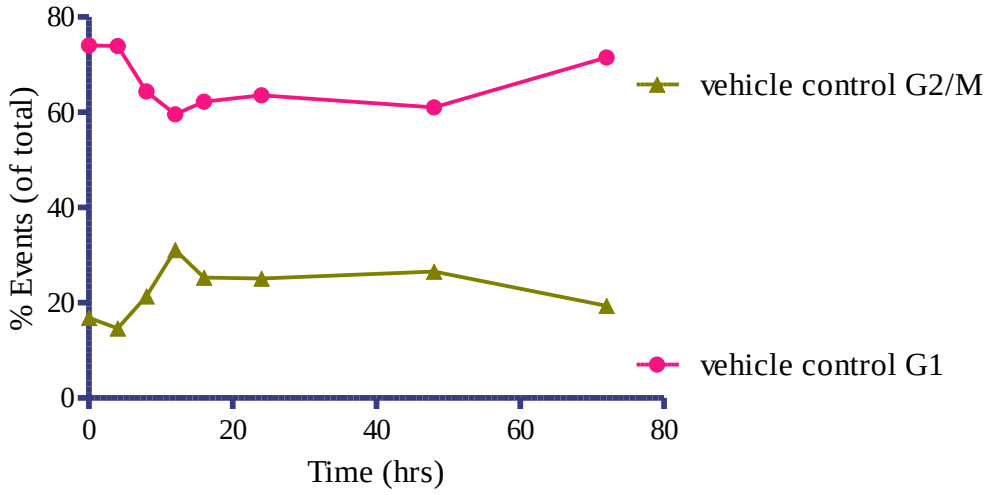

Figure 7.44 Effect of vehicle control (0.22% DMSO) treatment on G1 and G2/M phase in time course assay; times are incubation of compound with plated MDA-MB-231 cells

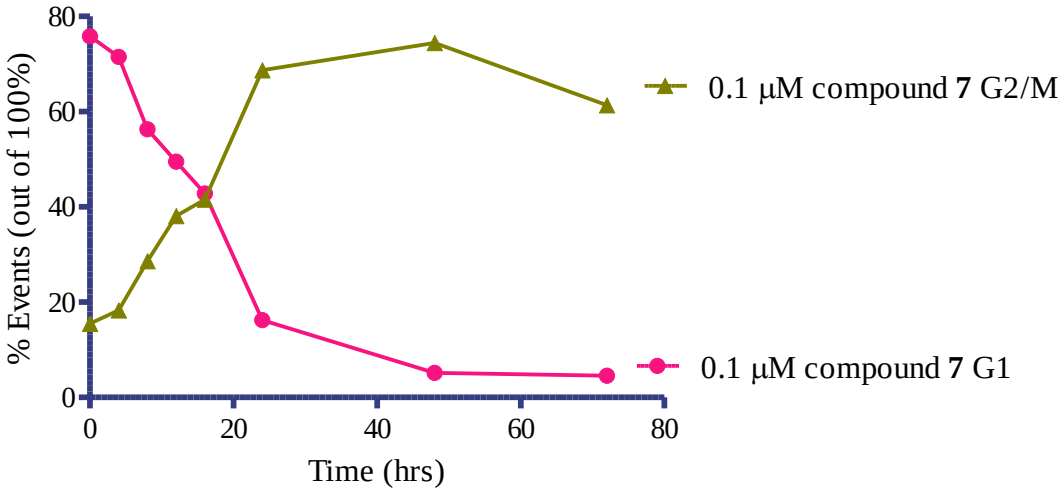

Figure 7.45 – Effect of compound **7** treatment on G1 and G2/M phase in time course assay; times are incubation of compound with plated MDA-MB-231 cells

an effect seen in the cell count graph in Figure 7.43.Analyzing the apoptotic fraction, at 16 hours there was a split in the percent cells in this phase in the control versus treated samples, Figure 7.46. Although interesting, this provides only a general idea of the sub G1 peak. For further insight into the apoptotic nature of these samples, annexin V or another apoptosis labeling assay will need to be performed. Although the apoptosis, G1 and G2/M effects were seen at approximately 16 hours, the phenotypic change was not observed until 24 hours with more distinct changes at 48 hours.

*Compound **8** Time Dependence Study*

The sample at time 0 was treated in a similar manner as was noted for compound **7** and from photographs taken immediately before harvesting, similar results were seen as there was not a significant difference between the treated and untreated samples. The adherence of the cells to the plate began at 16 hours with a slow increase noted in the 24 and 48 hour time points.

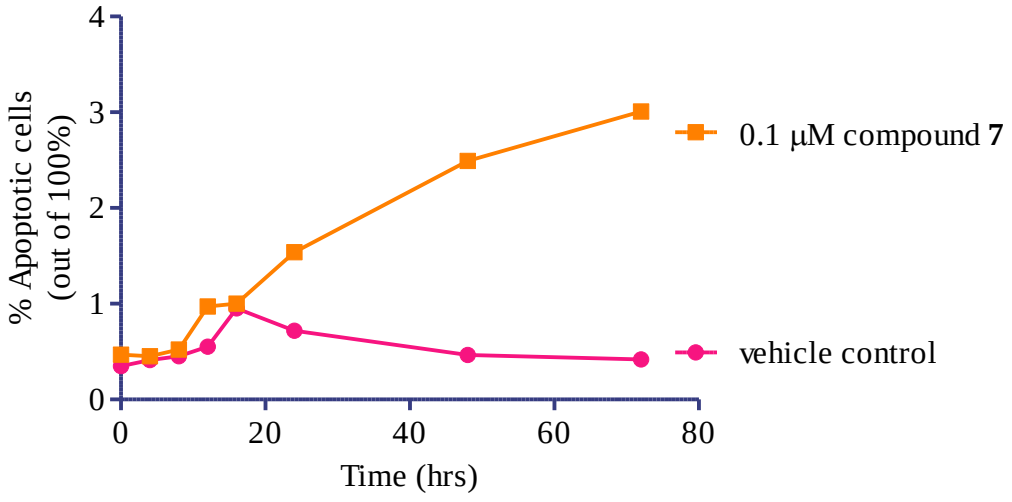

Figure 7.46 – Effect of compound **7** and vehicle control treatment on apoptosis in time course assay; times are incubation of compound with plated MDA-MB-231 cells

Table 7.8 – 20X magnification of MDA-MB-231 cells treated with vehicle control (water) or compound (compound **8**) at indicated times

Treatment time (hr)	Vehicle Control	0.1 µM compound **8**
0	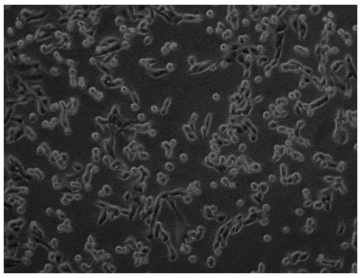	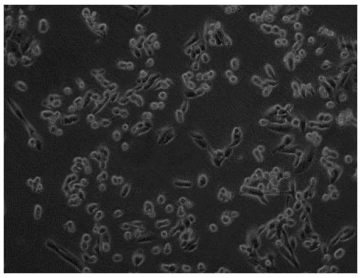
4	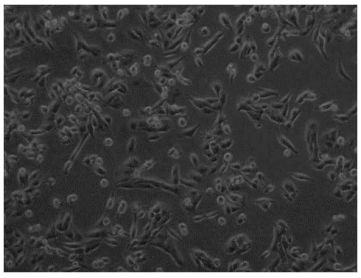	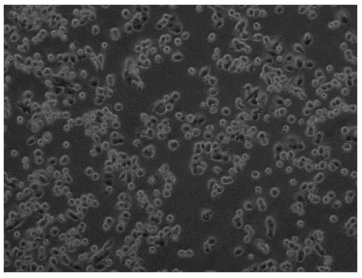
	Initial cell attachment	No cell attachement
8	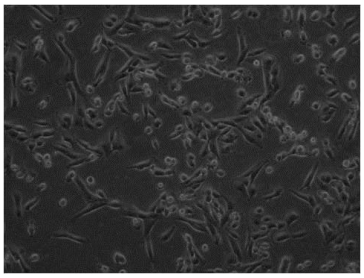	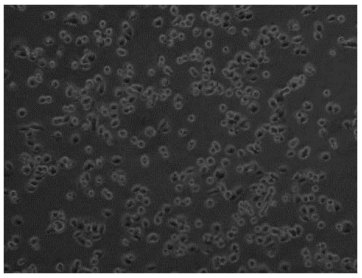
12	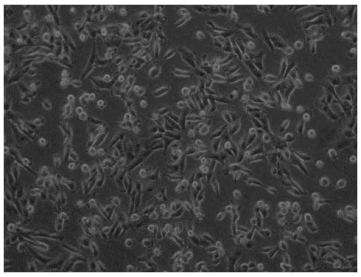	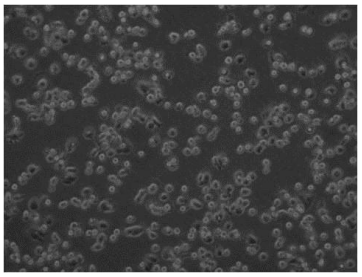

Table 7.7 continues

Treatment time (hr)	Vehicle Control	0.1 µM compound **8**
16	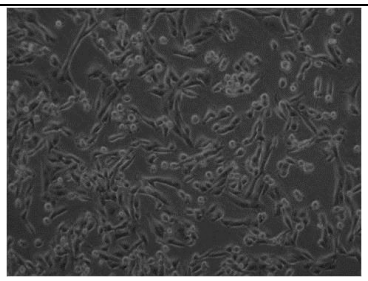	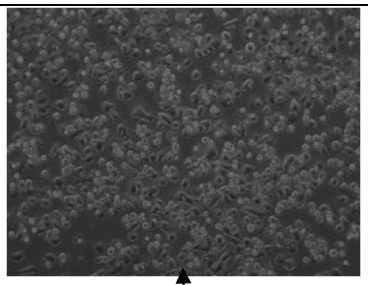 Initial cell attachment
24	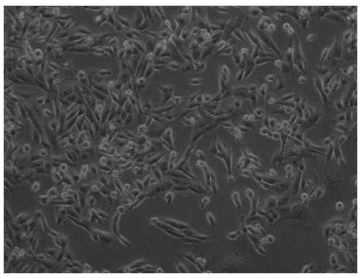	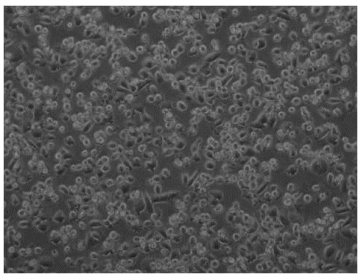 Increased/Significant cell attachment
48	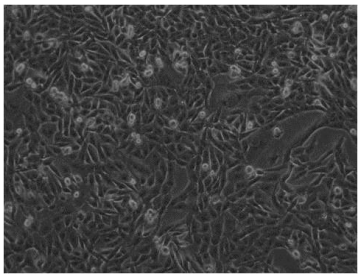	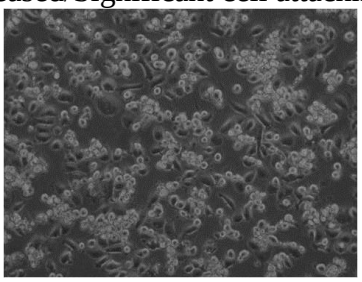
72	Picture not shown	

Graphing the cell number after harvesting the samples at various time points, it was evident that between 16 and 24 hours when doubling of the cells should begin that the treated cells were impeded from dividing. Analysis of the vehicle control time course, Figure 7.48, exhibited moderate stability of the events in G1 and G2/M after 16 hours. In

the samples treated with the disodium salt, compound **8**, the shift from the majority of cell events in the G1 to the G2/M phase occurred at between 12 and 16 hours, at a faster rate than compound **7**. Apoptosis analysis indicated a split in the percent cells of the treated versus untreated at the 16 hour time point, similar to the results seen for compound **7**.

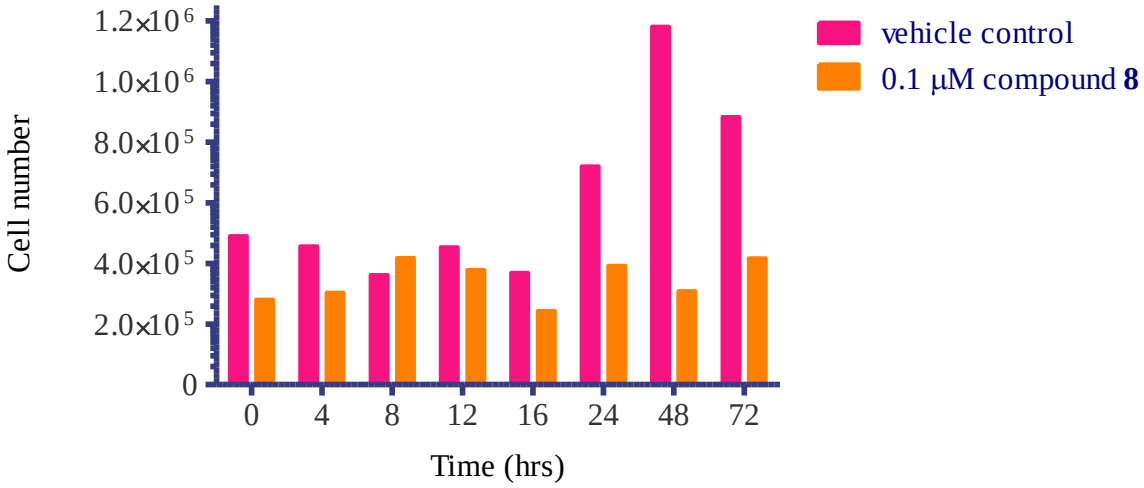

Figure 7.47 – Cell count (MDA-MB-231) after harvesting samples treated at indicated times with vehicle control (water) and 0.1 µM compound **8**

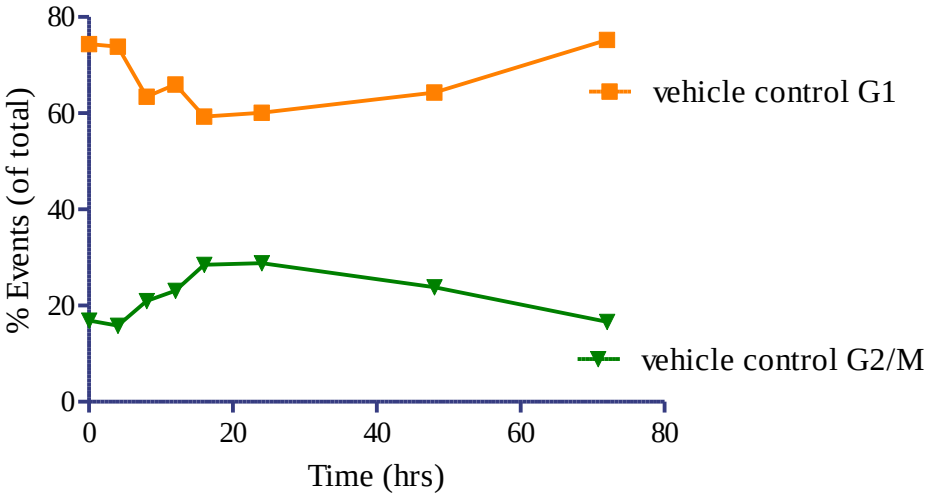

Figure 7.48 - Effect of vehicle control (water) treatment on G1 and G2/M phase in time course assay; times are incubation of vehicle/compound with plated MDA-MB-231 cells

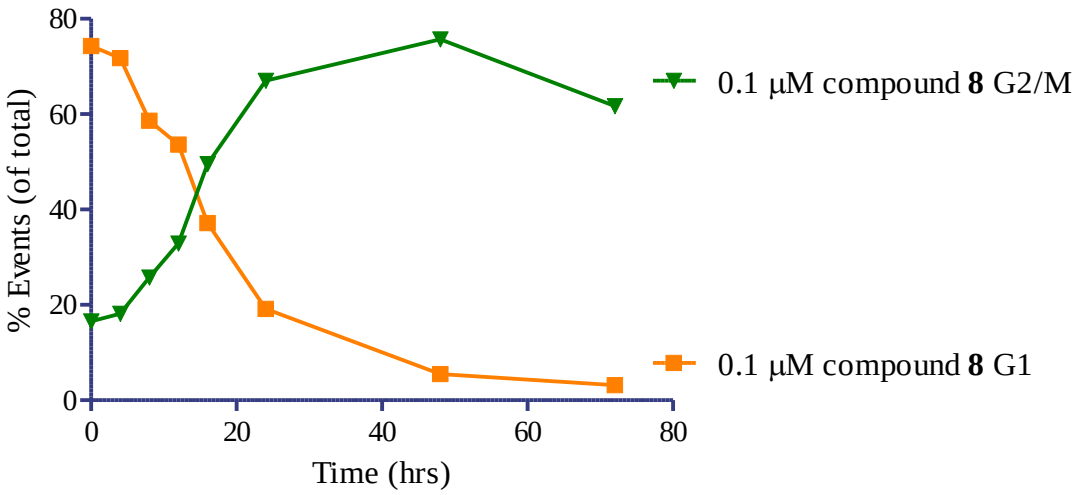

Figure 7.49 – Effect of compound **8** treatment on G1 and G2/M phase in time course assay; times are incubation of compound with plated MDA-MB-231 cells

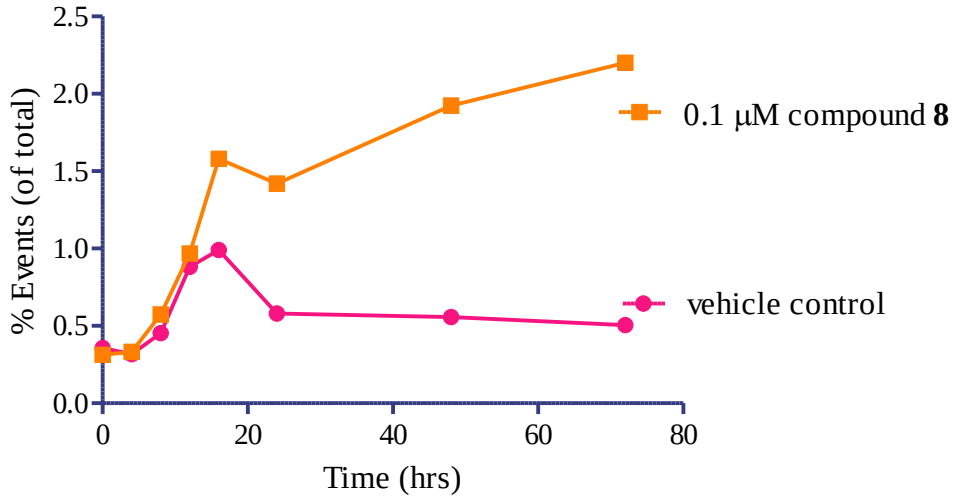

Figure 7.50 – Effect of compound **8** and vehicle control treatment on apoptosis in time course assay; times are incubation of compound with plated MDA-MB-231 cells

Preliminary RhoA Determination Studies

The proteolytic cascade involving microtubule dynamics, actin cytoskeleton organization and cell cycle progression includes the Rho protein family of GTPases. Different isoforms of Rho include RhoA, RhoB and RhoC, all of which are involved in

stress fiber formation and cell migration.[202] Rho proteins cycle through an active GTP bound state and inactive GDP bound state, activation of which is controlled by guanine exchange factors (GEFs), regulatory proteins that catalyze the GDP-GTP exchange. Disregulation of the Rho signal transduction pathway has been implicated in a variety of cancers.[203] RhoA is upstream from many proteins involved in stress fiber contraction and cytoskeletal components making it a viable target for VDAs, see Figure 7.51. RhoA was chosen as a target of this investigation for the mechanism of action of the VDA like compounds. It was proposed that because vascular disrupting agents interfere with vasculature by disrupting focal adhesion formation or cell-cell junctions that the effects upstream could be visualized by observing this protein. The active form of RhoA, GTP bound RhoA, has been reported in the human breast cancer cell line MDA-MB-231.[204]

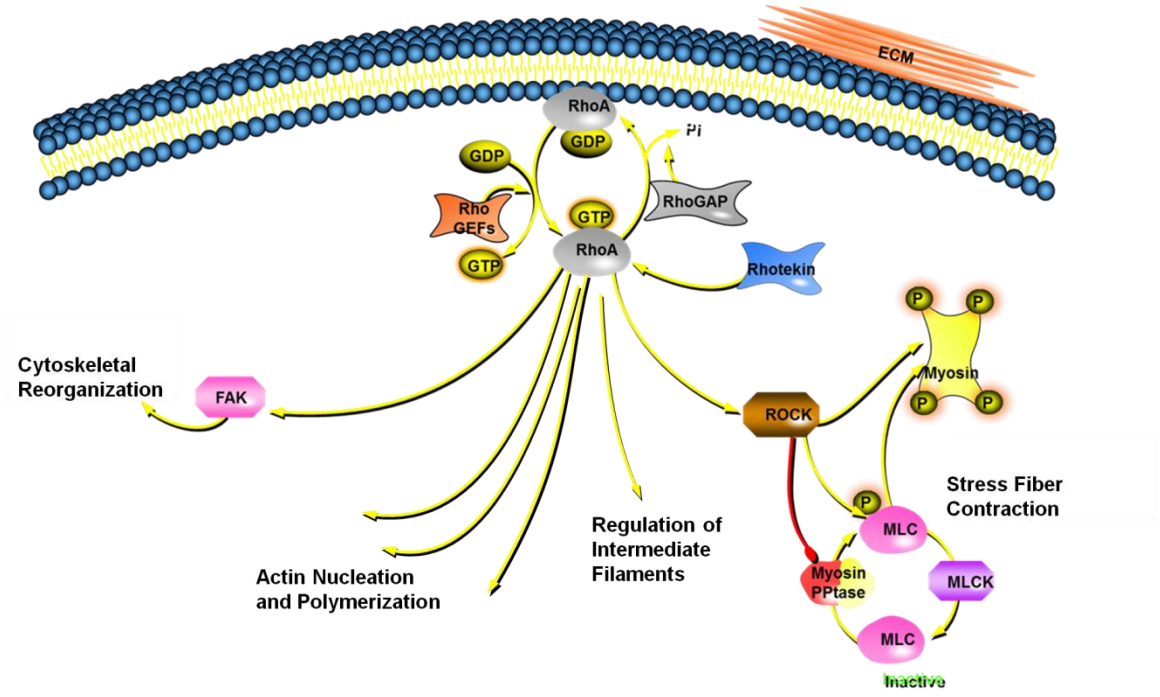

Figure 7.51 - RhoA pathway in mammalian cells, Proteinlounge.com/SA Biosciences 2008 (reprinted with permission from Qiagen 2013)

The percentage of active RhoA is 0.5-5% of total Rho in the cell which makes for a very low abundant protein and therefore can be difficult to image.[182] Due to this nature of the target, cell lysates were subjected to affinity precipitation to isolate and concentrate the active form of Rho. During the precipitation reaction, protein concentration was determined on the lysates but due to components of the lysis buffer, a typical Bradford assay was not viable. Comparing methods and compatibilities of protein determination assays, the RC-DC assay was selected. RC-DC refers to reducing agent and detergent compatibility of this modified Lowry assay, two major interfering agents in protein estimation. A representative standard curve for this assay is seen in Figure 7.52.

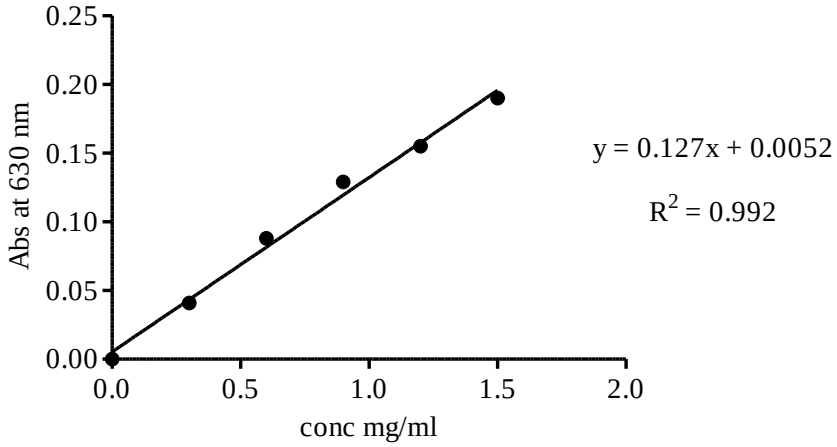

Figure 7.52 – Representative standard curve for RC/DC protein assay with bovine serum albumin

Affinity Precipitation

The affinity precipitation reaction, referred to as a pulldown assay, was performed on the cell lysates of MDA-MB-231 cells. A schematic of the steps involved in this assay is in Figure 7.53. Initially the agarose beads labeled with the glutathione affinity label were

incubated with the rhotekin RBD (rho binding domain), attaching what is known as the "bait protein" to the resin. Once the rhotekin was attached, the protein cell lysate sample

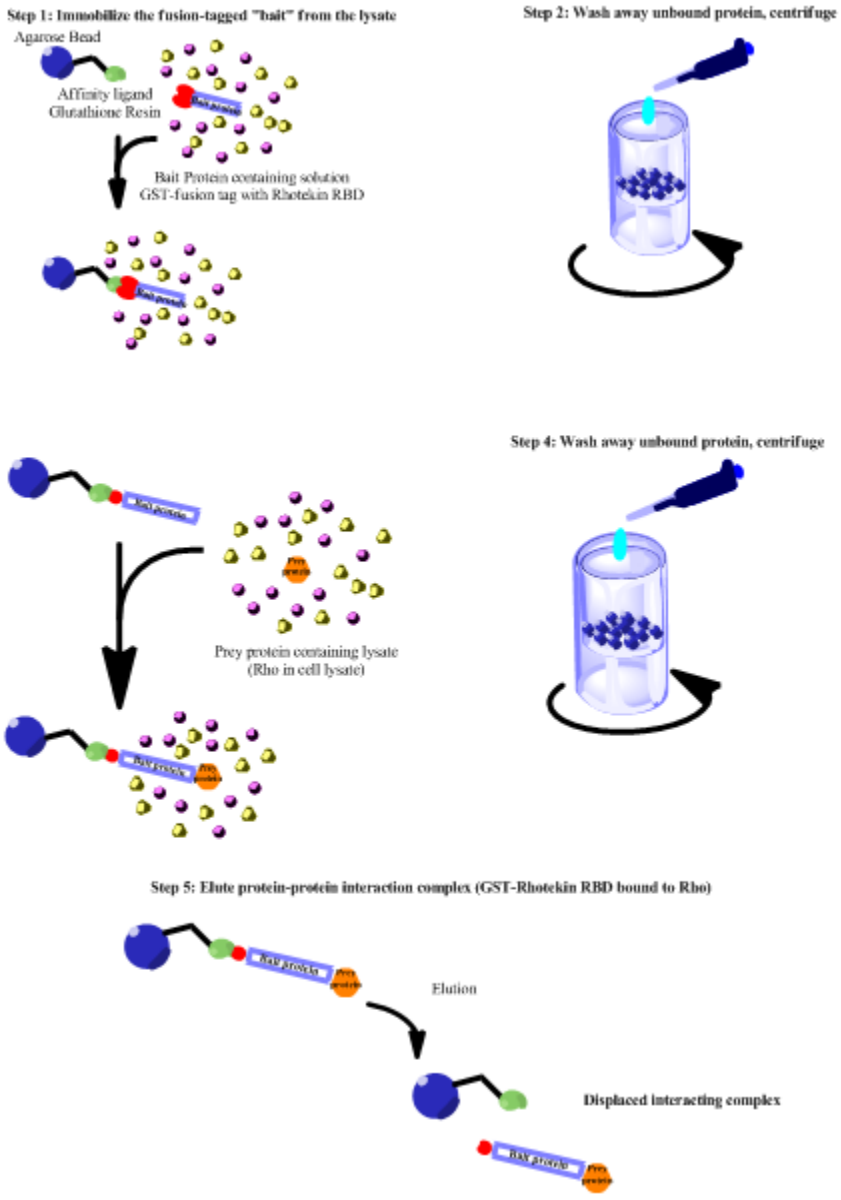

Figure 7.53 – RhoA affinity precipitation experiment scheme

was added and the rho proteins bound to the RBD. In this case, rhotekin RBD was specific for active forms of RhoA, B and C, referred to as the "prey" in this assay. Multiple wash steps removed excess proteins not bound to the binding domain and

elution of the desired target was achieved by addition of a strong reducing agent, 2 mercaptoethanol in this case, which displaced the prey. The active Rho protein was collected and analyzed via chemiluminescent methods as the low abundant nature of the protein required more sensitive methods than fluorescence. Once affinity precipitation was complete, isolated protein was run through gel electrophoresis followed by transfer to a membrane. It was previously mentioned that the assay pulls down all three active forms of Rho: A, B and C. The membrane was probed with a primary antibody specific for RhoA to visualize the target protein. Expression of GTP bound RhoA was seen in cell lysate samples in our hands although the isolation of such was difficult and the signal was weak. The active GTP bound form of RhoA is quickly hydrolysable to the inactive form, lending the assay to low yields. To combat this, lysates were kept on ice at all times and the procedure was performed as quickly as possible.

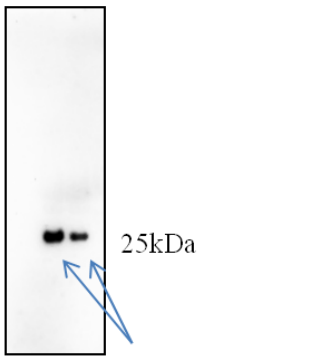

Figure 7.54 – Western blot of active RhoA pulldown by affinity precipitation

Figure 7.54 is a western blot of cell lysate from the human breast cancer cell line MDA-MB-231. Samples in this Figure have been treated with the non-hydrolyzable form of GTP to prevent any conversion of RhoA to the inactive form. The bands seen are approximately 25kDa, within the correct molecular weight range for the target of interest.

Samples not treated with GTPγS did show active GTP bound RhoA although the signal was extremely weak, data not shown. The molecular weight marker is not shown as a non-chemiluminescent marker was used and therefore was not visualized with the CCD imager.

Summary

The mechanism of action of the benzosuberene compound **7** and its analogues including the prodrug compound **8** was characterized by various methods used to assess disruption of microtubule dynamics. These included inhibition of tubulin polymerization assay, a competitive binding assay for the colchicine site on tubulin and cell cycle analysis by flow cytometry. Compound **7** inhibited tubulin polymerization with an IC_{50} values of 1 μM, comparable to that of CA4, demonstrating its ability to interfere with microtubule formation. Compound **7** inhibited ^{3}H-colchicine binding to tubulin with an IC_{50} of 0.36 μM, indicating its binding to the colchicine binding site of tubulin. Compound **7** exhibited time dependent cell cycle arrest in the G2/M phase after approximately 16 hours of treatment, although cell rounding effects were not observed after 24 hours. The effective concentration of the G2/M blockade was 0.1-0.01 μM for compound **7** which was equivalent to CA4P but not quite as potent as that of CA4, 0.005-0.001 μM. The prodrug compound **8** exhibited similar effects to that of compound **7** in regards to G2/M blockade. These results support the idea of benzosuberene **7** being a colchicine site tubulin binding VDA, and that its phosphate analogue **8** is an effective prodrug.

APPENDICES

APPENDIX A

Papain and cathepsin B amino acid sequence comparison [89]

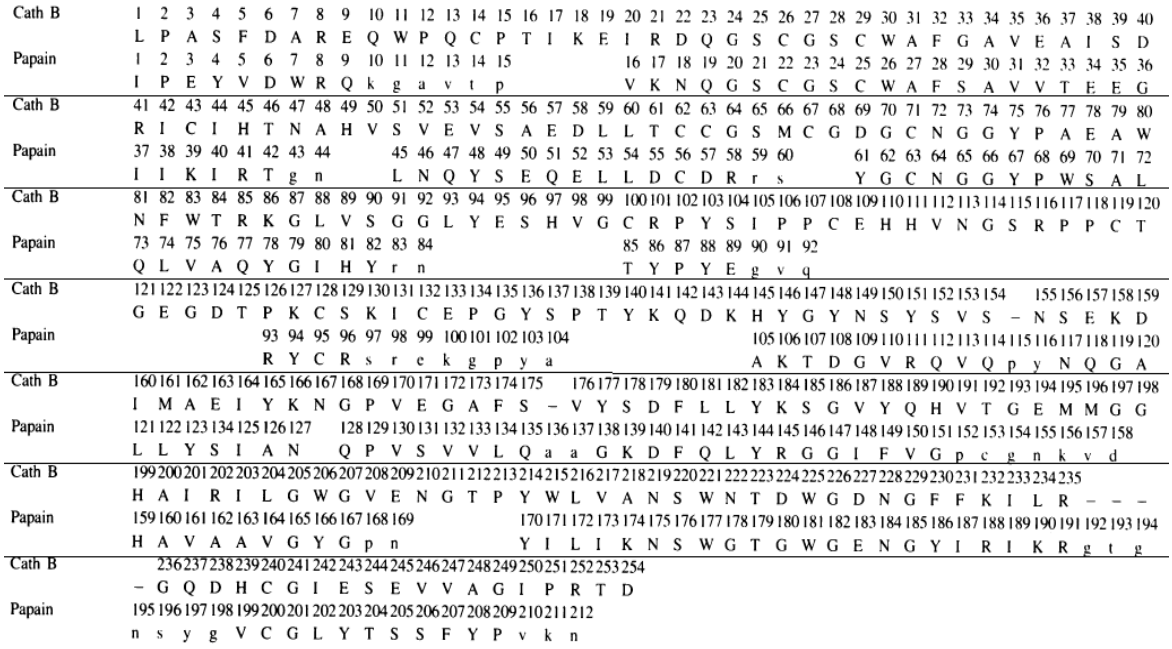

APPENDIX B

Thiosemicarbazone and ketone compounds tested against cathepsin B
(Compounds synthesized by Pinney laboratory)

Table B.1

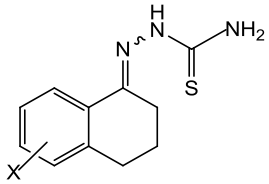

X	Compound	IC_{50}
5-Br	22	>10 μM
5,7-Br	23	>10 μM
N/A	24	>10 μM

Table B.2

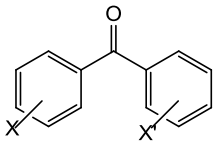

X	Compound	IC_{50}
4,4'-F	25	>10 μM
3,3'-F	26	>10 μM
3,3'-Br	27	>10 μM
3-Br, 2'-F	28	>10 μM
4-CH_3, 4'-Br	29	>10 μM
3-Br, 4'-F	30	>10 μM

Table B.3

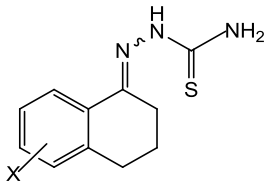

X	Compound	IC_{50}
7-Br	31	>10 μM
5-Br	32	>10 μM
5-OCH_3	33	>10 μM
7-OCH_3	34	>10 μM
6-OCH_3	35	>10 μM
5-NH_2	36	>10 μM
4-OH	37	>10 μM

Table B.4

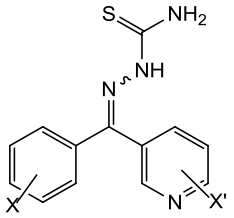

X	Compound	IC_{50}
N/A	38	>10 μM
3'-Br	39	>10 μM
2,3'-Br	40	>10 μM
6,3'-Br	41	>10 μM

Table B.5

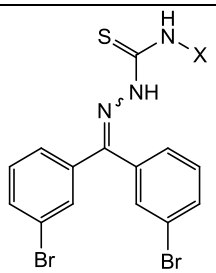

X	Compound	IC_{50}
Ph	42	>10 μM
CH_2Ph	43	>10 μM
Et	44	>10 μM

Table B.6

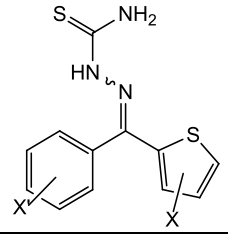

X	Compound	IC_{50}
N/A	45	>10 μM
5,3'-Br	46	>10 μM
3,4'-Br	47	>10 μM
3,3'-Br	48	>10 μM

Table B.7

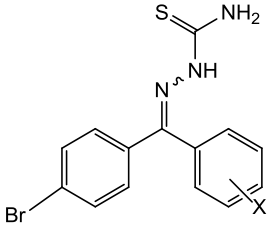

X	Compound	IC_{50}
4-F	49	>10 μM
4-Br	50	>10 μM
4-Cl	51	>10 μM
4- CH_3	52	>10 μM
4-CF_3	53	>10 μM
2-F	54	>10 μM
2-Br	55	>10 μM

Table B.8

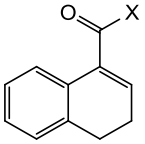

X	Compound	IC_{50}
CH_3	56	>10 μM
$CHCH_2$	57	>10 μM

Table B.9

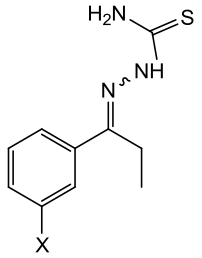

X	Compound	IC_{50}
Br	58	>10 µM
OH	59	>10 µM
NH_2	60	>10 µM
NO_2	61	>10 µM

Table B.10

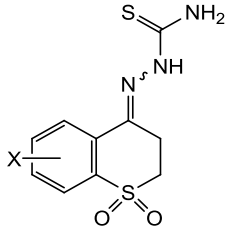

X	Compound	IC_{50}
6-Br	62	>10 µM
6-OCF_3	63	>10 µM
6-Cl	64	>10 µM
6- CH_3	65	>10 µM
6-OCH_3	66	>10 µM
6-Ch_2CH_3	67	>10 µM
N/A	68	>10 µM
NO_2	69	>10 µM
6-acetamide	70	>10 µM
6,7-F	71	>10 µM
OH	72	>10 µM
6,8-F	73	>10 µM
6-F, 8-Br	74	>10 µM
6-Br, 8-F	75	>10 µM
6,8-Br	76	>10 µM
6-isopropyl	77	>10 µM
6-F	78	>10 µM
6-NO_2	79	>10 µM
6-NH_2	80	>10 µM
6-SO_2CH_3	81	>10 µM

Table B.11

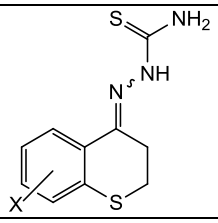

X	Compound	IC_{50}
N/A	82	>10 μM
Phe ring (fused on C4-5)	83	>10 μM
8-OCF_3	84	>10 μM
6-O CF_3	85	>10 μM
6-F	86	>10 μM
6-isopropyl	87	>10 μM
6-Br	88	>10 μM
6-OH	89	>10 μM
6-NO_2	90	>10 μM
6,7-F	91	>10 μM
6-F, 8-Br	92	>10 μM
6-Br, 8-F	93	>10 μM
6-Cl	94	>10 μM
6-CH_3	95	>10 μM
6-Et	96	>10 μM
6-CF_3	97	>10 μM
6-SCH_3	98	>10 μM
6-NH_2	99	>10 μM
6-NO_2	100	>10 μM
6-Acetamide	101	>10 μM
6-OCH_3	102	>10 μM
6-NO_2	103	>10 μM

Table B.12

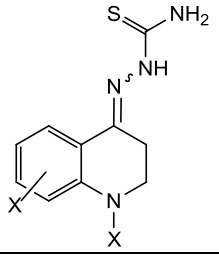

X	Compound	IC_{50}
$COCH_3$	104	>10 μM
NO_2	105	>10 μM
H	106	>10 μM
H, 4'-CH_2phenyl	107	>10 μM
H, 6'-Br	108	>10 μM
H,4'6'-NO_2	109	>10 μM
NO_2, 6'-NO_2	110	>10 μM
CH_3, 6'-Br	111	>10 μM
H, 6'-NO_2	112	>10 μM

Table B.13

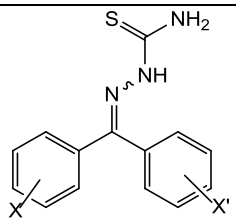

X	Compound	IC_{50}
3,4'-Br	113	>10 μM
3,2'-Br	114	>10 μM
3-Br	115	>10 μM
3-Br, Phe ring (fused on C3-4)	116	>10 μM
3-Br, 3'-OMePh	117	>10 μM
3-Br, 3'-CF_3	118	>10 μM
3-Br, 3'-F	119	>10 μM
3-Br, 3'-Cl	120	>10 μM
3-Br, 3'-CH_3	121	>10 μM
3-Br, 3'-OH	122	>10 μM
-	123	>10 μM
3-Br, 3'-F	124	>10 μM
3-Br, 4'-CF_3	125	>10 μM
3-Br, 3',5'-Cl	126	>10 μM
3-Br, 2'-F	127	>10 μM

Table B.13 continues

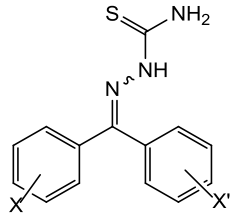

X	Compound	IC_{50}
3-Br, 4'-Cl	130	>10 μM
3-Br, 2'-CH_3	131	>10 μM
2-F	132	>10 μM
3,3'-F	133	>10 μM
4,2'-F	134	>10 μM
4,4'-F	135	>10 μM
3-Br, 3'-TBS	136	>10 μM
3,4,5-F, 3'-Br	137	>10 μM
2,3,4,5-F, 3'-Br	138	>10 μM
4-CH_3, 3',5'-CF_3	139	>10 μM
3-Br, 2',6'-F	140	>10 μM
3,3'-Br, 4'-F	141	>10 μM
3-Br, 2',3'-F	142	>10 μM
3,3'-Br, 2'-F	143	>10 μM
3,3'-Br, 4'-OTBS	144	>10 μM
3-CH_3, 3'5'-Cl	145	>10 μM
N/A	146	>10 μM
5-benzoyl	147	>10 μM
4-CH_3,3',5'-Cl	148	>10 μM
3,3'-Br, 5'-OTBS	149	>10 μM
3,3'-Br, 2'-OH	150	>10 μM
3,3'-Br, 5'-OH	151	>10 μM
3-OH	152	>10 μM
5- 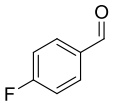 , 4'-F	153	>10 μM
5- 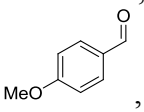 , 4'- OCH_3	154	>10 μM
4-CH_3,3',5'-Cl	155	>10 μM
5-phenyl ethanol	156	>10 μM
4',5'-fused cyclohexane ring	157	>10 μM
3-Br, 3',4',5'-F	158	>10 μM
3,3'-Br, 6'-OCH_3	159	>10 μM
5-(4-hydroxybenzoxyaldehyde)	160	>10 μM

Table B.13 continues

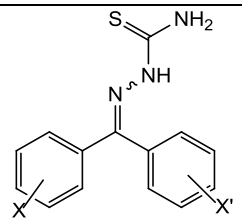

X	Compound	IC_{50}
2-F, 3'-Br, 5'-(1-(2-fluorophenyl)ethanone)	164	>10 µM

Table B.14

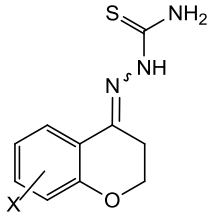

X	Compound	IC_{50}
4'-TSC, 6-Br	165	>10 µM
2'-TSC	166	>10 µM
4'-TSC	167	>10 µM
4'-TSC, 2'phenyl	168	>10 µM
4'-TSC, 6-Cl	169	>10 µM

Table B.15

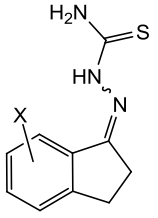

X	Compound	IC_{50}
-	170	>10 µM
3-Br	171	>10 µM

Table B.16

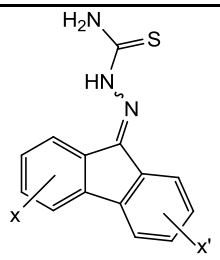

X	Compound	IC_{50}
3,3'-NO2	172	>10 µM
-	173	>10 µM
3,3'-Br	174	>10 µM

Table B.17

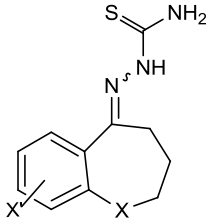

X	Compound	IC_{50}
6'NO_2, X = S	175	>10 µM
6' NO_2, X = SO_2	176	>10 µM
5'6'-F, X = S	177	>10 µM
5'6'-F, X = SO_2	178	>10 µM

Table B.18

X	Compound	IC_{50}
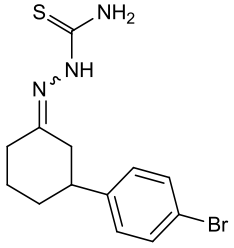	179	>10 µM

Table B.18 continues

X	Compound	IC50
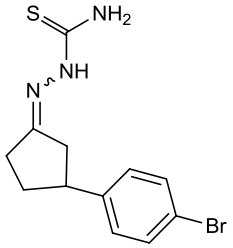	180	>10 µM
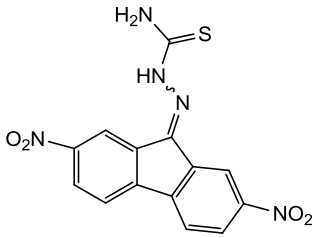	181	>10 µM
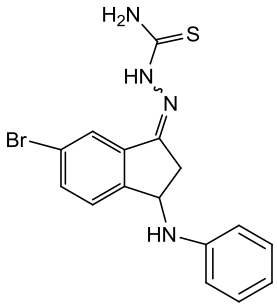	182	>10 µM
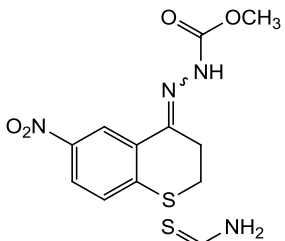	183	>10 µM
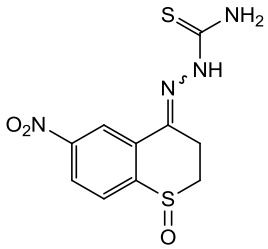	184	>10 µM
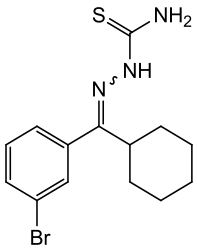	185	>10 µM

Table B.18 continues

X	Compound	IC_{50}
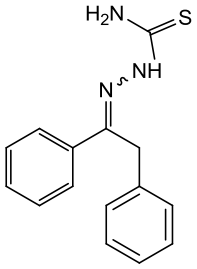	186	>10 µM
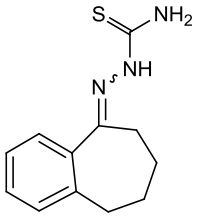	187	>10 µM
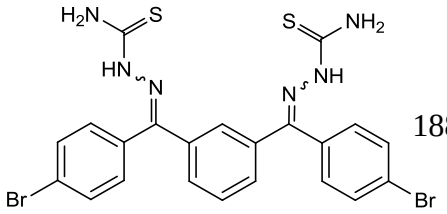	188	>10 µM

REFERENCES

1. Collins K, Jacks T, Pavletich NP. The cell cycle and cancer. Proceedings of the National Academy of Sciences. 1997;94(7):2776-2778.

2. Jordan A, Hadfield JA, Lawrence NJ, McGown AT. Tubulin as a target for anticancer drugs: Agents which interact with the mitotic spindle. Med Res Rev. 1998;18(4):259-296. doi: 10.1002/(SICI)1098-1128(199807)18:4<259::AID-MED3>3.0.CO;2-U.

3. Malarkey DE, Maronpot RR. Carcinogenesis. In: Editor-in-Chief: Philip Wexler, ed. Encyclopedia of toxicology (second edition). New York: Elsevier; 2005:445-466. http://dx.doi.org/10.1016/B0-12-369400-0/00192-7.

4. Luch A. Nature and nurture - lessons from chemical carcinogenesis. Nature Reviews Cancer. 2005;5(2):113-125. Accessed 31 July 2013.

5. Sancar A, Lindsey-Boltz L, Ünsal-Kaçmaz K, Linn S. Molecular mechanisms of mammalian DNA repair and the DNA damage checkpoints. Annu Rev Biochem. 2004;73(1):39-85. http://dx.doi.org/10.1146/annurev.biochem.73.011303.073723. doi: 10.1146/annurev.biochem.73.011303.073723.

6. Sperka T, Wang J, Rudolph KL. DNA damage checkpoints in stem cells, ageing and cancer. Nature Reviews Molecular Cell Biology. 2012;13(9):579-590.

7. Siegel R, Naishadham D, Jemal A. Cancer statistics, 2012. CA: A Cancer Journal for Clinicians. 2012;62(1):10-29. doi: 10.3322/caac.20138.

8. Ferrer. Drugs of the Future. 2010;35:11-18.

9. National Cancer Institute. NCI SEER training module. www,cancer,org. Accessed 11, 2012.

10. Fritz A. International classification of diseases for oncology: ICD-0. World Health Organization; 2000.

11. Robert G. McKinnell. The biological basis of cancer. Cambridge University Press; 1998.

12. Franks LLM, Teich NNM. Cellular and molecular biology of cancer. Oxford University Press; 1997.

13. Blade J, Rosinol L, Cibeira M, de Larrea C. Pathogenesis and progression of monoclonal gammopathy of undetermined significance. Leukemia. 2008;22(9):1651-1657.

14. Zhao XF, Reitz M, Chen QC, Stass S. Pathogenesis of early leukemia and lymphoma. Cancer Biomarkers. 2011;9(1):341-374.

15. Bair FE. Cancer sourcebook: Basic information on cancer types, symptoms, diagnostic methods, and treatments, including statistics on cancer occurrences worldwide and the risks associated with known carcinogens and activities. Vol 1. Omnigraphics Incorporated; 1990.

16. Hideshima T, Mitsiades C, Tonon G, Richardson PG, Anderson KC. Understanding multiple myeloma pathogenesis in the bone marrow to identify new therapeutic targets. Nature Reviews Cancer. 2007;7(8):585-598.

17. Kyle RA, Rajkumar SV. Multiple myeloma. N Engl J Med. 2004;351(18):1860-1873. http://dx.doi.org/10.1056/NEJMra041875. doi: 10.1056/NEJMra041875.

18. Hanahan D, Weinberg RA. Hallmarks of cancer: The next generation. Cell. 2011;144(5):646-674.

19. Hanahan D, Weinberg RA. The hallmarks of cancer. Cell. 2000;100(1):57-70.

20. Karp G, Pruitt NL. Cell and molecular biology: Concepts and experiments. John Wiley & Sons New York; 1996.

21. Artandi SE, DePinho RA. Telomeres and telomerase in cancer. Carcinogenesis. 2010;31(1):9-18.

22. Lemmon MA, Schlessinger J. Cell signaling by receptor tyrosine kinases. Cell. 2010;141(7):1117-1134.

23. Tsang WP, Kwok TT. The miR-18a* microRNA functions as a potential tumor suppressor by targeting on K-ras. Carcinogenesis. 2009;30(6):953-959.

24. Drosten M, Dhawahir A, Sum EY, et al. Genetic analysis of ras signalling pathways in cell proliferation, migration and survival. EMBO J. 2010;29(6):1091-1104.

25. Burkhart DL, Sage J. Cellular mechanisms of tumour suppression by the retinoblastoma gene. Nature Reviews Cancer. 2008;8(9):671-682.

26. Curto M, Cole BK, Lallemand D, Liu C, McClatchey AI. Contact-dependent inhibition of EGFR signaling by Nf2/merlin. J Cell Biol. 2007;177(5):893-903.

27. Morrow KA, Shevde LA. Merlin: The wizard requires protein stability to function as a tumor suppressor. Biochimica et Biophysica Acta (BBA) - Reviews on Cancer. 2012;1826(2):400-406. doi: http://dx.doi.org/10.1016/j.bbcan.2012.06.005.

28. Bretscher A, Chambers D, Nguyen R, Reczek D. ERM-merlin and EBP50 protein families in plasma membrane organization and function. Annu Rev Cell Dev Biol. 2000;16(1):113-143.

29. Shen S, Kepp O, Michaud M, et al. Association and dissociation of autophagy, apoptosis and necrosis by systematic chemical study. Oncogene. 2011;30(45):4544-4556.

30. Bronchud MH, Foote M, Giaccone G, Olopade O, Workman P, Antman K. Principles of molecular oncology. . 2008.

31. Amaravadi RK, Thompson CB. The roles of therapy-induced autophagy and necrosis in cancer treatment. Clinical Cancer Research. 2007;13(24):7271-7279.

32. Mathew R, Karantza-Wadsworth V, White E. Role of autophagy in cancer. Nature Reviews Cancer. 2007;7(12):961-967.

33. Rosenfeldt MT, Ryan KM. The role of autophagy in tumour development and cancer therapy. Expert reviews in molecular medicine. 2009;11:e36.

34. Weinberg RA. The biology of cancer. Vol 255. Garland Science New York; 2007.

35. Nagy JA, Chang S, Shih S, Dvorak AM, Dvorak HF. Heterogeneity of the tumor vasculature. . 2010;36(3):321.

36. Hanahan D, Folkman J. Patterns and emerging mechanisms of the angiogenic switch during tumorigenesis. Cell. 1996;86(3):353-364. doi: http://dx.doi.org/10.1016/S0092-8674(00)80108-7.

37. Holmgren L, O'Reilly MS, Folkman J. Dormancy of micrometastases: Balanced proliferation and apoptosis in the presence of angiogenesis suppression. Nat Med. 1995;1(2):149-153.

38. Baeriswyl V, Christofori G. The angiogenic switch in carcinogenesis. Semin Cancer Biol. 2009;19(5):329-337. doi: http://dx.doi.org/10.1016/j.semcancer.2009.05.003.

39. Gramatikoff K. VEGF, hypoxia, and angiogenesis pathway. http://www.biocarta.com/genes/PathwayGenesearch.asp. Updated 2013.

40. Sriram M, Hall JJ, Grohmann NC, et al. Design, synthesis and biological evaluation of dihydronaphthalene and benzosuberene analogs of the combretastatins as inhibitors of tubulin polymerization in cancer chemotherapy. Bioorg Med Chem. 2008;16(17):8161-8171.

41. Talmadge JE, Fidler IJ. AACR centennial series: The biology of cancer metastasis: Historical perspective. Cancer Res. 2010;70(14):5649-5669.

42. Stoletov K, Kato H, Zardouzian E, et al. Visualizing extravasation dynamics of metastatic tumor cells. J Cell Sci. 2010;123(13):2332-2341.

43. Coghlin C, Murray GI. Current and emerging concepts in tumour metastasis. J Pathol. 2010;222(1):1-15. doi: 10.1002/path.2727.

44. Gunasinghe ND, Wells A, Thompson EW, Hugo HJ. Mesenchymal–epithelial transition (MET) as a mechanism for metastatic colonisation in breast cancer. Cancer Metastasis Rev. 2012;31(3-4):469-478.

45. Pećina-Šlaus N. Tumor suppressor gene E-cadherin and its role in normal and malignant cells. Cancer cell international. 2003;3(1):17.

46. Mohamed MM, Sloane BF. Cysteine cathepsins: Multifunctional enzymes in cancer. Nature Reviews Cancer. 2006;6(10):764-775.

47. Devetzi M, Scorilas A, Tsiambas E, et al. Cathepsin B protein levels in endometrial cancer: Potential value as a tumour biomarker. Gynecol Oncol. 2009;112(3):531-536.

48. Sosič I, Mirković B, Arenz K, Štefane B, Kos J, Gobec S. Development of new cathepsin B inhibitors: Combining bioisosteric replacements and structure-based design to explore the Structure–Activity relationships of nitroxoline derivatives. J Med Chem. 2013;56(2):521-533.

49. Koblinski JE, Ahram M, Sloane BF. Unraveling the role of proteases in cancer. Clinica chimica acta. 2000;291(2):113-135.

50. Premzl A, Zavašnik-Bergant V, Turk V, Kos J. Intracellular and extracellular cathepsin B facilitate invasion of MCF-10A neoT cells through reconstituted extracellular matrix in vitro. Exp Cell Res. 2003;283(2):206-214.

51. Kishore Kumar G, Chavarria GE, Charlton-Sevcik AK, et al. Design, synthesis, and biological evaluation of potent thiosemicarbazone based cathepsin L inhibitors. Bioorg Med Chem Lett. 2010;20(4):1415-1419.

52. Kumar GDK, Chavarria GE, Charlton-Sevcik AK, et al. Functionalized benzophenone, thiophene, pyridine, and fluorene thiosemicarbazone derivatives as inhibitors of cathepsin L. Bioorg Med Chem Lett. 2010;20(22):6610-6615. doi: http://dx.doi.org/10.1016/j.bmcl.2010.09.026.

53. Siles R, Chen S, Zhou M, Pinney KG, Trawick ML. Design, synthesis, and biochemical evaluation of novel cruzain inhibitors with potential application in the treatment of chagas' disease. Bioorg Med Chem Lett. 2006;16(16):4405-4409.

54. Song J, Jones LM, Kumar GK, et al. Synthesis and biochemical evaluation of thiochromanone thiosemicarbazone analogues as inhibitors of cathepsin L. ACS Medicinal Chemistry Letters. 2012;3(6):450-453.

55. Chavarria GE, Horsman MR, Arispe WM, et al. Initial evaluation of the antitumour activity of KGP94, a functionalized benzophenone thiosemicarbazone inhibitor of cathepsin L. Eur J Med Chem. 2012.

56. Tozer GM, Kanthou C, Baguley BC. Disrupting tumour blood vessels. Nature Reviews Cancer. 2005;5(6):423-435.

57. Clémenson C, Chargari C, Deutsch E. Combination of vascular disrupting agents and ionizing radiation. Crit Rev Oncol. 2012;86:143-160.

58. Hua J, Sheng Y, Pinney KG, et al. Oxi4503, a novel vascular targeting agent: Effects on blood flow and antitumor activity in comparison to combretastatin A-4 phosphate. Anticancer Res. 2002;23(2B):1433-1440.

59. Rice L, Pampo C, Lepler S, Rojiani AM, Siemann DW. Support of a free radical mechanism for enhanced antitumor efficacy of the microtubule disruptor OXi4503. Microvasc Res. 2011;81(1):44-51.

60. Lynn Trawick M. An amino-benzosuberene analogue that inhibits tubulin assembly and demonstrates remarkable cytotoxicity. MedChemComm. 2012;3(6):720-724.

61. Turk V, Turk B, Turk D. EMBO Journal. 2001;20:4629-4633.

62. Bank U, Krüger S, Langner J, Roessner A. Review: Peptidases and peptidase inhibitors in the pathogenesis of diseases. In: Cellular peptidases in immune functions and diseases 2. Springer; 2002:349-378.

63. Turk V, Stoka V, Vasiljeva O, et al. Cysteine cathepsins: From structure, function and regulation to new frontiers. Biochimica et Biophysica Acta (BBA)-Proteins and Proteomics. 2012;1824(1):68-88.

64. Robinson MW, Dalton JJP. Cysteine proteases of pathogenic organisms. Vol 712. Springer; 2011.

65. Reinheckel T, Peters C, Krüger A, Turk B, Vasiljeva O. Differential impact of cysteine cathepsins on genetic mouse models of de novo carcinogenesis: Cathepsin B as emerging therapeutic target. Frontiers in pharmacology. 2012;3.

66. Watts C. The endosome–lysosome pathway and information generation in the immune system. Biochimica et Biophysica Acta (BBA)-Proteins and Proteomics. 2012;1824(1):14-21.

67. Gunatilleke SS, Barrios AM. Journal of Inorganic Biochemistry. 2008;102:555-563.

68. Frlan R, Gobec S. Current Medicinal Chemistry. 2006;13:2309-2327.

69. Turk V, Turk B. Acta Chimica Slovenica. 2008;55:727-738.

70. Coulibaly S, Schwihla H, Abrahamson M, et al. Modulation of invasive properties of murine squamous carcinoma cells by heterologous expression of cathepsin B and cystatin C. International journal of cancer. 1999;83(4):526-531.

71. Inayat S, Larsson A, Ronquist GK, et al. High levels of cathepsins B, L and S in human seminal plasma and their association with prostasomes. Andrologia. 2012;44(6):423-427.

72. Neves FAR, Duncan KG, Baxter JD. Hypertension. 1996;27:514-517.

73. Podgorski I, Sloane BF. Biochemical Society Symposia. 2003;70:263-276.

74. Wickramasinghea NS, Nagaraja NS, Vigneswaranc N, Zacharias W. Archives of Biochemistry and Biophysics. 2005;436:187-195.

75. Mohamed M, Cavallo-Medved D, Sloane BF. Biological Chemistry. 2008;389:1117-1121.

76. Im E, Venkatakrishnan A, Kazlauskas A. Cathepsin B regulates the intrinsic angiogenic threshold of endothelial cells. Mol Biol Cell. 2005;16(8):3488-3500.

77. Kruszewski WJ, Rzepko R, Wojtacki J, et al. Overexpression of cathepsin B correlates with angiogenesis in colon adenocarcinoma. Neoplasma. 2004;51(1):38-43.

78. Jedeszko C, Sloane BF. Cysteine cathepsins in human cancer. Biol Chem. 2004;385(11):1017-1027.

79. Bell-McGuinn KM, Garfall AL, Bogyo M, Hanahan D, Joyce JA. Inhibition of cysteine cathepsin protease activity enhances chemotherapy regimens by decreasing tumor growth and invasiveness in a mouse model of multistage cancer. Cancer Res. 2007;67(15):7378-7385.

80. Joyce JA, Baruch A, Chehade K, et al. Cathepsin cysteine proteases are effectors of invasive growth and angiogenesis during multistage tumorigenesis. Cancer cell. 2004;5(5):443-453.

81. Matarrese P, Ascione B, Ciarlo L, et al. Cathepsin B inhibition interferes with metastatic potential of human melanoma: An in vitro and in vivo study. Mol Cancer. 2010;9:207.

82. Withana NP, Blum G, Sameni M, et al. Cathepsin B inhibition limits bone metastasis in breast cancer. Cancer Res. 2012;72(5):1199-1209.

83. Ritonja A, Popovic T, Turk V, Wiedenmann K, Machleidt W. Amino acid sequence of human liver cathepsin B. FEBS Lett. 1985;181(1):169-172.

84. Pungerčar JR, Caglič D, Sajid M, et al. Autocatalytic processing of procathepsin B is triggered by proenzyme activity. FEBS Journal. 2009;276(3):660-668.

85. Bialas A, Kafarski P. Proteases as anti-cancer targets-molecular and biological basis for development of inhibitor-like drugs against cancer. Anti-Cancer Agents in Medicinal Chemistry (Formerly Current Medicinal Chemistry. 2009;9(7):728-762.

86. Caglič D, Pungerčar JR, Pejler G, Turk V, Turk B. Glycosaminoglycans facilitate procathepsin B activation through disruption of propeptide-mature enzyme interactions. J Biol Chem. 2007;282(45):33076-33085.

87. Brix K, Dunkhorst A, Mayer K, Jordans S. Cysteine cathepsins: Cellular roadmap to different functions. Biochimie. 2008;90(2):194-207.

88. Sameni M, Elliot E, Ziegler G, Fortgens PH, Dennison C, Sloane BF. Pathology Oncology Research. 1995;1:43-53.

89. Musil D, Zucic D, Turk D, et al. The EMBO Journal. 1991;10:2321-2330.

90. Roshy S, Sloane BF, Moin K. Cancer and Metastasis Reviews. 2003;22:271-286.

91. Tjäderhane L, Nascimento FD, Breschi L, et al. Optimizing dentin bond durability: Control of collagen degradation by matrix metalloproteinases and cysteine cathepsins. Dental Materials. 2013;29(1):116-135. doi: http://dx.doi.org/10.1016/j.dental.2012.08.004.

92. Horn M, Jílková A, Vondrášek J, Marešová L, Caffrey CR, Mareš M. Mapping the pro-peptide of the schistosoma mansoni cathepsin B1 drug target: Modulation of inhibition by heparin and design of mimetic inhibitors. ACS Chemical Biology. 2011;6(6):609-617.

93. Yan S, Sloane BF. Biological chemistry. 2003;384:845-854.

94. De Stefanis D, Demoz M, Dragonetti A, et al. Cell and Tissue Research. 1997;289:109-117.

95. Boatright KM, Salvesen GS. Caspase activation. Biochem Soc Symp. 2003;(70)(70):233-242.

96. Gerke V, Moss SE. Physiological Reviews. 2002;82:331-371.

97. Mai J, Finley RL, Waisman DM, Sloane BF. Journal of Biological Chemistry. 2000;275:12806-12812.

98. The UniProt Consortium. The universal protein resource (UniProt) in 2010. http://www.uniprot.org/uniprot/P07858.html. Accessed August 23, 2010.

99. Moreland JL, Gramada A, Buzko OV, Zhang Q, Bourne PE. The molecular biology toolkit (mbt): A modular platform for developing molecular visualization applications. BMCBioinformatics. http://www.pdb.org/robohelp/viewers/proteinworkshop.htm. Accessed August 4, 2010.

100. Sloane BF, Moin K, Krepela E, Rozhin J. Cathepsin B and its endogenous inhibitors: The role in tumor malignancy. Cancer Metastasis Rev. 1990;9(4):333-352.

101. Krupa JC, Hasnain S, Nagler DK, Menard R, Mort JS. Biochemical Journal. 2002;361:613-619.

102. Mort JS, Buttle DJ. International Journal of Biochemistry & Cell Biology. 1997;29:715-720.

103. Yamamoto A, Tomoo K, Matsugi K, et al. Structural basis for development of cathepsin B-specific noncovalent-type inhibitor: Crystal structure of cathepsin B–E64c complex. Biochimica et Biophysica Acta (BBA)-Protein Structure and Molecular Enzymology. 2002;1597(2):244-251.

104. Baudys M, Meloun B, Gan-Erdene T, Pohl J, Kostka V. Disulfide bridges of boviae spleen cathepsin B. Biol Chem Hoppe-Seyler. 1990;371(1):485-492.

105. Redzynia I, Ljunggren A, Abrahamson M, et al. Journal of Biological Chemistry. 2008;283:22815-22825.

106. Naudin C, Lecaille F, Chowdhury S, et al. The occluding loop of cathepsin B prevents its effective inhibition by human kininogens. J Mol Biol. 2010;400(5):1022-1035.

107. Schenker P, Alfarano P, Kolb P, Caflisch A, Baici A. A double- headed cathepsin B inhibitor devoid of warhead. Protein Science. 2008;17(12):2145-2155.

108. Illy C, Quraishi O, Wang J, Purisima E, Vernet T, Mort JS. Role of the occluding loop in cathepsin B activity. J Biol Chem. 1997;272(2):1197-1202.

109. Tomoo K. Development of cathepsin inhibitors and structure-based design of cathepsin B-specific inhibitor. Current topics in medicinal chemistry. 2010;10(7):696-707.

110. Turk B, Turk D, Turk V. Lysosomal cysteine proteases: More than scavengers. Biochimica et Biophysica Acta (BBA)-Protein Structure and Molecular Enzymology. 2000;1477(1):98-111.

111. Falgueyret J, Black WC, Cromlish W, et al. An activity-based probe for the determination of cysteine cathepsin protease activities in whole cells. Anal Biochem. 2004;335(2):218-227.

112. Portaro F, Santos A, Cezari M, Juliano M, JULIANO L, CARMONA E. Probing the specificity of cysteine proteinases at subsites remote from the active site: Analysis of P4, P3, P2′ and P3′ variations in extended substrates. Biochem J. 2000;347:123-129.

113. Hughes SJ, Glover TW, Zhu X, et al. A novel amplicon at 8p22–23 results in overexpression of cathepsin B in esophageal adenocarcinoma. Proceedings of the National Academy of Sciences. 1998;95(21):12410-12415.

114. Lin L, Aggarwal S, Glover TW, Orringer MB, Hanash S, Beer DG. Cancer Research. 2000;60:1341-1347.

115. Vasiljeva O, Dolinar M, Pungerčar JR, Turk V, Turk B. Recombinant human procathepsin S is capable of autocatalytic processing at neutral pH in the presence of glycosaminoglycans. FEBS Lett. 2005;579(5):1285-1290.

116. Turk B, Turk D, Salvesen GS. Current Pharmaceutical Design. 2002;8:1623-1637.

117. Turk B. Targeting proteases: Successes, failures and future prospects. Nature reviews Drug discovery. 2006;5(9):785-799.

118. Bevec T, Stoka V, Pungercic G, Dolenc I, Turk V. Major histocompatibility complex class II-associated p41 invariant chain fragment is a strong inhibitor of lysosomal cathepsin L. J Exp Med. 1996;183(4):1331-1338.

119. Watanabe D, Yamamoto A, Tomoo K, et al. Quantitative evaluation of each catalytic subsite of cathepsin B for inhibitory activity based on inhibitory activity–binding mode relationship of epoxysuccinyl inhibitors by X-ray crystal structure analyses of complexes. J Mol Biol. 2006;362(5):979-993.

120. Schaschke N, Assfalg-Machleidt I, Laßleben T, Sommerhoff C, Moroder L, Machleidt W. Epoxysuccinyl peptide-derived affinity labels for cathepsin B. FEBS Lett. 2000;482(1):91-96.

121. Dai Y, Hedstrom L, Abeles RH. Inactivation of cysteine proteases by (acyloxy) methyl ketones using S'-P'interactions. Biochemistry (N Y). 2000;39(21):6498-6502.

122. Cunha RL, Urano ME, Chagas JR, et al. Tellurium-based cysteine protease inhibitors: Evaluation of novel organotellurium (IV) compounds as inhibitors of human cathepsin B. Bioorg Med Chem Lett. 2005;15(3):755-760.

123. Zhou Z, Wang Y, Bryant SH. Journal of Computational Chemistry. 2009;30:2165-2175.

124. Ruettinger W, Dismukes GC. Chemical Reviews. 1997;97:1-24.

125. Conroy JL, Seto CT. Demonstration by 13C NMR studies that tetrahydropyranone-based inhibitors bind to cysteine proteases by reversible formation of a hemithioketal adduct. J Org Chem. 1998;63(7):2367-2370.

126. Scheidt KA, Roush WR, McKerrow JH, Selzer PM, Hansell E, Rosenthal PJ. Structure-based design, synthesis and evaluation of conformationally constrained cysteine protease inhibitors. Bioorg Med Chem. 1998;6(12):2477-2494.

127. Wieczerzak E, Rodziewicz-Motowidlo S, Jankowska E, Gieldon A, Ciarkowski J. Journal of Peptide Science. 2007;13:536-543.

128. Casini A, Edafe F, Erlandsson M, et al. Dalton Transactions. 2010;39:5556-5563.

129. Casini A, Gabbiani C, Sorrentino F, et al. Emerging protein targets for anticancer metallodrugs: Inhibition of thioredoxin reductase and cathepsin B by antitumor ruthenium(II)−Arene compounds. J Med Chem. 2008;51(21):6773-6781. http://dx.doi.org/10.1021/jm8006678.

130. Li Y, Qian Z, Kim S. Bioorganic & Medicinal Chemistry Letters. 2008;18:6130-6134.

131. Yong L, Zhong-Ji Q, Se-Kwon K. Bioorganic & Medicinal Chemistry letters. 2008;118:6130-6134.

132. Murayama S, Nakao Y, Matsunaga S. Tetrahedron Letters. 2008;49:4186-4188.

133. Du X, Guo C, Hansell E, et al. Synthesis and structure-activity relationship study of potent trypanocidal thio semicarbazone inhibitors of the trypanosomal cysteine protease cruzain. J Med Chem. 2002;45(13):2695-2707. Accessed 2 August 2013.

134. Fujii N, Mallari JP, Hansell EJ, et al. Discovery of potent thiosemicarbazone inhibitors of rhodesain and cruzain. Bioorganic and Medicinal Chemistry Letters. 2005;15(1):121-123. Accessed 2 August 2013.

135. Kumar G, Chavarria GE, Charlton-Sevcik AK, et al. Functionalized benzophenone, thiophene, pyridine, and fluorene thiosemicarbazone derivatives as inhibitors of cathepsin L. Bioorg Med Chem Lett. 2010;20(22):6610-6615.

136. Fersht A. Structure and mechanism in protein science: A guide to enzyme catalysis and protein folding. Macmillan; 1999.

137. Silverman RB. Organic chemistry of enzyme-catalyzed reactions. Access Online via Elsevier; 2002.

138. Copeland RA. Enzymes: A practical introduction to structure, mechanism, and data analysis. Wiley. com; 2004.

139. Copeland RA. Evaluation of enzyme inhibitors in drug discovery. A guide for medicinal chemists and pharmacologists. Methods Biochem Anal. 2005;46:1-265.

140. Uppuluri S, Knipling L, Sackett D, Wolff J. Proc Natl Acad Sci USA. 1993;90:11598-11602.

141. Morrison JF. The slow-binding and slow, tight-binding inhibition of enzyme-catalysed reactions. Trends Biochem Sci. 1982;7(3):102-105.

142. Strelow J, Dewe W, Iversen PW. Mechanism of action assay for enzymes. http://www.ncbi.nlm.nih.gov/books/NBK92001. Updated 2012. Accessed October 20, 2012.

143. Steverding D. The cathepsin B-selective inhibitors CA-074 and CA-074Me inactivate cathepsin L under reducing conditions. Open Enzyme Inhibition Journal. 2011;4:11-16.

144. Ritonja A, Popović T, Kotnik M, Machleidt W, Turk V. Amino acid sequences of the human kidney cathepsins H and L. FEBS Lett. 1988;228(2):341-345.

145. Serveau Avesque C, Martino MF, Hervé Grépinet V, et al. Active cathepsins B, H, K, L and S in human inflammatory bronchoalveolar lavage fluids. Biology of the Cell. 2006;98(1):15-22.

146. Gunatilleke SS. Inhibition of cysteine proteases by gold (I) complexes: A kinetic and mechanistic investigation. ProQuest; 2007.

147. Wisastra R, Ghizzoni M, Maarsingh H, Minnaard AJ, Haisma HJ, Dekker FJ. Isothiazolones; thiol-reactive inhibitors of cysteine protease cathepsin B and histone acetyltransferase PCAF. Organic & Biomolecular Chemistry. 2011;9(6):1817-1822.

148. Caglič D, Kosec G, Bojič L, Reinheckel T, Turk V, Turk B. Murine and human cathepsin B exhibit similar properties: Possible implications for drug discovery. Biol Chem. 2009;390(2):175-179.

149. Gounaris A, Slater E. Cathepsin B from human renal cortex. Biochem J. 1982;205:295-302.

150. Monk KA, Siles R, Hadimani MB, et al. Bioorganic & Medicinal Chemistry. 2006;14:3231-3244.

151. Siemann DW. The unique characteristics of tumor vasculature and preclinical evidence for its selective disruption by tumor-vascular disrupting agents. Cancer Treat Rev. 2011;37(1):63-74.

152. Bussolati B, Grange C, Camussi G. Tumor exploits alternative strategies to achieve vascularization. The FASEB Journal. 2011;25(9):2874-2882.

153. Neri D, Bicknell R. Tumour vascular targeting. Nature Reviews Cancer. 2005;5(6):436-446.

154. Brown NS, Bicknell R. Hypoxia and oxidative stress in breast cancer. oxidative stress: Its effects on the growth, metastatic potential and response to therapy of breast cancer. Breast Cancer Res. 2001;3(5):323-327.

155. Vaupel P, Mayer A. Hypoxia in cancer: Significance and impact on clinical outcome. Cancer Metastasis Rev. 2007;26(2):225-239.

156. Brown JM. Tumor hypoxia in cancer therapy. Meth Enzymol. 2007;435:295-321.

157. Kim Y, West XZ, Byzova TV. Inflammation and oxidative stress in angiogenesis and vascular disease. Journal of Molecular Medicine. 2013:1-6.

158. Hinnen P, Eskens F. Vascular disrupting agents in clinical development. Br J Cancer. 2007;96(8):1159-1165.

159. Clémenson C, Chargari C, Deutsch E. Combination of vascular disrupting agents and ionizing radiation. Crit Rev Oncol. 2012.

160. Zheng S, Zhong Q, Jiang Q, et al. Discovery of a series of thiazole derivatives as novel inhibitors of metastatic cancer cell migration and invasion. ACS medicinal chemistry letters. 2013;4(2):191-196.

161. Ty N, Pontikis R, Chabot GG, et al. Synthesis and biological evaluation of enantiomerically pure cyclopropyl analogues of combretastatin A4. Bioorg Med Chem. 2013;21(5):1357-1366. doi: http://dx.doi.org/10.1016/j.bmc.2012.11.056.

162. Jordan MA, Wilson L. Microtubules as a target for anticancer drugs. Nature Reviews Cancer. 2004;4(4):253-265.

163. Lin CM, Ho HH, Pettit GR, Hamel E. Antimitotic natural products combretastatin A-4 and combretastatin A-2: Studies on the mechanism of their inhibition of the binding of colchicine to tubulin. Biochemistry (N Y). 1989;28(17):6984-6991.

164. Tron GC, Pirali T, Sorba G, Pagliai F, Busacca S, Genazzani AA. Journal of Medicinal Chemistry. 2006;49:3033-3044.

165. Stokes JB, Adair SJ, Slack-Davis JK, et al. Inhibition of focal adhesion kinase by PF-562,271 inhibits the growth and metastasis of pancreatic cancer concomitant with altering the tumor microenvironment. Molecular cancer therapeutics. 2011;10(11):2135-2145.

166. Lippert III JW. Vascular disrupting agents. Bioorg Med Chem. 2007;15(2):605-615.

167. National Cancer Institute. www.cancer.org. Accessed August 7, 2010.

168. Karp G. The cytoskeleton and cell motility. In: Witt K, Osnato G, eds. Danvers, MA: john wiley and sons; 2008:32-356.

169. Birukova AA, Birukov KG, Smurova K, et al. FASEB Journal. 2004;18:1879-1890.

170. Mollinedo F, Gajate C. Apoptosis. 2003;8:413-450.

171. Desai A, Mitchison TJ. Microtubule polymerization dynamics. Annu Rev Cell Dev Biol. 1997;13(1):83-117.

172. Nakagawa-Goto K, Wu P, Lai C, et al. Antitumor agents. 284. new desmosdumotin B analogues with bicyclic B-ring as cytotoxic and antitubulin agents. J Med Chem. 2011;54(5):1244-1255.

173. Bhattacharyya B, Panda D, Gupta S, Banerjee M. Medicinal Research Reviews. 2008;28:155-183.

174. Uppuluri S, Knipling L, Sackett DL, Wolff J. Proceedings of the National Academy of Sciences of the United States of America. 1992;90:11598-11602.

175. Kiselyov A, Balakin KV, Tkachenko SE, Savchuk N, Ivachtchenko AV. Anti-Cancer Agents in Medicinal Chemistry. 2007;7:189-208.

176. Sorensen CS, Lukas C, Kramer ER, Peters JM, Bartek J, Lukas J. Molecular and Cellular Biology. 2001;21:3692-3703.

177. Lee RM, Gewirtz DA. Drug Development Research. 2008;69:352-358.

178. Ravelli RBG, Gigant B, Curmi PA, et al. Nature. 2004;428:198-202.

179. Dorleans A, Gigant B, Ravelli RBG, Mailliet P, Mikol V, Knossow M. Proceedings of the National Academy of Sciences of the United States of America. 2009;106:13775-13779.

180. Panda D, Daijo JE, Jordan M, Wilson L. Biochemistry. 1995;34:9921-9929.

181. Boureux A, Vignal E, Faure S, Fort P. Molecular Biology and Evolution. 2007;24:203-216.

182. Ren X, Kiosses WB, Schwartz MA. Regulation of the small GTP-binding protein rho by cell adhesion and the cytoskeleton. EMBO J. 1999;18(3):578-585.

183. Ren Y, Li R, Zheng Y, Busch H. The Journal of Biological Chemistry. 1998;273:34954-34960.

184. Pinney KP, Pettit GR, Trawick ML, Jelinek C, Chaplin DJ. The discovery and development of the combretastatins. InAntitumor agents from natural products. In: David Kingston, David Newman, and Gordon Cragg, ed. CRC press. Boca Raton, Florida: Taylor and Francis Group; 2010.

185. Limame R, Wouters A, Pauwels B, et al. Comparative analysis of dynamic cell viability, migration and invasion assessments by novel real-time technology and classic endpoint assays. PloS one. 2012;7(10):e46536.

186. Nakayama S, Torikoshi Y, Takahashi T, et al. Prediction of paclitaxel sensitivity by CDK1 and CDK2 activity in human breast cancer cells. Breast Cancer Res. 2009;11(1):R12.

187. Chavez KJ, Garimella SV, Lipkowitz S. Triple negative breast cancer cell lines: One tool in the search for better treatment of triple negative breast cancer. Breast disease. 2010;32(1):35-48.

188. O'Boyle NM, Carr M, Greene LM, et al. Synthesis and evaluation of azetidinone analogues of combretastatin A-4 as tubulin targeting agents. J Med Chem. 2010;53(24):8569-8584.

189. Stengel C, Newman S, Leese M, Potter B, Reed M, Purohit A. Class III β-tubulin expression and in vitro resistance to microtubule targeting agents. Br J Cancer. 2009;102(2):316-324.

190. Shelanski ML, Gaskin F, Cantor CR. Microtubule assembly in the absence of added nucleotides. Proceedings of the National Academy of Sciences. 1973;70(3):765-768.

191. Borisy GG, Taylor E. THE MECHANISM OF ACTION OF COLCHICINE binding of colchincine-3H to cellular protein. J Cell Biol. 1967;34(2):525-533.

192. Hettinger TP, Craig LC. Edeine. II. composition of the antibiotic peptide edeine A. Biochemistry (N Y). 1968;7(12):4147-4153.

193. Bradford MM. A rapid and sensitive method for the quantitation of microgram quantities of protein utilizing the principle of protein-dye binding. Anal Biochem. 1976;72(1):248-254.

194. Rajendra P. Tanpure, Clinton S. George, Tracy E. Strecker, Laxman Devkota, Justin K. Tidmore, Chen-Ming Lin, Christine A. Herdman, Matthew T. MacDonough, Madhavi Sriram, David J. Chaplin, Mary Lynn Trawick, and Kevin G. Pinney. Synthesis of structurally diverse benzosuberene analogues and their biological evaluation as anti-cancer agents. .

195. Mugabe BE. Structure-activity relationships and thermodynamics of combretastatin A-4 and A-1 derivatives as potential inhibitors of tubulin polymerization. 2005.

196. Hamel E, Lin CM. Stabilization of the colchicine-binding activity of tubulin by organic acids. Biochimica et Biophysica Acta (BBA)-General Subjects. 1981;675(2):226-231.

197. Ray K, Bhattacharyya B, Biswas BB. Anion-induced increases in the affinity of colcemid binding to tubulin. European Journal of Biochemistry. 1984;142(3):577-581.

198. Tahir SK, Kovar P, Rosenberg SH, Ng S. Rapid colchicine competition-binding scintillation proximity assay using biotin-labeled tubulin. BioTechniques. 2000;29(1):156-161.

199. Luyckx M, Brunet C, Cazin M. Binding of colchicine to beef brain tubulin: Influence of methodology on binding constants. Methods Find Exp Clin Pharmacol. 1984;6(11):679-684.

200. Pettit GR, Grealish MP, Herald DL, Boyd MR, Hamel E, Pettit RK. Antineoplastic agents. 443. synthesis of the cancer cell growth inhibitor hydroxyphenstatin and its sodium diphosphate prodrug. J Med Chem. 2000;43(14):2731-2737.

201. Z. Darzynkiewicz, H.D. Halicka, and H. Zhao. Analysis of cellular DNA content by flow and laser scanning cytophotometry. Adv Exp Med Biol. 2010;676:137-147.

202. Vega FM, Fruhwirth G, Ng T, Ridley AJ. RhoA and RhoC have distinct roles in migration and invasion by acting through different targets. J Cell Biol. 2011;193(4):655-665.

203. Shi S, Noda M, Kitayama H. Rap1 mutants with increased affinity for the guanine-nucleotide exchange factor C3G. Oncogene. 2004;23(54):8711-8719.

204. Cáceres M, Guerrero J, Martínez J. Overexpression of RhoA-GTP induces activation of the epidermal growth factor receptor, dephosphorylation of focal adhesion kinase and increased motility in breast cancer cells. Exp Cell Res. 2005;309(1):229-238.